25th International Scientific Conference

APPLIED MECHANICS 2024

AM 2024

BOOK OF ARTICLES

25th International Scientific Conference

APPLIED MECHANICS 2024

Department of Applied Mechanics
Faculty of Mechanical Engineering
University of Žilina

in cooperation with

Scientific and Technical Society at the University of Žilina

TOPICS OF THE CONFERENCE

Biomechanics
Computational mechanics
Durability and reliability of engineering structures
Dynamics
Experimental mechanics
Fluid mechanics
Fracture mechanics and fatigue
Mechatronics
Multibody dynamics
Noise and vibrations
Strength of materials, creep, plasticity
Structural mechanics

PARTNERS

HUMUSOFT®

MathWorks®
Authorized Reseller

SCHAEFFLER

ENGINEERING
TOMORROW

Danfoss

SCIENTIFIC COMMITTEE

Pawel Bachorz pawel.bachorz@polsl.pl
Department of Applied Mechanics, FME SUT, Gliwice (PL)

Miroslav Byrtus mbyrtus@kme.zcu.cz
Department of Mechanics, FAS UWB, Pilsen (CZ)

Karel Frydrýšek karel.frydrysek@vsb.cz
Department of Mechanics of Materials, VŠB-TUO, Ostrava (CZ)

Michal Hajžman mhajzman@kme.zcu.cz
Department of Mechanics, FAS UWB, Pilsen (CZ)

Radim Halama radim.halama@vsb.cz
Department of Mechanics of Materials, VŠB-TUO, Ostrava (CZ)

Pavel Hutař hutar@ipm.cz
Institute of Physics of Materials AS CR, Brno (CZ)

Roland Jančo roland.janco@stuba.sk
Institute of Applied Mechanics and Mechatronics, FME STU, Bratislava (SK)

Pawel Jureczko pawel.jureczko@polsl.pl
Department of Applied Mechanics, FME SUT, Gliwice (PL)

Vladimír Kutiš vladimir.kutis@stuba.sk
Institute of Automotive Mechatronics, FEI STU, Bratislava (SK)

Luboš Náhlík nahlik@ipm.cz
Institute of Physics of Materials AS CR, Brno (CZ)

Zdeněk Padovec zdenek.padovec@fs.cvut.cz
Department of Mechanics, Biomechanics and Mechatronics, FME CTU, Prague (CZ)

Radek Sedláček radek.sedlacek@fs.cvut.cz
Department of Mechanics, Biomechanics and Mechatronics, FME CTU, Prague (CZ)

Michal Sivčák michal.sivcak@tul.cz
Department of Applied Mechanics, FME TUL, Liberec (CZ)

Milan Vaško milan.vasko@fstroj.uniza.sk
Department of Applied Mechanics, FME ŽU, Žilina (SK)

APPLIED MECHANICS CONFERENCES

1st conference AM 1999	March 16–18	Brno, Czech Republic
2nd conference AM 2000	April 3–6	Liberec, Czech Republic
3rd conference AM 2001	April 2–5	Nečtiny, Czech Republic
4th conference AM 2002	April 8–11	Ostrava, Czech Republic
5th conference AM 2003	March 24–27	Jaworzynka, Poland
6th conference AM 2004	March 22–25	Kočovce, Slovakia
7th conference AM 2005	March 29–April 1	Hrotovice, Czech Republic
8th conference AM 2006	April 3–5	Srní, Czech Republic
9th conference AM 2007	April 16–19	Malenovice, Czech Republic
10th conference AM 2008	April 7–10	Wisła, Poland
11th conference AM 2009	April 6–8	Smolenice, Slovakia
12th conference AM 2010	April 19–21	Jablonec nad Nisou, Czech Republic
13th conference AM 2011	April 18–20	Velké Bílovice, Czech Republic
14th conference AM 2012	April 16–18	Plzeň, Czech Republic
15th conference AM 2013	April 15–18	Velké Karlovice, Czech Republic
16th conference AM 2014	April 14–16	Kraków, Poland
17th conference AM 2015	April 13–15	Kutná Hora, Czech Republic
18th conference AM 2016	April 11–13	Banská Štiavnica, Slovakia
19th conference AM 2017	April 25–27	Brno, Czech Republic
20th conference AM 2018	April 9–11	Myslovice, Czech Republic
21st conference AM 2019	April 15–17	Ostravice, Czech Republic
22nd conference AM 2021	April 22	Liberec, Czech Republic (online)
23rd conference AM 2022	April 4–6	Liblice, Czech Republic
24th conference AM 2023	April 19–21	Piešťany, Slovakia
25th conference AM 2024	April 17–19	Štrbské Pleso, Slovakia

https://am2024.uniza.sk/

TABLE OF CONTENTS

APPLIED MECHANICS 2024

April 17th – 19th, 2024
Hotel Toliar, Štrbské Pleso
Slovakia

DESIGN OF A LOW-COST ELECTRODYNAMIC SHAKER

Š. BERTA[1]*, V. GOGA[2]

The primary function of electrodynamic shakers involves generating a base vibrational excitation, enabling the measurement of the frequency response of various systems to obtain their modal properties. This article presents the design of a simple and cost-effective electrodynamic shaker, along with its power supply system, designed to generate the base excitation for investigating the energy harvesting capabilities of various configurations of piezoelectric energy harvesters.

Keywords: electrodynamic shaker, vibration excitation

INTRODUCTION

The electrodynamic vibration shaker is a device widely used in the industrial, automotive, and aerospace sectors for assessing the vibrational responses of various devices, equipment, and machinery. The electrodynamic shaker serves as a conventional instrument for conducting dynamic assessments on structures and can be correlated with base excitation of the system, wherein the excitation is prescribed in terms of kinematic motion parameters such as acceleration or displacement. Additionally, electrodynamic shakers are commonly used for cyclic fatigue testing, which involves performing a significant number of cycles near the endurance limit and is a costly and time-intensive process. Experimental tests are frequently carried out using electrodynamic testing machines to achieve a higher cycle count in a shorter time frame [1].

The general configuration of conventional electrodynamic shakers bears resemblance to that of a typical loudspeaker (Fig. 1a). Their principal characteristic entails the presence of an armature assembly actuated by a wound coil of wire exposed to a radial magnetic field. The armature is mechanically supported and situated within the housing of the shaker through the utilization of a flexure plate characterized by minimal axial rigidity. Although electrodynamic shaker systems find extensive use in various applications, comprehensive information concerning their design and the quantification of their performance advantages is notably scarce [2].

According to published research papers, most researchers today use electrodynamic shakers already developed by several companies (Philip Harris, Frederiksen, Pasco, etc.) (Fig. 1b). The primary focus of shaker research is to design various control strategies and controllers for precise

[1] **Ing. Šimon Berta**, Department of Applied Mechanics and Mechatronics, Institute of Automotive Mechatronics, Faculty of Electrical Engineering and Information Technology, Slovak University of Technology in Bratislava. Ilkovičova 3, Bratislava, Slovak Republic; simon.berta@stuba.sk
[2] **doc. Ing. Vladimír Goga, PhD.**, Department of Applied Mechanics and Mechatronics, Institute of Automotive Mechatronics, Faculty of Electrical Engineering and Information Technology, Slovak University of Technology in Bratislava. Ilkovičova 3, Bratislava, Slovak Republic; vladimir.goga@stuba.sk

displacement and acceleration control [3]. Other researchers propose identification and calibration methods for mathematical models of already developed shakers [4]. Commercially available electrodynamic vibration shakers provide superior stability, robustness, and accuracy of produced output signal. However, they are often expensive, heavy, and unsuitable for simpler applications where signal accuracy and stability are not essential. Therefore, a simpler and cost-effective device was designed to serve as a source of uniaxial base excitation. The device proposed in this paper is intended for researching vibrational piezoelectric energy harvesting and for educational purposes, specifically the modal analysis of small structures.

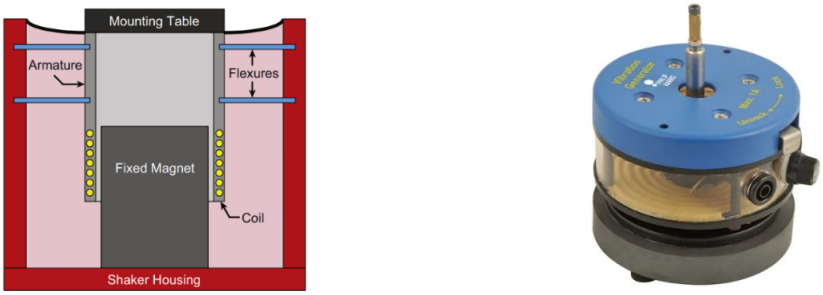

(a) **(b)**

Fig. 1 Simplified schematic (cross-section) of a typical electrodynamic shaker (a) [2], electrodynamic shaker – Philip Harris B8H30701 (b)

ELECTRODYNAMIC SHAKER DESIGN

The electrodynamic shaker, as shown in Fig. 2, utilizes a high-performance loudspeaker (VISATON SC13 8013) mounted inside the main body using a top cover and screws. A load table with a mounting platform is permanently fixed to the cone of the loudspeaker. The load table's uniaxial movement is secured by a support structure and plain bearing in the top cover (Fig. 2b). The bottom cover encloses the main body, which is fixed using screws. Four rubber legs are mounted on the bottom cover.

On the top cover, there is an additional mechanical protection particularly designed to prevent damage to the loudspeaker during the handling and installation of the measured equipment. This protection operates on a rotating principle, where in the closed position, four pillars support the load table (Fig. 2a). After turning the handle clockwise, the pillars move aside, unlocking the load table. All mechanical parts except loudspeaker were designed in Autodesk Inventor and 3D printed using PETG material (see Fig. 2a).

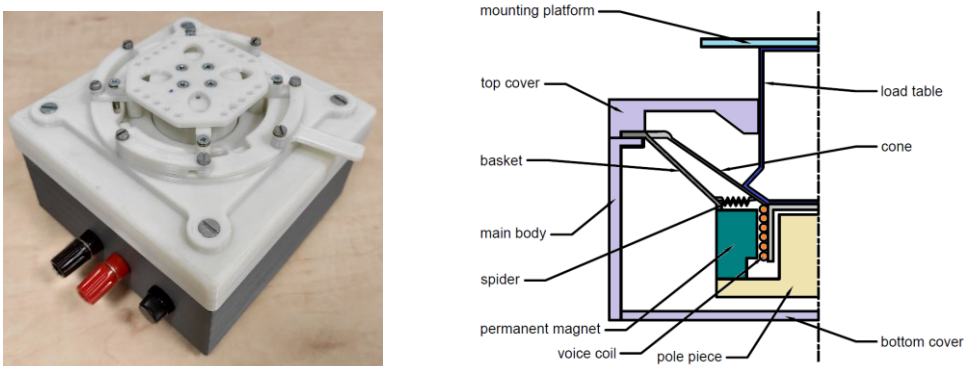

(a) **(b)**

Fig. 2 Designed electrodynamic shaker (a), cross-section of the shaker (b)

POWER SUPPLY SYSTEM

The power supply system comprises a power amplifier and a function arbitrary waveform generator (signal generator) (Fig. 3). The power amplifier is built around the TP3118 integrated circuit, which is a mono, class D amplifier equipped with overcurrent and overtemperature protection. The frequency response ranges from 20 Hz to 20 kHz while offering a maximum power output of 45 W (with THD less than 0.1 %) for a 4 Ohm loudspeaker. Efficiency at 21 V DC input voltage approaches 91%. The protection enclosure for the power amplifier was created utilizing Autodesk Inventor and fabricated on 3D printer using PETG material.

The signal generator utilized is the Rigol DG1012, a 2-channel analog output generator with a maximum output frequency of 15 MHz and a 100 MS/s sampling rate. It provides 14 bits of vertical resolution, a memory depth of 4k points, and generates signal output up to 10 Vpp. This signal generator can produce sine, triangle, ramp, square, and sawtooth signals, as well as conducting frequency sweeping.

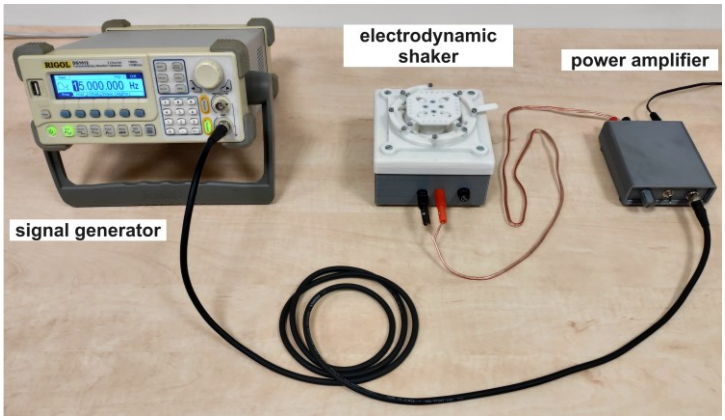

Fig. 3 Designed electrodynamic shaker with power amplifier and signal generator

SHAKER PERFORMANCE

As previously noted, the electrodynamic shaker employs the VISATON SC13 8013 high-performance loudspeaker with a resistance of 8 Ohms, a frequency range of 75 Hz to 13 kHz, and an output power rating of 40 W continuous and 60 W peak power. The loudspeaker is protected against overcurrent damage by a fast-blow replaceable fuse.

The shaker's load table can achieve a maximum displacement of ±2 mm (in the frequency range of 2 to 30 Hz), which gradually decreases as the frequency increases. The shaker has been tested to withstand a weight load of up to 0.15 kg without reaching electrical overload while still delivering a usable range of output acceleration and displacement when fully loaded. The usable frequency range of the shaker is primarily from 2 Hz to 1 kHz, as the undesired system's resonance frequencies tend to occur at higher frequencies.

To evaluate the device's performance, acceleration curves (Fig. 4) were measured using an ICP 352C33 piezoelectric accelerometer (sensitivity: 100 mV/g, measurement range: ±50 g, frequency range: 0.5 Hz to 10 kHz) from PCB Piezotronics. Data were collected using the National Instruments NI-9234 measurement module in a cDAQ-9171 chassis. The measurements were performed on a PC running a custom LabVIEW measurement program. The acceleration curves were measured with a constant 0.05 kg weight load and for various RMS voltage levels (3.5, 4.5, and 5.5 V) applied to the loudspeaker.

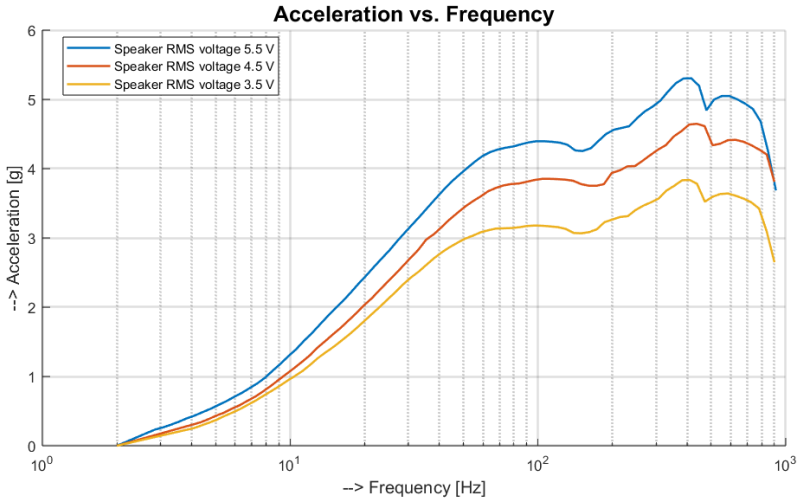

Fig. 4 Frequency response of the shaker with variable RMS voltage supply level

CONCLUSION

The electrodynamic shaker described in this paper was developed using CAD software and 3D printing technology. Its cost advantages in terms of simplicity and low production cost (approximately $35) are offset by its limited displacement amplitude at higher excitation frequencies and the limited weight load capacity of the load table. Nevertheless, it may be an effective tool in the future investigation of the frequency range applicability of simple piezoelectric energy harvesters or other small structures. In the future, precise measurements will be performed to develop a verified model of the shaker. Comparative analysis with commercially available devices will also be conducted to evaluate the performance of the shaker.

To enhance the device's design and functionality, a surge fuse protection system has been installed to prevent current overload damage to the loudspeaker. Additionally, mechanical protection has been added on top of the cover to safeguard the device against mechanical impact during manipulation and/or installation of measured devices.

ACKNOWLEDGEMENT

This work was supported by Grant Agency VEGA, grant No. 1/0416/21, and by Grant Agency KEGA, grant No. 006STU-4/2023. This work was also supported by the Young Researchers Support Programme of the Slovak University of Technology.

REFERENCES

[1] M. R. Machado, A. Appert, L. Khalij. Spectral formulated modelling of an electrodynamic shaker. *Mechanics Research Communications* **2019**, 97, 70-78.

[2] D.M. Harris, J. WM. Bush. Generating uniaxial vibration with an electrodynamic shaker and external air bearing. *Journal of Sound and Vibration* **2015**, 334, 255-269.

[3] M. Čala. Control system for a small electrodynamic exciter. Proceedings of the 2015 16th International Carpathian Control Conference. IEEE, 2015. 47-65.

[4] N. Tiwari, A. Puri, A. Saraswat. Lumped parameter modelling and methodology for extraction of model parameters for an electrodynamic shaker. *Journal of Low Frequency Noise, Vibration and Active Control* **2017**, 36, 99-115.

APPLIED MECHANICS 2024

April 17th – 19th, 2024
Hotel Toliar, Štrbské Pleso
Slovakia

CREATION OF ALGORITHMS IN MATLAB ENVIRONMENT FOR A NON-DESTRUCTIVE TESTING

L. DEGANOVÁ[1]*, V. DEKÝŠ[1], M. SAPIETA[1], B. DRVÁROVÁ[1]

To increase the effectiveness of non-destructive testing techniques, this paper examines algorithm development in the MATLAB environment. The algorithm was created in the MATLAB App Designer and was used to control two excitation sources, the halogen and the flash lamp. At the same time, an application was developed that produces a phase image based on the supplied input parameters. Both applications were tested in a lab setting on a specimen printed on a 3D printer using optical lock-in thermography. The objective was to find flaws in this specimen using an infrared (IR) camera. Finally, an evaluation of the phase images obtained from experimental measurements using optical lock-in thermography is presented. Also, the optimal settings for this kind of active thermography are concluded.

Keywords: active thermography, MATLAB App Designer, lock-in, NDT

INTRODUCTION

Non-destructive testing (NDT) is a crucial methodology for evaluating the integrity of materials and structures. NDT enables us to assess the reliability and durability of parts, equipment, or entire production systems while they are in use, without causing any mechanical or thermal damage to the objects under examination.

Thermography is one of the various NDT techniques. It is the process of measuring temperature variations on the surface of an object. It can be divided into two categories: passive and active. Flash thermography is a form of active thermography used for non-destructive material testing. A powerful optical flash produces a thermal pulse that stimulates the object being inspected. As the specimen takes the heat from the thermal wave, the heat transfers from the surface of the specimen to its interior. An infrared (IR) camera tracks the thermal wave as it returns to the surface. Heat is uniformly distributed in homogeneous specimen regions. Defective regions hamper thermal wave propagation and can be identified through infrared camera as regions with different temperatures.

[1] **Ing. Lucia Deganová**, Department of Applied Mechanics, Faculty of Mechanical Engineering, University of Žilina, Univerzitná 8215/1, Žilina, Slovak republic; lucia.deganova@fstroj.uniza.sk
[1] **doc. Ing. Vladimír Dekýš, CSc.**, Department of Applied Mechanics, Faculty of Mechanical Engineering, University of Žilina, Univerzitná 8215/1, Žilina, Slovak republic; vladimir.dekys@fstroj.uniza.sk
[1] **Ing. Milan Sapieta, PhD.**, Department of Applied Mechanics, Faculty of Mechanical Engineering, University of Žilina, Univerzitná 8215/1, Žilina, Slovak republic; milan.sapieta@fstroj.uniza.sk
[1] **Ing. Barbora Drvárová.**, Department of Applied Mechanics, Faculty of Mechanical Engineering, University of Žilina, Univerzitná 8215/1, Žilina, Slovak republic; barbora.drvarova@fstroj.uniza.sk

Thermograms are regularly taken to identify defects. Flash thermography is particularly useful for locating surface and subsurface defects. In summary, the IR camera displays a thermal profile that distinguishes between defect-free and defective regions.

APPLICATION FOR EXCITATION SOURCE CONTROL

The MATLAB App Designer user interface was used to construct the application. Before beginning the application development, the Data Acquisition Toolbox must be installed to control modules from National Instruments (NI). Applications and functions are provided in this toolbox for setting up hardware for data acquisition, reading data into MATLAB, and writing this data to analog and digital output channels.

The initial step of the application is to display the connected device on the computer and confirm the connectivity of the NI module. Users are then offered a choice between using a halogen or flash lamp as an excitation source. The input settings that users can modify include the period length, number of periods, and the flash ignition time in case of a flash lamp.

Experimental setup and the test specimen

National Instruments (NI) modules were used to control two excitation sources in an experiment. The modules, connected to a PC via a USB cable, were programmed using MATLAB App Designer to control a Godox QS 1200 II flash lamp and a Kaiser Videolight 4 halogen lamp. An NI 9481 module, linked to the flash lamp using an AUX cable, provided a digital output channel to control it. Another NI 9264 module was used to add an analog output channel to the halogen lamp. By using these modules, we were able to accurately control both lamps and ensure the success of the experiment.

We used a 120 mm x 120 mm x 5 mm specimen with artificially induced surface defects during the experiment. The specimen was created with PET-G material using Fused Modeling technology (FDM). Nine square-shaped holes, each with sides of 20 mm, were present in the specimen, located 30 mm away from the edge and 1 mm below the measured surface. We applied black paint to reduce surface reflectivity (emissivity value of 0.96). Fig. 1 shows the specimen's appearance, the location and size of the holes, and its dimensions.

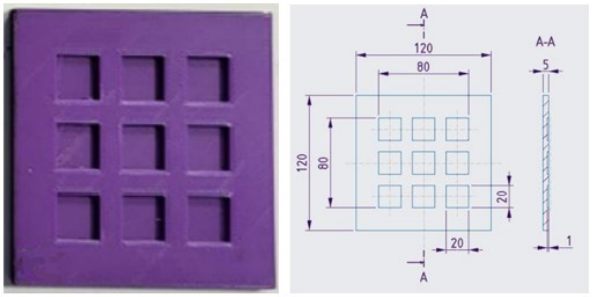

Fig. 1 Specimen's appearance and dimensions

APPLICATION FOR DATA PROCESSING FROM EXPERIMENTAL MEASUREMENT

The created application is employed to process experimental measurement data. The user can pick between the two excitation sources that were used in the experiment: flash and halogen lamp. The measured data are loaded in the first stage, after that the user is informed in a text field as to whether

this process was successful or failed. The number of periods and frequency we want to display can then be altered. Since 5 experimental measurements were made, the numeric field for entering the number of periods had a 5 upper bound. The phase image can then be loaded straight into the program window or opened in a new window for a more detailed look, depending on the preference of the user.

Experimental setup for the second application

The same excitation sources were used as in the first experimental setup. We used a FLIR SC7500 infrared (IR) camera to collect the data. As a paint with the same emissivity value was applied to one side of the specimen, the emissivity value was set at $\varepsilon = 0.96$ in the IR camera before the measurement. The IR camera was placed $(0{,}5 \pm 0{,}1)$ m away from the specimen being measured. We positioned the flash lamp and afterward the halogen lamp at the same distance from the specimen. The utilized halogen lamp had a power of 1 kW and the flash lamp had a power of 1,2 kW.

We performed measurements using two excitation sources - a flash lamp and a halogen lamp, with each source being repeated 5 times. Each measurement cycle lasted 10 minutes and 3000 thermograms were recorded. Input parameters for a flash lamp were set in the first application as follows:

- Period length = 120 s,
- flash duration = $\frac{1}{800}$ s,
- number of periods = 5.

For the second excitation source (which in our case was the halogen lamp) we set the lamp switch on and off every 60 seconds. The recorded data was exported to a MATLAB file for further processing using the NDT Data Processing App. The user can choose to display one to five periods and adjust the frequency values.

PHASE IMAGES

This section gives an overview of the phase images rendered by the second application. We can observe that changing the number of periods and frequency influences the resulting phase image.

When rendering the images in variant (a), we specified a frequency value of 0.0083 and in variant (b) the frequency value was 0.01. For comparison, we plotted the 3rd and 5th period of the phase image when the specimen is excited by both flash and halogen lamp. In Fig. 2 and Fig. 3, we can observe the rendered phase images of the sample excited by the flash lamp. In Fig. 4 and Fig. 5, we can see the phase images plotted for the specimen that was excited by the halogen lamp.

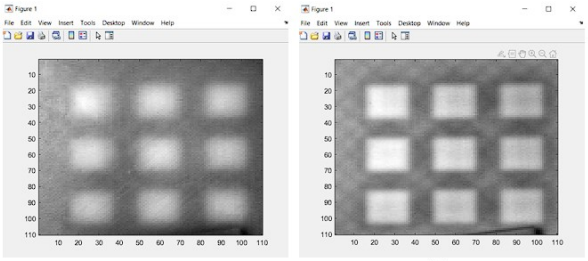

a) b)

Fig. 2 The test specimen, excited by a flash lamp, third period

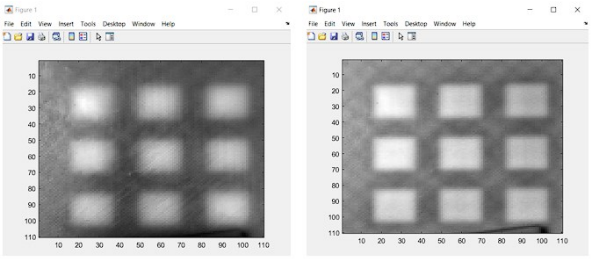

a) b)

Fig. 3 The test specimen, excited by a flash lamp, fifth period

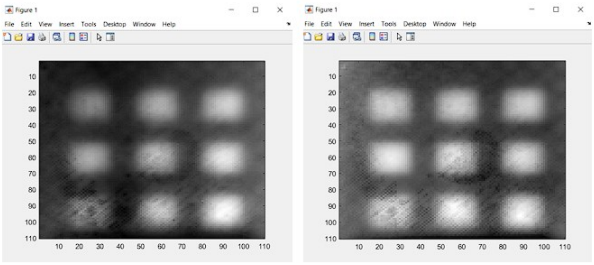

a) b)

Fig. 4 The test specimen, excited by a halogen lamp, third period

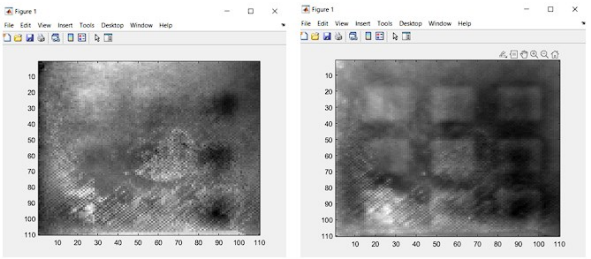

a) b)

Fig. 5 The test specimen, excited by a halogen lamp, fifth period

CONCLUSION

In the case of the flash lamp excited specimen, we can observe that a higher number of periods does not negatively affect the quality of the phase image. Defects were well visible at the third and the fifth excitation periods. We can also see that when the value of the frequency is increased, the phase images appear sharper and the defects in the specimen under study are thus better visible.

On the contrary, in the case of excitation of the specimen with a halogen lamp, the number of periods had a considerable influence on the resulting phase image. In the third period, the defects in the specimen are still sufficiently visible. However, in the fifth period with a frequency value of 0.0083, the defects are hardly detectable. Improvement occurred when the frequency was increased to 0.01.

We assume that this result occurred because when the specimen was excited with the halogen lamp, the specimen heated up more than when the flash lamp was used. The temperature rise could have damaged the specimen with a higher number of excitation periods. This problem could be eliminated by using a higher-power halogen lamp and shortening the excitation time. All things

considered, it seems that using a flash lamp as an external excitation source is a preferable option for thermographic testing. The defects in the investigated specimen are clearly visible even with a higher number of excitation cycles.

ACKNOWLEDGMENT

This work was supported by the KEGA 011 ŽU-4/2022.

REFERENCES

[1] Baldev Raj, T. Jayakumar, M. Thavasimuthu. *Practical Non-destructive Testing.* New Delhi : Narosa Publishing House, 2002. ISBN 1-85573-600-4

[2] *Infrared Thermography for Temperature Measurement and Non-Destructive Testing.* Usamentiaga Rubén, Venegas Pablo, Guerediaga Jon. s.l. : Sensors, 2014. ISSN 1424-8220

[3] Flir: The ultimate infrared handbook dor R&D professionals. DOI: http://www.flirmedia.com/MMC/THG/Brochures/T559243/T559243_EN.pdf

[4] *Development and Application of Infrared Thermography Non-Destructive Testing Techniques.* Qu Zhi, Jiang Peng, Zhang Weixu. s.l. : Sensors, 2020, Zv. Vol. 20, no. 14, s. 3851

[5] Aktivní termografie jako metoda NDT. *termokamery-flir.* DOI: https://www.termokamery-flir.cz/aktivni-termografie-jako-metoda-ndt-nedestruktivniho-testovani/

[6] MATLAB Data Acquisition Toolbox. *MathWorks*. DOI: https://www.mathworks.com/products/data-acquisition.html

[7] Passive and Active Thermography. *MoviTherm*. DOI: https://movitherm.com/knowledgebase/passive-and-active-thermography/

APPLIED MECHANICS 2024

April 17th – 19th, 2024
Hotel Toliar, Štrbské Pleso
Slovakia

FATIGUE LIFE INVESTIGATION OF THE FREIGHT TRAIN WHEEL WEB

P. DLHÝ[1]*, P. POKORNÝ[2], T. VOJTEK[3], O. PETER[4], R. FAJKOŠ[5], P. HUTAŘ[6], M. JAMBOR[7]

During the operation of train wheels, they not only undergo normal driving conditions but also experience braking cycles. When brakes are applied through brake blocks, heat is produced, leading to additional thermal stress on the wheel. This uneven thermal stress can locally diminish the yield strength of the wheel material and cause residual stresses to form once the wheel cools down. Such conditions can lead to fatigue crack initiation either in the area where the rail and wheel meet (known as rolling-contact fatigue) or at the web of the wheel. Despite current standards not considering the thermal loading as an important one, this study explores the critical position determination under the combined loading and examines how numerical simulations prediction can differ.

Keywords: railway wheel, fatigue, numerical simulations

INTRODUCTION

Maintaining railway wheelsets is essential for ensuring the safety, minimizing maintenance expenses, and preserving the reliability of the railway system. As one of the most heavily burdened components of the train carriage, the wheelset's integrity is vital for the safe operation of trains. During their operation, railway wheels endure continuous rolling and frequent braking, leading to common surface damages at the areas of rail-wheel contact [1–4]. However, damage is not limited to this contact surface alone. Fig. 1 schematically describes the wheelset construction.

The wheel web profile is frequently designed with curves to counteract the effects of thermal expansion that occur when the wheel heats up. Despite this precaution, these curvatures can act as stress concentrators and introduce additional bending loads on the wheel, potentially leading to

[1] **Ing. Pavol Dlhý, PhD.**, Institute of Physics of Materials of the Czech Academy of Sciences, v.v.i. Žižkova 513/22, Brno, Czech Republic; dlhy@ipm.cz
[2] **Ing. Pavel Pokorný, PhD.**, Institute of Physics of Materials of the Czech Academy of Sciences, v.v.i. Žižkova 513/22, Brno, Czech Republic; pokorny@ipm.cz
[3] **Ing. Tomáš Vojtek, PhD.**, Institute of Physics of Materials of the Czech Academy of Sciences, v.v.i. Žižkova 513/22, Brno, Czech Republic; vojtek@ipm.cz
[4] **Ing. Ondřej Peter,** BONATRANS GROUP a.s., Revoluční 1234, 735 94, Bohumín, Czech Republic; ondrej.peter@ghh-bonatrans.com
[5] **Ing. Rostislav Fajkoš, PhD.**, BONATRANS GROUP a.s., Revoluční 1234, 735 94, Bohumín, Czech Republic; rostislav.fajkos@ghh-bonatrans.com
[6] **prof. Ing. Pavel Hutař, PhD.**, Institute of Physics of Materials of the Czech Academy of Sciences, v.v.i. Žižkova 513/22, Brno, Czech Republic; hutar@ipm.cz
[7] **Ing. Michal Jambor, PhD.**, Institute of Physics of Materials of the Czech Academy of Sciences, v.v.i. Žižkova 513/22, Brno, Czech Republic; jambor@ipm.cz

areas susceptible to fatigue cracks, particularly in the web area. This makes the web a critical zone that requires careful consideration during the wheel's design phase. To address and mitigate these issues, numerical simulations are utilized, allowing designers to identify and evaluate potential problematic areas within the web. By incorporating such simulations, designers can better predict and prevent fatigue crack initiation, ensuring the wheel's integrity and longevity. The wheel design standard EN 13979 [5] specifies solely the mechanical loadings that a designed wheel should withstand, outlining three distinct loading scenarios based on the train's motion: straight track, curved track, and turnout.

This contribution deals with numerical modelling of the railway wheel from both mechanical and thermal perspectives. Complex fatigue investigation is than proposed to validate the numerical models and determined critical areas where fatigue cracks can occur.

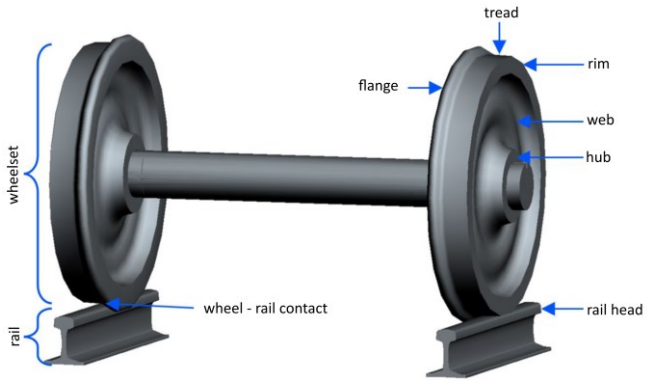

Fig. 1 Typical structure of a wheelset with marked names of the wheel parts [4]

NUMERICAL MODELLING

To explore the issue of wheel fatigue, numerical simulations were carried out using ANSYS software, employing both mechanical and thermal finite element models. The mechanical model was constructed with a symmetry plane, incorporating around 143,000 quadratic elements. It defined the material as isotropic and linearly elastic, characterized by a Poisson's ratio of 0.3 and Young's modulus of 206 GPa. The boundary conditions for this model were set in accordance with the type of track being investigated, as specified in relevant standards.

For thermal analysis, a 2D axisymmetric model was developed, using 5072 quadratic elements. This model treated the material as isotropic elastoplastic with multilinear kinematic hardening, considering various material properties such as Young's modulus, Poisson's ratio, yield stress, the dependency of plastic strain on true stress, thermal expansion, thermal conductivity, and specific heat. Importantly, all these material constants were made temperature-dependent to accurately simulate real-world conditions. The boundary conditions for the thermal model were established to mimic the braking cycle, based on testing conducted on a test stand. This involved a 45-minute period of braking, generating heat, followed by several hours of cooling down to room temperature. Heat flux was applied at the wheel tread, where interaction with the braking blocks occurs, and convection was utilized across the wheel's surface to model the heat dissipation process accurately.

RESULTS

The development of the mechanical model allowed for a detailed examination of loading conditions for the different tracks. Fig. 2 shows Von Mises equivalent stress distribution for the curved track ride with marked maximum at the wheel web area. Different ride conditions predict different critical

areas. Therefore, from mechanical numerical simulation we obtain three areas to investigate deeper. After the development of the thermal numerical model new loading conditions were obtained. Fig. 3 shows radial stress distribution in the room temperature after the breaking cycles, also may be called as residual stress. With superposition of residual stresses and the mechanical model results, completely new critical areas are obtained.

Fig. 4 shows the radial stress behaviour at the marked position in Fig. 3. The radial stress distribution is illustrated by the blue line, while the evolution of temperature throughout the braking cycles is shown by the orange line. At the onset and conclusion of the braking cycle, significant radial stress gradients were observed. Starting from room temperature, the radial stress is at its maximum, then falls to its lowest point quite rapidly. Subsequently, due to the decrease in yield stress and the redistribution of stress in the surrounding material, the radial stress slowly increases. The lowest point of radial stress is observed after 1000 seconds of the breaking. After the breaking stops, the radial stress rises to its maximum again, showcasing the complex interplay between thermal effects and material stress responses during braking cycles.

As previously mentioned, a mechanical model alone predicts some critical areas. However, after integration of findings from both thermal and mechanical analyses, another critical areas were predicted. Thermal analysis provides insights into the mean stress experienced during loading cycles and the temperature distribution that alters material properties, including yield stress and fatigue limit. From mechanical analysis, we derive amplitudes and adjustments to mean stress, which allow us to compile overall loading cycles for various rail track conditions. This combined approach enhances our understanding and assessment of the wheel's performance variable operating conditions.

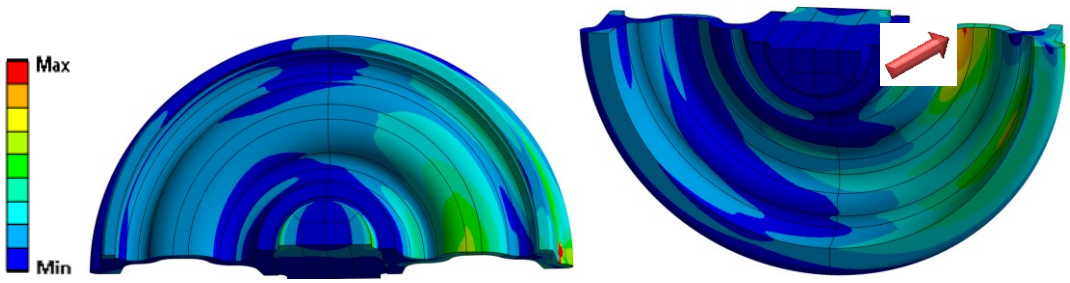

Fig. 2 Von Mises equivalent stress for the train ride on a curved track with marked wheel web maximum stress

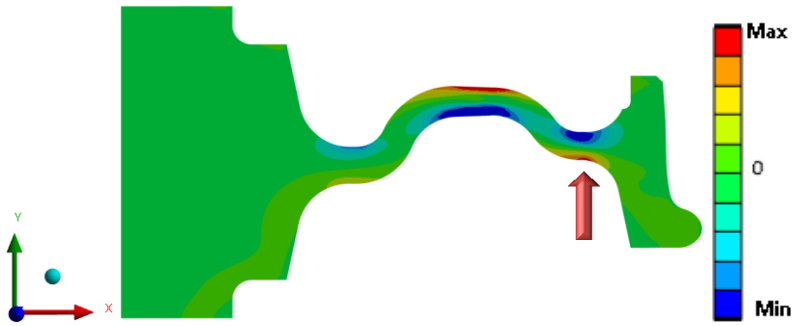

Fig. 3 Radial (X direction) residual stress distribution at the room temperature after the breaking cycle

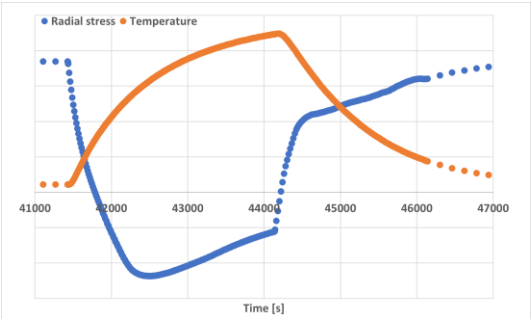

Fig. 4 Radial stress and temperature evolution during the breaking cycle of the marked position in Fig. 3

CONCLUSION

By merging the numerical outcomes of both mechanical and thermal analyses, it becomes possible to construct the loading cycle for a railway wheel. Nevertheless, to ensure the accuracy of these numerical models, their validation against experimental data is crucial. This process requires collecting substantial experimental data, especially since the mechanical properties of materials change with temperature. Therefore, it's necessary to acquire experimental data such as Whöler curves at various temperatures and under different loading asymmetries.

Following thorough experimental testing, it is possible to create the Haigh diagram. This diagram illustrates that the fatigue limit is influenced by both the stress amplitude and the mean stress. Consequently, pinpointing critical areas within the railway wheel's web for potential failure is a complex task that requires a detailed and nuanced approach, blending both extensive experimental insights and sophisticated numerical modelling.

ACKNOWLEDGEMENT

This research has been supported by grant No. FW03010149 "New wheel design for freight transport with higher utility properties" of The Technology Agency of the Czech Republic and the equipment and the base of research infrastructure IPMinfra were used during the research activities.

REFERENCES

[1] M. Asplund, M. Palo, S. Famurewa, M. Rantatalo. A study of railway wheel profile parameters used as indicators of an increased risk of wheel defects. *Proceedings of the Institution of Mechanical Engineers, Part F: Journal of Rail and Rapid Transit* **2016**, 230 (2), 323-334. ISSN 20413017.

[2] E. Steyn. Railway wheel steel behaviour upon thermo-mechanical loadings. 2022. Chalmers University of Technology

[3] A. Alemi. Railway wheel defect identification. 2019. Delft University of Technology.

[4] M. Dick, N. Sundaram, E. Sherrock. Wheel Failure Investigation Program: Phase I. 2021, 68 p.

[5] EN 13979-1. Railway applications - Wheelsets and bogies - Monobloc Wheels - Technical approval procedure - Part 1: Forged and rolled wheels. 2020.

APPLIED MECHANICS 2024

April 17th – 19th, 2024
Hotel Toliar, Štrbské Pleso
Slovakia

EXPLORING THE IMPACT OF PRINTING POSITION ON MECHANICAL PROPERTIES OF ADDITIVELY MANUFACTURED TI6AL4V

V. DRÁTOVSKÁ[1]*, A. KRATOCHVÍL[2], R. SEDLÁČEK[3], Z. PADOVEC[4], S. KONVIČKOVÁ[5]

This study investigates the influence of position within the printing area on the mechanical properties of Ti6Al4V specimens produced via LPBF additive manufacturing. Mechanical properties, including ultimate tensile strength, yield strength, elastic modulus, and ductility were determined through uniaxial testing, with a focus on understanding how variations in printing position affect these properties. Statistical analysis was conducted on the results to discern and quantify the impact of printing position on the mechanical properties of the specimens.

Keywords: Additive manufacturing, Printing position, Ti6Al4V, Mechanical properties

INTRODUCTION

Additive manufacturing, particularly Laser Powder Bed Fusion (LPBF), has revolutionized the production of complex components in various industries. LPBF offers design freedom and the ability to fabricate parts with intricate geometries directly from digital models. However, the quality and performance of LPBF-produced parts are influenced by a multitude of parameters, both tuneable and less controllable.

Conventionally, the focus of research in LPBF has primarily rested on the influence of tuneable parameters such as laser power, scanning speed, layer thickness, and scanning strategy on the quality of printed parts [1-3]. While these factors undoubtedly play a significant role, there exists a realm of less tuneable variables that can equally impact the final outcome. Factors like powder purity, chamber fullness, oxygen content in the protective atmosphere, and even the positioning

[1] **Ing. Veronika Drátovská**, Department of Mechanics, Biomechanics and Mechatronics, Faculty of Mechanical Engineering, Czech Technical University in Prague, Technická 4, 160 00 Prague, Czech Republic; veronika.dratovska@fs.cvut.cz
[2] **Ing. Adam Kratochvíl**, Department of Mechanics, Biomechanics and Mechatronics, Faculty of Mechanical Engineering, Czech Technical University in Prague, Technická 4, 160 00 Prague, Czech Republic; adam.kratochvil@fs.cvut.cz
[3] **Doc. Ing. Radek Sedláček, PhD.**, Department of Mechanics, Biomechanics and Mechatronics, Faculty of Mechanical Engineering, Czech Technical University in Prague, Technická 4, 160 00 Prague, Czech Republic; radek.sedlacek@fs.cvut.cz
[4] **Ing. Zdeněk Padovec, PhD.**, Department of Mechanics, Biomechanics and Mechatronics, Faculty of Mechanical Engineering, Czech Technical University in Prague, Technická 4, 160 00 Prague, Czech Republic; zdenek.padovec@fs.cvut.cz
[5] **Prof. Ing. Svatava Konvičková, CSc.**, Department of Mechanics, Biomechanics and Mechatronics, Faculty of Mechanical Engineering, Czech Technical University in Prague, Technická 4, 160 00 Prague, Czech Republic; svatava.konvickova@fs.cvut.cz

of the parts within the printing area can exert subtle yet critical effects on the mechanical properties of the printed specimens [4, 5].

In this work, we present our findings on the effects of position within the printing area on the mechanical properties of LPBF-produced specimens. Beyond the traditional parameters, understanding how the location within the printing area influences the final properties of the printed parts is crucial for ensuring consistent quality and performance.

METHODS AND MATERIALS

The specimens were produced via the LPBF additive manufacturing technique. Titanium alloy Ti6Al4V powder was used as the raw material for fabricating the specimens. A M2 Cusing machine (Concept Laser) was utilized for printing these specimens. They were positioned in five locations within the printing area: one in each corner and one in the middle. Consequently, the specimens were categorized into five groups, designated as 1, 2, 3, 4 for the corner specimens, and 5 for the middle specimen. The specimens were round, with a tested section diameter of 3 mm and a total length of 55 mm (Fig. 1). A total of 222 specimens were tested, with the exact diameter of each specimen measured.

Uniaxial tensile testing was conducted to determine the mechanical properties of the specimens, including ultimate tensile strength, yield strength, Young's modulus of elasticity, and ductility. The mechanical testing was carried out using the MTS 858.2 MINI BIONIX testing system, with an optical extensometer X-Sight One (Fig. 2). All necessary parameters were derived from the measured stress-strain curves for each specimen.

Fig. 1 Specimens before and after testing.

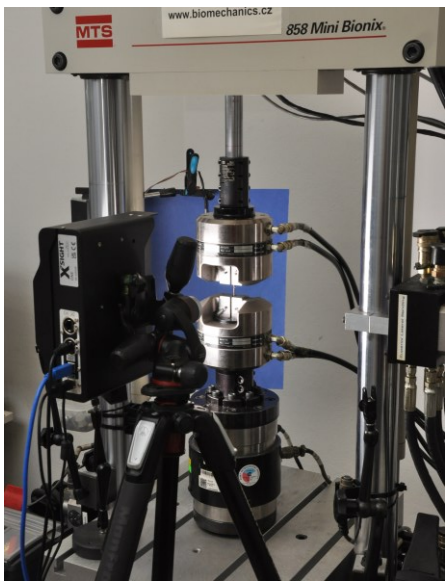

Fig. 2 Measuring setup.

Subsequently, a statistical analysis was performed to ascertain any statistically significant differences among the five groups. The Shapiro-Wilk test and Levene's test were employed to assess the normality of the data and the equality of variances. The Kruskal-Wallis test and one-way ANOVA were utilized to identify potential statistically significant differences between the mean values of the tested groups. If necessary, the tests were followed by a multiple comparison test to pinpoint the specific differences between groups.

RESULTS AND DISCUSSION

The ultimate tensile strength, yield strength, Young's modulus of elasticity, and ductility were assessed through uniaxial tensile tests for each specimen across the five groups. The number of specimens in groups 1 to 5 was 46, 45, 48, 47, and 36, respectively. The evaluated data are presented in form of boxplots in the figures below (Fig. 3 and Fig. 4).

The Shapiro-Wilk test indicated non-normal distribution for all datasets except ductility. Thus, the Kruskal-Wallis test, a nonparametric method, was employed to compare group differences. However, due to big enough sample sizes (>30 samples) and equal variances, ANOVA was also utilized, providing results consistent with the Kruskal-Wallis test.

Regarding ultimate tensile strength, yield strength, and elastic modulus, no statistically significant differences were found among the five groups. However, mean values of ductility exhibited variations among groups, notably between pairs 1-3, 2-3, 4-5, and 3-5 as indicated in the Fig. 4 (right). Boxplots in this figure include notches representing confidence intervals for medians; non-overlapping notches indicate significantly different medians.

For pairs 1-3 and 2-3, the null hypothesis, which assumes the equality of mean values, was rejected at a 5% significance level, while for pairs 3-5 and 4-5, it was rejected at a 1% significance level. The effect size represented by Fischer's η^2 equals 0.11, which means that the position within the printing area explains 11 % of the variance from the average.

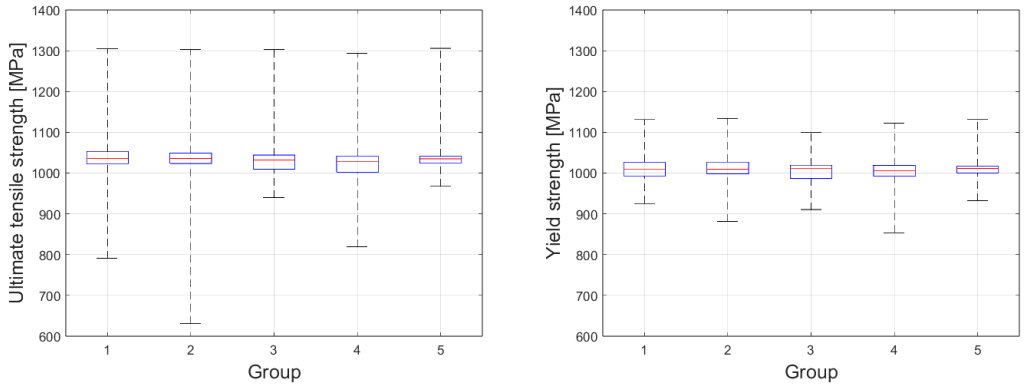

Fig. 3 Boxplots for ultimate tensile strength (left) and yield strength (right).

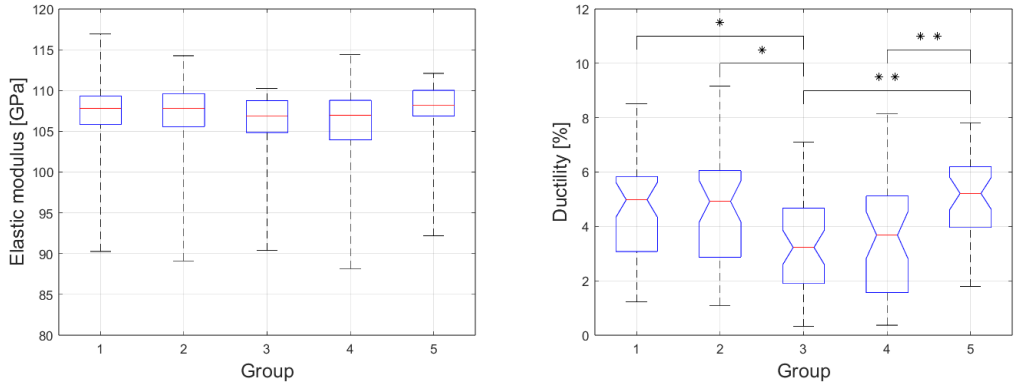

Fig. 4 Boxplots for elastic modulus (left) and notched boxplot for ductility with statistically significant differences denoted by * for p<0.05 and ** for p<0.01 (right).

CONCLUSION

The study examined how the placement of specimens within the printing chamber could affect their mechanical properties. Key parameters such as ultimate tensile strength, yield strength, Young's modulus, and ductility were measured through uniaxial tensile tests. Statistical analysis revealed significantly lower mean values of ductility in groups 3 and 4, suggesting that the position within the printing area could impact the toughness of printed parts. The other investigated mechanical properties seem to be unaffected by the specimen location.

ACKNOWLEDGEMENT

This study was supported via a grant project awarded by Czech Technical University in Prague, grant number SGS22/149/OHK2/3T/12.

REFERENCES

[1] Q. Luo, L. Yin, T.W. Simpson, A.M. Beese. Effect of processing parameters on pore structures, grain features, and mechanical properties in Ti-6Al-4V by laser powder bed fusion. Online. *Additive Manufacturing* **2022**, 56. ISSN 22148604. [cit. 2024-03-22]. DOI: https://doi.org/10.1016/j.addma.2022.102915.

[2] M. Gor, H. Soni, V. Wankhede, P. Sahlot, K. Grzelak, et al. A Critical Review on Effect of Process Parameters on Mechanical and Microstructural Properties of Powder-Bed Fusion Additive Manufacturing of SS316L. Online. *Materials* **2021**, 14 (21). ISSN 1996-1944. [cit. 2024-03-22]. DOI: https://doi.org/10.3390/ma14216527.

[3] S.E. Saghaian, M. Nematollahi, G. Toker, A. Hinojos, Alejandro; N.S. Moghaddam, et al. Effect of hatch spacing and laser power on microstructure, texture, and thermomechanical properties of laser powder bed fusion (L-PBF) additively manufactured NiTi. Online. *Optics & Laser Technology* **2022**, 149. ISSN 0030-3992. [cit. 2024-03-22]. DOI: https://doi.org/10.1016/j.optlastec.2021.107680.

[4] T.P. Moran, D.H. Warner, A. Soltani-Tehrani, N. Shamsaei, N. Phan. Spatial inhomogeneity of build defects across the build plate in laser powder bed fusion. Online. *Additive Manufacturing* **2021**, 47. ISSN 2214-8604. [cit. 2024-03-22]. DOI: https://doi.org/10.1016/j.addma.2021.102333.

[5] A. Mussatto, R. Groarke, R.K. Vijayaraghavan, C. Hughes, M.A. Obeidi, et al. Assessing dependency of part properties on the printing location in laser-powder bed fusion metal additive manufacturing. Online. *Materials Today Communications* **2022**, 30. ISSN 2352-4928. [cit. 2024-03-22]. DOI: https://doi.org/10.1016/j.mtcomm.2022.103209.

APPLIED MECHANICS 2024

April 17th – 19th, 2024
Hotel Toliar, Štrbské Pleso
Slovakia

EFFECT OF PETG COMPOSITE FIBRE ORIENTATION ON DAMPING

B. DRVÁROVÁ[1]*, L. DEGANOVÁ[1], V. DEKÝŠ[1], M. SAPIETA[1]

This paper discusses the investigation of damping in specimens made of composite materials. The samples are produced using a 3D printer and have various filament orientations. Specifically, the paper compares samples made of PETG material that have 25 layers with fibers oriented at 45° and 90° angles to the axis of the sample. The sample is excited pulse-wise, and the oscillation is detected non-contact. The damping is evaluated using two methods: the envelope curve method and the logarithmic decrement method. Finally, the paper presents a comparison of the two methods used and an evaluation of the effect of fiber orientation on damping in the composite.

Keywords: composite, damping, PETG, fiber orientation, 3D printing

INTRODUCTION

Composite materials are increasingly replacing traditional construction materials such as steel, aluminium, and others. As early as the 1980s, composite materials began to be introduced into dynamically loaded structures such as aircraft, cars, ships, and satellites. Their success lies, for example, in their high stiffness-to-weight ratio or high strength-to-weight ratio. Of course, the 3D printing method also enables the production of geometrically more complex components. However, the mechanics of composites are much more complex than that of isotropic materials [1]. Each layer in the composite can have a different fiber orientation and thickness. In this context, fiber orientation is one of the key factors influencing the mechanical properties of the composite. The use of static stiffness to predict natural frequencies is common, but the evaluation of damping properties is problematic. There are a limited number of reviews focusing on this topic, which makes it difficult to consider the damping of composite materials in design and analysis. The damping of composite materials has the potential to be several orders of magnitude higher than that of traditional materials, making them a more attractive choice for components subjected to dynamic loading [2-4].

In this paper, we focus on how fiber orientation affects the damping ratio. Specifically, the material under investigation is PETG (Polyethylene Terephthalate Glycol). In order to determine the damping ratio, we utilize not only the logarithmic decrement method but also the envelope curve method, enabling us to quantify the damping. The objective is to gain a deeper understanding of this

[1] **Ing. Barbora Drvárová**, **Ing. Lucia Deganová**, **doc. Ing. Vladimír Dekýš, CSc.**, **Ing. Milan Sapieta, PhD.**, Department of Applied Mechanics, Faculty of Mechanical Engineering, University of Žilina, Univerzitná 8215/1, Žilina, Slovak republic; barbora.drvarova@fstroj.uniza.sk, lucia.deganova@fstroj.uniza.sk, vladimir.dekys@fstroj.uniza.sk, milan.sapieta@fstroj.uniza.sk

issue, which could lead to improved design of composite structures with optimized damping properties.

EXPERIMENTAL MEASUREMENTS

To assess the impact of fiber orientation on damping ratio, it is imperative to incorporate at least two distinct fiber orientations.

Tested sample

3D printing is an additive manufacturing method wherein the desired object is fabricated by gradually applying and fusing materials. Fused Deposition Modeling (FDM) technology was utilized to produce the samples. FDM involves the direct deposition of material by melting it in the print head and applying it point by point. The three-dimensional model generated in the software is then transformed according to specified parameters into two-dimensional surfaces—layers of the model. Each layer consists of lines, with the melted plastic fused together to create a homogeneous body. The dimensions of the samples are depicted in Fig. 1 b). In the first sample, the individual layers were oriented at 0°/90° with respect to the sample axis, as illustrated in Fig. 1 c). For the second sample, the fibers were oriented at 45°/-45° relative to the sample axis (as shown in Fig. 1d)). Each sample comprises 25 layers, with each layer having a thickness of 0.2 mm. The layers are printed in the XY plane.

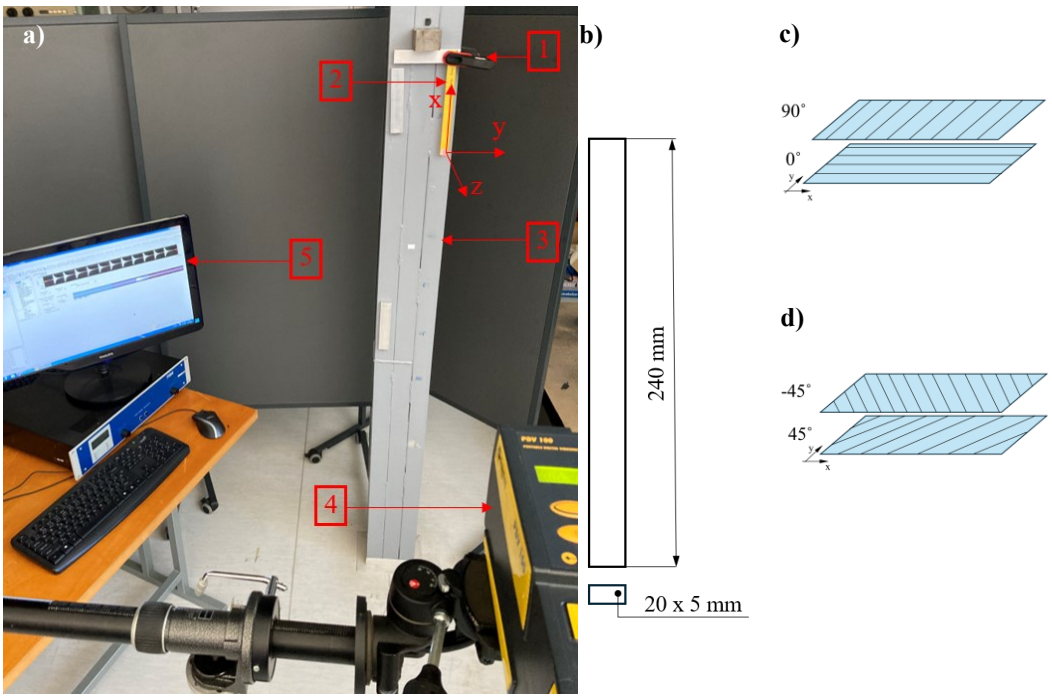

Fig. 1 a) experimental measurement setup, **b)** specimen dimensions, **c)** 0˚/90˚ printing direction in layers, **d)** 45˚/-45˚ printing direction in layers

Experimental measurement setup

Fig. 1 a) depicts the setup for conducting the experimental measurements. The test specimen (2) is fixed 2 cm away from a rigid column (3). Its motion is constrained by a clamp at position (1). The specimen is impulsively excited by being deflected from its equilibrium position and then released.

The oscillation is captured non-contactly using the Portable Doppler Vibrometer, Polytec PDV 100 (4). The Polytec PDV 100 (2) is positioned at a distance of 120 cm from the structure being measured, based on the vibrometer's specifications. The vibrometer data is acquired using an NI USB-4431 analyzer and subsequently processed and displayed using SignalExpress software on a computer (5). Only the first bending mode of a given specimen was established. The coordinate system is illustrated in Fig. 1a) for better comprehension of the direction in which the specimen oscillates. Both excitation and sensing of the oscillation are performed along the z-axis.

RESULTS

Each sample underwent 10 measurements. The time waveform of the signal was recorded, with the vibrometer capturing information about the instantaneous rate of oscillation. Damping ratio can be determined from the time waveform using either the envelope curve or the logarithmic decrement method. The instantaneous deflection is described by equation (1). The waveform of instantaneous deflection exhibits an exponential decay pattern and can thus be approximated by an exponential curve, i.e., an envelope curve ($A = A_0 e^{-\xi t}$) [6, 7]. Another approach involves determining the attenuation as the ratio of two consecutive amplitudes. The logarithmic decrement is then calculated as the natural logarithm of this attenuation [6].

$$y(t) = A_0 e^{-\xi t} \sin(\omega_d t + \varphi_0) \tag{1}$$

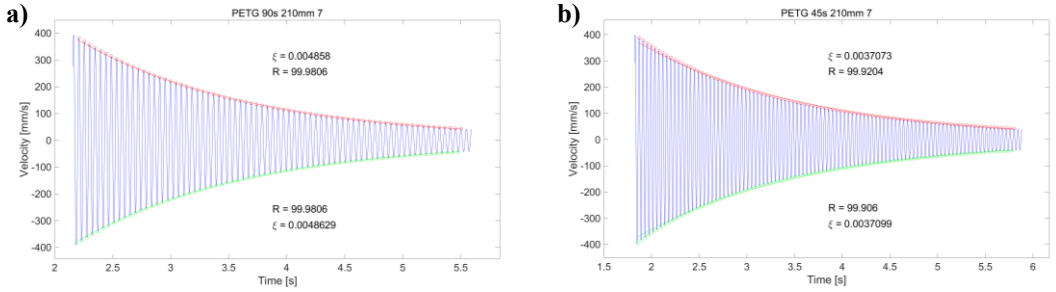

Fig. 2 a) time course of sample signal with 0˚/90˚ fiber orientation, **b)** time course of sample signal with 45˚/-45˚ fiber orientation

The data were analyzed using MATLAB software. In the time signal, the segment where the amplitude decreased from 400 mm/s to 50 mm/s was chosen. This interval was selected because it represents a steady oscillation without transient phenomena. When evaluating smaller amplitudes, noise can interfere with the analysis. As shown in Fig. 2 a), the time history of the sample with a fiber orientation of 0°/90° is depicted. The first natural frequency is 21.56 Hz. Fig. 2 b) displays the time waveform of the sample with a fiber orientation of 45°/-45°. The first natural frequency of this sample is 24.16 Hz. The damping ratio obtained from both methods was assessed in the selected segment. Additionally, Fig. 2 illustrates the value of parameter R, which indicates the correlation of the calculated envelope curve with our data. For a clearer overview, the results, along with the deviations between the utilized methods, are presented in Tab. 1.

Tab. 1 Damping ratio results and variations between methods (ln decrement – logarithmic decrement, A -amplitude, damping r. – damping ratio)

	0˚/90˚		**45˚/-45˚**	
positive A	**ln decrement**	**envelope curve**	**ln decrement**	**envelope curve**
damping r. [-]	0,004862674	0,004854554	0,003744045	0,003701865
difference [%]	0,18		1,13	

negative A	ln decrement	envelope curve	ln decrement	envelope curve
damping r. [-]	0,004861052	0,004857878	0,003740616	0,003706956
difference [%]	0,09		0,9	

As can be seen in Tab. 1, the time course was divided into two parts. The first part represents that part of the selected signal when the amplitude of the instantaneous deflection is positive. The second part of the evaluated signal is in the region where the amplitude of the instantaneous deflection is negative.

CONCLUSION

Fiber orientation has been demonstrated to have a significant impact on damping ratio. Samples with a fiber orientation of 0°/90° exhibit up to 31% higher relative attenuation compared to samples with a fiber orientation of 45°/-45°. It can be inferred that fiber orientation notably influences the damping capacity of the samples. Damping ratio in composites is orders of magnitude higher than that of conventional engineering materials. Understanding the damping mechanisms in composites can greatly impact the design and optimization of structural components. Therefore, it is imperative to elucidate the damping characteristics of composite materials, including whether damping is frequency-dependent.

ACKNOWLEDGEMENT

This article was supported by the UNIZA grant system, the project entitled "Research on damping of composites, polymers and metallic materials" and by the grant projects 01/0753/24 VEGA and 011/ŽU-4/2022 KEGA.

REFERENCES

[1] R. Jones. Mechanics of Composite Materials. 2. edition. New York City, McGraw-Hill, 1999. 538 p. DOI: 10.1201/9781498711067.

[2] A. Treviso, B. Van Genechten, D. Mundo, M. Tournour. Damping in composite materials: Properties and models. *Composites Part B: Engineering* **2015**, 78, 144-152. DOI: 10.1016/j.compositesb.2015.03.081.

[3] B. Benchekchou, M. Coni, H. V.C. Howarth, R. G. White. Some aspects of vibration damping improvement in composite materials. *Composites Part B: Engineering* **1998**, 29 (6), 809-817. DOI: 10.1016/S1359-8368(98)00024-9.

[4] R. Chandra, S. P. Singh, K. Gupta. Damping studies in fiber-reinforced composites – a review. *Composite Structures* **1999**, 46 (1), 41-51. DOI: 10.1016/S063-8223(99)00041-0.

[5] Protolabs network by Hubs. What is FDM (fused deposition modeling) 3D printing, 2024. URL: https://www.hubs.com/knowledge-base/what-is-fdm-3d-printing/

[6] A. Bilošová. Aplikovaný mechanik jako součást týmu konstruktérů a vývojářů: část modální zkoušky. Ostrava: VŠB – Technická univerzita Ostrava, 2012. 129 p. ISBN 978-80-248-2758-2.

[7] C. W. De Silva et al. Vibration Damping, Control and Design. UK: Taylor & Francis Group, 2007. ISBN: 978-1-4200-5321-0.

APPLIED MECHANICS 2024

April 17th – 19th, 2024
Hotel Toliar, Štrbské Pleso
Slovakia

STUDY OF AUXILIARY ELECTRIC TRAILER TRACTION SYSTEM ON ELECTRIC VEHICLE RANGE

G. GÁLIK[1]*, T. DELNIK

The range of electric cars is affected by many factors, one of them is aerodynamics, therefore these cars are not recommended for towing large trailers, because the parameters of the trailer have a great influence on the range of the vehicle. The aim of the article is to study the increase of driving range of an electric car with the help of an additional electric trailer traction system, to analyze the driving resistance of an electric car with a trailer, to create a system model of the car and, based on the results of the simulation, to determine the appropriate parameters of the components of the trailer traction system and then to perform a parametric study and examine the influence of various parameters for the range of the electric vehicle.

Keywords: system model, traction system, trailer,

INTRODUCTION

The range of electric cars is affected by many factors, one of them is aerodynamics, therefore these cars are not recommended for towing trailers, because the parameters of the trailer have a great influence on the range of the vehicle [1]. To increase the driving range of an electric vehicle using an additional electric traction system of a trailer. Analyze the driving resistance of an electric vehicle with a trailer, to create a system model of the driving vehicle and, based on the results of the simulation, to determine the appropriate parameters of the components of the trailer traction system and then to carry out a parametric study and examine the influence of various parameters on the driving range of the electric vehicle.

SYSTEM MODEL OF VEHICLE WITH TRAILER

System modeling represents an interdisciplinary approach to the development process [2], which is characterized by a structured approach. The system model of the traction system is used to simulate the real range of the rolling stock. The range is simulated based on different driving cycles. Using the system model, various parameters are evaluated, e.g. coefficient of air resistance or different driving cycles affect the driving range.

A rolling stock means that the vehicle pulls a trailer, so a rolling stock consists of a vehicle and a trailer. In this case, the trailer is equipped with a traction system, which means that the trailer has its

[1] **Ing. Gabriel Gálik, PhD.**, Institute of Automotive Mechatronics, Faculty of Electrical Engineering and Information Technologies, Slovak University of Technology in Bratislava, Ilkovičova 3, Bratislava, Slovak republic; gabriel.galik@stuba.sk

own drive system (electric motor, battery pack and control electronics), which is independent of the vehicle's traction system, thus the connection between the vehicle and the trailer is an important part of the system. As already mentioned, the trailer has its own electric motor, which facilitates the vehicle's propulsion system [3]. It is important to remember that the trailer's electric motor provides only part of the driving force, the rest must be provided by the vehicle's drive system. The vehicle and the trailer are connected purely mechanically by means of a trailer joint and ball towing coupling. During operation, it is necessary to ensure that the vehicle and trailer move as one unit.

The system model shown on Fig. 1, that is, the vehicle and trailer connected mechanically, and the trailer will maintain the dynamics of the vehicle. The vehicle and the trailer have different drive systems, so the trailer also has its own battery system and electric motor. The task of the trailer's traction system is to relieve the vehicle's traction system, thereby reducing the vehicle's consumption and increasing the range.

Fig. 1 System model overview

Components such as the electric motor, battery pack and power electronics increase the weight of the trailer and must therefore be placed in such a way as to maximize stability while driving.

These factors were also considered in the set-up of the model. The nominal parameters for the trailer auxiliary traction system are listed in Tab. 1.

Tab. 1 Auxiliary traction system nominal parameter

Battery pack energy	78.5	[kWh]
Battery pack voltage	392.2	[V]
Electric motor Nom. Power	43.5	[kW]
Electric motor Max. Power	64.3	[kW]

PARAMETRIC SIMULATION RESULTS

a simulation that illustrates how the range of an electric vehicle with and without a trailer changes. The simulation is based on the parameters of the Tesla model X. The range of this vehicle is 470 km according to the WLTP cycle.

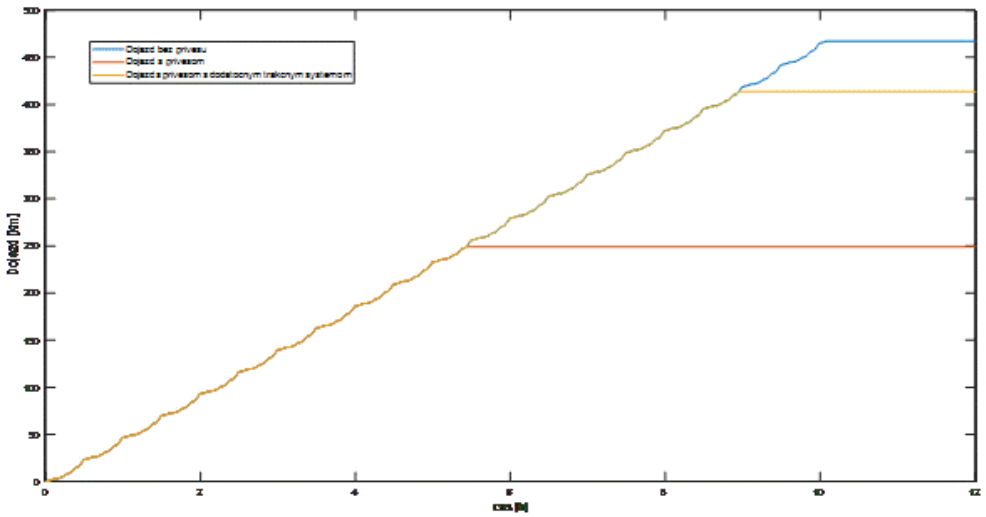

Fig. 2 Drive range with / without trailer and auxiliary system

The graph in Figure 2 shows the distance traveled by the vehicle over time. Reaching the ceiling value for individual waveforms means that the driving set exhausted the traction batteries during driving, i.e. SoC 0% was reached, and the vehicle stopped. As can be seen from the graph, the range when towing a trailer is drastically reduced, by 47% compared to without a trailer. With an additional traction system that makes it easier to drive the towing vehicle, and with the help of this system, this range can be effectively increased. In this case, the driving range with an additional trailer traction system increased by 40% compared to a trailer without a traction system.

One of the easiest solutions to increase range seems to be to increase battery power. Increasing the energy in the battery system can be achieved by increasing the number of battery cells, but this has several disadvantages. One is that increasing the size of the battery cells increases the weight of the trailer, which proportionally increases the rolling resistance, as a result of which the overall driving resistance also increases. Another important aspect is that the price increases drastically with the addition of battery cells.

Fig. 3 shows the dependence of the distance traveled and the SoC of the vehicle set over time for different energy values. From the simulations, by increasing the energy of the Battery pack, the range can be significantly increased, but only up to a certain value. This method is effective as long as the energy of the trailer battery does not cover the range of the car, that is, the trailer provides part of the driving power in the entire range of the vehicle. Above that, it no longer makes sense to increase the battery's energy, because in this case only the weight and driving resistances increase.

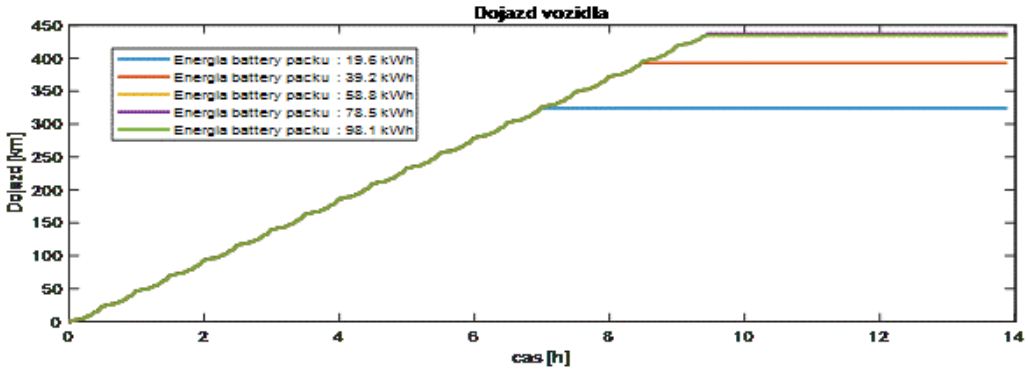

Fig. 3 Drive range depending on battery pack energy

CONCLUSION

The additional traction system connected to the trailer can significantly increase the driving range. This increase in range is achieved because most of the necessary driving force for pulling the vehicle is provided by the trailer's traction system, which significantly reduces the load on the vehicle's original drive system. The results showed that there are several options to increase the driving range. This can be an increase in the capacity of the battery in the trailer, a reduction in the total weight of the trailer or an improvement in its aerodynamics.

ACKNOWLEDGEMENT

This work was supported by the Slovak Grant Agency: KEGA 006STU-4/2023

REFERENCES

[1] Ehsani et al. Modern electric, hybrid electric and fuel cell vehicles. 3rd edition, 2018, ISBN: 978-1-4987-6177-2

[2] G. Rill, A.A. Castro. Road Vehicle Dynamics: Fundamentals and Modeling with MATLAB®. May 2020, DOI: 10.1201/9780429244476, ISBN: 9780429244476

[3] M. Frivaldský, et al. Elektromobilita. 2020, ISBN: 9788055415987

APPLIED MECHANICS 2024

April 17th – 19th, 2024
Hotel Toliar, Štrbské Pleso
Slovakia

USE OF IMU SENSORS FOR MOTION ANALYSIS

J. GARANOVÁ KRIŠŤÁKOVÁ[1]*, M. DANIEL[1]

Shoulder pain is a widespread issue with significant impact on well-being and productivity, often becoming chronic and placing a burden on society. Current diagnostic tools, while useful, lack objectivity and fail to fully capture shoulder dynamics. Advanced tracking technologies offer detailed analyses but are limited by cost and space. Mobile inertial sensor systems provide a novel and accessible way to record real-time kinematic data, enhancing shoulder assessment outside laboratory settings. Objective evaluation of movement traits is essential for diagnosing potential pathologies and developing effective rehabilitation strategies. IMU sensors stand out for their objective data capture and real-time tracking, proving critical for treatment assessment and rehabilitation planning, particularly for shoulder disorders where compensatory movements indicate the severity and nature of impairment.

Keywords: scapulohumeral rhythm, shoulder girdle, IMU units, non-invasive measurement, motion monitoring

INTRODUCTION

Shoulder pain is a frequent health issue in Western society, significantly impacting social well-being, the ability to engage in sporting activities, and work productivity. It often turns into a recurring or chronic condition, posing a significant burden both on individuals and the wider socio-economic fabric. Being identified as the third most common musculoskeletal issue, shoulder dysfunctions restrict the movement of the upper limbs. This leads to a detrimental effect on performing daily activities and on the overall autonomy of the individuals [1].

In light of the challenges presented by the diagnosis and treatment of shoulder pain, emphasis has been placed on developing precise diagnostic instruments and effective therapeutic strategies. Present-day clinical evaluations of the shoulder encompass a variety of tests and scales. Although these tools are beneficial, they frequently fall short due to subjectivity and fail to offer a comprehensive view of the movement dynamics and positioning of the shoulder girdle [2].

Alternative approaches to analysis involve the employment of advanced technologies, like optoelectronic or electromagnetic tracking systems, which deliver detailed and objective insights into motor performance and the quality of movement. Despite the accuracy of these laboratory-based methods, their applicability is constrained by spatial and financial considerations [2].

[1] **Ing. Jana Garanová Krišťáková**, **prof. RNDr. Matej Daniel, Ph.D.**, Ústav mechaniky, biomechaniky a mechatroniky, Fakulta strojní ČVUT v Praze. Technická 4, 160 00 Praha – Dejvice; garanjan@cvut.cz, matej.daniel@cvut.cz

Mobile measurement systems, which utilize inertial sensor technology, offer an innovative alternative. Commonly equipped with accelerometers, gyroscopes, and magnetometers, these systems enable the capture of kinematic data, including speed, acceleration, and orientation, in real-time and within real-world settings. Consequently, they expand the possibilities for shoulder evaluations beyond the confines of laboratory environments and present a cost-effective alternative to traditional methodologies [3].

Equally important is the emphasis on the need for objective evaluation of specific movement characteristics, including speed, smoothness, and range of motion, along with the compensatory movements of other joints during motion. These traits can significantly influence the functional state of the shoulder girdle and may indicate the presence of potential pathologies. Contemporary methods frequently neglect these aspects, potentially leading to suboptimal rehabilitation strategies. The application of dynamic motion analysis and mobile measurement systems presents a solution to this oversight, offering more comprehensive information that can enhance the diagnosis, treatment, and final outcomes for individuals experiencing shoulder issues.

METHODS

To evaluate the performance of upper limb motion estimation, we selected Physilog® 5 sensor units as our experimental tools. In our experimental measurements, sensor units which were used (each containing 3-D gyroscopes and 3-D accelerometers). These units can be synchronized, making the output signals/data equally long.

IMU accuracy testing

The accuracy testing of IMU sensors was conducted as follows. An IMU sensor was affixed to the arm using a mounting strap. The participant was then instructed to stand next to a wall on which a scale marked with angles from 0° to 180° was placed, with the pivot point aligned with the shoulder joint. This scale was utilized to compare the actual angles with those measured by the sensor. Fig. 1 illustrates the schema for performing the movements.

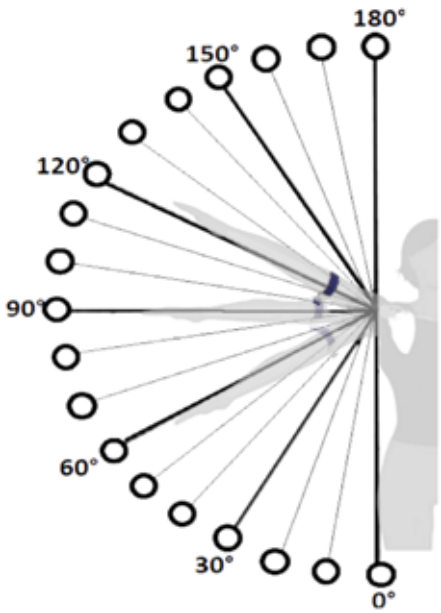

Fig. 1 Experimental measurement scheme

The measurement process proceeded in the following manner: the participant stood in a neutral stance, with the upper limb hanging freely at the side. This position was considered as 0°. Then, the participant incrementally raised the upper limb by 10°, 20°, 30°, and then returned to 0°. This motion was repeated progressively until reaching 180°.

Scapulohumeral rhythm

Frequently used assessment scales and scores fail to consider variations in the coordination between the scapula and the arm, notably scapular dyskinesia. These evaluations lack components specifically designed to assess scapular movements, and evaluators are not instructed to examine such movements. This oversight can lead to the misclassification of patients, which, in turn, may result in the misjudgment of therapeutic outcomes and the improper formulation of rehabilitation plans.

The measurement of the scapulohumeral rhythm was conducted using two sensors that could be synchronized with each other. For the actual arm movement measurement, one sensor was attached to the lateral side of the arm. To measure the scapulohumeral rhythm, a second sensor was attached beneath the infraspinatus area of the scapula bone (Fig. 2) [4].

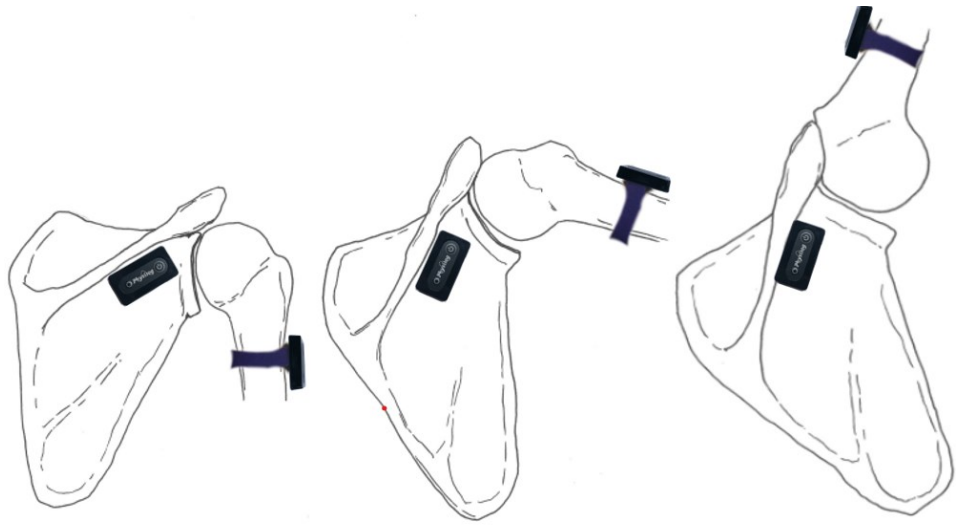

Fig. 2 Scapulohumeral rhythm measurement scheme

According to the study, the highest accuracy of measurements was observed up to 120°; hence, movements were conducted solely within this range.

RESULTS

On the graph (Fig. 3), the angles recorded using the gyroscope of the IMU unit are plotted. This was followed by the need for signal modification in Matlab, as illustrated in the subsequent graphs. The benefits include repeatability (allowing for revisiting the recordings) and the capability to monitor motion over time.

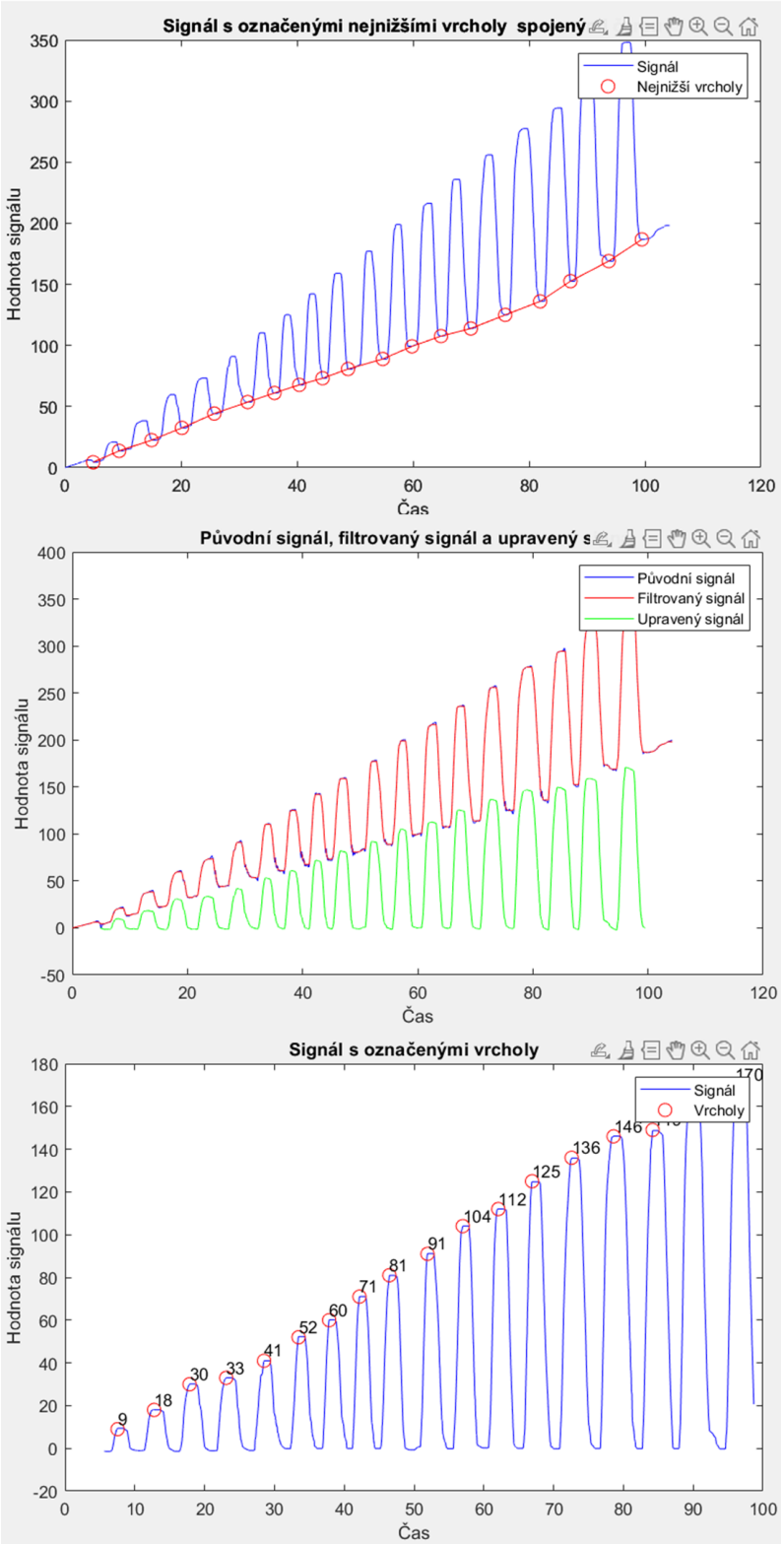

Fig. 3 Graphs of angle corrections from accuracy testing

In the graph, we observe the results from the sensor accuracy testing. Gyroscope sensors are known to exhibit significant drift during measurements, as evidenced by the top graph. To ascertain precise angles, it's necessary to eliminate this drift, depicted in the middle graph. The lower graph displays the angles numerically at their peaks, following signal adjustment. The discrepancies between the measured angles and actual values are attributed to several factors:

- loss of signal part after adjustments for drift removal and smoothing,
- sensor rotation along additional axes during physiological movements of the arm at higher angles,
- inherent measurement error of the subject.

Given that zero-error precision is not a requirement for our purposes of testing arm motion, the results and accuracy of the sensors are deemed adequate.

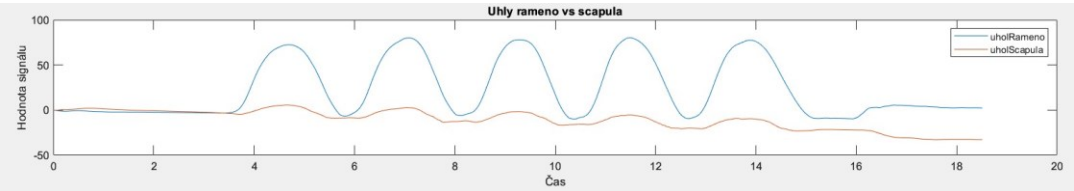

Fig. 4 Graph of scapula movement relative to the arm

The graph (Fig. 4) illustrates the scapulohumeral rhythm, specifically the movement of the scapula relative to the shoulder. In non-invasive measurement of scapular movements using IMU units, the precision of the angle measurements is influenced by the sensor's placement on the skin. Additionally, the body composition of the subject being measured, such as the amount of muscle mass or subcutaneous fat, significantly affects the accuracy [5]. Furthermore, the exact placement of the sensor plays a crucial role.

CONCLUSION

Accurate assessment of the scapulohumeral rhythm is crucial for a detailed evaluation of the shoulder girdle's condition, playing a vital role in the diagnosis and subsequent treatment of the upper limb's musculoskeletal system. Utilizing IMU units offers a contemporary approach that moves beyond traditional methods, yet, as a non-invasive technique, it comes with its own set of limitations and inaccuracies.

The merit of IMU sensors rests in their provision of objective and quantifiable movement data, coupled with the advantage of real-time motion tracking and recording. This information is valuable for assessing treatment efficacy, guiding rehabilitation efforts, and advancing patient movement research.

In patients experiencing shoulder disorders, compensatory movements frequently arise as a direct consequence of pain, or the challenge associated with executing pain-free actions. In such contexts, the data garnered from positional monitoring can offer significant benefits for clinical interventions and the rehabilitation process. For patients suffering from shoulder ailments, compensatory movements are common responses to pain or the challenge of executing movements without discomfort. In these instances, insights gained from position monitoring can be invaluable for clinical practice and rehabilitation planning.

ACKNOWLEDGEMENT

This publication was supported by the scientific project registered under number: 12131-301-3012301 B001.

REFERENCES

[1] N.E. D'hondt, et al. Reliability of performance-based clinical measurements to assess shoulder girdle kinematics and positioning: systematic review. *Physical therapy & Rehabilitation Jour.* **2017**, 97 (1), 124-144. DOI: https://doi.org/10.2522/ptj.20160088

[2] L. De Baets, et al. Shoulder assessment according to the international classification of functioning by means of inertial sensor technologies: A systematic review. *Gait & posture* **2017**, 57, 278-294. DOI: https://doi.org/10.1016/j.gaitpost.2017.06.025

[3] A.G. Cutti, et al. The Constant score and the assessment of scapula dyskinesis: Proposal and assessment of an integrated outcome measure. *Journal of Electromyography and Kinesiology* **2016**, 29, 81-89. DOI: https://doi.org/10.1016/j.jelekin.2015.06.011

[4] M. Mantovani, et al. Accuracy of measuring scapular position and motion with a novel motion capture system. *JSES Reviews, Reports, and Techniques* **2023**, 3 (3), 303-311. DOI: https://doi.org/10.1016/j.xrrt.2023.03.007

[5] D. Meng, T. Shoepe, G. Vejarano. Accuracy improvement on the measurement of human-joint angles. *IEEE Journal of Biomedical and Health Informatics* **2015**, 20 (2), 498-507. DOI: 10.1109/JBHI.2015.2394467

APPLIED MECHANICS 2024

April 17th – 19th, 2024
Hotel Toliar, Štrbské Pleso
Slovakia

CALIBRATION OF POLYMER BY MEANS OF THE PRF MATERIAL MODEL IMPLEMENTED IN ABAQUS

M. HANČINOVÁ[1]*, E. DUBŇANSKÁ[2], R. HUŇADY[3]

In modern engineering development, the role of finite element simulations is irreplaceable. To achieve maximum accuracy in simulations using commercial software, it is essential to have a carefully formulated material model. This paper is focused on the polymeric material PPC3TF2, which is widely used in the manufacture of HVAC (Heating, Ventilation, and Air Conditioning) components and automotive interior trim. The article discusses the calibration process of an advanced PRF (Parallel Rheological Framework) material model that is integrated in the commercial software Abaqus. The material model coefficients initially calculated in Excel served as input values for the structure of the material model in Abaqus. In order to reduce computational time, the unit cube model was used for the simulations. To achieve optimal results, optimization of the coefficients was performed using Isight software.

Keywords: PRF; polymer material; calibration

INTRODUCTION

In finite element analysis, it is necessary to use a suitable constitutive model to simulate the material properties. Polymeric materials are nowadays considered as reliable and advanced materials with outstanding mechanical properties. In the commercial software Abaqus, in order to represent specific material properties such as hyperelasticity, non-linear viscoelasticity and plasticity, the PRF (Parallel Rheological Framework) model can be used. PRF provides the ability to represent the material behaviour of polymers comprehensively, which allows more realistic simulations, but requires more complex calibration methods [1-3].

[1] **Ing. Martina Hančinová**, Department of Applied Mechanics and Mechanical Engineering, Faculty of Mechanical Engineering, Technical University of Košice, Letná 1/9, Košice-Sever, Slovak Republic; martina.hancinova@tuke.sk
[2] **Ing. Erika Dubňanská**, Department of Applied Mechanics and Mechanical Engineering, Faculty of Mechanical Engineering, Technical University of Košice, Letná 1/9, Košice-Sever, Slovak Republic; erika.dubnanska@tuke.sk
[3] **Doc. Ing. Róbert Huňady, PhD.**, Department of Applied Mechanics and Mechanical Engineering, Faculty of Mechanical Engineering, Technical University of Košice, Letná 1/9, Košice-Sever, Slovak Republic; robert.hunady@tuke.sk

MATERIAL AND METHODS

The chosen PRF model (Fig. 1) consists of one equilibrium elastoplastic network and three viscoelastic networks.

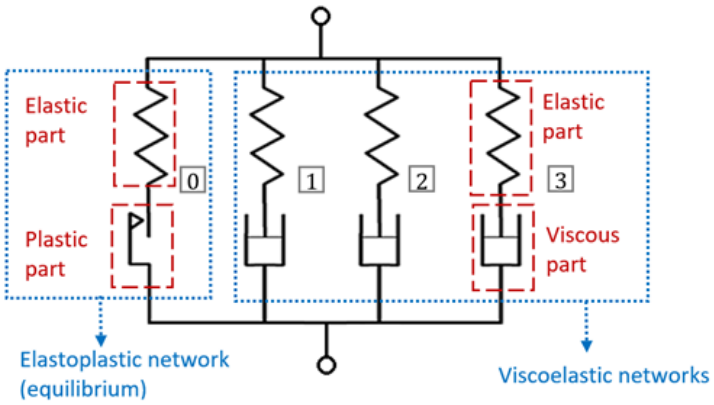

Fig. 1 Applied PRF model

For the calibration of plastic materials, the number of viscoelastic branches of the model, with respect to the number of parameters, is generally appropriate to choose $N = 3$. The elastic part of the response is specified for all branches by using a hyperelastic material model. For each of the branches, the same definition of the hyperelastic material is used. As a result, the model requires only one definition of hyperelasticity along with the stiffness ratio for each branch.

Calibration data

Calibration data from uniaxial tensile tests and relaxation tests were provided by Axel Products, Inc.

- **Hyperelasticity parameters**

In general, the Yeoh model was chosen to describe the hyperelastic behaviour. Since the material is isotropic, two material constants are required to represent the material properties. Based on the Young's modulus of elasticity determined from the tensile curves and the Poisson's number for polypropylene, the constants C_{10} and D_1 of the Yeoh model were calculated.

- **Viscoelasticity parameters**

Viscoelasticity is used to define the behaviour of viscous dampers as well as the ratio of the stiffness of individual springs to the total stiffness. Relaxation test data were used to estimate the viscoelasticity parameters and the Prony series was defined. The Prony series parameters were then converted to the PRF model parameters SR and A.

With the use of the estimated parameters from Tab. 1 and for $n = 1, m = 0$ for each of the three branches, the PRF model is linearly viscoelastic.

Tab. 1 Estimated parameters of material model

Hyperelasticity	$C_{10} = 474.87$ MPa	$D_1 = 0.000309$ MPa^{-1}
Viscoelasticity	$SR_1 = 0.0228$	$A_1 = 0.0154$ MPa^{-1}
	$SR_2 = 0.0876$	$A_2 = 0.000236$ MPa^{-1}
	$SR_3 = 0.1540$	$A_3 = 0.0000144$ MPa^{-1}

Material model

The material model includes the definition of hyperelasticity and viscoelasticity (with parameters given in Tab. 1). The specification in Abaqus looks as follows:

*Material, name=M1;PPC3TF2
*Hyperelastic, yeoh, moduli=INSTANTANEOUS
<C10>, <C20>, <C30>, <D1>, <D2>, <D3>.
*Viscoelastic, Nonlinear, NetworkId=1, SRatio= <SR1>, Law=STRAIN
<A1>, <n1>, <m1>
*Viscoelastic, Nonlinear, NetworkId=2, SRatio=<SR2>, Law=STRAIN
<A2>, <n2>, <m2>
*Viscoelastic, Nonlinear, NetworkId=3, SRatio=<SR3>, Law=STRAIN
<A3>, <n3>, <m3>

A unit cube was used as a simplified model of the specimen in the simulations. A comparison of the results of the first simulation (using the estimated coefficients from Tab. 1) with the curves obtained from the material tests is shown in Fig. 2.

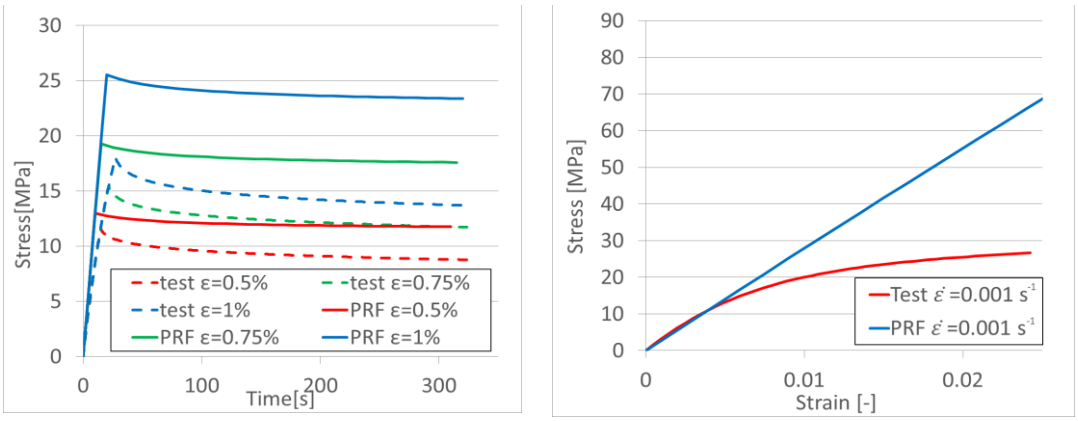

Fig. 2 PRF model response (before parameter optimization) compared to test data

From the comparison of the responses, the need for the adjustment of the model parameters is evident. The optimization requires modification of the shape of the tensile curve, which can be done primarily by changing the hyperelasticity parameter C_{10}. At earlier times, stress relaxation also needs to be emphasized. This can be achieved by optimizing the n, m parameters.

Two types of material tests were used in the Isight material coefficient fitting process. In the calibration scheme, one network for uniaxial test and three networks for relaxation tests are used.

The optimization algorithm AMGA - Archive based Micro Genetic Algorithm was used to optimize the coefficients in Isight. The hyperelasticity parameter C_{10} is optimized first. In the next optimization the viscoelasticity parameters $SR_1, SR_2, SR_3, A_1, A_2, A_3, n_1, n_2, n_3, m_1, m_2, m_3$ are refined. Out of ten thousand calculated solutions, the optimal solution for which the objective function in the form of squared error takes the lowest value, was selected. The results from the simulation using the final coefficients of the model are shown in Fig. 3. The used parameter values are shown in Tab. 2.

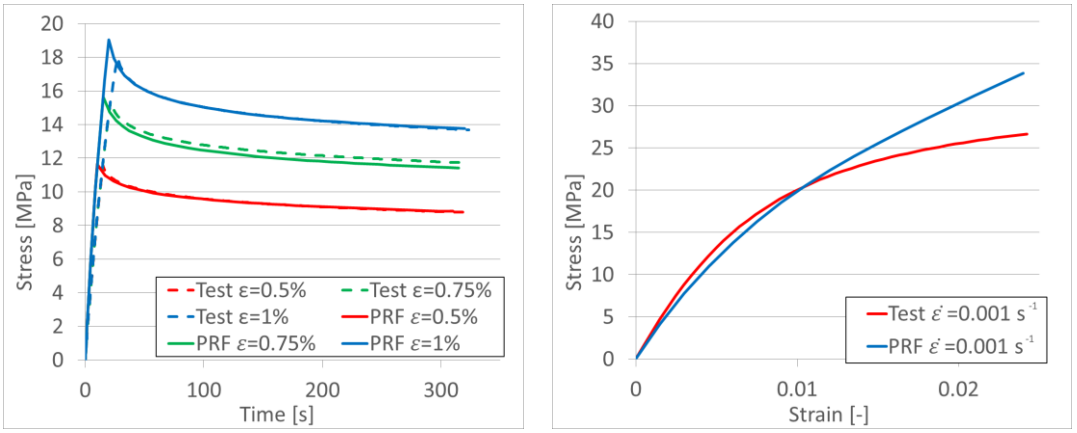

Fig. 3 PRF model response (after parameter optimization) compared to test data

Tab. 2 Optimized parameters of material model

Hyperelasticity	$C_{10} = 493.62$ MPa	$D_1 = 0{,}000309$ MPa^{-1}		
Viscoelasticity	$SR_1 = 0.0979$	$A_1 = 0.0000226$ MPa^{-1}	$n_1 = 4{,}708$	$m_1 = -0{,}335$
	$SR_2 = 0.3720$	$A_2 = 0.0000151$ MPa^{-1}	$n_2 = 3{,}47$	$m_2 = -0{,}524$
	$SR_3 = 0.2470$	$A_3 = 2.15 \cdot 10^7$ MPa^{-1}	$n_3 = 4{,}45$	$m_3 = -0{,}369$

CONCLUSION

By calibration with the use of the PRF material model, a material model of the PPC3TF2 plastic was created for use in FEM calculations in Abaqus. Optimization of the proposed coefficients in Isight ensured that the relaxation curves were approximated. To further improve the model, it would be possible to build on this work and extend the material model to include plasticity parameters. It would also be feasible to make the material model strain rate dependent and temperature dependent.

ACKNOWLEDGEMENT

The work has been supported by the grant project VEGA 1/0516/22.

REFERENCES

[1] J. Bergström. Mechanics of Solid Polymers. Theory and Computational Modeling. Elsevier Inc., 2015. ISBN 978-0-323-31150-2.

[2] M.R. Karim, Z. Zhang, Y. Zhu. Prediction of Nonlinear Viscoelastic Recovery of Thermoplastic Polymers using Abaqus Parallel Rheological Framework (PRF) Model. Simulia user meeting 2016.

[3] R.Ch. Goyal, Uncertainity Quantification in non-linear seismic wave propagation. Thesis. Carleton University: Ottawa, Canada, 2017.

APPLIED MECHANICS 2024

April 17th – 19th, 2024
Hotel Toliar, Štrbské Pleso
Slovakia

THERMO-MECHANICAL SIMULATION OF DRUM BRAKE

M. HANZALÍK[1*], J. PAULECH[2]

Brakes are a key element of car safety and are therefore subject to high standards. An important parameter is brake heating during braking. This paper focuses on the thermo-mechanical simulation of a drum brake. We use Ansys Mechanical software to numerically simulate the brake thermal loading due to mechanical friction during braking.

Keywords: FEM, Thermo-mechanical analysis, Ansys, APDL, Drum brake

INTRODUCTION

Drum brake is a friction brake. This means that it converts kinetic energy into heat energy due to friction. If the brake overheats, this can lead to a so-called brake fade, where the coefficient of friction and thus the braking efficiency are significantly reduced. We simulated the effect of braking on the thermal state of the brake drum. For simulation we used the finite element method (FEM). Vehicle braking is a dynamic process and for this reason we simulated it as a transient analysis with large displacements. The simulation was composed of three main steps. In the first step, we spin the brake drum to a speed that corresponds to the desired vehicle speed. In the second step, the drum is held in a steady state at a constant speed. In the last step, we simulate the actual braking maneuver by pressing the friction pad against the drum to brake the vehicle. Due to the friction between the pad and the drum, heat is generated which heats the brake drum.

FEM SIMULATION MODEL

We have created a simplified CAD model of the drum brake. The CAD model consisted of three components - brake drum, friction lining and auxiliary shaft. The brake drum was divided into two components (yellow and grey in Fig.1), which together formed one component. This division allowed us to define each component with a different material. The division was only fictitious, and its purpose was to capture in the simulated model that the brake must convert part of the kinetic energy of the moving car into heat when braking, even though this part of the car wasn't in the CAD model.

[1] **Ing. Matej Hanzalík**, Department of Automotive Mechatronics, Faculty of Electrical Engineering and Information Technology, Slovak University of Technology in Bratislava, Ilkovičova 3, Bratislava, Slovak republic; matej.hanzalik@stuba.sk
[2] **Ing. Juraj Paulech, PhD.**, Department of Automotive Mechatronics, Faculty of Electrical Engineering and Information Technology, Slovak University of Technology in Bratislava, Ilkovičova 3, Bratislava, Slovak republic; juraj.paulech@stuba.sk

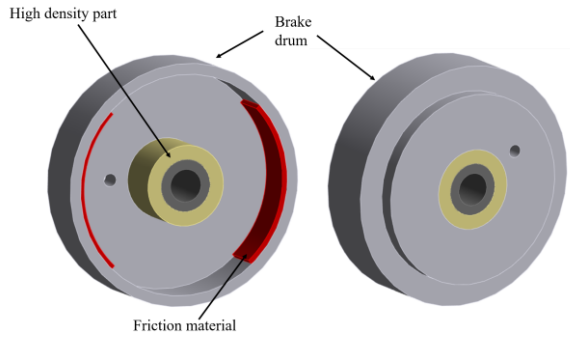

Fig. 1 CAD model of drum brake

The grey part of brake drum was made of cast iron. The yellow one was made of a fictitious material with high density which we used to model an energy equivalent replacement for the rest of the car. The other material properties of the yellow part were identical to the cast iron. For the friction lining, we used the material properties described in Tab. 1. The auxiliary shaft served to eliminate numerical error and was used only in the preparation phase (steps 1 and 2). It was deactivated during the actual braking (step 3) and did not interfere with the braking (step 3).

Tab. 1 Material properties used in simulation [1].

	Brake Drum	**Friction Material**
Density	7100 $kg \cdot m^{-3}$	3660 $kg \cdot m^{-3}$
Young's modul	$1.25 \cdot 10^{11}$ Pa	$8.2 \cdot 10^{8}$ Pa
Poisson number	0.25	0.25
Thermal conductivity	54 $W \cdot m^{-1} \cdot K^{-1}$	1.01 $W \cdot m^{-1} \cdot K^{-1}$
Specific heat capacity	568 $J \cdot kg^{-1} \cdot K^{-1}$	1034 $J \cdot kg^{-1} \cdot K^{-1}$

As stated, it was necessary to design a suitable equivalent substitute for the vehicle. The substitute was calculated so that the kinetic energy of the rotating brake is equal to the kinetic energy of the vehicle Eq.1.

$$\frac{1}{2} \cdot m \cdot v^2 = E_K = E_{rot} = \frac{1}{2} \cdot I \cdot \omega^2 \tag{1}$$

We collected vehicle data from publicly available data. We used a Ford Fiesta mk5 as a reference vehicle. The maximum speed of the vehicle was v = 160 km/h. The tyres on the vehicle were 175/65/R14. Based on the tyre size, we determined the dynamic wheel radius to be 0.28 m. We used this radius to convert the translational velocity to rotational velocity (ω). The maximum weight of the vehicle was 1530 kg. We assumed a weight distribution of 60 % on the front axle and 40 % on the rear axle. We simulated only one wheel on the rear axle so the mass attributable to this wheel was m = 306 kg (20 % of 1530 kg). To achieve equilibrium between kinetic energy of vehicle and rotational energy of our model we calculate an artificial density for the yellow part of brake drum (Fig. 1). The formula of moment of inertia for hollow cylinder is in the equation Eq. 2. The Eq. 3 shows calculation of density. The variable V represents the volume of the hollow cylinder for which we are calculating the density. We have assumed a worst-case scenario where the vehicle is maximally loaded and travelling at maximum speed [2].

$$I = \frac{1}{2} \cdot \rho \cdot V \cdot (r_1^2 + r_2^2) \tag{2}$$

$$\rho = \frac{4 \cdot E_K}{V \cdot (r_1^2 + r_2^2) \cdot \omega^2} \cong 134 \cdot 10^6 \ \ kg \cdot m^{-3} \tag{3}$$

In the design, it was necessary to divide the simulation into a suitable number of substeps. Too few sub-steps led to convergence problems as even small drum rotations represent large displacements of nodal points in the FEM analysis. On the other hand, using too many substeps resulted in a significant increase in simulation time. We had to solve a similar dilemma when creating the finite element mesh.

The finite element mesh forms the basis of the FEM analysis. In general, we can say that the denser the mesh (more elements and nodal points), the better the result we get. On the other hand, increasing the number of elements increases the computational complexity and simulation time. For this reason, we simplified the mesh to make it less computationally intensive. The network contains 1692 elements and 2922 nodal points. We replaced the original mechanical elements with SOLID225 multiphysic elements [3].

We defined contacts between the different parts of the model. Between the brake drum and the friction material there was a frictional contact with a coefficient of friction 0.35. Between the drum and the auxiliary shaft there was a bonded contact which was deactivated during braking (step 3). We also defined the joints that limited the degrees of freedom of the model. The drum and the auxiliary shaft were allowed to rotate about their axis. The friction material could move translationally along the horizontal axis.

In the simulation we neglected the heat convection from the brake. Since braking is a short-duration action and we assumed that during the braking all the generated heat remains in the brake and heats it up. We have neglected thermal expansion of the components in the analysis. This is because the pressure force of the pad on the drum is realized in the simulation through a constant value of the displacement of the friction lining. If we were to assume thermal expansion of the components in the simulation, we would introduce an error because the drum would increase its diameter with temperature and there would be a change in the braking force.

SIMULATION RESULTS

In this chapter we will present the results of the FEM simulation. We simulated braking with multiple initial velocities. During braking, we assumed vehicle decelerations of approximately 1g. In Fig. 2 we can see the kinetic energy of the system at different velocities. At constant deceleration, the rotational speed of the drum decreases linearly with time. The kinetic energy decreases parabolically which corresponds to the equation for calculation of kinetic energy. Tab.2 shows the results for braking time and brake temperature.

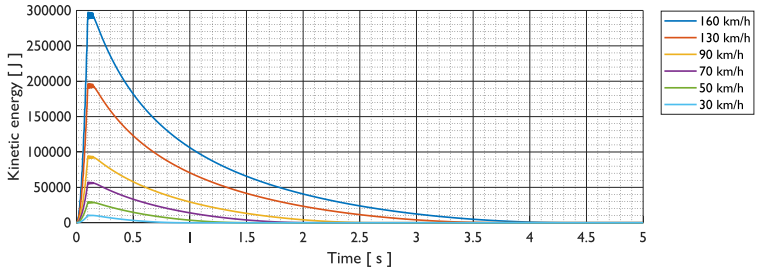

Fig. 2 Kinetic energy result of brake simulation

Fig. 3 shows the time progression of the temperature maximum. The temperature maximum is always at the contact between the friction material and the drum. The maximum temperature represents the maximum of all temperature values at the nodal points, which is calculated at each sub-step. In the worst-case scenario, the maximum temperatures reach up to 257 ºC. However, this is only the point value at the contact surface.

Tab. 2 Brake time and temperature simulation results

Velocity [km/h]	Brake time [s]	Max. temperature [°C]	Average temp. increase [°C]
30	0.81	54.6	3.5
50	1.36	88.4	9.3
70	1.94	124.2	16.9
90	2.5	157.8	25.5
130	3.55	216.5	31
160	4.23	256.7	57.5

In terms of overall brake heating, the average brake temperature is more interesting. The kinetic energy decreases parabolically, the amount of heat generated is greater at the beginning of braking. As we can see in Fig. 3, the maximum temperature decreases with time as heat is conducted from the friction surface to other parts of the drum.

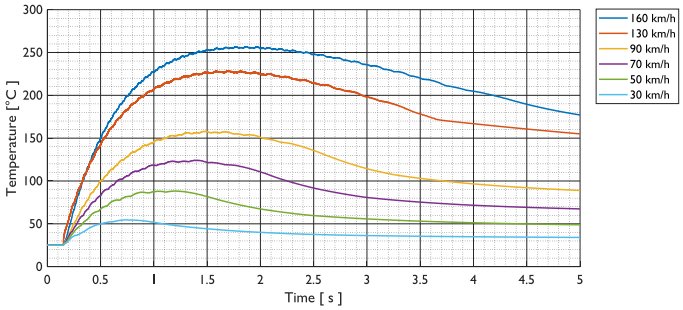

Fig. 3 Maximum temperature of brake

CONCLUSION

This paper focused on the thermomechanical simulation of a drum brake. In the first part, we created a FEM model. Then we simulated the braking for different initial speeds. We assumed a worst-case scenario where the vehicle is fully loaded and brakes with the maximum possible deceleration. In the result, we can see the change of the brake thermal state due to mechanical friction during braking.

ACKNOWLEDGEMENT

This work was supported by Grant Agency KEGA, grant No. 006STU-4/2023.

REFERENCES

[1] C. Watson, T.P. Newcomb. A Three-Dimensional Finite Element Approach to Drum Brake Analysis. *Journal of Automobile Engineering* **1990**, 1 (204), 93-101.

[2] Auto-Data.net, 2001 Ford Fiesta VI (Mk6) 5 door 1.3 Duratec (70 Hp), auto-data.net, [Online]. Available: https://www.auto-data.net/en/ford-fiesta-vi-mk6-3-door-1.3-duratec-8v-70hp-44908. [Cit. 21 March 2023]

[3] Ansys Inc., Ansys Help 2023 R1 Element reference SOLID225, Canonsburg, 2023.

APPLIED MECHANICS 2024

April 17th – 19th, 2024
Hotel Toliar, Štrbské Pleso
Slovakia

DETERMINATION OF SHAPE MEMORY ALLOYS' PROPERTIES

J. HARTWICH[1]*, S. SŁAWSKI[2], M. KCIUK[3], S. DUDA[4]

The presented experimental research investigated the influence of cyclic stretching and thermal activation of NiTi alloy wire on its electrical resistance, in addition determination of the stress-strain curve was presented. The purpose of the presented research was to determine the properties of NiTi alloys identifying their potency for use as sensors.

Keywords: NiTi; sensors; phase transformation; shape memory alloy

INTRODUCTION

Smart materials are defined as substances that have one or more properties that can be significantly modified in a controlled means by external stimuli; such as stress, temperature, electric or magnetic field, radiation, pH, moisture, or chemical compounds [1]. Smart materials can be used both in the sensor and actuator application because of their unique properties. Another advantage of smart materials is the possibility to use them in self sensing application. An important group among smart materials is that of Shape-Memory Alloys (SMA). SMA, in response to a change in the environmental conditions, change their internal structure (phase), which leads to a change in the properties of the alloy [2]. Among the SMAs, the nickel–titanium (NiTi) alloys have raised great scientific interest and have the largest number of industrial applications. The shape memory effect (SME) in NiTi alloys is due to the phase transformation (from martensite to austenite and reverse) related to the temperature change of the alloy [3]. There are three main crystal structures in NiTi alloys: twinned martensite, detwinned martensite and austenite; in some commercially produced alloys, a rhombohedral (R) phase may also be observed [4].

The purpose of the presented research was to analyze the sensory properties of NiTi alloys. The influence of the number of stretching cycles on the electrical resistance value of a NiTi alloy wire was measured. The resistance changes during activation of a thin NiTi alloy wire acting as an actuator was also measured. The stress-strain curve was also determined.

[1] **Jonasz Hartwich, MSc.**, Department of Theoretical and Applied Mechanics, Silesian University of Technology, Konarskiego 18A, 44-100 Gliwice, Poland; jonasz.hartwich@polsl.pl
[2] **Sebastian Sławski, PhD.**, Department of Theoretical and Applied Mechanics, Silesian University of Technology, Konarskiego 18A, 44-100 Gliwice, Poland; sebastian.slawski@polsl.pl
[3] **Marek Kciuk, PhD.**, Department of Mechatronics, Silesian University of Technology, Akademicka 2A, 44-100 Gliwice, Poland; marek.kciuk@polsl.pl
[4] **Assoc. Prof. Sławomir Duda, PhD.**, Department of Theoretical and Applied Mechanics, Silesian University of Technology, Konarskiego 18A, 44-100 Gliwice, Poland; slawomir.duda@polsl.pl

MATERIALS AND METOD

This paper determines the properties of NiTi alloy wires manufactured by Dynalloy, whose trade name is flexinol. It is an LT (low temperature) alloy, which means that the final temperature of transformation of martensite to austenite for this material is 70°C. The main properties of the material used according to the manufacturer are shown in Table 1.

Tab. 1 Manufacturer's stated properties of Flexinol wires [5].

Parameters	Density	Young's Modulus	Poisson Ratio	Specific Heat	Electrical Resistivity
Units	g/cm^3	GPa	-	cal/g*°C	μΩ*cm
Martensite	6.45	28	0.33	0.2	80
Austenite	6.45	75	0.33	0.2	100

In the sample preparation process, NiTi alloy wires were cut into 100mm long pieces. Holders, which are also electrical contacts, were mounted on the ends of the wires. Wires with different diameters of 100 and 150μm were used as research samples.

This paper presents: investigation of the effect of cyclic stretching of NiTi alloy wire on its electrical resistance, analysis of the change in electrical resistance during thermal activation of NiTi alloy wire, and determination of the stress-strain curve to calibrate the material model.

In order to perform this research, an easily reconfigured test stand was developed. The discussed research was performed on two different stand configurations. Measurements of cyclic loading and determination of the stress-strain curve of the NiTi alloy wire were performed for a test stand consisting of*:* STAV 500/280 stand (AXIS, Gdańsk, Poland) for mounting the sample (using the designed handle) and measure the displacement, FB50 force gauge (AXIS, Gdańsk, Poland). The process of recording measurement data was performed by the cDAQ-9174 data acquisition system (NI, Austin, TX, USA). The test stand is shown in Figure 1. The test stand for measuring electrical resistance during activation was updated with a spring-loaded system and a DC power supply for thermal activation of the wire [6].

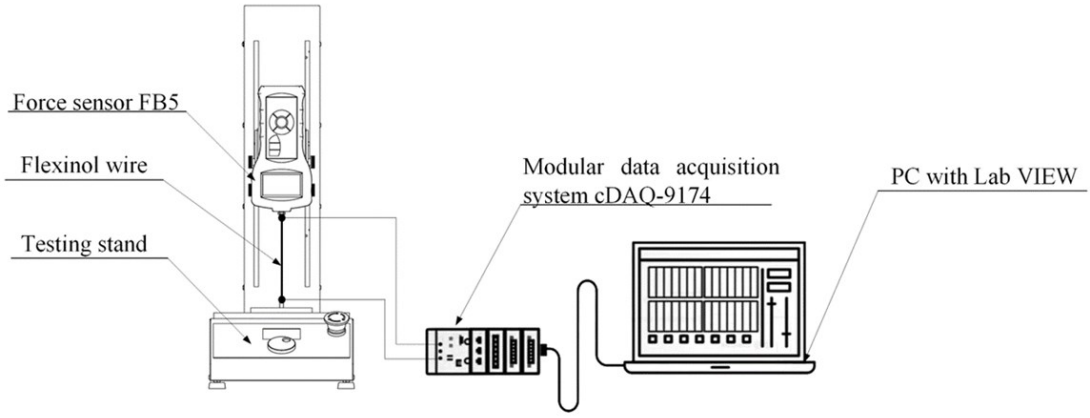

Fig. 1 Test stand scheme

RESULTS

During cyclic stretching of the sample, the electrical resistance decreased after each successive stretching cycle. The decrease in the electrical resistance value after the first cycle was significant, while for each following cycle the decrease in the electrical resistance value was smaller. The average value of the electrical resistance of NiTi alloy samples with a diameter of 100 µm and 150 µm after each successive stretching cycle is presented in Figure 2

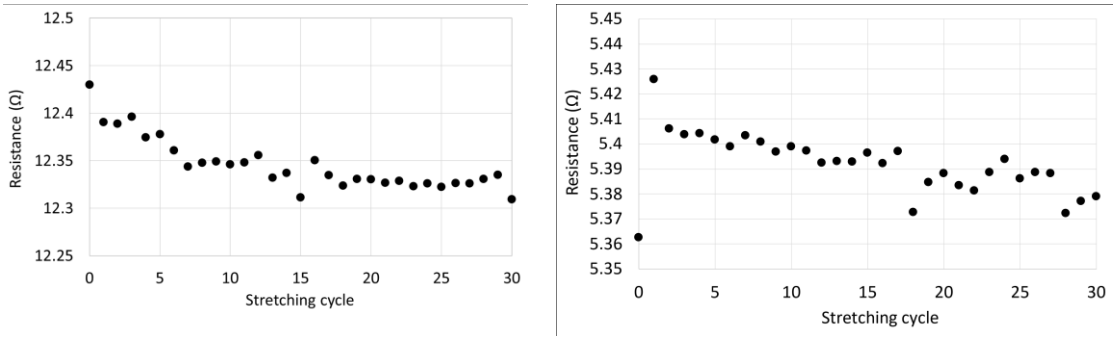

a) b)

Fig. 2 Change in resistance with time induced by cyclic stretching of NiTi alloy wire: a) wire diameter 100 µm b) wire diameter 150 µm

During the activation of the NiTi alloy sample, the length of the wire is shortened and the spring is deformed, which generates a force in the system. Shortening of the wire decreases its length with a minor change in wire diameter. This leads to a rapid decrease in electrical resistance. The waveforms of NiTi alloy samples' electrical resistance, force generation and displacement for 100 µm and 150 µm diameter samples are shown in Figure 3.

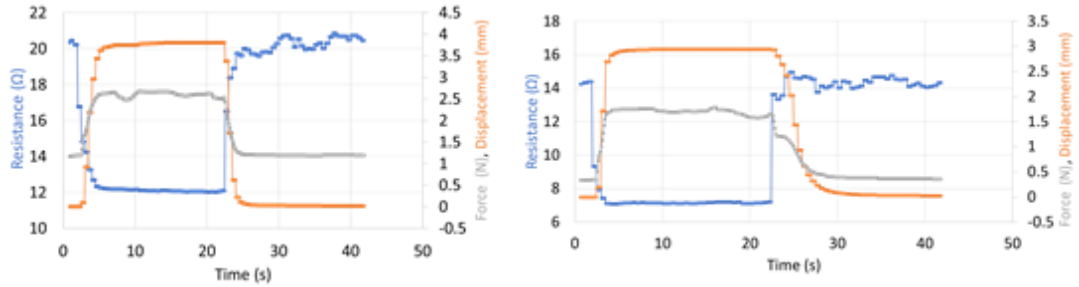

a) b)

Fig. 3 The waveform of the displacement, force and resistance of the NiTi wire during the heating process: a) wire diameter 100 µm b) wire diameter 150 µm

The determined stress-strain curve of the NiTi alloy sample was divided into stages. A trend line was determined for each stage. The coordinates of the intersection points of trend lines are the key values for calibrating the material model. The stress-strain curve is presented in Figure 4.

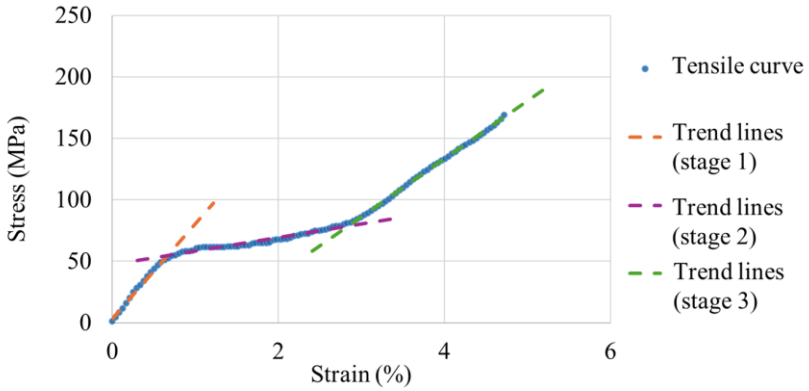

Fig. 4 Stress-strain curve by stage

CONCLUSION

The cyclic stretching for small elongations decreases NiTi wire electrical resistance with each stretching cycle. A potential application suggested by presented research is the use of NiTi wire sensory systems for structural monitoring. During the activation of the wire, the resistance values decrease even though the resistivity of austenite is higher than that of martensite. This is due to the reduction in the length of the wire and can be used for self-sensing of the actuator. The determined tensile curve is in accordance with expectations and allows to determine the parameters of the material model possible for use in numerical research.

REFERENCES

[1] I. Chopra. Review of current status of smart structures and integrated systems. Proceedings of SPIE - The International Society for Optical Engineering, 1996, 2717, 20-62. DOI: https://doi.org/doi:10.1117/12.239018

[2] J. Strittmatter, P. Gümpel, M. Hiefer. Intelligent Materials in Modern Production–Current Trends for Thermal Shape Memory Alloys. *Procedia Manuf.* **2019**, 30, 347-356. DOI: https://doi.org/10.1016/j.promfg.2019.02.049

[3] E. Abel, H. Luo, M. Pridham, A. Slade. Issues Concerning the Measurement of Transformation Temperatures of NiTi Alloys. *Smart Mater. Struct.* **2004**, 13, 1110-1117. DOI: https://doi.org/10.1088/0964-1726/13/5/016

[4] X. Ren, N. Miura, J. Zhang, K. Otsuka, K. Tanaka, M. Koiwa, T. Suzuki, Y.I. Chumlyakov, M. Asai. A Comparative Study of Elastic Constants of Ti-Ni Based Alloys Prior to Martensitic Transformation. *Mater. Sci.* DOI: https://doi.org/10.1016/S0921-5093(00)01876-1

[5] DYNALLOY, Inc. Flexinol® Nickel-Titanium Alloy Physical Properties. Available online: https://www.dynalloy.com/pdfs/TCF1140.pdf (accessed on 8 December 2023)

[6] J. Hartwich, S. Sławski, M. Kciuk, S. Duda. Determination of Thin NiTi Wires' Mechanical Properties during Phase Transformations. *Sensors* **2023**, 23 (3), 1153, 22 p. DOI: https://doi.org/10.3390/S23031153

APPLIED MECHANICS 2024

April 17th – 19th, 2024
Hotel Toliar, Štrbské Pleso
Slovakia

DESCRIPTION OF FATIGUE BEHAVIOR OF ADDITIVELY MANUFACTURED POLYMER METAMATERIAL STRUCTURE

P. HELEŠICOVÁ[1]*, L. TRÁVNÍČEK[2], J. PODUŠKA[3], L. NÁHLÍK[4], P. HUTAŘ[5]

This paper deals with the creation of material model of a 3D printed polymer metamaterial structure and characterization of its fatigue behavior. Metamaterials are structures with properties that are tunable or unusual for conventional materials. In order to safely use these materials in engineering applications, the fatigue behavior must be classified to qualify the weak spots and estimate the lifetime of the structures. Material model of the 3D printed material is created with quasi-static and fatigue testing. Simulation model of a metamaterial geometry configuration is used to localize the critical locations and obtain the stress state present. With criteria available from the literature, the fatigue lifetime can be predicted.

Keywords: additive manufacturing; quasi-static behavior; fatigue behavior; finite element method; lifetime estimation

INTRODUCTION

Metamaterials became highly researched thanks to the development of additive manufacturing (AM). AM allows complex geometries to be created with great precision. Metamaterials gain their properties not only by their material structure and composition, but also by their geometry.

The complexity of the topology results in complex stress state within the geometry. To ensure safe use of metamaterials, short- and long-term behavior must be known. A metamaterial structure with tunable stiffness (Fig.1) fabricated from PA12 by fused deposition modelling (FDM) was analyzed, the mechanical properties were measured, and the material model defined. Utilizing finite element analysis (FEA), the fatigue lifetime of the structure can be predicted.

[1] **Bc. Petra Helešicová**, Institute of Solid Mechanics, Mechatronics and Biomechanics, Faculty of Mechanical Engineering, Brno University of Technology, Technická 2896, 61669 Brno, Czech Republic, Institute of Physics of Materials, Czech Academy of Sciences, Žižkova 513/22, 616 00 Brno, Czech Republic; helesicova@ipm.cz

[2] **Ing. Lukáš Trávníček, Ph.D.**, Department of Polymer Engineering and Science, Montanuniversitaet Leoben, 8700, Leoben, Austria; lukas.travnicek@unileoben.ac.at

[3] **Ing. Jan Poduška, Ph.D.**, Institute of Physics of Materials, Czech Academy of Sciences, Žižkova 513/22, 616 00 Brno, Czech Republic. Email: poduska@ipm.cz

[4] **Prof. Ing. Luboš Náhlík, Ph.D**., CEITEC IPM, Žižkova 513/22, 616 00 Brno, Czech Republic; nahlik@ipm.cz

[5] **Prof. Ing. Pavel Hutař, Ph.D**., Institute of Physics of Materials, Czech Academy of Sciences, Žižkova 513/22, 616 00 Brno, Czech Republic; hutar@ipm.cz

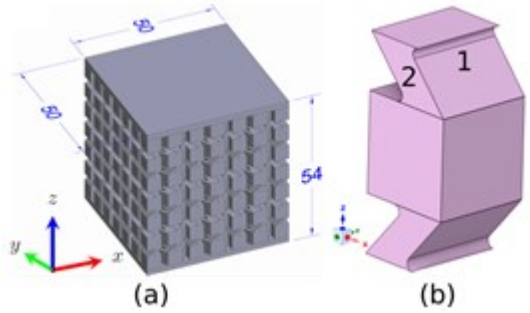

Fig. 1 (a) Computer-aided design (CAD) model of the whole metamaterial structure [1], (b) a cell with struts

MATERIAL MODEL

The additively manufactured material can have different material properties compared to the virgin material. Thus, the material model must be created for the 3D printed structure separately. Quasi-static and fatigue tests were carried out on dog-bone specimens, following the standards ASTM D638-22 [2] and ASTM D7791-22 [3], respectively. The specimens were manufactured in 6 printing orientations: flat 90°/90°, flat 0°/0°, flat 0°/90°, flat 45°/135°, upright 0°/90°, and upright 45°/135° (Fig. 2). Compression tests were conducted on printed blocks following the ISO 604 standard [4]. These were printed in all "flat" orientations. Electrodynamic testing machine INSTRON E10000 was used for the experimental testing.

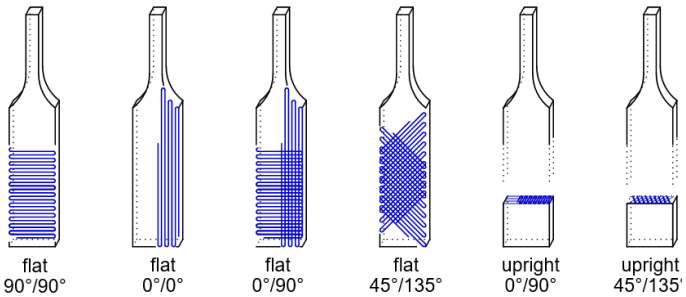

Fig. 2 Dog-bone specimens in six printing orientations used for material testing

Quasi-static testing

The tensile tests were carried out at testing speed of 5 mm/min in accordance with the standard ISO 527-1:2019 [5].. Deformation was measured using an extensometer and the force was recorded until fracture occurred. From uniaxial tensile tests, the elastic modulus was calculated following the standard. Compressive tests were conducted analogously, with testing speed of 1 mm/min.

The resulting tensile elastic moduli for each printing orientation are shown in Fig. 3(a). The "flat" printing orientations are comparable, but "upright" printed specimens proved very weak in tension, as the fracture is determined by low cohesion of individual layers in this printing orientation. Compressive elastic moduli for "flat" printed block specimens are shown in Fig. 3(b).

Fatigue testing

Fatigue tests for R-ratio of 0.1 were measured for all six printing orientations. Loading frequency was 10 Hz to prevent internal heating of the material and thermal failure. Infinite lifetime was considered after 1e6 cycles. S-N curves for the printing orientations are shown in Fig. 4. Similarly to quasi-static results, the "upright" printing directions proved much weaker than "flat" directions.

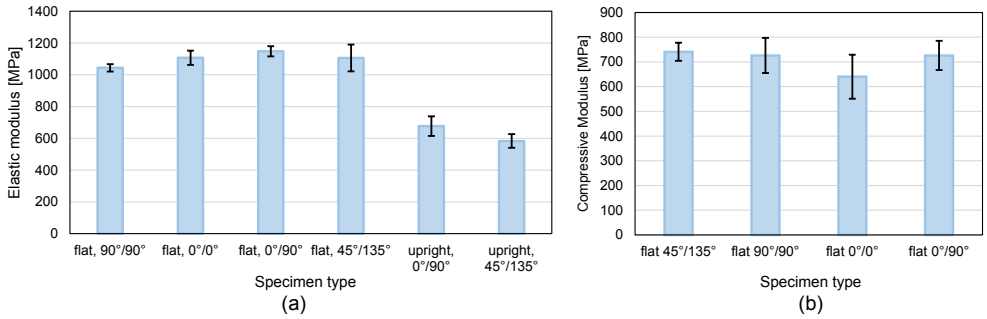

Fig. 3 (a) Tensile elastic moduli and (b) compressive elastic moduli for respective printing orientations

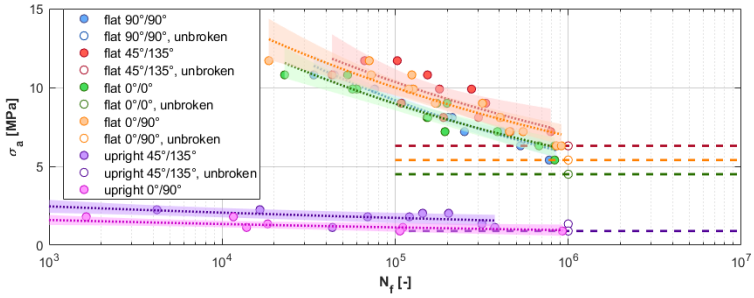

Fig. 4 S-N curves for respective printing orientations

Material model parameters

Considering the printing directions of the full structure, the "flat 0°/0°" direction was deemed most suitable to describe the printing in the areas of interest (struts connecting the cubes). Using the data from quasi-static and fatigue experiments, the following material model is proposed:

Tab. 1 Material model for flat 0°/0°printing direction

Material parameter	***Tensile elastic modulus***	***Tensile yield strength***	***Fatigue limit***	***Compressive elastic modulus***	***Compressive yield strength***
Value [MPa]	1106.79	22.9	4.5	641	27.7

NUMERICAL SIMULATION AND LIFETIME ESTIMATION CRITERIA

Using finite element method, the metamaterial structure with presented material model was created and its response to loading calculated. Two types of critical locations were distinguished within the struts; on the inclined planes, and the vertical planes (point 1 and 2 in Fig. 1(b), respectively).

The stress state is noted in each the two critical locations and four criteria from literature were applied to predict the fatigue lifetime of the structure. These criteria are first principal stress criterion [6] (Eq. (1)), von Mises criterion [6] (Eq. (2)), Berrehili et al. second invariant criterion [7] (Eq. (3)), and Nitta et al. strain energy density criterion [8] (Eq. (4)).

$$\sigma_{\mathrm{a},1} = \sigma_{\mathrm{f}} \cdot N^{-1/\mathrm{m}} \tag{1}$$

$$\sigma_{\mathrm{a,vM}} = \sigma_{\mathrm{f}} \cdot N^{-1/\mathrm{m}} \tag{2}$$

$$\sigma_{\mathrm{eq}} = \sqrt{J_{2,\max} + \alpha J_{2,\mathrm{mean}}} \leq \beta + \frac{\mathrm{A}}{N^{\mathrm{c}}} \tag{3}$$

$$\Delta W_1 = \frac{\Delta\sigma_1}{2}\Delta\varepsilon_1 = A_1 N^{-\beta_1} \quad (4)$$

Comparison of lifetime predicted by the individual criteria and the lifetime of the structure, which was measured for verification, is shown in Fig. 5.

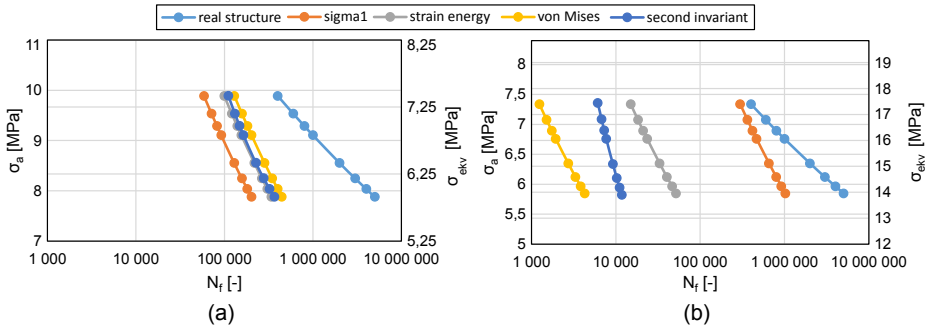

Fig. 5 Predicted and measured lifetimes in strut critical locations on (a) inclined plane, (b) vertical plane.

CONCLUSION

The material model of AM PA12 structure was established and fatigue lifetime predicted in two critical locations. Vertical plane location proved harder to describe, as significant negative third principal stress is present. However, when using the first principal stress criterion, the results are conservative and predict the lifetime well in both cases, while requiring the least material parameters. This combination makes the first principal stress criterion a useful method for estimating the lifetime.

ACKNOWLEDGEMENT

This research was conducted under the projects TN01000071 “National Competence Centre of Mechatronics and Smart Technologies for Mechanical Engineering” within the National Centres of Competence Programme of the Technological Agency of Czech Republic and COMET-Module project “Chemitecture” at the Polymer Competence Center Leoben within the framework of the COMET-program of the Federal Ministry for Transport, Innovation and Technology and the Federal Ministry for Digital and Economic Affairs.

REFERENCES

[1] M. Fleisch, A. Thalhamer, G. Meier, I. Raguž, P. Fuchs, P. et al. Functional mechanical metamaterial with independently tunable stiffness in the three spatial directions. *Materials Today Advances* **2021**, 11, 100-155.

[2] ASTM D638-22: Test Method for Tensile Properties of Plastics. ASTM International.

[3] ASTM D7791-22: Test Method for Uniaxial Fatigue Properties of Plastics. ASTM International.

[4] ISO 604:2002: Plastics - Determination of compressive properties. Int. Organization for Standardization.

[5] ISO 527-1:2019: Plastics. Determination of tensile properties – General principles. International Organization for Standardization.

[6] B. Klimkeit, Y. Nadot, S. Castagnet, C. Nadot Martin, C. Dumas, et al. Multiaxial fatigue life assessment for reinforced polymers. *International Journal of Fatigue* **2011**, 33 (6), 766-780.

[7] A. Berrehili, S. Castagnet, Y. Nadot. Multiaxial fatigue criterion for a high-density polyethylene thermoplastic. *Fatigue & Fracture of Engineering Materials & Structures* **2010**, 33 (6), 345-357.

[8] A. Nitta, T. Ogata, K. Kuwabara. Fracture mechanisms and life assessment under high-strain biaxial cyclic loading of 304 stainless steel. *Fatigue & Fracture of Engineering Materials & Structures* **1989**, 12 (2), 77-92.

APPLIED MECHANICS 2024

April 17th – 19th, 2024
Hotel Toliar, Štrbské Pleso
Slovakia

A SEMI-ANALYTICAL APPROACH FOR DETERMINATION OF THE WALL HEAT TRANSFER COEFFICIENT OF A CYLINDRICAL CONCENTRIC ANNULUS

D. HRON[1], J. VIMMR[2], V. SLÁMA[3]

One of the long-term research goals of Doosan Škoda Power s.r.o. is to develop an effective and fast method for determining the wall heat transfer coefficient on important parts of steam turbines during various operations. One of the geometrically simplest investigated parts of a steam turbine is the cylindrical annulus. In this paper, a semi-analytical solution of the Graetz problem in a concentric cylindrical annulus is presented, assuming a fully developed velocity profile of turbulent fluid flow regime. This semi-analytical solution is compared with the solution of the commercial computing system Ansys CFX when solving the same problem.

Keywords: wall heat transfer coefficient, Graetz problem, cylindrical annulus, Ansys CFX

INTRODUCTION

The wall heat transfer coefficient is one of the main inputs of temperature-deformation numerical calculations. Knowledge of analytical or semi-analytical methods is necessary for the validation of CFD software tools and for the validation of the methodology for evaluating the wall heat transfer coefficient from the numerical calculations. In addition, a suitable semi-analytical method can possibly replace a time-consuming numerical calculation in selected cases. The development of a methodology for determining the wall heat transfer coefficient on significant parts of steam turbines for important operations is therefore one of the long-term research goals of Doosan Škoda Power s.r.o.

This paper presents a semi-analytical method for determining the heat transfer coefficient through the wall of a cylindrical annulus assuming a fully developed steady-state velocity profile in the entire computational domain and an evolving temperature profile of an incompressible Newtonian viscous fluid, i.e. the so-called Graetz problem. In work [4], a semi-analytical method for solving the laminar Graetz problem was presented. In our paper, we extend this method to solve the turbulent Graetz problem. The results obtained by this new method are compared with the numerical results calculated using the commercial computing system Ansys CFX.

[1] **Ing. David Hron**, Department of Mechanics, Faculty of Applied Sciences, University of West Bohemia, Technicka 8, Pilsen, Czech Republic; hrond@kme.zcu.cz
[2] **Prof. Ing. Jan Vimmr, Ph.D.**, Department of Mechanics, Faculty of Applied Sciences, University of West Bohemia, Technicka 8, Pilsen, Czech Republic; jvimmr@kme.zcu.cz
[3] **Ing. Václav Sláma, PhD.**, R&D department, Doosan Škoda Power s.r.o., Tylova 1/57, Pilsen, Czech Republic; vaclav.slama@doosan.com

FORMULATION OF THE PROBLEM

The flow and heat transfer in a cylindrical concentric annulus of length L formed by an inner cylinder of radius r_i and an outer cylinder of radius r_o is investigated, see Fig. 1. Dirichlet temperature boundary conditions are introduced on the inlet of the computational domain T_e, on the inner wall T_i and on the outer wall T_o of the cylindrical annulus, therefore the boundary conditions are

$$T(0,r) = T_e; T(x,r_i) = T_i; T(x,r_o) = T_o. \tag{1}$$

Steady and fully developed velocity $u(r)$ corresponding to turbulent flow regime is considered throughout the computational domain.

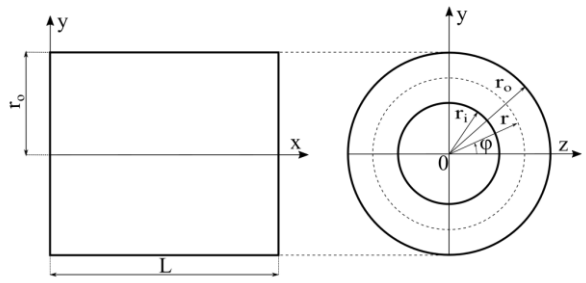

Fig. 1 The geometry of the considered computational domain.

STEADY AND FULLY DEVELOPED VELOCITY OF THE FLUID

In the case of the laminar flow regime, the fully developed velocity corresponding to the Poiseuille flow regime can be determined analytically from the Navier-Stokes equations with the application of the boundary conditions of zero velocities on the walls of the cylindrical annulus. Then the velocity profile is given by the well-known Poiseuille formula.

In the case of a turbulent flow regime, it is necessary to settle for formulations in which empiricism enters to a greater or lesser extent. In this paper, we apply the empirical formula of the fully developed velocity from [1],

$$\frac{u(r)}{u_{max}} = \left(\frac{r_o - r}{r_o - r_m}\right)^{0.142} \quad \text{for } r_m \le r \le r_o; \tag{2}$$

$$\frac{u(r)}{u_{max}} = \left(\frac{r - r_i}{r_m - r_i}\right)^{0.102} \quad \text{for } r_i \le r \le r_m; \tag{3}$$

$$\frac{u_m}{u_{max}} = 0.876; \ \frac{r_m}{r_o} = \left(\frac{r_i}{r_o}\right)^{0.343}\left(1 + \left(\frac{r_i}{r_o}\right)^{0.657} - \left(\frac{r_i}{r_o}\right)\right), \tag{4}$$

where $u_{max} = u(r_m)$ is the maximum flow velocity and u_m is the mean flow velocity of the fluid.

DETERMINATION OF TEMPERATURE

The simplest algebraic turbulence model, the so-called Prandtl mixing length model, is applied by introducing turbulent (eddy) viscosity near the rigid wall

$$\nu_t = l^2 \left|\frac{\mathrm{d}u}{\mathrm{d}r}\right|, \tag{5}$$

where l is Nikuradse mixing length for concentric annular duct, see [2],

$$l = \frac{r_o - r_i}{2}\left(0.14 - 0.08\left(2\,\frac{r - r_i}{r_o - r_i} - 1\right)^2 - 0.06\left(2\frac{r_o - r_i}{r_o - r_i}\right)^4\right). \tag{6}$$

The turbulent diffusivity in radial direction is

$$\varepsilon_{hr}(r) = \frac{\nu_t}{Pr_t}. \tag{7}$$

The Prandtl turbulent number Pr_t is set to 0.9, see [3]. The energy equation valid for higher Peclet number $Pe = \frac{\rho \cdot c_p \cdot u_m \cdot 2r_o}{k}$ is

$$\rho c_p u(r) \frac{\partial T}{\partial x} = \frac{1}{r}\frac{\partial}{\partial r}\left(r g(r) \frac{\partial T}{\partial r}\right), \tag{8}$$

where $g(r) = k + \rho c_p \varepsilon_{hr}(r)$, k is the thermal conductivity of the fluid, ρ is the fluid density and c_p is the specific heat capacity at constant pressure of the fluid.

In [4], a semi-analytical method was presented for solving equation (8) for the case corresponding to the laminar flow regime. That is, for lower speeds and $\varepsilon_{hr}(r) = 0$. In our paper, we build on this method and extend it to solve the turbulent flow regime.

After the introduction of dimensionless coordinates $\xi = \frac{r}{r_o}$; $\zeta = \frac{1-\xi_i}{Pe(r_o - r_i)}$ and constant $\xi_i = \frac{r_i}{r_o}$, energy equation (8) with boundary conditions (1) is converted into a problem consisting of the solution of a Sturm-Liouville type equation

$$\frac{d}{d\xi}\left(\xi g(\xi) \frac{dR(\xi)}{d\xi}\right) + \left(\frac{u}{2u_m}\right)^2 \frac{\lambda^2}{2} R(\xi)\xi = 0 \tag{9}$$

with boundary conditions $R(1) = R(\xi_i) = 0$ and the solution of an ordinary differential equation

$$\frac{1}{\xi}\frac{\partial}{\partial \xi}\left(\xi g(\xi) \frac{\partial z_f}{\partial \xi}\right) = -\frac{\partial g}{\partial \xi}\frac{1}{1-\xi_i} - \frac{g(\xi)}{\xi(1-\xi_i)} \tag{10}$$

with boundary conditions $z_f(1) = z_f(\xi_i) = 0$.

Equation (9), respectively its eigenvalues λ, eigenfunctions $R(\xi)$ and derivatives of eigenfunctions $\frac{dR(\xi)}{d\xi}$, are solved numerically by the method of finite volumes, see [5].

Equation (10) has solution

$$z_f(\xi) = -\frac{\xi - \xi_i}{1-\xi_i} + \frac{1}{\int_{\xi_i}^{1} \frac{1}{\tilde{\xi} g(\tilde{\xi})} d\tilde{\xi}} \int_{\xi_i}^{\xi} \frac{1}{\tilde{\xi} g(\tilde{\xi})} d\tilde{\xi}. \tag{11}$$

The integrals in equation (11) are calculated numerically using the trapezoidal rule. Note that for the laminar flow regime, $g(\xi) = k$, the solution $z_f(\xi)$ can be calculated analytically without the need for numerical integration as was stated in [4].

The final solution of temperature is

$$T = \left(\phi + \frac{\xi - \xi_i}{1-\xi_i}\right)(T_e - T_i) - T_i + \left(\psi + \frac{1-\xi}{1-\xi_i}\right)(T_e - T_o) + T_o - T_e, \tag{12}$$

where

$$\phi = \sum_{n=0}^{\infty} C_n R_n(\xi) e^{-\lambda_n^2 \zeta} + z(\xi); \psi = \sum_{n=0}^{\infty} D_n R_n(\xi) e^{-\lambda_n^2 \zeta} - z(\xi). \tag{13}$$

Constants C_n, D_n are solved numerically using the Moore-Penrose inverse to ensure the validity of the boundary conditions (1).

COMPUTATION OF WALL HEAT TRANSFER COEFFICIENT

The heat transfer coefficient of the inner wall h_i, or the heat transfer coefficient of the outer wall h_o, is calculated by substituting into Newton's cooling law in the form

$$h_i = \frac{q_i''}{T_i - T_b}; \quad h_o = \frac{q_o''}{T_o - T_b} \tag{14}$$

where

$$q_i'' = -k\frac{\partial T}{\partial r}|_{r=r_i};\quad q_o'' = k\frac{\partial T}{\partial r}|_{r=r_o};\quad T_b = \frac{\int_{r_i}^{r_o} uTr\,dr}{\int_{r_i}^{r_o} ur\,dr}. \tag{15}$$

The integrals appearing in the expression of the bulk temperature T_b are calculated numerically by the trapezoidal rule.

SELECTED RESULTS

Definition of the solving example

The presented semi-analytical solution is compared with the solution of temperature and wall heat transfer coefficient by the commercial computing system Ansys CFX with the implementation of k-omega SST turbulence model when solving the same problem. Definition of the solving example was provided by Doosan Škoda Power s.r.o, see Tab. 1. The parameters of the incompressible viscous liquid were chosen to best match the parameters of real steam.

The fully developed turbulent velocity profile in concentric annulus predicted by equations (2) to (4), denoted 'empirical', and the velocity profile calculated by the commercial computing system Ansys CFX using k-omega SST model, denoted 'CFX', are shown in Fig. 2.

Tab. 1 Problem entry.

Physical quantity	[unit]	Value	Description
μ	10^{-5}[kg m^{-1}s^{-1}]	2.7941	Dynamic viscosity
ρ	10[kg m^{-3}]	1.0278	Density
k	[W m^{-1}K^{-1}]	0.0675	Thermal conductivity
c_p	10^3[J kg^{-1}K^{-1}]	2.2687	Specific heat capacity
r_i	[m]	0.3150	Inner radius of annuli
r_o	[m]	0.3250	Outer radius of annuli
L	[m]	0.6051	Length of annuli
u_m	[m s^{-1}]	2.2945	Mean flow velocity
T_e	[°C]	484.4	Inlet temperature
T_i	[°C]	407.0	Temperature of inner wall
T_o	[°C]	335.0	Temperature of outer wall

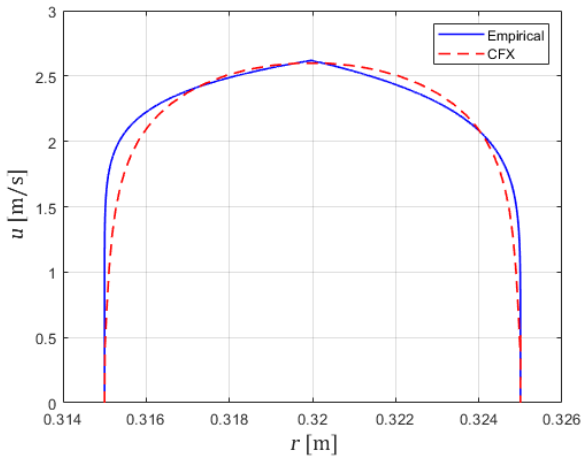

Fig. 2 The empirically predicted and numerically computed velocity profile in concentric annulus.

Temperature and wall heat transfer coefficient solution

The comparison of temperature profiles in selected cross-sections of the cylindrical annulus are shown in Fig. 3. The semi-analytical solution, see equation (12), was calculated for the first thirty terms of the infinite series. Fig. 4 shows the wall heat transfer coefficient of the inner and outer wall. The wall heat transfer coefficient denoted 'CFX' was calculated from the numerical results of the commercial computing system Ansys CFX on selected cross-sections by substituting into equation (14). The differences between the wall heat transfer coefficient calculated by the semi-analytical model (h_i, h_o) and from the results by commercial computing system Ansys CFX (h_i^{CFX}, h_o^{CFX}) are calculated in Tab. 2.

The differences between the semi-analytical and numerical solutions are probably due to the different choice of turbulent models and the choice of the approximate velocity profile in the case of the semi-analytical model, see Fig. 2.

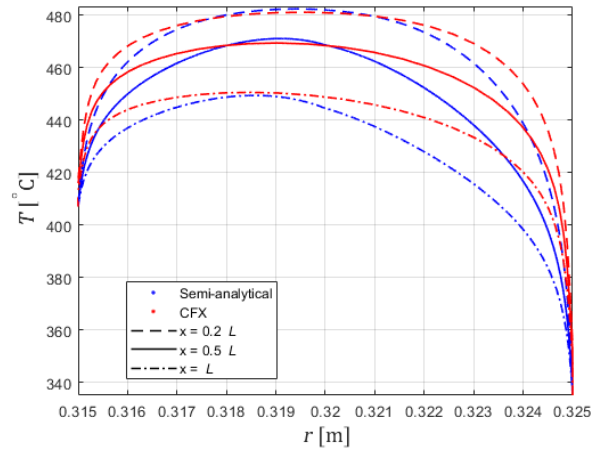

Fig. 3 The semi-analytically and numerically computed temperature in concentric annulus.

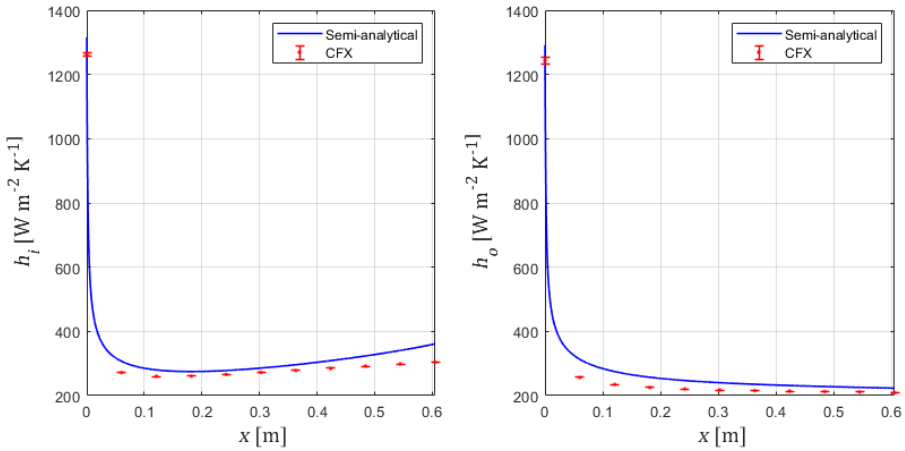

Fig. 4 The semi-analytically and numerically computed heat transfer coefficient of the inner wall (left) and the outer wall (right) of the concentric annulus.

Tab. 2 The semi-analytically and numerically computed heat transfer coefficient, where $\Delta h = \left|1 - \frac{h}{h^{CFX}}\right|$.

x	h_i [$\mathrm{Wm^{-2}K^{-1}}$]	Δh_i [%]	h_o [$\mathrm{Wm^{-2}K^{-1}}$]	Δh_o [%]
0.2 L	280.0	3.0	274.7	7.0
0.4 L	278.1	6.6	247.0	9.7
0.5 L	285.7	7.5	240.2	9.0
0.6 L	296.2	8.9	235.3	8.2
0.8 L	323.5	13.6	228.3	6.8
1.0 L	360.9	20.9	223.2	5.6

CONCLUSION

In this paper, a new semi-analytical method was presented for solving the Graetz problem in a concentric cylindrical annulus assuming a fully developed turbulent velocity profile. We observe fairly good trend agreement when comparing numerical and semi-analytical results of temperature. In addition, the semi-analytical model provides the results of the wall heat transfer coefficient, which are in approximate agreement with the results of the numerical simulation when solving the same problem, see Tab. 2.

Follow-up steps of our investigation will be the more precise calculation of the semi-analytical model by choosing a more accurate estimate of the fully developed velocity profile or by applying a more sophisticated mixing length appearing in the turbulent algebraic model. The semi-analytical model will be potentially used by Doosan Škoda Power s.r.o. to estimate the wall heat transfer coefficient on selected parts of the steam turbine.

ACKNOWLEDGEMENT

This work was supported by the student grant project SGS-2022-008.

REFERENCES

[1] S. Kakac, R.K. Shah, W. Aung. Handbook of single-phase convective heat transfer. United States: N. p., 1987. Web.

[2] B. Weigand, M. Wolf, H. Beer. Heat transfer in laminar and turbulent flows in the thermal entrance region of concentric annuli: Axial heat conduction effects in the fluid. *Heat and Mass Transfer* **1997**, 33, 67-80. DOI: https://doi.org/10.1007/s002310050162

[3] A. Malhotra, S.S. Kang. Turbulent Prandtl number in circular pipes. *International Journal of Heat and Mass Transfer* **1984**, 27, 2158-2161. https://doi.org/10.1016/0017-9310(84)90203-5

[4] R. Viskanta. Heat transfer with laminar flow in a concentric annulus with prescribed wall temperatures. *Appl. Sci. Res.* **1964**, 12, 463-476. DOI: https://doi.org/10.1007/BF03184658

[5] J. Siedlecki, M. Ciesielski, T. Błaszczyk. The Sturm-Liouville eigenvalue problem - A numerical solution using the Control Volume Method. *Journal of Applied Mathematics and Computational Mechanics* **2016**, 15, 127-136. DOI: https://doi.org/10.17512/jamcm.2016.2.14

APPLIED MECHANICS 2024

April 17th – 19th, 2024
Hotel Toliar, Štrbské Pleso
Slovakia

EXPLORING TENSILE TESTING TECHNIQUES FOR STEEL WIRE ROPE COMPONENTS: STRANDS, WIRES AND CORE

J. HRONCEK[1]*, P. MARSALEK[2], M. FUSEK[3], M. LESNAK[4]

The contribution deals with the experimental testing of steel wire rope 20 6x37M-SFC 1770 B sZ. The rope is disentangled and individual units are tested with regard to the overall load-bearing capacity of the rope and the possibilities of testing the load-bearing capacity. Tensile tests are carried out on individual wires and strands. The influence of the surface defect of the strand on its load-bearing capacity is observed. Two experimental test approaches are investigated. Two different grips are used to hold the wires. The processed data are used to develop the methodology of the numerical model in terms of accuracy and low computational complexity.

Keywords: Wire rope, tensile testing, load-bearing capacity, grips

INTRODUCTION

Steel wire rope is a mechanical component that has versatile uses and on which human lives depend. One of the basic parameters that serve to describe the rope is its load-bearing capacity. The static load-bearing capacity is a mechanical property characterized by the limited static force that the rope is able to endure before it breaks. This value depends mainly on the cross-section and the material of the rope. The load-bearing capacity of the entire rope is obtained in tensile experimental tests.

Furthermore, often when handling the rope, it is mechanically broken in the outer layer by breaking several wires. Therefore, it is necessary to experimentally verify the required load-bearing capacity of the steel rope and also to observe the effect of the surface defect on this parameter.

The main goal of the contribution is to determine the load-bearing capacity of the undamaged and damaged steel rope with the help of experiments and the material properties of rope components. After successfully obtaining the required outputs, the numerical model of the rope will be design in the near future.[1, 2]

[1] **Ing. Juraj Hroncek**, Department of Applied Mechanics, Faculty of Mechanical Engineering, VSB-Technical University of Ostrava, 17. listopadu 2172/15, Ostrava, Czech Republic; juraj.hroncek@vsb.cz
[2] **doc. Ing. Pavel Marsalek, Ph.D.**, Department of Applied Mechanics, Faculty of Mechanical Engineering, VSB-Technical University of Ostrava, 17. listopadu 2172/15, Ostrava, Czech Republic; pavel.marsalek@vsb.cz
[3] **doc. Ing. Martin Fusek, Ph.D.**, Department of Applied Mechanics, Faculty of Mechanical Engineering, VSB-Technical University of Ostrava, 17. listopadu 2172/15, Ostrava, Czech Republic; martin.fusek@vsb.cz
[4] **doc. Dr. Ing. Michal Lesnak**, Department of Work and Process Safety, Faculty of Safety Engineering, VSB-Technical University of Ostrava, 17. listopadu 2172/15, Ostrava, Czech Republic; michal.lesnak@vsb.cz

Subject of Research

The subject of the contribution is rope 20 6x37M-SFC 1770 B sZ. It is a counter-rotating, clockwise multi-strand steel rope with an outer diameter of d = 20 mm and a strength class of 1770 MPa.

The rope is composed of 6 strands that are wound around a plastic core. Fig. 1 shows the cross-section of the given rope. Each strand consists of 37 wires placed in 4 layers (items 1, 2, 3 and 4 on Fig. 1) with a construction of 1 + 6 + 12 + 18 wires in individual layers. The plastic core (item 5 on Fig. 1) is made up of 3 plastic strands woven together instead of one strand. The manufacturer of the given rope is ŽDB Drátovna a.s. from Bohumín and the declared guaranteed load-bearing capacity of the entire rope is 209 kN.[3] More than 90 % of the entire load is carried by strands, therefore it is possible to roughly estimate the load-bearing capacity of one strand by dividing the total load-bearing capacity of the rope by the number of strands.[4]

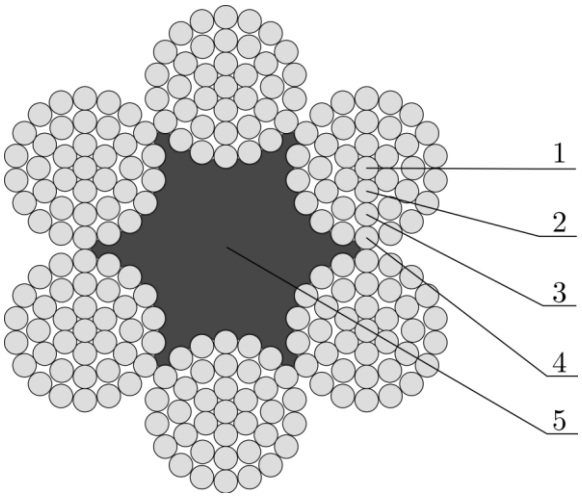

Fig. 1 Cross section of 6x37M-SFC steel wire rope

MATERIAL AND METHODS

Test Equipment

The rope samples were tested on a TESTOMETRIC 500-50CT universal testing device (Testometic, Rochdale, UK). Tensile tests were controlled by displacement u at a speed of 50 mm/min and the response force F was measured. The maximum load cell is 50 kN and accuracy of +/- 0.5 % of the load cell capacity. Therefore, for capacity reasons, the wires, core, and springs were tested. The entire rope has a much greater load-bearing capacity, so it was not possible to test it on the premises of the university laboratory. An extensometer was also used to accurately measure the elongation of the wires during the test, but was unsuccessful. Due to the small diameter of the wires, the extensometer was not able to properly attach to the wire and record the results.

Two types of grips were used in the experimental tests. Mechanical grips with wrapping were used first (Grips 1, see Fig. 2). Grips were supplied by Labormachine s.r.o. upon request. These grips are specifically designed for testing ropes and wires. The sample string is wound around the drum several times before being secured with a type of vise fixture. The working principle for these grips involves the coefficient of friction of the underlying material. By winding the rope around itself several times, the frictional area is increased. This technique spreads the testing stress over a larger section of the rope which reduces the chance of failed tests due to bad sample breaks or slippage.[5] Individual wires in different layers of the strand, core, original strands, and also damaged strands were tested using these grips.

Second, classic wedge mechanical grips were used (Grips 2, see Fig. 2). Due to the maximum allowed load, these grips were only used when testing individual wires.[6]

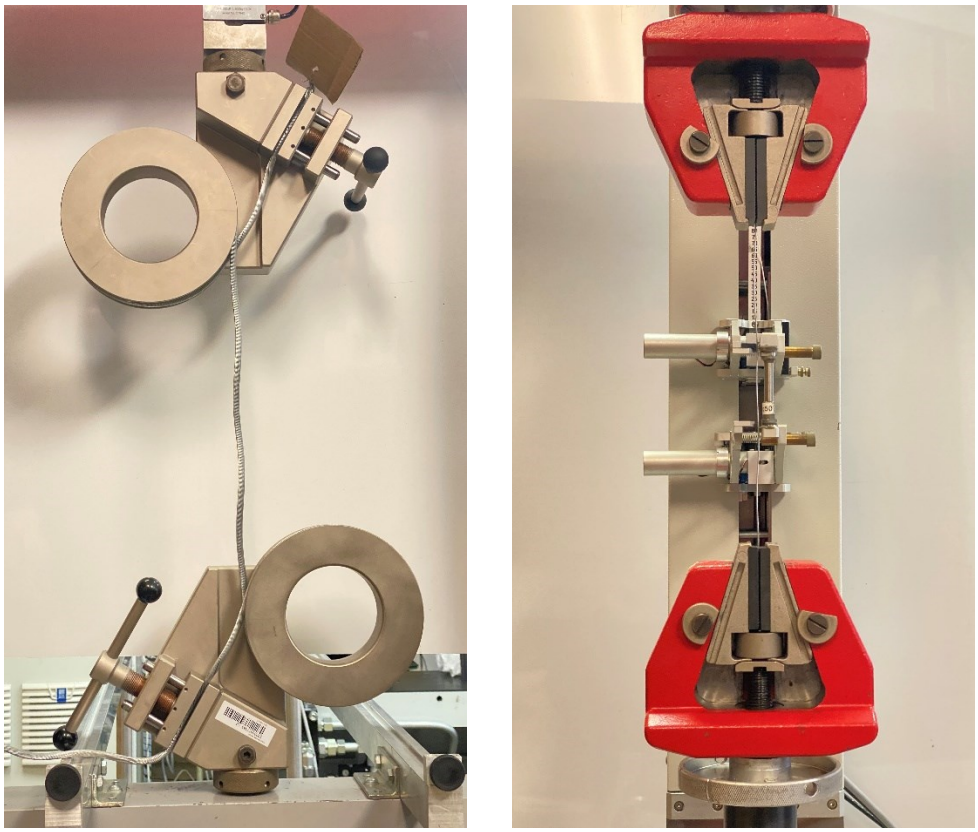

Fig. 2 Mechanical grips with wrapping (Grips 1, left) and wedge grips (Grips 2, right)

Sample Preparation

The goal was to test individual wires in layers, strands, and core separately, so it was necessary to unravel the entire rope. In the case of the first grips with wrapping, samples of 2 meters in length were created due to wrapping and the test-free part between the grips was 300 mm (minimum test length according to ISO 3108[7]). In the case of wedge grips, there were also samples of 300 mm length. Due to the mentioned capacity limitations of the machine, it was not possible to test the whole rope, because its load-bearing capacity exceeds several times the maximum load of the machine. This was the reason why only strands were tested, not the whole rope.

Another goal was to observe the effect of a surface defect on the load-bearing capacity of the strand of the given rope. The rupture of two wires in the surface layer was chosen. This was done by first unraveling the two outer wires of the strand, cutting them in the middle of the sample, and then braiding them back. This simulates a real defect situation where the wires break, but the wires remain entangled in the rope.[6, 8]

RESULTS

The output of tensile tests of samples of wires, strands, and cores are always the responses of the influence of the loading force F on the displacement u (see Fig. 3 – Fig. 8). Experiments were performed on two different grips, these outputs were compared on Fig. 4 – Fig. 6.

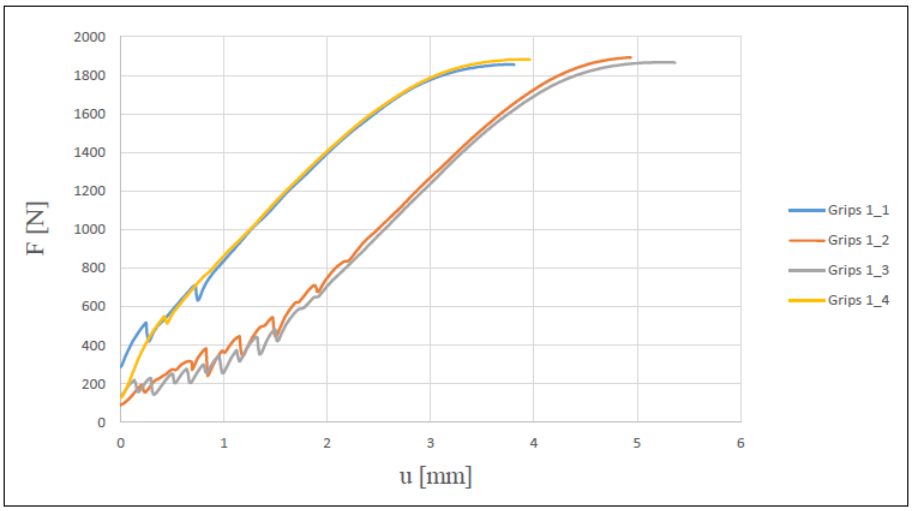

Fig. 3 Tensile test of the middle wire (item 1 on Fig. 1)

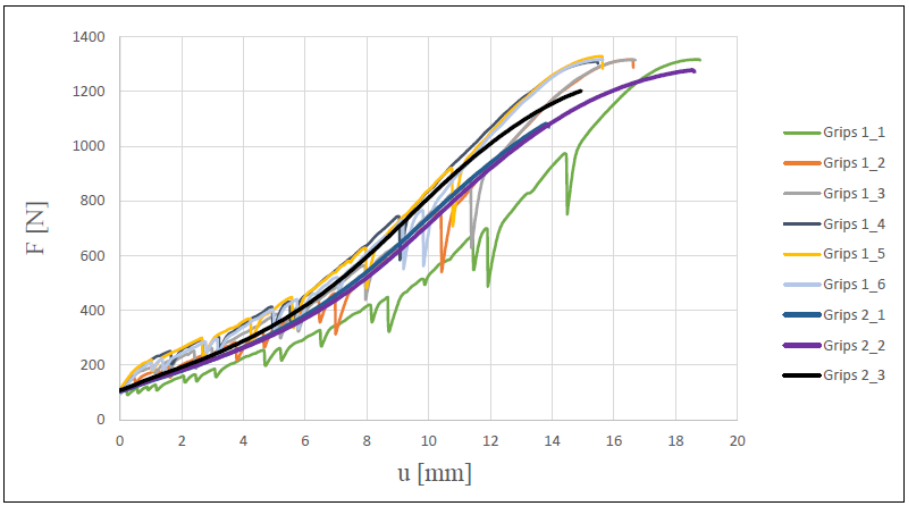

Fig. 4 Tensile test of the 2nd layer wire (item 2 on Fig. 1)

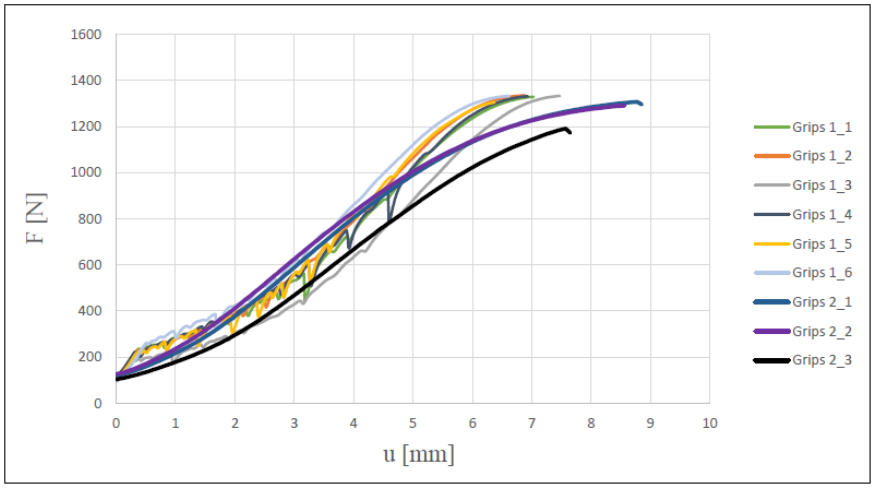

Fig. 5 Tensile test of the 3rd layer wire (item 3 on Fig. 1)

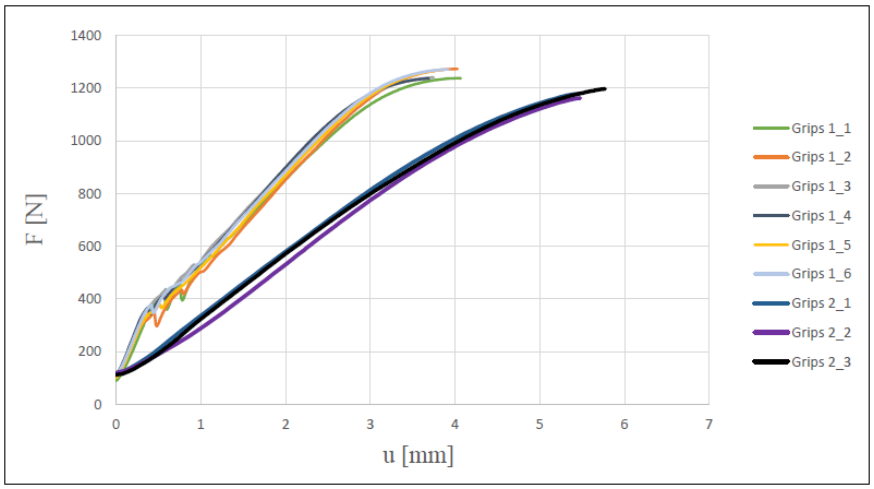

Fig. 6 Tensile test of the 4th layer wire (item 4 on Fig. 1)

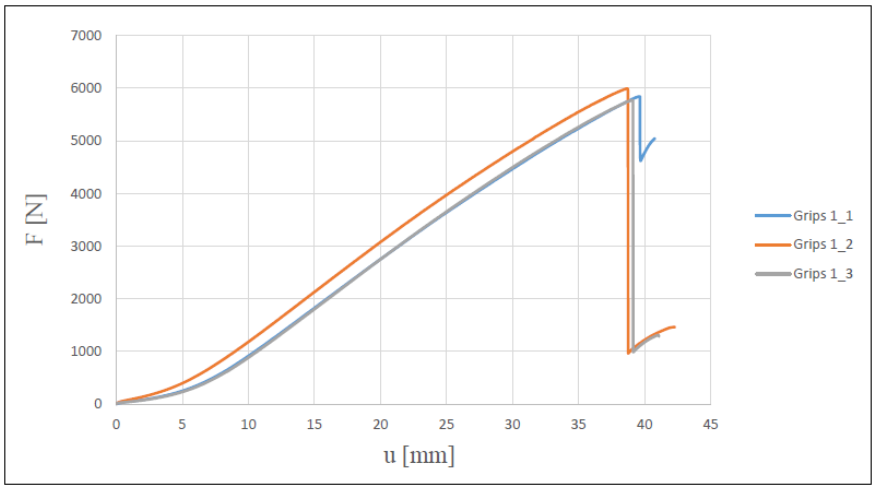

Fig. 7 Tensile test of the core strand (item 5 on Fig. 1)

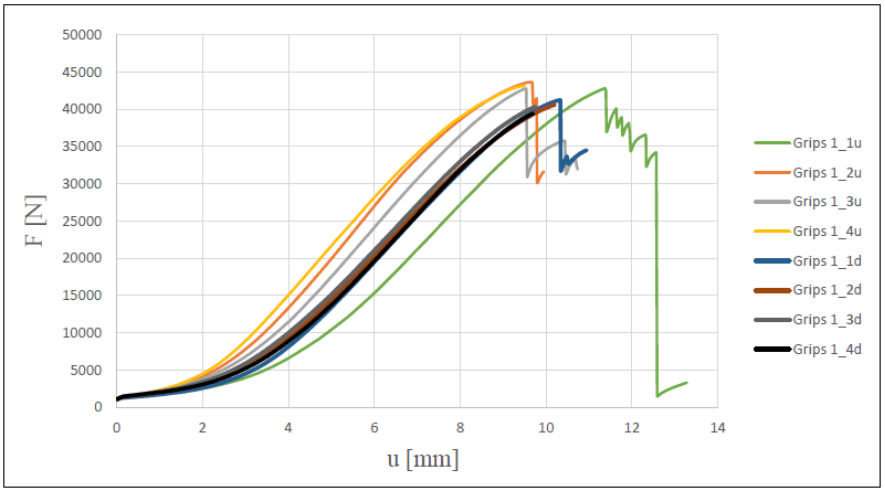

Fig. 8 Tensile test of undamaged and damaged rope strand

In Tab. 1, can be seen a comparison of the static load-bearing capacities of the samples, which were obtained as an average value of experiments.

Tab. 1 Experimentally determined load-bearing capacity

Sample	Diameter d [mm]	Grips 1 F_{C1} [N]	Grips 2 F_{C2} [N]
Middle wire	1.10	1 875	-
2nd layer wire	0.92	1 317	1 188
3rd layer wire	0.92	1 327	1 263
4th layer wire	0.90	1 255	1 180
Core strand	5.00	5 869	-
Undamaged rope strand	6.50	43 083	-
Damaged rope strand	6.50	40 366	-

DISCUSSION

Several negative factors occurred during testing: inappropriate use of the extensometer, curved wire, and strand samples due to unraveling of the already entangled rope, unknown exact value of the coefficient of friction between the grips and samples in the case of grips with wrapping, inaccuracies due to clamping in the case of wedge grips, etc. Due to these factors, it is not possible to determine the exact material parameters of each wire layer using this method. Another possible limitation is the use of a rope sample from only one manufacturer (ŽDB Drátovna a.s.). In the case of several manufacturers (Fatzer and so on), it would probably be samples of different quality.

CONCLUSION

We tested the individual components of the chosen steel rope to determine their static load-bearing capacity. Based on this analysis, the total load-bearing capacity of the rope was estimated to be 258.5 kN. The manufacturer, however, specifies a minimum guaranteed capacity of 209 kN. This built-in reserve ensures the rope can withstand more load than stated, accounting for potential variations in production quality.

If two wires in the outer layer of each strand are damaged, the estimated load-bearing capacity is reduced to 242.2 kN. Unfortunately, despite using two different types of mechanical grips, we couldn't fully reinterpret the tensile test results and establish a clear correlation between them. The absence of an extensometer makes it challenging to determine the exact material properties.

We are currently preparing a new test that will utilize the DIC (Digital Image Correlation) method. The real material parameters obtained from this test will be used to calibrate a material model. This model will account for the individual properties of each wire layer and the rope core. This data will then be used to create more accurate numerical simulations of future experiments.

ACKNOWLEDGEMENT

This work has been supported by Specific Research „Experimental and Numerical Modeling for Solving Problems in Mechanics and Biomechanics“ (SP2024/037).

REFERENCES

[1] M. Lesnak, P. Marsalek, P. Horyl, J. Pistora. Load-Bearing Capacity Modelling and Testing of Single-Stranded Wire Rope. *Acta Montan. Slovaca* **2020**, 25, 192-200.

[2] J. Hroncek, P. Marsalek, D. Rybansky, M. Sotola, L. Drahorad, M. Lesnak, M. Fusek. Simplified Numerical Model for Determining Load-Bearing Capacity of Steel-Wire Ropes. *Materials* **2023**, 16 (3756). https://doi.org/10.3390/ma16103756

[3] ŽDB Drátovna a.s. Online. Available from: https://www.dratovna.cz/

[4] G.A. Costello. Theory of Wire Rope. 2nd Edition, Springer, New York, 1997, 11-43. http://dx.doi.org/10.1007/978-1-4612-1970-5

[5] The Universal Grip Company. [Online] https://www.universalgripco.com/rope-grips

[6] H. Mouradi, A. El Barkany, A. El Biyaali. Steel wire ropes failure analysis: Experimental study. *Engineering Failure Analysis* **2018**, 91, 234-242. ISSN 1350-6307, https://doi.org/10.1016/j.engfailanal.2018.04.019

[7] ISO 3108:2017. Steel wire ropes - Test method - Determination of measured breaking force. International Organization for Standardization, Geneva, Switzerland, 2017.

[8] N. Mouhib, A. Wahid, F. Sabah, H. Chakir, M. El Ghorba. Experimental characterization and damage reliability analysis of central core strand extracted from steel wire rope. *Engineering Failure Analysis* **2021**, 120 (105103). ISSN 1350-6307, https://doi.org/10.1016/j.engfailanal.2020.105103

APPLIED MECHANICS 2024

April 17th – 19th, 2024
Hotel Toliar, Štrbské Pleso
Slovakia

SIMPLIFIED FEM MODEL OF THE ALUMINUM BOSCH REXROTH PROFILE

L. JAKUBOVIČOVÁ[1]*, M. VAŠKO[2], O. PIROH [3], F. SYNÁK [4]

The Profile Modular System provides variability, flexible construction and rebuilding, corrosion resistance and quick assembly in meeting customer requirements. It has a wide range of applications, using different elements offered by the largest structural framing system in the world from light enclosures, and protective walls to special and serial machines, high-load worktables, and frames for machines. Although the manufacturer declares recommended profile dimensions for the required load capacity, in many cases, it is necessary to verify the structural design from a strength point of view. This paper compares two FEM analysis results with the analytical solution for the sample example. The first version of the profile is created with a beam element and the second is shell elements. The advantages and disadvantages of the chosen approaches are evaluated.

Keywords: Aluminum profile, FEM, SHELL element, BEAM element

INTRODUCTION

Aluminium profile combines high strengths with minimum use of materials. This gives us a cost-effective and stable solution for the construction of tables, protection devices or frames, for instance.

The use of aluminum profiles has increased significantly in recent times due to their flexibility and variability, especially in the design, creation, and assembly of conveyor lines [1]. It provides the possibility of connecting the reconstruction according to the current requirements of the workplace and the possibility of repeated use. It offers the possibility of connecting the structure to the current requirements of the workplace and the possibility of repeated use.

A major benefit is the quick assembly using a small number of assembly tools. Aluminum profiles have high corrosion resistance, which eliminates the need for regular surface maintenance. Modular systems made of these profiles are increasingly preferred in the automotive industry.

[1] **Ing. Lenka Jakubovičová, PhD.**, Department of Applied Mechanics, Faculty of Mechanical Engineering, University of Žilina, Univerzitná 8215/1, Žilina, Slovak republic; lenka.jakubovicova@fstroj.uniza.sk
[2] **doc. Ing. Milan Vaško, PhD.**, Department of Applied Mechanics, Faculty of Mechanical Engineering, University of Žilina, Univerzitná 8215/1, Žilina, Slovak republic; milan.vasko@fstroj.uniza.sk
[3] **Ing. Ondrej Piroh**, Department of Applied Mechanics, Faculty of Mechanical Engineering, University of Žilina, Univerzitná 8215/1, Žilina, Slovak republic; ondrej.piroh@fstroj.uniza.sk
[4] **Ing. František Synák, PhD.**, Department of Road and Urban Transport, Faculty of Operation and Economics of Transport and Communications, University of Žilina, Univerzitná 8215/1, Žilina, Slovak republic; frantisek.synak@uniza.sk

In the final design of any structural assembly, it is important to perform a strength analysis to verify the ability of the structure to safely carry the required loads [2]. Subsequently, it is necessary to evaluate the safety factor in the most loaded parts of the profile while meeting the specified requirements. Particular attention is paid to the maximum displacement and the maximum stress value.

METHODOLOGY

There are three options for creating a finite element Bosch profile.

The aluminum profile created by a beam element is the least demanding in terms of the scope of geometry modifications. Along the length of the profile, the beam element is represented by a line that has the defined properties of the cross-section of the given profile. Modification of the entire geometry from the point of view of modeling the cross-sections of profiles is not necessary. In practice, it is often used and gives a high degree of agreement with experimental measurements. However, this methodology cannot be used if it is necessary to consider the connection of the profile to another structural geometry using screws and to consider the preload of the screws together with the assessment of its influence on the individual parts of the structure [3].

For this reason, the most suitable modeling technique is the use of shell elements. Although it is the most time-consuming approach from the point of view of model preparation, given the complexity of the cross-sections used. For these reasons, Bosch profiles are modelled with shell elements. This approach is often used, but there are not enough relevant studies on it [4].

We can also model the beam of aluminum profile using volume elements. The finite element mesh formed by volume elements must meet the necessary correctness conditions when mesh is created. It is necessary to ensure that the finite element mesh consists of at least 3 to 5 elements per 2 mm of profile thickness. In this case, the number of elements and the number of equations to be solved increase rapidly. From the time point of view, this method is significantly demanding. The complexity of the problem being solved is also reflected in the higher demands on computing resources and therefore we will not pay further attention to it.

Numerical solution

Our attention is focused on the first two approaches, and the results are compared with a numerical solution of an example problem where the exact solution is known. The presented analytical solution of the numerical task, Fig. 1, and its comparison with the two types of finite element models allow us to see the advantages and disadvantages of the chosen approaches. The first model is created using a beam element, and the second uses shell elements.

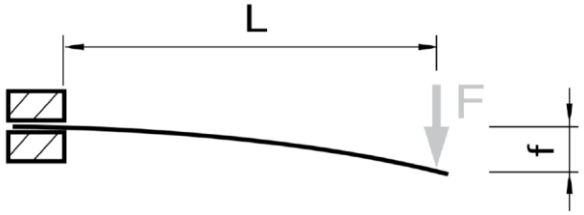

Fig. 1 Schematic example of a Bosch profile [5]

Consider a simple example of a beam with a length of L = 1000 mm, anchored at one and loaded with a force of F = 500 N at the other end. The beam profile is a Bosch profile of 80x80 mm.

The maximum deflection f of the profile is calculated as:

$$f = \frac{F.L^3}{3.E.I.10^4} = \frac{500\,N\,.\,1000^3\,mm^3}{3\,.\,70\,000\,MPa\,.\,132.1\,.10^4\,mm^4} = 1.802\,mm \quad (1)$$

Al-Mg-Si alloy material sheets are freely available from Bosch Rexroth [5], Tab. 1.

Tab. 1 Material characteristics and mechanical properties of the alloy

Material	**Young's modulus for aluminium E [MPa]**	**Poisson's ratio μ [-]**	**Yield strength R_e [MPa]**	**Tensile strength R_m [MPa]**
AlMgSi 0.5 F25	70 000	0.34	200	250

Cross-sectional characteristics and dimensions of the aluminum profile are mentioned in the Tab. 2.

Tab. 2 Cross section characteristics

Profile	**Cross section with dimensions**	**Cross-sectional characteristics**	**Material**
Bosch profile 80x80L	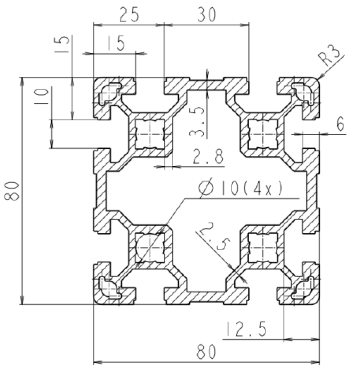	A = 18.2 cm^2 I_x = 132.1 cm^4 I_y = 132.1 cm^4 W_x = 33.0 cm^3 W_y = 33.0 cm^3	ISO: AlMgSi 0.5 F25

To compare the results, the value of the maximum bending stress is important. In the analytical solution, it is determined from the following relationship:

$$\sigma_{max} = \frac{F.L}{W_o} = \frac{500\,N\,.1000\,mm}{33\,.10^3\,mm^3} = 15.151\,MPa. \quad (2)$$

The maximum bending stress in the Bosch profile 80x80 mm, loaded according to Fig. 1, is, based on the analytical calculation, Eq. 2, $\sigma_{max} = 15.151\,MPa$. This value is used to compare the results obtained from the following two methods used for finite element analysis performed in Ansys [6, 7].

Finite element solution

Modifying the profile geometry, such as removing chamfers and edge fillets, is necessary during the creation of the model using shell elements, so that it is possible to extract the mid-surface that define the shell element from the volume model of the profile [8]. These modifications were made in PTC Creo, Fig. 2.

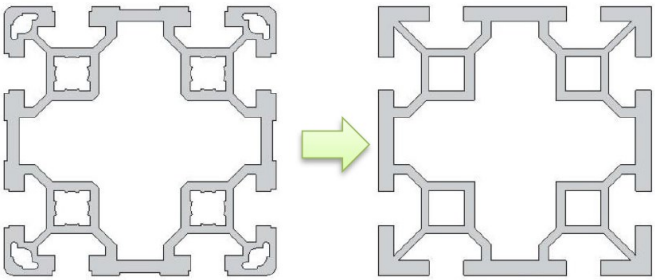

Fig. 2 Original (left) and modified (right) cross-section geometry of the profile used for the shell model

The difference in the cross-sectional area of the Bosch profile with dimensions 80x80 mm after modification is 0.5%. Subsequently, in Ansys Workbench, the mid-surface is extracted to ensure compatibility of the entire modelled profile [9].

The element size of the mesh is 5 mm, which is a sufficiently dense mesh for a structure of these dimensions [10]. The BEAM188 element type is used for the beam element model, and the SHELL181 element type is used for the shell element model [11]. Boundary conditions and loading are defined exactly according to the given example problem, Fig. 1, [12]. The resulting Equivalent Von-Mises Stress values for the profile defined by the beam element are shown in Fig. 3a and for the profile defined by the shell elements in Fig. 3b.

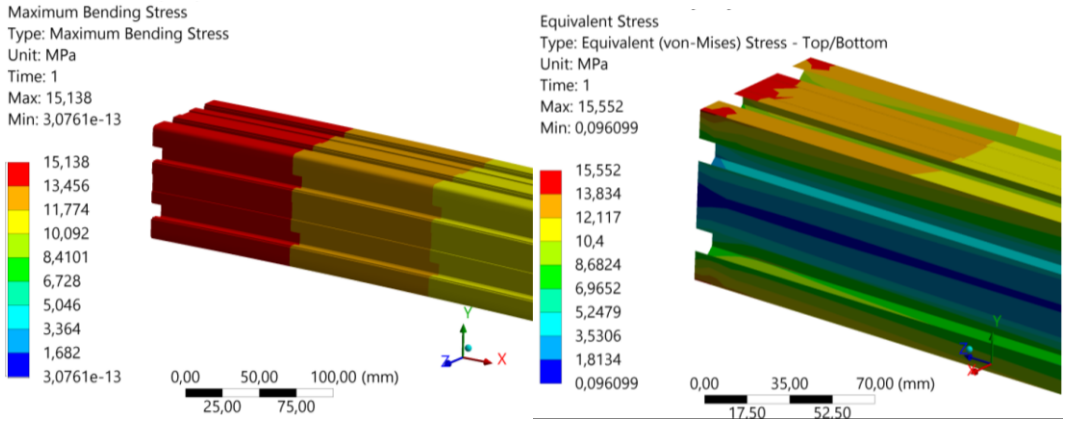

(a) beam element (b) shell elements

Fig. 3 Bosch profile 80x80 mm, finite element results

In the case of creating a model using shell elements, it is possible to get Equivalent Von-Mises Stress values along the entire cross-section their distribution. In the second case, when the profile is created by using a beam element, it is only possible to obtain averaged values of Equivalent Von-Mises Stress.

RESULTS AND CONCLUSION

This article aimed to compare the results of two FEA analyses with an example problem, using two different approaches to creating the finite element model: an analytical model and a numerical model. This was done to verify the structural design of beams from a strength perspective. The numerical model was divided into a shell model and a beam model. When comparing, the main

focus was on the maximum displacement value and the maximum stress value. For comparison of different models, the analytical model solution was considered to be accurate.

Compared to the analytical model, the maximum displacement value for the shell model differed by 0.115 mm, which represents a 6.38% deviation. In this case, the displacement value was lower than the displacement value calculated using the analytical model. For the beam model, the calculated value was higher by 0.049 mm than the value found using the analytical model. The increase in the maximum displacement value was 2.72%.

As can be seen from the results of comparing the maximum stress value, Tab 3, found using the analytical and then numerical shell and beam models, the difference in results was lower than when comparing the maximum displacement. A higher deviation, similar to the previous case, was found for the numerical shell model, i.e. 2.65%. For the numerical beam model, the deviation was 0.09%, which can be considered a negligible deviation.

Tab. 3 Percentage deviations of the maximum values of stress and displacement of the numerical and analytical solution

Calculation variant	**Maximum displacement value f [mm]/ deviation [%]**	**Maximum stress value σ_{max} [MPa] / deviation [%]**
Analytical model	1.802 / 0.00 %	15.151 / 0.00 %
Numerical (shell model)	1.687 / 6.38 %	15.552 / 2.65 %
Numerical (beam model)	1.851 / 2.72 %	15.138 / 0.09 %

Based on the results summarized in Table 3, it can be stated that the most demanding method in terms of time required for modeling aluminum profiles, using a numerical shell model, was also associated with the highest deviation. However, this method is more suitable for stress verification in the area of connecting other types of bodies and other more complex bodies that were not included in the objectives of this publication. For solving the given example problem after verifying the accuracy of the selected numerical approaches, a numerical solution using beam elements is sufficient. Compared to the numerical shell model, this approach is associated with significantly lower time requirements, which can lead to significant time and financial savings in dimensioning costs, provided that it is not necessary to solve the connection of profiles to other bodies and other types of geometry.

The objective of comparing different models can therefore be considered to have been met. Further research may focus on comparing different methods of beam dimensioning for other types of bodies and more complex tasks.

ACKNOWLEDGEMENT

This work has been supported by the gran project KEGA 002ŽU-4/2023 and 005ŽU-4/2024.

REFERENCES

[1] J. Burák, K. Semrád. Základy navrhovania konštrukcií technických, technologických a energetických zariadení. Elfa: Košice, SK, 2013.

[2] J.F. Doyle, K. Semrád. Static and Dynamic Analysis of Structures with an Emphasis on Mechanics and Computer Matrix Methods. Indiana : Purdue University, 1991, p. 424. ISBN 978-0-7923-1208-6

[3] DIN EN ISO 898-1: Mechanické vlastnosti spojovacích súčastí z uhlíkovej a legovanej ocele - Časť 1: Skrutky s uvedenými triedami vlastností - hrubý závit a jemné stúpanie, 2013.

[4] D. Broaekaart. 5 reasons to use a mid-surface shell mesh for thin-walled parts FEA. online: 2016. <https://info.simuleon.com/blog/5-reasons-why-your-fea-simulations-should-be-setup-with-a-mid-surface-shell-mesh-for-thin-walled-parts>

[5] BOSCHREXROTH.COM. online: 2014. <https://www.boschrexroth.com/en/dc/>

[6] ANSYS.COM. online: 2015. <https://www.ansys.com/products/structures/strength-analysis/simulating-bolted-assemblies>

[7] ANSYS HELP. online: 2020. <https://ansyshelp.ansys.com >

[8] M. Žmindák, I. Grajciar, J. Nozdrovický. Modelovanie a výpočty v metóde konečných prvkov: Modelovanie v ANSYSe. Diel I. Žilina : VTS pri Žilinskej univerzite, 2004, 208 p. ISBN 80-968823-5-X

[9] X. Chen, Y. Liu. Finite Element Modeling and Simulation with ANSYS Workbench. CRC Press, 2015, 411 p. ISBN 978-1439873847

[10] ANSYS. ANSYS Meshing User's Guide 2020R2 [pdf]. ANSYS, 2020.

[11] ANSYS. ANSYS Mechanical User's Guide 2020R2 [pdf]. ANSYS, 2020.

[12] ANSYS. ANSYS Contact Technology Guide. ANSYS Release 9.0 [pdf]. ANSYS, 2004.

APPLIED MECHANICS 2024

April 17th – 19th, 2024
Hotel Toliar, Štrbské Pleso
Slovakia

ANALYSIS OF PRESSING JOINT OF CONICAL PIPE

R. JANČO[1]*

This paper presents a stress analysis of a pressed joint of two conical pipes with the aim to find out whether this kind of connection is suitable for telecommunication masts. The analysis can be considered a complex spatial problem of a thin-walled shell, where the local bending stress influence might be dominant. In this paper a solution using engineering approach and numerical analysis with finite element method (FEM) will be compared.

Keywords: conical pipes, finite element analysis, thin-walled shell, contact pressure

INTRODUCTION

This paper presents a stress analysis of a pressed joint of two conical pipes with the aim to find out whether this kind of connection is suitable for telecommunication masts.

In this paper a solution using theoretical solution and numerical analysis using shell element in finite element method (FEM) will be compared.

THEORETICAL BACKGROUND

The model consists of two conical pipes with a taper ratio "k" and contact length a, as can be seen in the fig. 1 (up). The parameters of the pipes are: the wall thickness of the inner pipe is h, the wall thickness of the outer pipe is h_v and the smaller radius outer of pipe is r_1. Because the systems of two conical pipes are loaded by assembling load F_Z, the contact pressure is nonzero, in fig. 1 (down). Loading by assembling load will be displacement between outer and inner pipes increase by Δa (in fig. 1 down).

Contact pressure is p at arbitrary location x. Radial change of outer radius of pipes, which have unit width is

$$\Delta r = \frac{pr^2}{Eh} \tag{1}$$

The circumferential stress at location x is

$$\sigma = \frac{pr}{h} \tag{2}$$

where E is Young's modulus and $r_S = r - h/2 \doteq r$ is mean radius of the joint. Radial change of outer radius of outer pipe will be Δr_v, mean radius of outer pipe is $r_s = r + h/2 \doteq r$.

[1] **Prof. Ing. Roland Jančo, PhD.**, Institute of Applied Mechanics and Mechatronics, Faculty of Mechanical Engineering, Slovak University of Technology in Bratislava, Nám. slobody 17, 81231 Bratislava, Slovak republic; roland.janco@stuba.sk

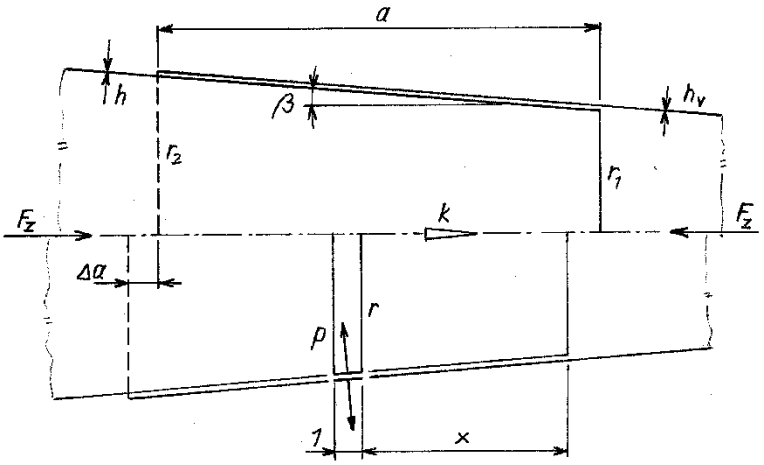

Fig. 1 Model of two conical pipes [4]

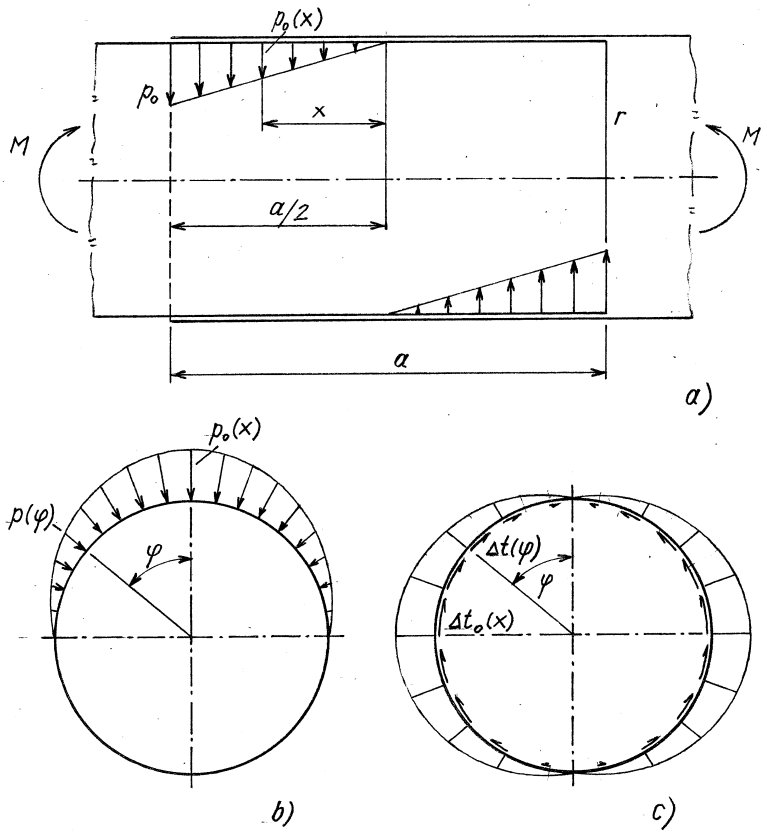

Fig. 2 Contact pressure a) for loading by bending moment
b) pressure in inner pipe c) assumed distribution [4].

The full theoretical background is in [4]. We assume, that contact pressure along surface line lying at surface of applied bending moment is linear in the Fig. 2a, if

$$p_o(x) = p_o \frac{2x}{a} = \frac{12}{\pi r}\frac{M}{a^2}\frac{2x}{a} = \frac{24M}{\pi r a^3}x \tag{3}$$

We assume, that the contact pressure along circumference is cosine distribution according to Fig. 2b and transfer of transversal loading along the length of pipe will be carry out shear flow with sine distribution.

NUMERICAL SOLUTION

Numerical solution was made by transfer of bending moment between two thin-walled pipes without clearance and without lap.

Parameters of joint:

- contact diameter of pipes is 1202 mm,
- thickness of outer wall is h = 10 mm,
- thickness of inner wall is h_v = 12 mm,
- length of female pipe is a = 2150 mm.

Value of bending moment is $M_B = 629.10^6$ N.mm. Solution was solved using finite element methods in program ANSYS. This problem is solution of contact between two shells.

In fig. 3 is shown contact pressure [MPa] at outer pipes, maximum value of contact pressure is p_k = 1.665 MPa at right top side and contact pressure at left bottom side is p'_k = 1.378 MPa.

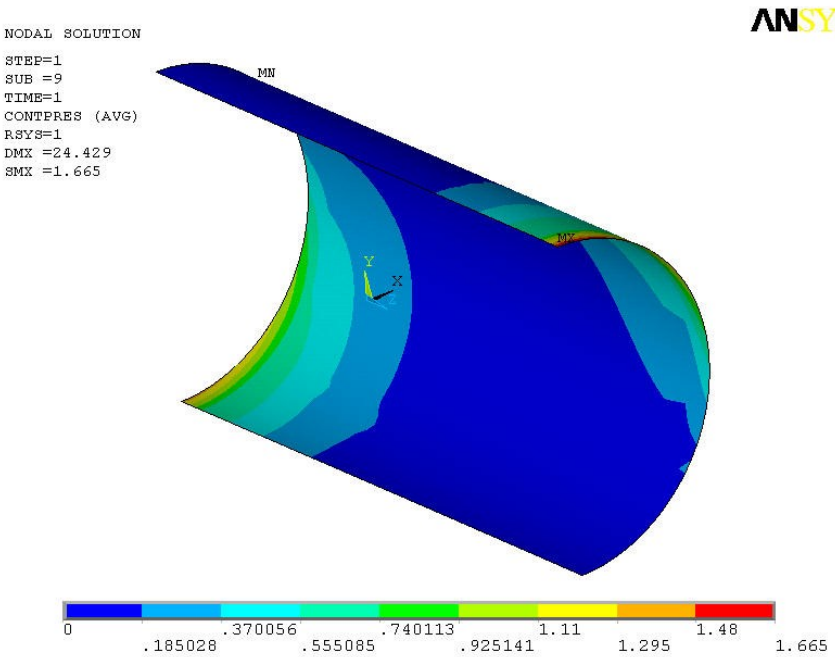

Fig. 3 Contact pressure at outer pipe (MPa) [4]

CONCLUSION

In this paper is comparing the theoretical solution and numerical solution by finite element methods for conical connection of two pipes. The value of contact pressure of theoretical and numerical results is very similar, see fig. 4.

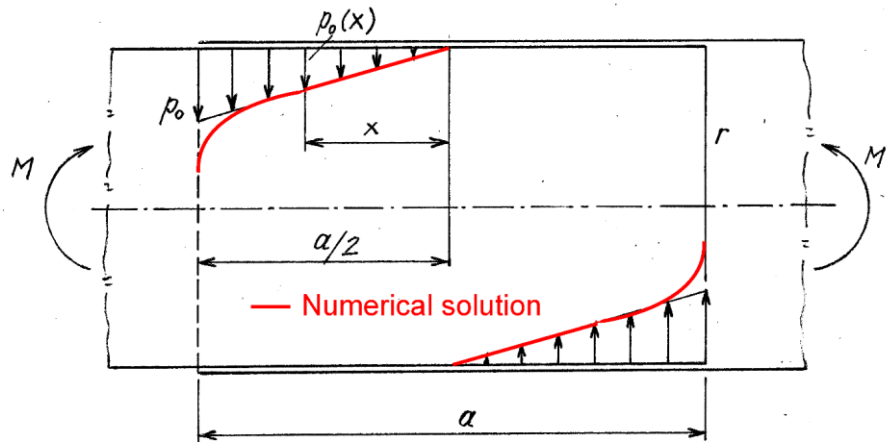

Fig. 4 Comparison of theoretical solution with numerical solution [4]

ACKNOWLEDGEMENT

This publication was funded by the KEGA 016STU-4/2023 grant. The resources are greatly appreciated.

REFERENCES

[1] S. Timoshenko. Strength of Materials, Part I: Elementary Theory and Problems. Second Edition , D. Van Nostrand Company, Inc., 1947.

[2] S. Timoshenko. Strength of Materials, Part II: Advanced Theory and Problems. Second Edition , D. Van Nostrand Company, Inc., 1947.

[3] ANSYS Users Manual

[4] R. Jančo. Stress Analysis of Pressing Joint of Two Conical Pipes. *Strojnícky časopis – Journal of Mechanical Engineering* **2023**, 73 (1), 117-124. DOI: 10.2478/scjme-2023-0009

APPLIED MECHANICS 2024

April 17th – 19th, 2024
Hotel Toliar, Štrbské Pleso
Slovakia

VEHICLE VIBRATION REDUCTION BY ELIMINATION OF CRANKSHAFT TORSIONAL VIBRATION

M. KAČÍR[1]*, L. ŽUĽOVÁ[2], R. GREGA[3]

Emission standards and environmental pressures are forcing internal combustion engine manufacturers to make significant modifications to reduce emissions while maintaining engine power and torque. Such changes are noticeable not only in structural but also in software parts of internal combustion engines. As a result of these changes, there is an increase in torsional vibration of crankshaft, which manifests itself in the vehicle as an undesirable effect in the form of vibrations. This fact can cause failures in components of drive system as well as other parts of the vehicle. In order to prevent failures, it is necessary to deal with development of new elements to eliminate torsional oscillations as a response to current trends in the development of internal combustion engines.

Keywords: dual-mass flywheel, vibration, automotive drive

INTRODUCTION

In general, internal combustion engines were intended to drive equipment in transport, agriculture, but also in the field of energy production. Due to the improvement of efficiency, increase in performance and especially reduction in emissions of combustion engines, design of individual parts of engine was changed and various technological improvements were added. Over time, the Euro emission standards was introduced into the European standards, which determines the maximum emissions produced by automobile transport. As automotive industry had to adapt to these conditions, engineers and developers made several changes to meet emission limits. Although these changes increased engine performance and reduced emission production, they also brought with them undesirable consequences as a by-product of the mentioned changes [1].

TORSIONAL VIBRATION IN COMBUSTION ENGINES

In recent years, the main task of automotive industry has been reduction of consumption and production of CO_2. One of effective measures to achieve these aims is use of low engine speeds while driving. To achieve low engine speeds without losing power, torque must be maintained or

[1] **Ing. Matúš KAČÍR**, Department of Engineering for Design of Machines and Transport Equipment, Technical university of Košice, Letná 9, Košice, Slovak republic; matus.kacir@tuke.sk
[2] **Ing. Lucia ŽUĽOVÁ**, Department of Engineering for Design of Machines and Transport Equipment, Technical university of Košice, Letná 9, Košice, Slovak republic; lucia.zulova@tuke.sk
[3] **prof. Ing. Robert GREGA, PhD.**, Department of Engineering for Design of Machines and Transport Equipment, Technical university of Košice, Letná 9, Košice, Slovak republic; robert.grega@tuke.sk

increased. An engine can thus run just above idling speed and therefore in the range of extremely low consumption. One of possibilities is to achieve adequate isolation of engine from the drivetrain even at these low engine speeds while still providing a standard level of driver comfort.

The rapid development of vehicle technology over the past few decades has brought ever higher engine performance in parallel with increased requirements for driver comfort. Weight-saving vehicle concepts and car structure optimized in the wind tunnel allow driver to perceive other noise sources.

To improve fuel economy and reduce exhaust emissions, engine development strategies included engine downsizing and revolution reduction.

Figure 1 shows the change in crankshaft rotation speed for engines with six and three cylinders while maintaining the same power and torque [2].

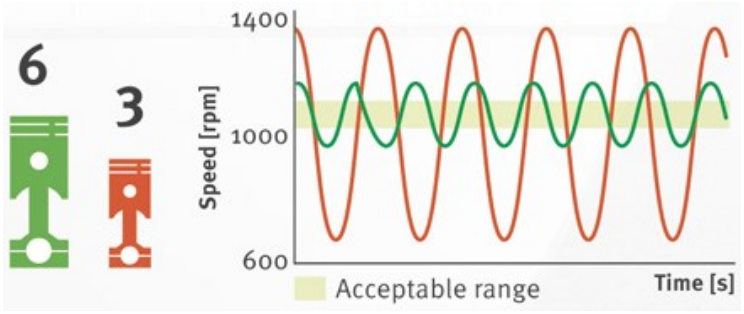

Fig. 1 Comparison of piston speed of three-cylinder and six-cylinder engines [3]

POSSIBILITIES OF TORSIONAL VIBRATION ELIMINATION

Torsional oscillations or vibrations have a negative effect on all vehicle components. This fact leads to designers to reduce torsional oscillations to a minimum value. One of the possibilities is to limit the occurrence of torsional oscillations or to eliminate torsional oscillations that have occurred. Implementing one or more of these strategies can degrease torsional vibrations in an internal combustion engine, improving its performance, operating life and overall smoothness of operation. Possibilities to reduce or degrease torsional vibration in an internal combustion engine are following:

- **Balancing**

  Proper balancing of rotating engine components, such as the crankshaft, flywheel or balancer shaft can significantly reduce torsional oscillations. Balancing ensures an even distribution of mass around the axis of rotation, thus minimizing torques.

- **Engine mounts**

  Improvement of engine mounts with stiffer or more sophisticated designs can reduce transmission of torsional vibrations to the vehicle's chassis, thus improving overall smoothness, noise and vibration.

- **Tuning and Optimization**

  Ensuring engine's ignition timing, fuel mixture and other operating parameters are properly tuned can minimize torsional vibrations. A well-tuned engine operates more smoothly, reducing the occurrence of vibrations.

- **Stiffer Components**

  Improvements of certain engine components, such as the crankshaft or connecting rods to stiffer materials or designs can reduce torsional deflection and minimize vibrations.

- **Torsional vibration eliminators**

  Installing torsional vibration eliminators or harmonic balancers can better absorb and dissipate torsional vibration. These components usually consist of two masses that are flexibly located against each other. One of such components is a dual-mass flywheel (DMF) [4-6].

PROPOSAL FOR IMPROVING THE EFFICIENCY OF DUAL-MASS FLYWHEEL

Modern engines run with lower idle speeds and higher torques, generating more vibrations. Therefore, it is necessary to improve the filtering capacity or to lower a point at which filtration begins without compromising the torque capacity. As vehicles are becoming more silent and a chassis is becoming lighter and more rigid, the level of vibration is becoming more apparent.

For innovative design of DMF and distribution of inertia masses make it possible to shift the resonance frequency under engine idle speed by changes in their parts that provide connection of these masses. The new DMF design can be described by mathematical models shown in Fig. 2a, b. [7], [8].

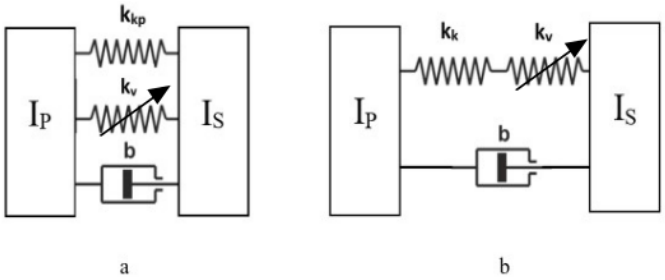

Fig. 2 Mathematical models of new dual-mass flywheel

In Figure 2a is a DMF model with parallel-ordered stiffnesses, in comparison, in Fig. 2b stiffnesses in DMF are ordered one after the other. Both mathematical models are characterized by pair of elements with two different stiffnesses. One of elements is characterized by a constant stiffness k_k and other element represents a variable stiffness k_v.

The variable stiffness k_v ensures better adaptability of DMF to operating conditions of a drive. The element with variable stiffness is a pneumatic spring, in which the pressure can be changed from the p_{min} to p_{max} value. Variable stiffness can therefore be achieved by using an elastic element in which the air pressure can be continuously changed and therefore the stiffness k_v can be changed in the range from kv_{min} to kv_{max} [9-11].

New design of Pneumatic Dual-Mass Flywheel

The construction of pneumatic dual-mass flywheel (PDMF) with an air bag is similar to construction of the pneumatic dual-mass flywheel with a metal spring unit. The difference is in flexible member of a different construction and a different material - rubber. The PDMF structure (Fig. 3) with air bags also consists of a primary mass (1), a casing (2), two centre plates (3), a hub

(4), a pair of rubber pneumatic bags (5), a center disc (6), a pair of bent coil springs (7), six compression springs (8), rivets (9) and secondary mass (10).

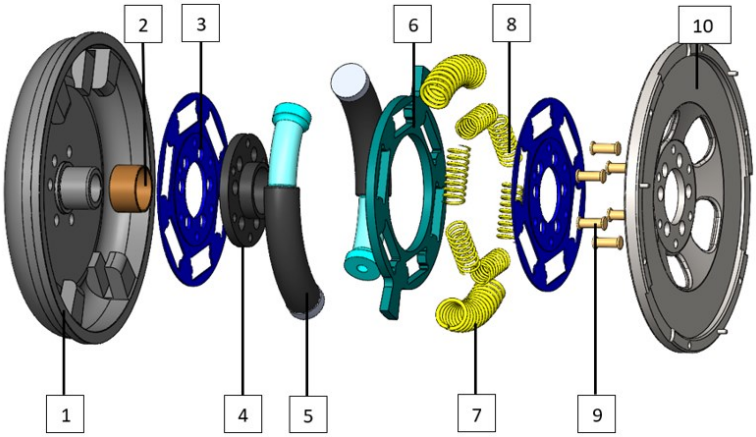

Fig. 3 Parts of Pneumatic Dual-Mass Flywheel

The principle of the proposed flywheel consists in adjustable stiffness of the elastic elements, which ensures the possibility of optimal adaptation to the current conditions and requirements for arising torsional vibration of the crankshaft. Pneumatic bags are placed between the primary mass and the central disk, which is flexibly placed against the secondary mass. Figure 4 shows the maximum (a) and minimum (b) twist angle. This alternative is characterized by non-linear characteristics and enables a twist angle up to 65°.

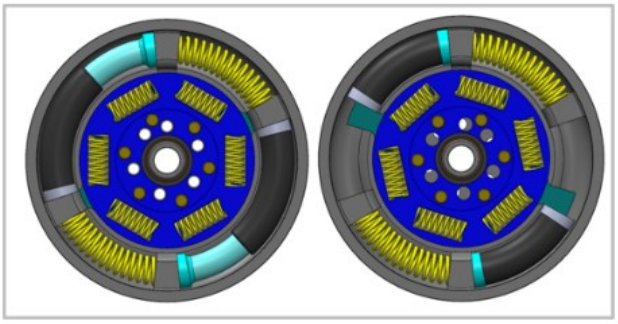

Fig. 4 Pneumatic dual-mass flywheel at maximum versus minimum twist angle

CONCLUSION

The comfort of traveling in a car is constantly increasing and the requirements for elimination of vibrations, as well as the requirements for the life of components, are increasing. One of the components for eliminating vibrations is a dual-mass flywheel. From the research done so far, it seems that the possibilities of conventional two-mass flywheels are probably insufficient, so it is necessary to propose new elements to the drive train of cars.

Technologies that are applied to vehicles due to requirements to reduce emissions have an adverse effect on travel comfort. Our aim is therefore to propose options for ideal adaptation to

conditions in real time during engine operation and thus ensure more optimal engine operation, increased travel comfort and reduced wear and tear on vehicle drivetrain components.

ACKNOWLEDGEMENT

The work has been supported by the grant project KEGA: 037 TUKE-04/2024, KEGA: 044 TUKE-4/2024 and VEGA 1/0224/23.

REFERENCES

[1] E.H. Porto, S.J. Idehara. Evaluation of Torsional Vibration with a Novel Clutch Damper for the Nonstationary Drive Condition. *Journal of Vibration Engineering & Technologies* **2023**, 11 (2), 403-414. ISSN 2523-3920

[2] Valeo Service Cataloque: Valeo Transmission Systems Dual-Mass Flywheel valeoscope product, 2016, Ref: 9988116.

[3] X-ENGINEER, Dual Mass Flywheel (DMF). Available online: https://x-engineer.org/dual-mass-flywheel-dmf/.

[4] R. Grega, P. Kaššay. Experimental Methods and Devices for the Identification of the Properties of Pneumatic Dual Mass Flywheel. Current Methods of Construction Design: Proceedings of the ICMD 2018. Springer International Publishing, 2020, 47-55.

[5] D. Maffiodo, R. Sesana, D. Paolucci, S. Bertaggia. Finite life fatigue design of spiral springs of dual-mass flywheels: Analytical estimation and experimental results. *Advances in Mechanical Engineering* **2018**, 10 (6). ISSN 1687-8140

[6] L.Q. Song, L.P. Zeng, S.P. Zhang, J.D. Zhou, H.E. Niu. Design and analysis of a dual mass flywheel with continuously variable stiffness based on compensation principle. *Mechanism and Machine Theory* **2014**, 79, 124-140.

[7] R. Grega, et al. Analysis of the impact of flexible couplings on gearbox vibrations. *Zeszyty naukowe politechniky Śląskiej: Seria Transport* **2016**, 91. ISSN 0209-3324

[8] H.J. Lee, J.K. Shim. Multi-objective optimization of a dual mass flywheel with centrifugal pendulum vibration absorbers in a single-shaft parallel hybrid electric vehicle powertrain for torsional vibration reduction. *Mechanical Systems and Signal Processing* **2022**, 163.

[9] R. Grega, J. Krajňák, P. Baran. The Reduction of Vibrations in A Car - The Principle of Pneumatic Dual Mass Flywheel. *Zeszyty naukowe Politechniki Śląskiej* **2014**, 84. ISSN 0209-3324

[10] A European Green Deal. 2021. Available online: https://ec.europa.eu/info/strategy/priorities-2019-2024/european-green-deal_en (accessed on 12 December 2022).

[11] P. Charles, J.K. Sinha, F. Gu, L. Lidstone, A.D. Ball. Detecting the crankshaft torsional vibration of diesel engines for combustion related diagnosis. *J. Sound Vib.* **2009**, 321, 1171–1185

APPLIED MECHANICS 2024

April 17th – 19th, 2024
Hotel Toliar, Štrbské Pleso
Slovakia

INTRODUCTION TO HIGHER ORDER NEURAL NETWORKS BASED ON RIEMANN SOLVER

P. KOVÁŘ[1]*, A. TATER[2], J. FÜRST[3]

Riemann problem stands as a cornerstone in the domain of computational fluid dynamics (CFD), particularly in the context of finite volume methods (FVM). This contribution deals with approximation of the exact Riemann solver by means of artificial neural networks that can offer more accurate solution than standard widely used approximative solvers. Furthermore, the evaluation of the numeric flux can be much faster.

Keywords: Riemann solvers, Approximative solvers, Higher order neural networks

INTRODUCTION

Riemann problem stands as a cornerstone in the domain of computational fluid dynamics (CFD), particularly in the context of finite volume methods (FVM). The problem addresses the fundamental challenge of solving hyperbolic partial differential equations (PDEs) governing fluid flow.

In essence, Riemann problem involves the examination of the flow behaviour at the interface between two different states of a fluid. It serves as a pivotal test case for understanding the propagation of discontinuities, shocks, and rarefactions through the fluid medium [1].

The primary function of a Riemann solver is to determine the fluxes of conserved quantities (such as mass, momentum, and energy) across the interfaces between adjacent computational cells. This is achieved by solving Riemann problem at each cell interface. There are various means or approaches to solving Riemann problem [2]. Exact solver involves solving Riemann problem analytically using the exact solution of the governing hyperbolic PDEs. While providing accurate results, exact solvers are computationally expensive and often impractical for complex flow scenarios due to their high computational cost. Approximate Riemann solvers, such as the HLL and HLLC solvers [2, 3], aim to approximate the solution to Riemann problem using simplified models or assumptions. These solvers strike a balance between accuracy and computational efficiency and are widely used in practice for simulating a broad range of flow conditions.

[1] **Ing. Patrik Kovář**, Department of Technical Mathematics, Center of Aviation and Space Research, Faculty of Mechanical Engineering, Czech Technical University in Prague; Patrik.Kovar@fs.cvut.cz
[2] **Ing. Adam Tater**, Department of Technical Mathematics, Center of Aviation and Space Research, Faculty of Mechanical Engineering, Czech Technical University in Prague;
[3] **Prof. Ing. Jiří Fürst, Ph.D.**, Department of Technical Mathematics, Faculty of Mechanical Engineering, Czech Technical University in Prague;

Another approach is represented by approximation of the exact Riemann solver by means of artificial neural networks (ANNs) that can offer more accurate solution than standard approximative solvers. Furthermore, the evaluation of the numeric flux can be much faster.

METHOD

ANNs are computational models inspired by the structure and functioning of the human brain. They consist of interconnected nodes organized in layers as it is shown in Fig. 1. Activation functions $\sigma(\cdot)$ introduce non-linearity to the output of a neuron. The previous synaptic operation can be also defined as non-linear or higher order [4, 5] as it can be seen in Equation (1)

$$S = w_0 x_0 + \sum_{i=1}^{n} w_i x_i + \sum_{i=1}^{n}\sum_{j=i}^{n} w_{ij} x_i x_j + \cdots + \sum_{i_1=1}^{n} \cdots \sum_{i_N=i_{N-1}}^{n} w_{i_1 i_2 \ldots i_n} x_{i_1} x_{i_2} \cdots x_{i_n}, \quad (1)$$

where $x_0 = 1$ denotes threshold and n stands for length of input feature vector.

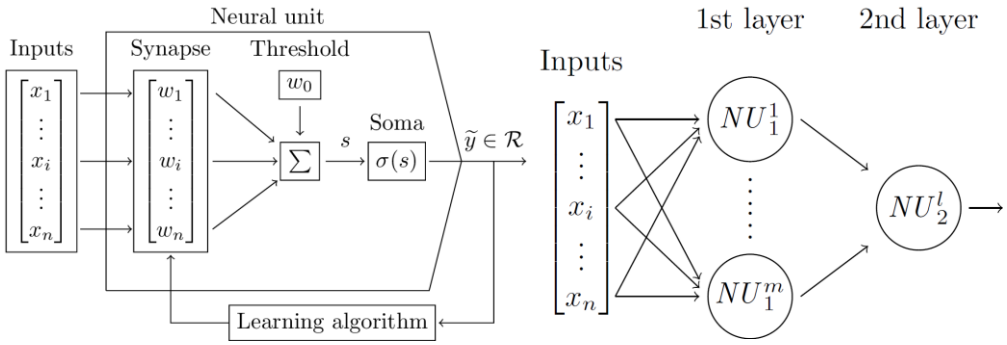

Fig. 1 Neural network: single neural unit (left); shallow neural network (right)

Computational complexity increases as the order of synaptic operation in each layer and number of neurons in individual layers increase, for more detail see [6]. To preserve simplicity of the approach, tested ANN architectures were varied from the simplest two-layered networks to five neurons in the first layer and synaptic operation up to third order in both layers. Firstly, numerical flux was modelled separately, i.e., via three individual neural nets. Second approach assumed the only network to capture numerical flux pattern as a coupled problem.

Training data set

To obtain training data set, exact Riemann solver described by Toro [2], was used. It contained five thousand samples generated via Latin hypercube sampling (LHS) within boundary conditions of well-known Sod's shock tube task as it is listed in Tab. 1.

Tab. 1 Ranges of individual quantities in the training data set

Ranges for LHS	$\rho[\mathrm{kg \cdot m^{-3}}]$	$u[\mathrm{m \cdot s^{-1}}]$	$p[\mathrm{Pa}]$
State on the left side	$\langle 0.05;\ 1.1\rangle$	$\langle -1;\ 1.1\rangle$	$\langle 0.05;\ 1.1\rangle$
State on the right side	$\langle 0.05;\ 1.1\rangle$	$\langle -1;\ 1.1\rangle$	$\langle 0.05;\ 1.1\rangle$

RESULTS

Both inputs and resulting numerical flux were scored using minmax method to fall within the range of $\langle 0;\ 1\rangle$. A constant learning rate of $\mu = 0.05$ was utilized, and total number of epochs was set to 10 000. During the training, five folds were employed for each neural network.

In the Fig. 2 (left), there are the best results of the learning from designed neural architectures. The lowest testing error showed architecture with three neurons in the first layer and three output neurons, i.e., single net for coupled problem. Neural net reached testing error 1.1e-4 after 5271 epochs before overfitting as it can be seen in Fig. 2. (right). For more information about overfitting and methods how to check this phenomenon can be found e.g. in [7, 8].

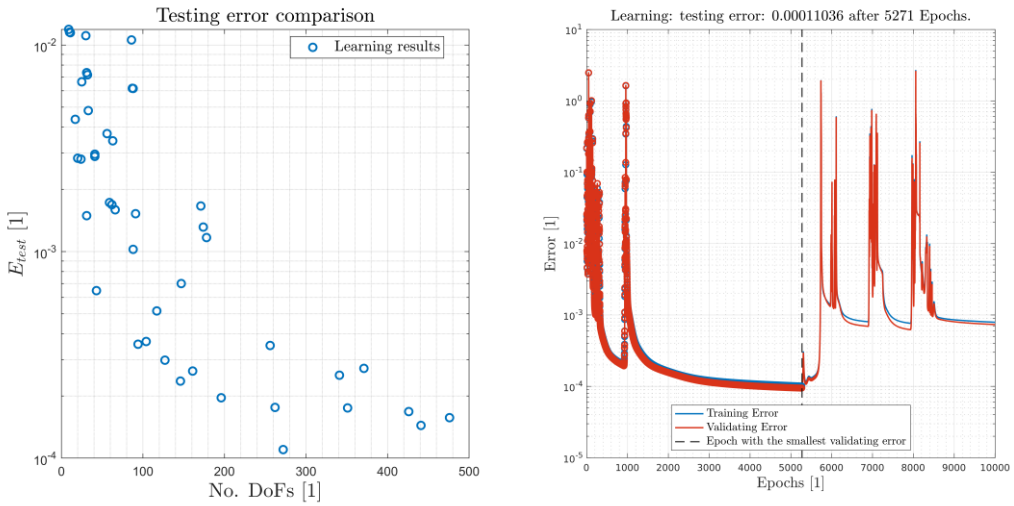

Fig. 2 Learning quality comparison (left); progress of the learning (right)

Performance of the best candidates was compared to widely used approximative Riemann solvers in terms of accuracy and time complexity of the evaluation as it is shown in Fig. 3. Mean squared error (MSE) was measured as the difference against exact Riemann solver using following Equation (2)

$$MSE = \frac{1}{3n}\sum_{i=1}^{n}\sum_{j=1}^{3}\left(f_{ij}^{exact} - f_{ij}\right)^2. \tag{2}$$

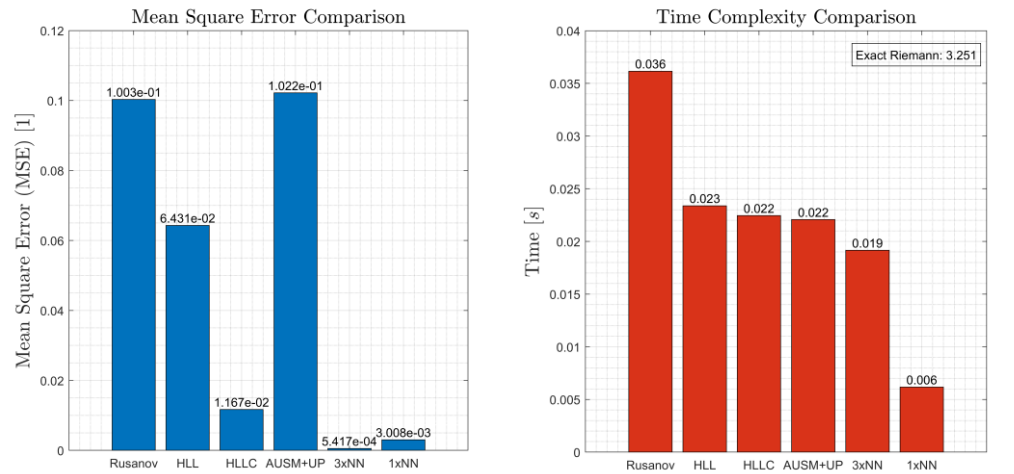

Fig. 3 Comparison of the performed MSE and time complexity averaged over one thousand folds

Numeric flux HLLC performed the best from standard approximative solvers. When single neural network for the numeric flux approximation was used, it turned out that the error is almost by an order of magnitude lower. The approach using three neural nets for each component of numeric flux has shown the smallest error by almost two orders of magnitude in comparison with HLLC.

Time complexity comparison was evaluated as average over one thousand folds. Single neural net performed more accurately and more than three times faster than standard approximative numeric fluxes. Furthermore, the evaluation is three orders of magnitude faster against exact solver.

CONCLUSION

Riemann problem and its importance in CFD together with approaches of Riemann solvers were introduced. Basic ideas of higher order neural networks were also discussed. Based on the Sod's shock tube task, training data set was generated via Exact Riemann solver and several approaches to approximate exact solver using neural network were investigated.

It turned out that more complex ANN architecture does not necessarily lead to better approximation of the task. Both approaches led to more accurate results than approximative Riemann solvers including the best performing HLLC scheme. There is a slight improvement when separated approach using three NNs is applied in terms of the time effectiveness. On the other hand, single neural network performed more accurately and more than three times faster than standard approximative numeric fluxes. Furthermore, the evaluation is three orders of magnitude faster against exact Riemann solver, thus, there should be further investigation in this field.

Further work should improve properties and performance of the designed approximative neural-based Riemann solver as, e.g., extension to cases where vacuum can occur, consistency of the numerical scheme or application to more complex and time-consuming tasks in more dimensions.

ACKNOWLEDGEMENT

This work was supported by the grant agency of the Czech Technical University in Prague, grant No. SGS22/148/OHK2/3T/12.

The authors would also like to thank for the support from the ESIF, EU Operational Programme Research, Development and Education, and from the Center of Advanced Aerospace Technology (CZ.02.1.01/0.0/0.0/16019/0000826), Faculty of Mechanical Engineering, Czech Technical University in Prague.

REFERENCES

[1] R.J. LeVeque. Finite volume methods for hyperbolic problems. Vol. 31. Cambridge university press, 2002.

[2] E.F. Toro. Riemann solvers and numerical methods for fluid dynamics: a practical introduction. *Springer Science & Business Media* **2013**.

[3] E.F. Toro, M. Spruce, W. Speares. Restoration of the contact surface in the HLL-Riemann solver. Shock waves 4, 1994, 25-34.

[4] M.M. Gupta, L. Jin, N. Homma. Static and dynamic neural networks: from fundamentals to advanced theory. John Wiley & Sons, 2004.

[5] M.M. Gupta, I. Bukovsky, N. Homma, A. Solo, Z.G. Hou. Fundamentals of higher order neural networks for modeling and simulation. *Artificial Higher Order Neural Networks for Modeling and Simulation* **2013**, IGI Global, 103-133.

[6] P. Kovář, A. Tater, J. Pařez, J. Fürst. About the appropriate neural network size for the engineering applications. Proceedings of Computational Mechanics, University of West Bohemia, 91-94, 2023. ISBN 978-80-261-1177-1

[7] P. Kovář, J. Fürst. Compressor cascade correlations modelling at design points using artificial neural networks. *Applied and Computational Mechanics* **2023**, 17 (2), 1-16. ISSN 1802-680X

[8] J. Pařez, P. Kovář, A. Tater. Prediction of temperature field distribution in a gas turbine using higher order neural network. *Acta Polytechnica* **2023**, 63 (6), 430-438. ISSN 1805-2363

APPLIED MECHANICS 2024

April 17th – 19th, 2024
Hotel Toliar, Štrbské Pleso
Slovakia

THE IMPACT OF VARIED HILL-TYPE MUSCLE MODEL FORMULATIONS ON GLENOHUMERAL JOINT LOADING

A. KRATOCHVÍL[1]*, M. DANIEL[2]

The issue of glenohumeral joint loading is multifaceted, impacted by various factors. One of the aspects is the selection of a musculoskeletal shoulder model, which differs in muscle count, skeletal geometry, and muscle wrapping points or surfaces. Additionally, the choice of muscle model formulation is crucial, particularly in accounting for passive muscle force contributions to overall loading. In our study, we examined four prevalent Hill-type muscle models and their influence on glenohumeral joint loading across three distinct movements.

Keywords: Shoulder, muscle model, glenohumeral load, passive muscle force

INTRODUCTION

The longevity and effectiveness of shoulder replacements are closely linked to the loading of the glenohumeral joint (GHJ). Understanding the intricate dynamics of force magnitude and direction within the shoulder is crucial for ensuring the stability and durability of these implants. Given the complexities and ethical considerations of *in vivo* experimental load measurements, the mathematical modeling is used as a pragmatic solution. Critical to the success of these models is not only the selection of a precise musculoskeletal representation of the shoulder but also the choice of muscle model employed. This study aims to evaluate the impact of muscle model selection on GHJ load predictions by examining four Hill-type muscle models that are commonly used in literature. We specifically focus on the GHJ load during abduction–a critical movement in evaluating shoulder mechanics and it give us the availability of comparation with experimental data published by Bergmann et al., 2007 [1].

METHODS

We utilized the musculoskeletal model of the human shoulder (Fig. 1) proposed by Seth et al., 2019 [2]. This model consisting of 16 muscles (33 muscle segments) integrates a swift and precise skeletal representation of scapulothoracic kinematics, as introduced by Seth et al., 2016 [3].

[1] **Ing. Adam Kratochvíl**, Department of Mechanics, Biomechanics, and Mechatronics, Faculty of Mechanical Engineering, Czech Technical University in Prague, Technická 1902/6, Prague, Czech Republic; adam.kratochvil@fs.cvut.cz
[2] **Prof. RNDr. Matej Daniel, Ph.D.**, Department of Mechanics, Biomechanics, and Mechatronics, Faculty of Mechanical Engineering, Czech Technical University in Prague, Technická 1902/6, Prague, Czech Republic; matej.daniel@cvut.cz

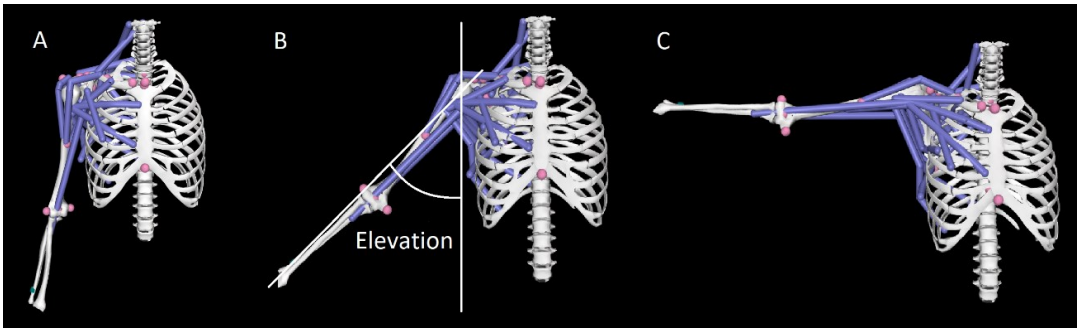

Fig. 1 Kinematics of abduction in OpenSim software in three positions: initial position (A), 45 degrees (B), and 90 degrees (C) shown on musculoskeletal model introduced by Seth et al., 2019 [2].

The arm abduction kinematics were obtained from 26-year-old healthy female subject (height: 162 cm, weight: 52 kg) [2]. Three trials of abduction without weight from the dominant shoulder (right) were evaluated. The arm position was described by an elevation angle. Elevation angle is defined as an angle between the vertical and arm axis running through the center of rotation of GHJ and the center of gravity of hand (Fig. 1).

Four different Hill-type muscle models were employed–Haeufle et al., 2014 [4], Thelen, 2003 [5], McLean et al., 2003 [6], and Geyer et al., 2003 [7]. All the muscle tendon complexes (MTC) consist of three elements, which can be divided to active (muscle) and passive (tendon) part (Fig. 2). The active part includes contractile element (CE), responsible for active force production and parallel elastic element (PEE), aligned parallel to the CE and which simulates passive response of the muscle fibers. The passive part includes serial elastic element (SEE), positioned in series with the CE and simulating the elastic response of tendon.

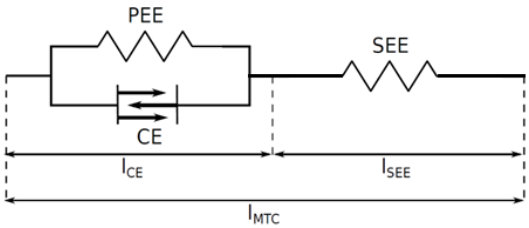

Fig. 2 The configuration of the three elements MTC

The muscle models are defined by mathematical expression of each of the three elements. Normalized musculotendon force of each muscle model for middle deltoid with 100 % activation according to muscle strain is depicted in Fig. 3. The elementary force and length relations in the MTCs are defined by equations (1), (2), and (3).

$$F_M = F_{CE} + F_{PEE} = F_{SEE}\ , \tag{1}$$

$$l_{MTC} = l_{SEE} + l_{CE}\ , \tag{2}$$

where

$$l_{CE} = l_{PEE}\ . \tag{3}$$

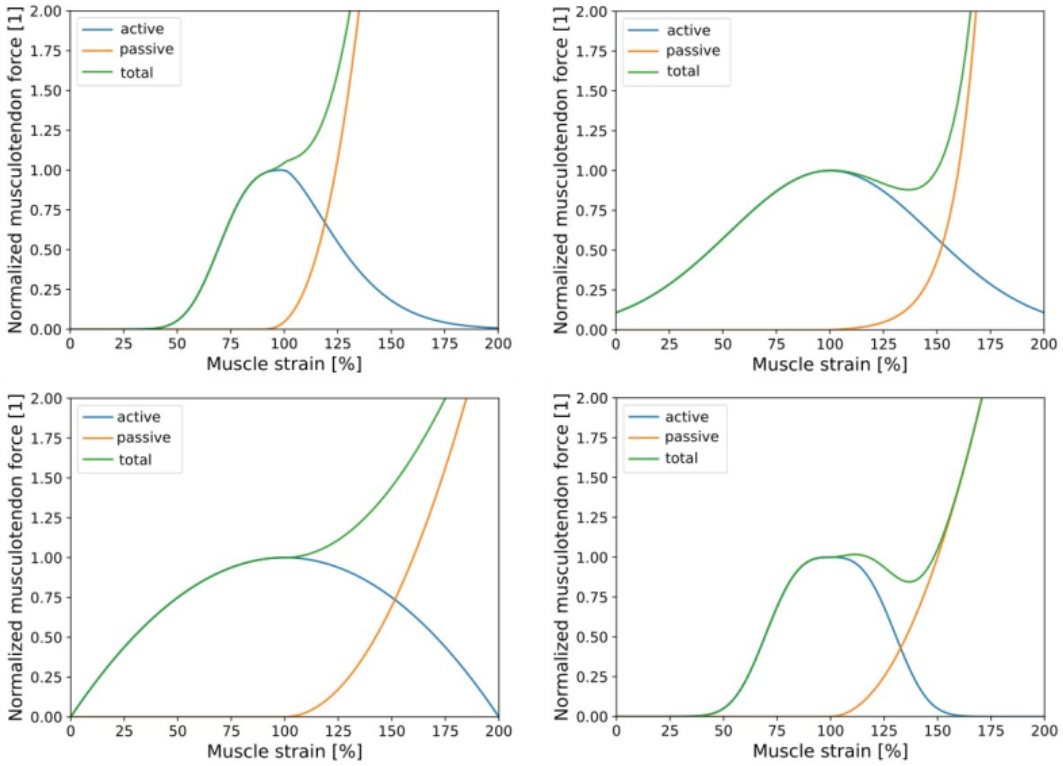

Fig. 3 Force-length relation of the contractile element (CE, blue line), the parallel elastic element (PEE, orange line), and green line indicates total muscle force in Haeufle et al., 2014 [4] (left up), in Thelen, 2003 [5] (right up), in McLean et al., 2003 [6] (left down), and in Geyer et al., 2003 [7] (right down). Data is shown for middle deltoid with 100 % activation.

RESULTS

GHJ load for both active and passive abduction are depicted in Fig. 4. The choice of muscle model significantly impacted GHJ load. The highest load occurred when employing the Haeufle et al., 2014 [4] muscle model, while the lowest forces were observed with the Thelen, 2003 [5] muscle model. Although the muscle models showed the same qualitative trend, they varied quantitatively.

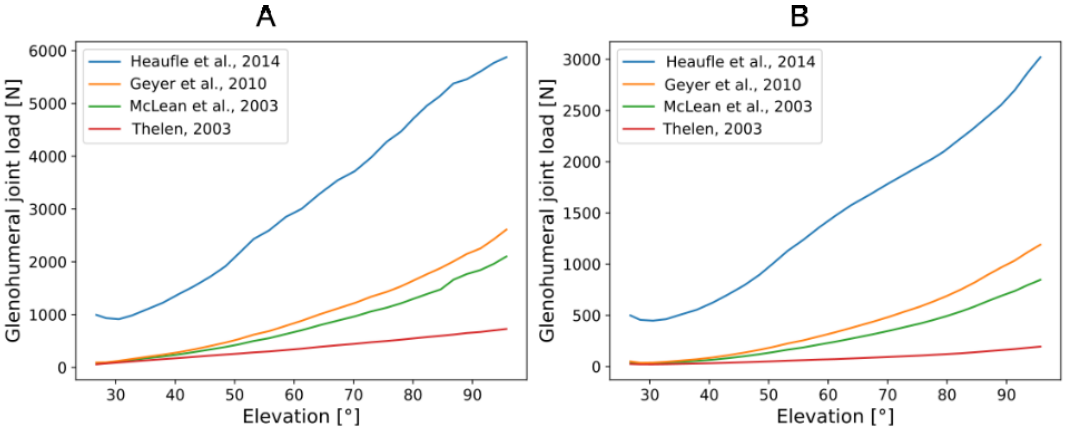

Fig. 4 The effect of formulation of Hill-type muscle model on GHJ load during active abduction (A) and passive abduction (B)

DISCUSSION AND CONCLUSION

The choice of muscle model can significantly impact the outcomes of GHJ load (Fig. 4). This influence stems not only from the formulation of the Hill-type muscle model but also from the muscle constants, which profoundly shape the muscle's characteristics. In their work, Haeufle et al., 2014 [4] utilized these constants derived from a cat's soleus muscle. Consequently, these constants influenced the stiffness of both parallel and serial elastic elements, rendering them stiffer compared to other muscle models. This adjustment resulted in significantly higher passive forces and thus GHJ load up to 6 000 N.

Bergmann et al., 2007 [1] in *in vivo* experiments, observed GHJ loads at 90 degrees of abduction ranging between 500 and 900 N based on patient weight. This range is comparable to the 800 N estimated using the Thelen, 2003 [5] muscle model. Based on this finding can be state that Thelen, 2003 [5] muscle model gave realistic values of GHJ load during abduction.

ACKNOWLEDGEMENT

The work has been supported by grant project of the Student Grant Competition of CTU No. SGS22/149/OHK2/3T/12.

REFERENCES

[1] G. Bergmann et al. In vivo glenohumeral contact forces—Measurements in the first patient 7 months postoperatively. [Online] *Journal of Biomechanics* **2007**, 40 (10), 2139-2149. DOI: https://doi.org/10.1016/j.jbiomech.2006.10.037

[2] A. Seth et al. Muscle Contributions to Upper-Extremity Movement and Work From a Musculoskeletal Model of the Human Shoulder. [Online] *Frontiers in Neurorobotics* **2019**, 13. DOI: https://doi.org/10.3389/fnbot.2019.00090

[3] A. Seth et al. A Biomechanical Model of the Scapulothoracic Joint to Accurately Capture Scapular Kinematics during Shoulder Movements. [Online] *PLOS ONE* **2016**, 11 (1). DOI: https://doi.org/10.1371/journal.pone.0141028

[4] D.F.B. Haeufle, M. Günther, A. Bayer, P. Schmitt. Hill-type muscle model with serial damping and eccentric force–velocity relation. [Online] *Journal of Biomechanics* **2014**, 47 (6), 1531-1536. DOI: https://doi.org/10.1016/j.jbiomech.2014.02.009

[5] D.G. Thelen. Adjustment of Muscle Mechanics Model Parameters to Simulate Dynamic Contractions in Older Adults. [Online] *Journal of Biomechanical Engineering* **2003**, 125 (1), 70-77. DOI: https://doi.org/10.1115/1.1531112

[6] P.G. McLean, A. Su, A.J. van den Bogert. Development and Validation of a 3-D Model to Predict Knee Joint Loading During Dynamic Movement. [Online] *Journal of Biomechanical Engineering* **2003**, 125 (6), 864-874. DOI: https://doi.org/10.1115/1.1634282

[7] H. Geyer, A. Seyfarth, R. Blickhan. Positive force feedback in bouncing gaits? [Online] *Proceedings of the Royal Society of London. Series B: Biological Sciences* **2003**, 270 (1529), 2173-2183. DOI: https://doi.org/10.1098/rspb.2003.2454

APPLIED MECHANICS 2024

April 17th – 19th, 2024
Hotel Toliar, Štrbské Pleso
Slovakia

IMPLEMENTATION OF TWO TYPES OF MUSCLE MODELS AND THEIR COMPARISON WHEN APPLIED TO THE SHOULDER JOINT

J. KRIVOŠEJ[1]*, J. ŠVADLENA[2], J. BODNÁROVÁ[3], Z. ŠIKA[4]

The paper deals with the implementation of a muscle model for a part of the upper limb, namely the shoulder joint. For comparison, two muscle models are used in the implementation. The first is based on Hill's muscle model and the second is Thelen muscle model, which is a slight modification of Hill's muscle model. The muscle actuation is solved using the computed torque control with proportional-derivate controller and inversion of muscle model. At the same time, optimization of the distribution of activations is used for muscle redundancy, where different approaches are compared between each other.

Keywords: Hill's muscle model; Thelen muscle model; Computed torque control; Muscle redundancy; Muscle activation optimization

INTRODUCTION

The targeted area of the paper is glenohumeral joint, often referred to as the shoulder joint. It is one of the most mobile and complex joints in the human body. It's formed by the articulation between the head of the humerus (the upper arm bone) and the glenoid cavity of the scapula (the shoulder blade) [1]. The paper deals mainly with the implementation methodology, therefore a reduced planar model of the arm with two muscles is considered, which is intended to be extended in the future into a spatial model with an expanded number of muscles [2].

The muscle models used in the paper are based on Hill muscle model type, which is a classical model used to describe the force-generating capabilities of skeletal muscles. It's a fundamental framework in biomechanics and muscle physiology. The model proposes that the force generated by a muscle is a function of its contractile element, series elastic element, and parallel elastic element.

[1] **Ing. Jan Krivošej**, Department of Mechanics, Biomechanics and Mechatronics, Faculty of Mechanical Engineering, Czech Technical University in Prague, Technická 4, 160 00 Praha 6, Czech Republic; jan.krivosej@fs.cvut.cz
[2] **Bc. Jakub Švadlena**, Department of Mechanics, Biomechanics and Mechatronics, Faculty of Mechanical Engineering, Czech Technical University in Prague, Technická 4, 160 00 Praha 6, Czech Republic; jakub.svadlena@fs.cvut.cz
[3] **Ing. Júlia Bodnárová**, Department of Mechanics, Biomechanics and Mechatronics, Faculty of Mechanical Engineering, Czech Technical University in Prague, Technická 4, 160 00 Praha 6, Czech Republic; julia.bodnarova@fs.cvut.cz
[4] **prof. Ing. Zbyněk Šika, PhD.**, Department of Mechanics, Biomechanics and Mechatronics, Faculty of Mechanical Engineering, Czech Technical University in Prague, Technická 4, 160 00 Praha 6, Czech Republic; Zbynek.Sika@fs.cvut.cz

The first implemented model is based on the equations derived by M. Vilimek in [3] and is a certain simplification of the complex equations, which preserve the main supporting features of the model in a certain range of forces. The second model implemented is the more comprehensive and community accepted Thelen muscle model and is based on [4]. Overall, the model has more parameters that affect the subsequent behavior in dynamic simulations and more complex equations. The main differentiation from Vilimek's approach is the extraction of muscle length by integration from velocity during dynamic simulation.

MUSCLE MODEL IMPLEMENTATION

Both models were validated on a simple system representing mass and muscle. Damping was added to such a system to better reflect reality, since the Vilimek and the Thelen muscle model mentioned above and considered does not include damping.

Mass-Muscle Model

The equation of motion of such system can be written as:

$$m\ddot{y} + b\dot{y} = F_{MUSCLE} - mg, \tag{1}$$

where m represents mass, b represents damping, g is the gravitational acceleration, y is the vertical coordinate and F_{MUSCLE} is force given by muscle model. The schematic model of mass muscle system is shown in the Fig. 1 a). Fig. 1 b) shows the simulation curves and dynamic behavior of the position of the mass for a different value of muscle activation from 0% to 100%. Firstly, in case of $a_{0\%}$ there is only the passive force component of muscle force and mass drops slightly. Secondly, in case of $a_{5\%}$ and $a_{10\%}$ the passive and active muscle force lift slightly the mass without exceeding the limit of free length of muscle. And finally, in the case of $a_{20\%}$, $a_{50\%}$ and $a_{100\%}$ the limit of free length of muscle is exceeded.

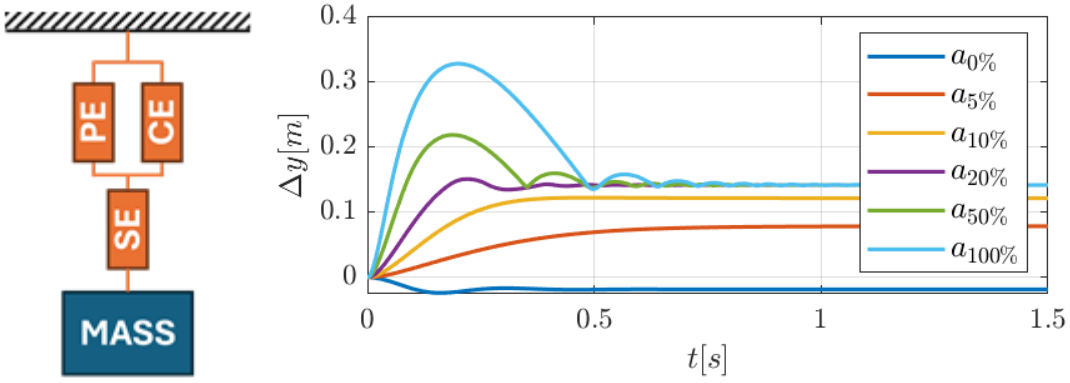

a) b)

Fig. 1 The schematic model of mass-muscle model for a muscle model verification is shown on the left a); the simulation curves of dynamic behavior of mass-muscle model with Thelen approach implementation are shown on the right b)

Control strategy of muscle active force

In the case of the passive force component of the muscle, the resulting force is determined by the geometry of the muscle and mass position. In the case of the active force component of the muscle, a strategy based on computed torque control (CTC) with a PD controller was implemented to

control the activation of muscle to reach the desired position. The simplified schematic simulation model is shown in Fig. 2.

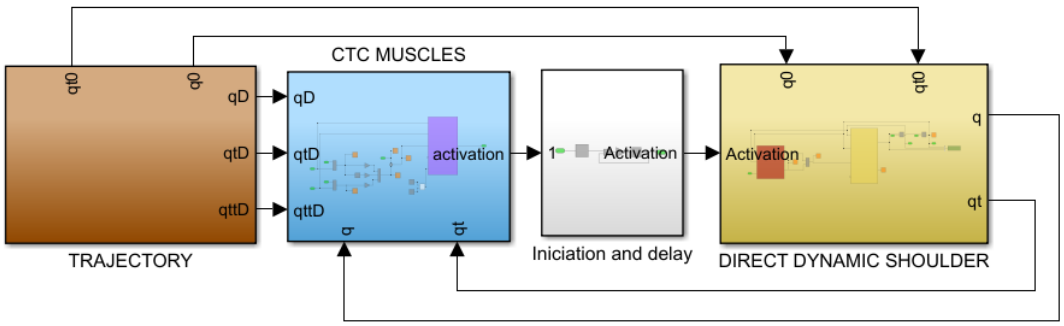

Fig. 2 CTC schematic simulation model of shoulder joint

SHOULDER JOINT MUSCLE MODEL

After verifying the models on a simple mass-muscle system, the implementation to a shoulder joint has been done. The planar geometry is estimated on the basis of the thoracoscapular muscle model implemented in OpenSim software [5]. The simplified view of muscle geometry is shown in Fig. 3 and Fig. 4.

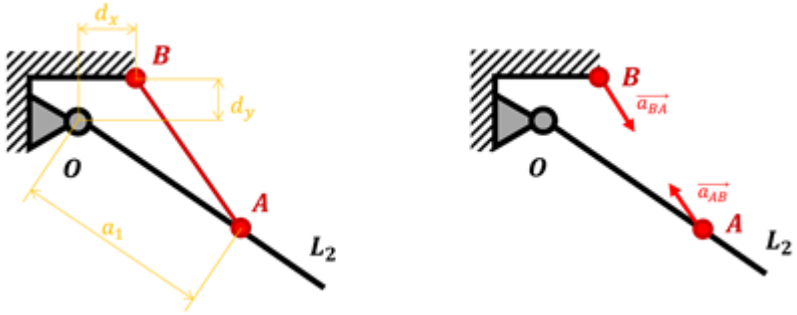

Fig. 3 Shoulder muscle geometry in upper joint configuration

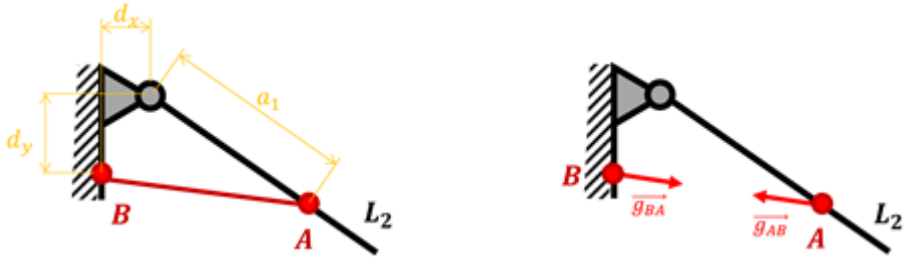

Fig. 4 Shoulder muscle geometry in lower joint configuration

Another important point of the implementation is to solve the muscle redundancy, in this case an optimization method was implemented to minimize the squared muscle activations:

$$\min_{a_i \in \langle 0,1 \rangle} \sum a_i^2. \tag{2}$$

The example of the implementation is shown in Fig. 4, where Vilimek muscle model is used in CTC with one upper and one lower muscle configuration of shoulder joint. The reference trajectory used is based on repetitive sin wave. It can be seen that activation a_1 represents the upper muscle

and its magnitude is higher than the lower muscle activation magnitude. The error normalized to one meter arm length of this repetitive shoulder motion is in millimeters.

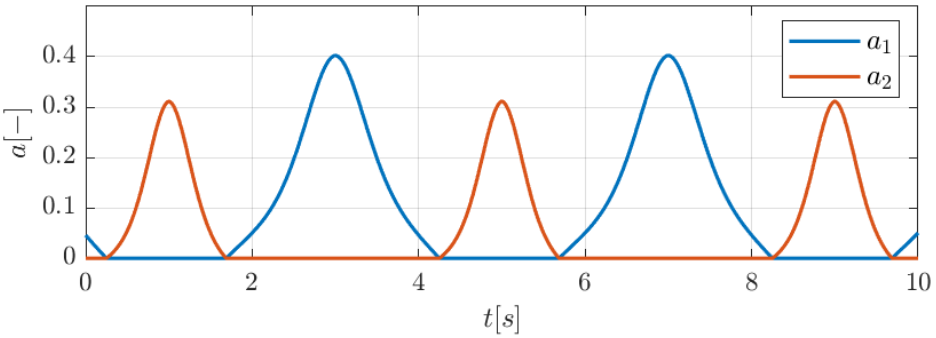

Fig. 4 CTC with Vilimek muscle model implementation into shoulder joint with one upper and one lower muscle during repetitive trajectory based on a sin wave

CONCLUSION

Two muscle models and their verification on a simple mass-muscle system were introduced. Subsequently, a CTC strategy with a PD controller was implemented. The muscle redundancy was solved by optimization in a feedback loop. The muscle modelled in this way was implemented in the shoulder geometry. Subsequently, the movement of the arm was controlled by several muscles to the desired trajectory.

ACKNOWLEDGEMENT

The presented research was supported by the Czech Science Foundation under the project 23-06920S *Functionally biomimetic exoskeleton of human upper limb for selective muscle augmentation*.

REFERENCES

[1] L.-R. Chang, P. Anand, M. Varacallo. Anatomy, Shoulder and Upper Limb, Glenohumeral Joint. StatPearls, StatPearls Publishing, Treasure Island (FL), 2023.

[2] A. Seth, M. Dong, R. Matias, S. Delp. Muscle Contributions to Upper-Extremity Movement and Work From a Musculoskeletal Model of the Human Shoulder. *Frontiers in Neurorobotics* **2019**, 13. https://doi.org/10.3389/fnbot.2019.00090

[3] M. Vilimek. Musculotendon forces derived by different muscle models. *Acta of bioengineering and biomechanics* (Wroclaw University of Technology) **2007**, 9, 41-47.

[4] D.G. Thelen. Adjustment of muscle mechanics model parameters to simulate dynamic contractions in older adults. *J. Biomech. Eng.* **2003**, 125 (1), 70-77. https://doi.org/10.1115/1.1531112

[5] A. Seth, J.L. Hicks, T.K. Uchida, A. Habib, C.L. Dembia, J.J. Dunne, et al. OpenSim: Simulating musculoskeletal dynamics and neuromuscular control to study human and animal movement. *PLoS Comput. Biol.* **2018**, 14 (7). https://doi.org/10.1371/journal.pcbi.1006223

APPLIED MECHANICS 2024

April 17th – 19th, 2024
Hotel Toliar, Štrbské Pleso
Slovakia

EFFECT OF HEAT TREATMENT ON THE SUPER ELASTIC PROPERTIES OF NITI WIRES

K. KUBÁŠOVÁ[1]*, A. KRATOCHVÍL[1], M. LOSERTOVÁ[2], M. KOPELENT[2], R. SEDLÁČEK[1]

Superelasticity is of major relevance in biomedicine, especially in the field of orthopedics and dentistry. Superelastic materials such as Nitinol, a NiTi alloy, have the ability to return to their original form even after extreme deformation, which is exceptionally useful in the production of various medical devices and implants. In orthopedics, superelastic Nitinol can be used, for example, as wires and springs for bone fixation. These materials can be easily inserted into the body and then returned to their original form, minimizing the invasiveness of surgery and reducing recovery time. This work investigates the effect of heat treatment on the superelastic mechanical properties of NiTi wires.

Keywords: NiTi alloy; Nitinol; Superelasticity; Shape Memory Effect; Experiment

INTRODUCTION

Nitinol, an alloy of nickel and titanium (NiTi), has established itself as an important material in the biomedical field in recent decades due to its unique properties. Its superelastic properties and shape memory effect enable innovative approaches in medical applications. This material is able to adapt to different shapes and sizes, making it ideal for the manufacture of implants, stents, orthodontic wires and other medical devices. The superelastic character of nitinol allows these implants to be easily applied and adapt to the patient's anatomy, while the shape memory effect allows them to return to their original shape after deformation. Another advantage is its elastic modulus, which is similar to bone, and its very good biocompatibility [1-3].

Nitinol's mechanical properties, superelasticity and shape memory effect depend on a range of parameters – from manufacturing parameters, to heat treatment, to size and shape. Heat treatment affects the range of transformation temperatures, aging or annealing in solution dissolves unwanted secondary phases and promotes the superelastic behavior of the alloy. Finding the optimum production combined with appropriate heat treatment is key to getting the sorted properties right for the application.

[1] **Ing. Kristýna Kubášová, Ing. Adam Kratochvíl, doc. Ing. Radek Sedláček, Ph.D.**, Department of Mechanics, Biomechanics and Mechatronics, Faculty of Mechanical Engineering, Czech Technical University in Prague. Technicka 4, 160 00 Praha 6, Czech Republic; kristyna.kubasova@fs.cvut.cz, adam.kratochvil@fs.cvut.cz, radek.sedlacek@fs.cvut.cz

[2] **doc. Dr. Ing. Monika Losertová, Ing. Michal Kopelent**, Department of Materials Engineering and Recycling, Faculty of Materials Science and Technology, VSB—Technical University of Ostrava, 17. listopadu 2172/15, 708 00 Ostrava, Czech Republic; mlosertova@vsb.cz, michal.kopelent@vsb.cz

MATERIALS AND METHODS

In this project we investigate the effect of heat treatment on the mechanical and superelastic properties of NiTi wires. A total of 36 samples (nominal diameter 1.3 mm and length 150 mm) were tested, divided into 7 groups – without heat treatment ("as received" AR group) and after heat treatment (aging) at different temperatures. The main objective of this work is to find the optimum heat treatment for advantageous superelastic properties of the wire.

The specimens were loaded at a strain rate of $3 \cdot 10^{-4}$ s^{-1} on MTS Mini Bionix 858.02 (MTS, Minnesota, USA) testing system, and were clamped in pneumatic jaws, the strain was measured using the MTS Extensometer (see all in Figure 1 and 2). The displacement, force and time including their maximum values were recorded during the experiment. The data recorded during the test were processed into graphical stress-strain dependence, from which the above-mentioned parameters were evaluated at each point (see Figure 3).

Fig. 1 Testing system Mini Bionix 858.02, load cell and pneumatic jaws

Fig. 2 Detail of NiTi wire sample attached in pneumatic jaws and MTS extensometer

The methodology of the experiment was based on the determination of the superelastic stress plateau, elastic modulus and the strengths of the specimens during tensile test. The superelastic behavior was evaluated as the stress difference between points A and B in the load curve, the modulus of elasticity was evaluated as the tangent directive of the linear region of the load curve (between 150 and 250 MPa, R = 0.999) and the strength corresponds to the maximum stress (see Figure 3). Other parameters evaluated were the relative deformations at each point of the load curve (A, B, C – see Figure 3).

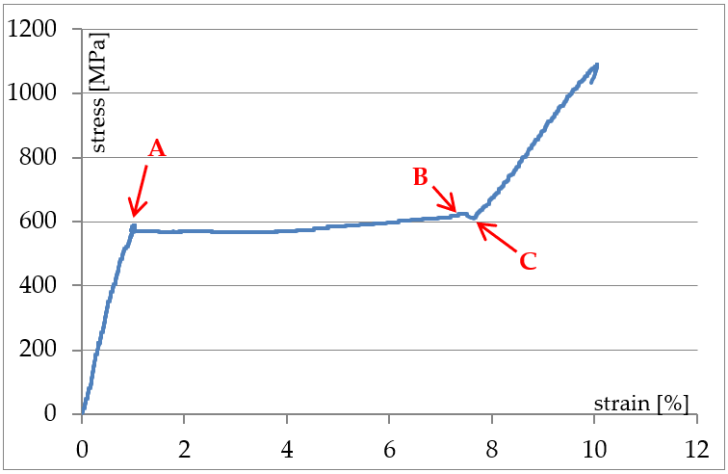

Fig. 3 Stress-strain loading curve and highlighting of important points (A, B, C)

RESULTS

All the evaluated parameters were subjected to statistical analysis and compared with the control group ("as received" AR group) and then also with the previous condition, i.e. with a lower heat treatment temperature (this evaluation may reveal a dependency between heat treatment temperature and mechanical properties). In the figures below (see Figure 4–6) you can see the boxplots for the selected parameters.

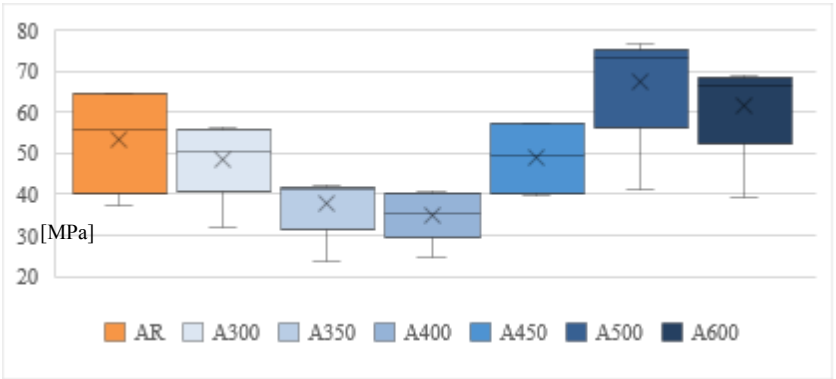

Fig. 4 Boxplots of superelastic stress plateau for all groups

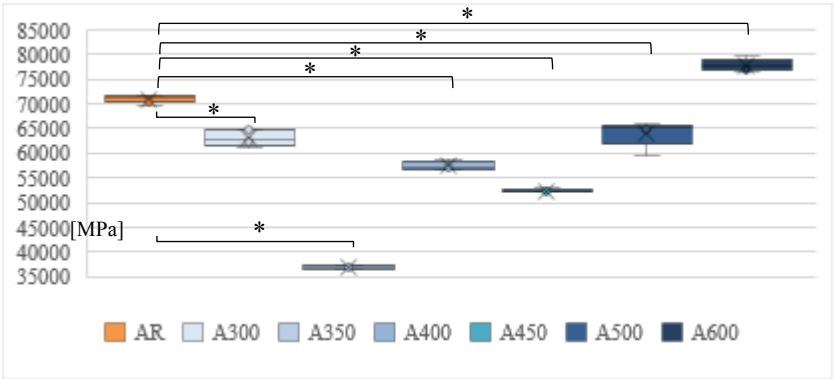

Fig. 5 Boxplots of elastic modulus for all groups (* statistical significance)

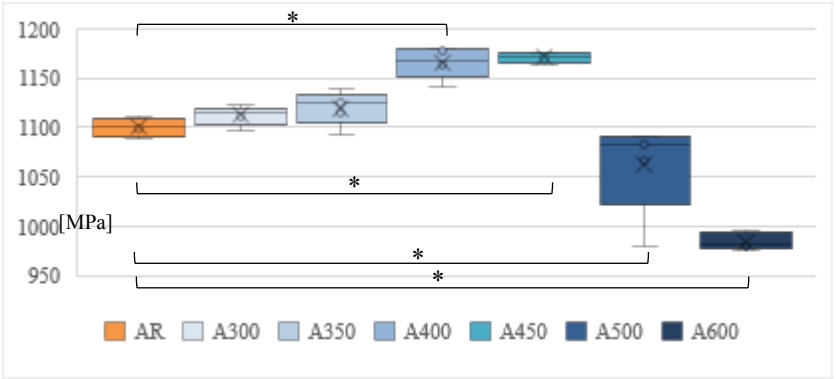

Fig. 6 Boxplots of strength for all groups (* statistical significance)

The figures (see Figure 4–6) show that the superelasticity region does not change significantly statically (compared to AR), while the strength or modulus of elasticity shows statistically significant changes between some (or all) groups, compared to the control ("as received" AR group). Statistical significance is shown by an asterisk (*), the confidence interval of the test was 95%.

CONCLUSION

Tensile tests of NiTi wires were performed and mechanical and superelastic parameters at different heat treatments were compared. The highest strength was achieved for the A450 group, which corresponds to aging at 450 °C. However, this data was further statistically processed, and it was found that heat treatment doesn´t affect the stress plateau, but does affect the strength and elastic modulus, all compared to the control (with "as received" AR group). such as correlation and comparison with the previous condition.

ACKNOWLEDGEMENT

The research was supported by the Ministry of Health of the Czech Republic, grant nr. NU23-08-00043.

REFERENCES

[1] K. Kubášová, V. Drátovská, M. Losertová, P. Salvetr, M. Kopelent, F. Kořínek, V. Havlas, J. Džugan, M. Daniel. A Review on Additive Manufacturing Methods for NiTi Shape Memory Alloy Production. *Materials* **2024**, 17 (1248). https://doi.org/10.3390/ma17061248A

[2] K. Otsuka, X. Ren. Physical metallurgy of Ti–Ni-based shape memory alloys. *Progress in materials science* **2005**, 50 (5), 511-678. https://doi.org/10.1016/j.pmatsci.2004.10.001

[3] A. Wadood, et al. Brief overview on nitinol as biomaterial. *Advances in Materials Science and Engineering* **2016**, (4173138). https://doi.org/10.1155/2016/4173138

APPLIED MECHANICS 2024

April 17th – 19th, 2024
Hotel Toliar, Štrbské Pleso
Slovakia

CRACK CLOSURE DEVELOPMENT FOLLOWING AMPLITUDE CHANGES

R. KUBÍČEK[1]*, T. VOJTEK[2], P. POKORNÝ[3], L. NÁHLÍK[4], P. HUTAŘ[5]

This contribution investigates the impact of variable amplitude loading on crack growth rates, highlighting the phenomena of retardation and acceleration in material behaviour. Variable loading conditions, characterised by differing magnitudes and sequences, can significantly influence crack growth, either slowing down or speeding up compared to constant loading. Through the study of compact tension specimens under two consecutive loading blocks at a constant load ratio (R=0.1), using a strip-yield model. The findings emphasise the importance of accurately modelling these dynamics for ensuring structural reliability and safety under variable loading conditions, offering valuable insights for materials engineering and structural integrity.

Keywords: Variable amplitude loading; plasticity induced crack closure; strip-yield model; steel

INTRODUCTION

Understanding and predicting the residual fatigue life of engineering structures under variable amplitude loading is paramount for ensuring safety, reliability, and cost-effectiveness. In sectors where safety is non-negotiable, such as aviation, energy, and transportation, the accurate estimation of fatigue life is a critical aspect of design and maintenance strategies. These estimations obtained by damage tolerant design are crucial not only for preventing catastrophic failures but also for optimising material and energy consumption in accordance with sustainable and environmentally friendly practices.

Historically, models for predicting crack growth under variable loading have been divided into two main categories. The first is based on the interaction of plastic zones, modelled through residual stresses. These models, such as those proposed by Wheeler [1] and Willenborg [2], have laid the groundwork by introducing retardation factors and adjusting crack growth rates based on plastic

[1] **Ing. Radek Kubíček**, Institute of Physics of Materials, Czech Academy of Sciences, Zizkova 22, 612 62 Brno, Czech Republic; Department of Engineering Mechanics, Faculty of Mechanical Engineering, Brno University of Technology. Technicka 2896/2, 61669 Brno, Czech Republic; kubicek@ipm.cz
[2] **Ing. Tomáš Vojtek, PhD.**, Institute of Physics of Materials, Czech Academy of Sciences, Zizkova 22, 612 62 Brno, Czech Republic; vojtek@ipm.cz
[3] **Ing. Pavel Pokorný, PhD.**, Institute of Physics of Materials, Czech Academy of Sciences, Zizkova 22, 612 62 Brno, Czech Republic; pokorny@ipm.cz
[4] **Prof. Ing. Luboš Náhlík, PhD.**, Institute of Physics of Materials, Czech Academy of Sciences, Zizkova 22, 612 62 Brno, Czech Republic; nahlik@ipm.cz
[5] **Prof. Ing. Pavel Hutař, PhD.**, Institute of Physics of Materials, Czech Academy of Sciences, Zizkova 22, 612 62 Brno, Czech Republic; hutar@ipm.cz

zone interactions. However, these models often predict immediate crack retardation following an overload which is inconsistent with the gradual retardation and the development of crack closure over time.

On the other hand, plasticity-induced crack closure models represent the other type of crack growth modelling. They are either based on empirical relations or on numerical simulations which can be highly computationally demanding or integration challenging with existing engineering codes. One of the most successful cycle-by-cycle numerical crack closure models are the strip-yield models based on Dugdale model [3], e.g. the one developed by Newman [4]. This model correctly predicts the delayed retardation following an overload and it can also deal with sequences of mutually interacting overload and underload effects.

STRIP-YIELD MODEL

Since the integration of Newman strip-yield model [4] with broader engineering applications and considering other crack closure mechanisms poses significant difficulties, this work aims to set analytical expressions that capture the essence of crack closure effects with greater computational efficiency.

For this reason the commercial software FASTRAN [5] was used and two consecutive loading blocks with different amplitudes and equal load ratio $R = 0.1$ are assumed. Fig. 1 shows the descending sequence of the loading amplitude, $\Delta K_1 > \Delta K_2$, where the change is described as $\text{drop} = (\Delta K_1 - \Delta K_2)/\Delta K_1$ and the delayed retardation effect occurs. On the other hand, the acceleration of the fatigue crack follows the increase in the loading amplitude, see Fig. 2, defined as $(\Delta K_2 - \Delta K_1)/\Delta K_1$.

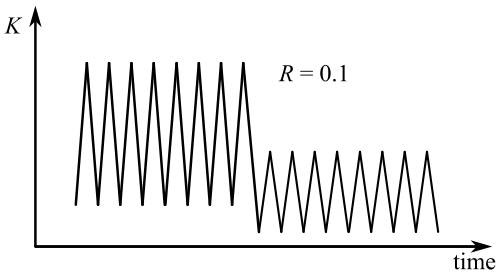

Fig. 1 Overload block scheme – retardation

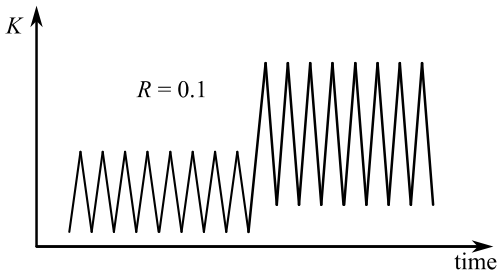

Fig. 2 Underload block scheme – acceleration

Retardation

Crack growth retardation is caused by the crack closure increase which can be described by the proposed parabolic and exponential functions

$$f_{\text{OL}} = \begin{cases} b_{\text{p}}\left(\Delta a_{\text{OL}} - c_{\text{p}}\right)^2 + d_{\text{p}} & \text{for } 0 \geq \Delta a \geq \Delta a_{\text{OL,ch}} \\ b_{\text{e}} + c_{\text{e}} e^{d_{\text{e}}\sqrt{\Delta a_{\text{OL}} - \Delta a_{\text{OL,ch}}}} & \text{for } \Delta a \geq \Delta a_{\text{OL,ch}} \end{cases}, \tag{1}$$

where parameters $b_{\text{p}}, c_{\text{p}}, d_{\text{p}}, b_{\text{e}}, c_{\text{e}}, d_{\text{e}}$ describe different overload block schemes.

In case of $\Delta K_1 = 18$ MPa·m$^{0.5}$ and $\text{drop} = 40\%$, see Fig. 3, the results obtained from FASTRAN software are extrapolated by parabolic function $-672.6(\Delta a_{\text{OL}} - 0.0153)^2 + 0.655$ and exponential function $0.3 + 0.277e^{-6.814\sqrt{\Delta a_{\text{OL}} - \Delta a_{\text{OL,ch}}}}$, where $\Delta a_{\text{OL,ch}} = 0.026$ defines the function change. Same extrapolation procedure was made for the FASTRAN simulations with drops from 5 to 45% and with ΔK_1 from 15 to 25 MPa·m$^{0.5}$.

Acceleration

When the loading is in ascending sequence, the crack is accelerated due to a decrease in crack closure f_{UL} which can be described by exponential function

$$f_{\mathrm{UL}} = b_{\mathrm{UL}} - c_{\mathrm{UL}} e^{d_{\mathrm{UL}}\sqrt{\Delta a_{\mathrm{UL}}}}. \tag{2}$$

Fig. 4 shows the fitting result for $\Delta K_1 = 8$ MPa·m$^{0.5}$ and rise $= 60\%$ that is given by the expression $0.3 - 0.187e^{-9.523}$. Same procedure was made for the FASTRAN simulations with rises from 5 to 90% and with ΔK_1 from 5 to 15 MPa·m$^{0.5}$.

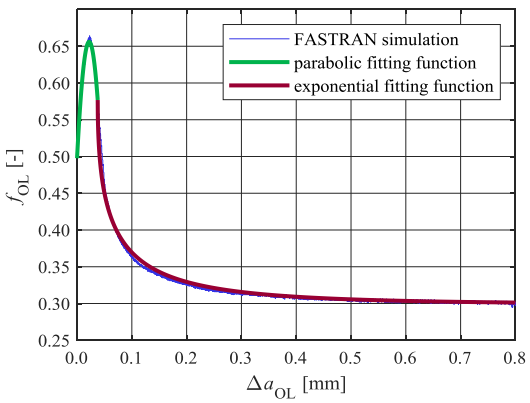

Fig. 3 The crack closure development during overload – $\Delta K_1 = 18$ MPa·m$^{0.5}$, drop $= 40\%$

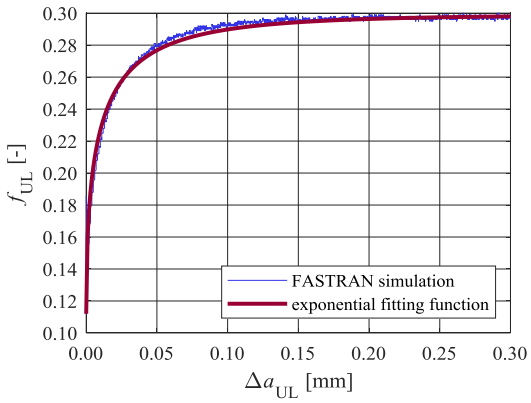

Fig. 4 The crack closure development during underload – $\Delta K_1 = 8$ MPa·m$^{0.5}$, rise $= 60\%$

CRACK GROWTH SIMULATION

To validate the effectiveness of the proposed equations in calculating crack growth rates, a sequence containing both overloads and underloads, as defined in Tab. 1, was repeated twice for the crack growth simulation.

Tab. 1 Variable amplitude loading sequence

Block number i		1	2	3	4	5	6	7	8
Cycles N_i [–]		30 000	30 000	30 000	13 000	40 000	40 000	40 000	13 000
Loading ΔK_i [MPa·m$^{0.5}$]		18	16	14	18	14	12	10	18
Loading Change	drop [%]		11.2	12.5		22.3	14.3	16.7	
	rise [%]				28.6				80

The difference between the simulations taking and not taking the interaction effects into account, is shown in Fig. 5. While the proposed analytical equations, green dashed line, are in perfect agreement with the original solution obtained by the strip-yield model in software FASTRAN, the simulation considering the constant crack closure, blue dashed line, predicts globally faster crack growth which is represented by a piecewise linear dependence a-N. This difference is given by dynamically developing crack closure which in this loading sequence leads dominantly to crack slowing during overloads than to accelerating due to underloads. This is strongly dependent on the loading and other crack closure mechanisms such as oxide induced crack closure.

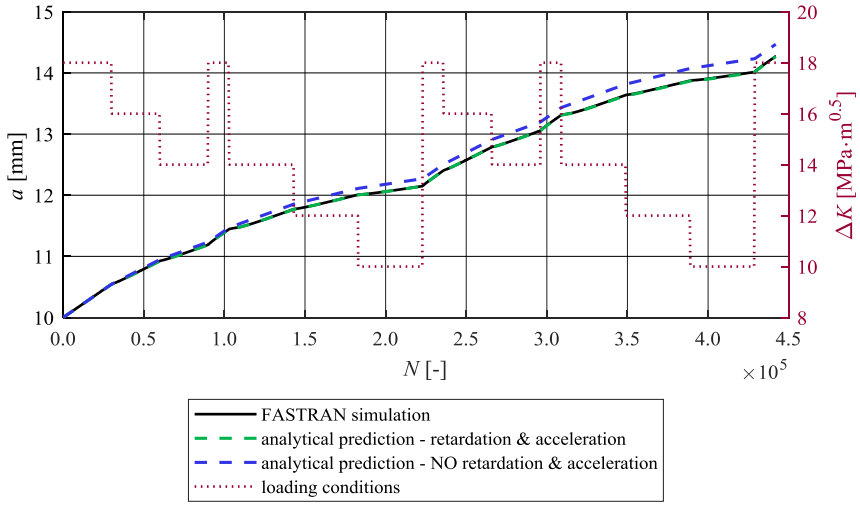

Fig. 5 Crack propagation with and without interaction effects during variable amplitude loading

CONCLUSION

This work introduces an efficient methodology for analysing fatigue crack retardation and acceleration under variable amplitude loading which is demonstrated for the constant load ratio $R = 0.1$. The methodology overcomes the computational challenges of variable-amplitude loading seen in finite element models and the difficulty of integrating the strip-yield model with other computational frameworks.

Simple analytical formulas based on residual stress sometimes fail to accurately predict the crack closure mechanism, potentially resulting in non-conservative estimates. In contrast, new analytical equations successfully capture the delayed crack retardation following an overload, offering broader applicability across various crack closure mechanisms.

ACKNOWLEDGEMENT

This work was financially supported by the Czech Science Foundation in the frame of the project No. 22-28283S. The work was also supported by the Brno University of Technology through the project FSI-S-23–8240.

REFERENCES

[1] O.E. Wheeler. Spectrum Loading and Crack Growth. *J. Basic Eng.* **1972**, 94, 181–186. https://doi.org/10.1115/1.3425362

[2] J. Willenborg, R.M. Engle, H.A. Wood. A crack growth retardation model using an effective stress concept. Air Force Flight Dynamics Lab Wright-Patterson Afb Oh; 1971.

[3] D.S. Dugdale. Yielding of steel sheets containing slits. *J. Mech. Phys. Sol.* **1960**, 8, 100-104. https://doi.org/10.1016/0022-5096(60)90013-2

[4] J.C. Newman Jr. Prediction of Fatigue Crack Growth Under Variable-Amplitude and Spectrum Loading Using a Closure Model. NASA Tech Memo 81942, 1981, 36.

[5] J.C. Newman Jr. FASTRAN A Fatigue Crack Growth Life-Prediction Code Based on the Crack-Closure Concept. Eupora: Fatigue & Fracture Associates, LLC, 2013.

APPLIED MECHANICS 2024

April 17th – 19th, 2024
Hotel Toliar, Štrbské Pleso
Slovakia

SUITABLE APPROACH FOR ARRANGING FIBERS FOR THE TENSILE TESTING OF ADDITIVELY MANUFACTURED THERMOPLASTIC COMPOSITES

J. MAJKO[1]*, M. VAŠKO[1], O. PIROH[1], M. HANDRIK[1], Z. ŠAVRNOCH[1], P. MICHAL[1], M. PAULEC[1]

The production of composite structures has experienced significant advancement, primarily due to progress in 3D printing technology. During the assessment of the mechanical properties of these composites, one crucial question arises: how to effectively perform tensile testing. Experience indicates that standards designed for conventionally manufactured composites are insufficient. Therefore, the authors have proposed their own design of specimen shape, aiming to enhance strength and induce failure in the neck region. However, it has been observed that increasing the number of reinforced laminates leads to the interaction between individual fibre. The article's objective is to identify the most suitable strategy for arranging unidirectionally oriented fibres to ensure that specimens break in the narrowed region.

Keywords: FFF method; fibre reinforced composites; tensile testing; fibre arrangement

INTRODUCTION

Additive manufacturing represents a relatively novel production methodology grounded in the gradual layering of materials. This distinctive approach sets it apart significantly from traditional manufacturing techniques. Among the fundamental methods of 3D printing are extrusion, sintering, fusion, and lamination [1]. Extrusion, in particular, stands out as the most prevalent technique, relying on the gradual extrusion of material through an extruder to the printing head.The cornerstone of this technology lies in the Fused Filament Fabrication (FFF) method. The principle is based on the material filament fed into the printer head, where it's heated to its melting point. This molten material is then extruded through a nozzle and deposited onto the printing desk as the printer head follows a predefined path. Layer by layer, the printer builds upon the preceding ones until the desired object is formed [2].

This approach boasts several advantages, including cost-effectiveness, diversity of printable materials, the ability to fabricate intricate geometries, adaptability to varied customer specifications, and accessibility to the general public. However, users must also be mindful of its drawbacks. In the

[1] **Ing. Jaroslav Majko, PhD.**, **Assoc. Prof. Milan Vaško, PhD.**, **Ing. Ondrej Piroh**, **Ing. Marián Handrik, PhD.**, **Ing. Zdenko Šavrnoch**, **Ing. Pavol Michal**, **Ing. Michal Paulec**, Department of Applied Mechanics, Faculty of Mechanical Engineering, University of Žilina, Univerzitná 8215/1, Žilina, Slovak republic; jaroslav.majko@fstroj.uniza.sk, milan.vasko@fstroj.uniza.sk, ondrej.piroh@fstroj.uniza.sk, marian.handrik@fstroj.uniza.sk, zdenko.savrnoch@fstroj.uniza.sk, pavol.michal@fstroj.uniza.sk, michal.paulec@fstroj.uniza.sk

case of the FFF method, these include compromised mechanical properties, diminished precision, and slower production speed. Therefore, it's essential to carefully assess whether this method aligns with the production requirements of their specific products before proceeding [3].

The rapid advancement of 3D printing has broadened the spectrum of usable materials. Previously, the technology allowed only the printing of thermoplastics, significantly constraining the practical application of additive manufacturing. However, ongoing advancements and refinements have substantially increased the scope of printing possibilities. One notable development is the ability to print composites, which has introduced new avenues for their production [4]. Traditional technologies employed in composite manufacturing are intricate and financially burdensome. Moreover, fabricating geometrically complex objects using these methods poses significant challenges. While 3D printing has partially mitigated some of these constraints, it still confronts numerous drawbacks. These include the presence of voids within the structure, reduced composite strength, and technical limitations of the printing apparatus. Nonetheless, it remains a promising frontier, continually pushing the boundaries of what's achievable in manufacturing.

The primary objective of research on 3D-printed composites is to characterize their mechanical properties. So far, published studies have predominantly centred on assessing tensile properties, bending properties, or impact toughness. However, a fundamental challenge in composite materials lies in devising the appropriate experimental methodologies. For instance, when conducting tensile or fatigue tests, it's crucial to develop suitable approaches to ensure the repeatability and relevance of results for accurately evaluating material performance [5].

Based on the authors' findings, it appears that existing standards typically applied to conventionally manufactured composites or pure polymers, may not always be suitable for additively manufactured composites. This article aims to evaluate the optimal arrangement of reinforcing fibres within a composite structure when their orientation is parallel to the loading direction.

EXPERIMENT PREPARATION

In the first step, it was necessary to choose an appropriate specimen shape. Previous studies have referred to ASTM D3039 and ASTM D638-14 standards (Fig. 1).

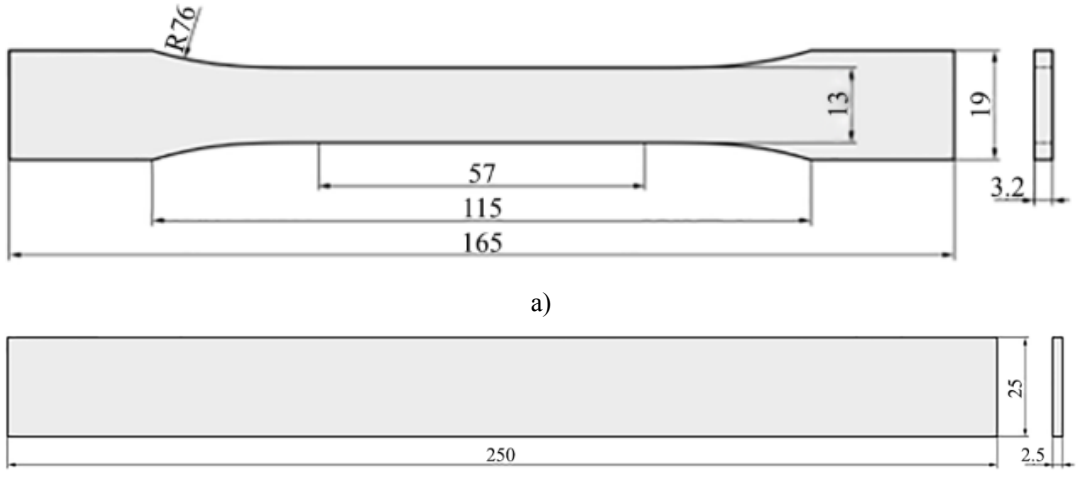

Fig. 1 Shape of specimen according to standards: a) ASTM D638-14; b) ASTM D3039

Based on published studies, both specimen shapes are unsuitable due to the occurrence of stress concentrators in the rounded region or gripping area. Consequently, premature specimen failure ensues, resulting in lower strength than the material's theoretical strength. To overcome this problem, a new specimen shape was proposed by modifying the dog bone shape. According to the author's experience, this shape is appropriate for specimens with a lower fibre volume fraction (FVF) - specifically, those reinforced with a single lamina.

The specimens of the mentioned shape were designed using Inventor software and saved in .stl format. Subsequently, they were imported into slicing software, where users could modify printing parameters (Tab. 1). Printing was realized using the Markforged MarkTwo printer.

Tab. 1 Printing parameters

Parameter	Value
Matrix	Nylon reinforced with chopped carbon fibres
Reinforcement	Long glass fibres
Lamina thickness [mm]	0.1
Matrix orientation [°]	45/-45
Reinforcement orientation [°]	0
Infill density [%]	100

The specimens were printed in the XY plane. The matrix was composed of nylon reinforced with chopped carbon fibres arranged at a 45/-45-degree angle. Long glass fibres, aligned parallel to the loading axis, functioned as reinforcement.

RESULTS

The experimental measurements were conducted using the INOVA device. The tested specimens consisted of two reinforced layers. In the first step, authors chose a strategy of fibre arrangement, which led to failure in the gauge section of specimens with a single reinforced layer (Fig. 2).

Fig. 2 Specimen with long fibers arranged across the entire lamina plane

However, the specimen with two reinforced layers of this arrangement ruptured in the shoulder region (Fig. 3). This failure type is a sign of premature failure of the specimen. It is questionable why specimens of this configuration ruptured outside the gage area, whereas specimens with a single reinforced layer ruptured correctly. The strength of the specimen was approximately 150 MPa.

Fig. 3 Ruptured specimen. Fracture in the shoulder region

Therefore, the authors proposed a modification of the reinforcement arrangement, aiming to eliminate the presence of fibres in the shoulder area (Fig. 4). The purpose was to eradicate the presence of fibre ends in the area, as they contribute to the occurrence of stress concentrations.

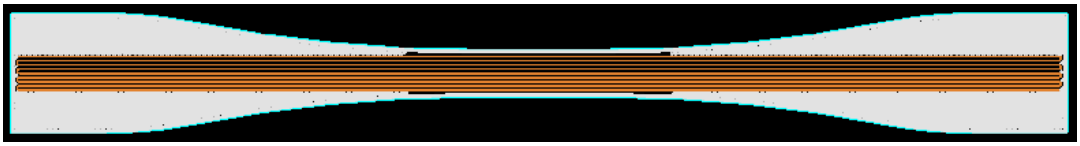

Fig. 4 Specimen with long fibres arranged in part bounded by gage region

In each tensile test, the specimen with this arrangement of long glass fibers consistently ruptured in the gage area (Fig. 5).

Fig. 5 Fracture of the specimen in the gage region

At the same time, compared to the previous fiber arrangement, the specimens achieved significantly higher strength, up to 180 MPa.

CONCLUSION

The study aimed to identify a suitable arrangement of long glass fibres in the composite structure of a specimen intended for tensile testing. According to the results, only specimens with long fibres deposited in a plane bounded by the narrowest part of the specimen (without the presence of fibres in the shoulder area) led to failure in the gage region. Also, these specimens achieved the highest tensile strength. In the future, the authors will investigate whether this fibre arrangement is suitable for more brittle fibre types (such as carbon fibres) or specimens with higher fibre volume fractions (more than 50%).

ACKNOWLEDGEMENT

The work has been supported by the grant project KEGA 005ŽU-4/2024 and Grant system UNIZA project No. 18728.

REFERENCES

[1] A. Al Rashid, S.A. Khan, S.G. Al-Ghamdi, M. Koç. Additive manufacturing: Technology, applications, markets, and opportunities for the built environment. *Autom. Constr.* **2020**, 118, 1-20. DOI: https://doi.org/10.1016/j.autcon.2020.103268

[2] G.D. Goh, Y.L. Yap, S. Agarwala, W.Y. Yeong. Recent progress in additive manufacturing of fiber reinforced polymer composite. *Adv. Mater. Technol.* **2019**, 4 (1), 1-22. DOI: https://doi.org/10.1002/admt.201800271

[3] A. Haleem, M. Javaid. Additive Manufacturing Applications in Industry 4.0: A Review. *J. Ind. Integr. Manag.* **2019**, 4 (4). DOI: https://doi.org/10.1142/S2424862219300011

[4] J. Wong, A. Altassan, D.W. Rosen. Additive manufacturing of fiber-reinforced polymer composites: A technical review and status of design methodologies. *Composites Part B: Engineering* **2023**, 255, 1-17. DOI: https://doi.org/10.1016/j.compositesb.2023.

[5] B. Fazlali, S.V. Lomov, Y. Swolfs. Reducing stress concentrations in static and fatigue tensile tests on unidirectional composite materials: A review. *Composites Part B: Engineering* **2024**, 273, 1-11. DOI: https://doi.org/10.1016/j.compositesb.2024.

APPLIED MECHANICS 2024

April 17th – 19th, 2024
Hotel Toliar, Štrbské Pleso
Slovakia

MEASUREMENT OF MECHANICAL PROPERTIES OF ALLOY STEEL UNDER IMPACT LOADING

M. MÁNEK[1]*, M. FUSEK[2]

The article describes the measurement of the mechanical properties of steel 42CrMo4+QT with using the Split Hopkinson pressure bar apparatus. This method is used for testing material properties under high strain rate in range of approximately 10^2 - 10^4 s^{-1}. Based on measured data for four different strain rates were set parameters for Cowper-Symonds material model for FEM analyses. The test was simulated with the use of Ansys explicit solver and the set material parameters and results were compared.

Keywords: Split Hopkinson bar; high strain rate; explicit solver; steel 42CrMo4; Cowper-Symonds strength

INTRODUCTION

The alloy steel 42CrMo4+QT is one of the most used materials for high-loaded parts like a race car chassis. The chassis must connect the car parts together and withstand the load. In the event of an accident, it must protect the driver. The crash analyses were the topic of the diploma thesis at our department. For accurate computational model, it is necessary to know accurate material parameters which respect variable strain rate during analysis. For measurement of material behavior in applications where wave propagation of stress and inertia effect of material cannot be neglected, it is appropriate to use the Split Hopkinson bar. With this method behavior can be measured under strain rate in range 10^2 – 10^4. The use of bar for measurement of mechanical properties was reported by B. Hopkinson [1]. The current form of test was designed by H. Kolsky [2].

SPLIT HOPKINSON PRESSURE BAR

The Split Hopkinson Pressure Bar apparatus consists of incident and transmitted coaxially mounted bars, gas gun with striker and strain gauges on the bars (Fig. 1). The specimen is sandwiched between the bars. The striker is accelerated by compressed air in the gas gun. It impacts the frontal face of incident bar and generates an incident stress pulse, which travels along the bar. The pulse reaches the interface between incident bar and specimen, and part of the pulse is transferred to transmitted bar, and the rest is reflected. The amplitude of the pulse depends on the striker velocity. Pulses are measured by strain gauges, amplified, and recorded to the digital oscilloscope.

[1] **Ing. Martin Mánek,** Department of Applied Mechanics, Faculty of Mechanical Engineering, VSB – Technical University of Ostrava, 17. listopadu 2172/15, Ostrava, Czech Republic; martin.manek@vsb.cz
[2] **doc. Ing. Martin Fusek PhD.**, Department of Applied Mechanics, Faculty of Mechanical Engineering, VSB – Technical University of Ostrava, 17. listopadu 2172/15, Ostrava, Czech Republic; martin.fusek@vsb.cz

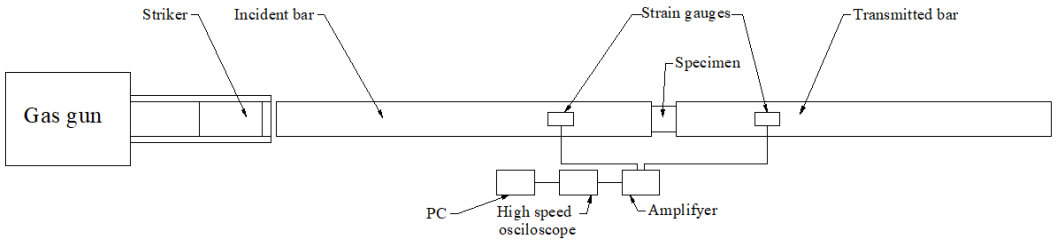

Fig. 1 Split Hopkinson Pressure bar apparatus

The stress σ(t), strain ε(t) and strain rate $\dot{\varepsilon}(t)$ in the specimen can be directly evaluated from recorded reflected and transmitted waves in the bars.

$$\sigma(t) = \frac{A_b \cdot E}{A_s} \cdot \varepsilon_t(t), \tag{1}$$

$$\dot{\varepsilon}(t) = \frac{2 \cdot c_b}{l_s} \cdot \varepsilon_r(t), \tag{2}$$

$$\varepsilon(t) = \frac{2 \cdot c_b}{l_s} \cdot \int_0^t \varepsilon_r(t)dt. \tag{3}$$

Where A_b is the cross section of the incident and transmitted bars, E is Young´s modulus of the bars, A_s is the cross section of the specimen, c_b is the velocity of wave propagation in the bars, l_s is length of the specimen, ε_r is reflected pulse and ε_t is transmitted pulse.

EXPERIMENT

For the experiment, a set of 16 circular specimens, 12 with length 10 mm and diameter 10 mm and 4 with length 5 mm and diameter 10 mm. In the gas gun 3 different pressures, 5, 10 and 13 bars were set. The striker with length of 200 mm were used. The impact velocity for each pressure is shown in Tab. 1.

Tab. 1 Striker velocity

Pressure [bar]	Striker velocity [m/s]
5	18.5
10	26.1
13	30

The strain waves were recorded in the oscilloscope. The reflected and transmitted waves were separated for evaluation of stress, strain and strain rate for each specimen (Fig. 2). The third order Savitzky-Golay filter with window length 499 was used because of the noise in raw signal [3]. Using equations (1), (2) and (3), the stress strain curves for each strain rate were evaluated (Fig. 3). The strain rate for each set of specimens is shown in Tab. 2.

Tab. 2 Strain rate for specimens

Specimen length [mm]	Initial pressure [bar]	Strain rate [s^{-1}]
10	5	695
	10	1256
	13	1593
5	13	2662

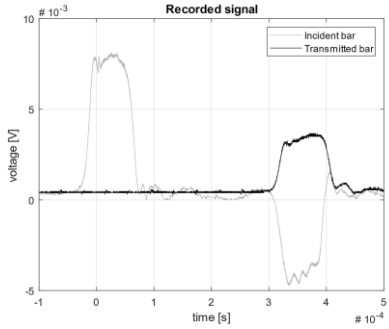

Fig. 2 Recorded signal

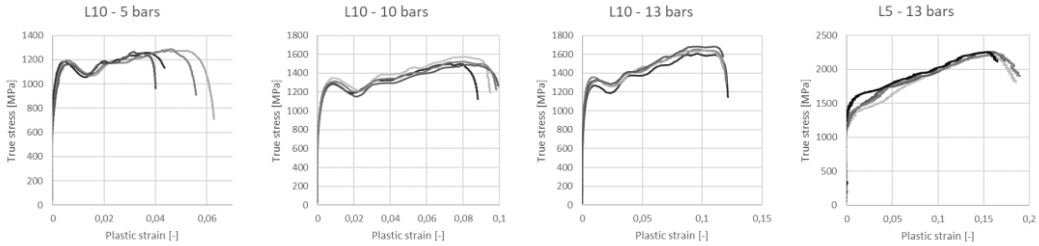

Fig. 3 Stress-strain curves

COWPER-SYMONDS CONSTITUTIVE MODEL

The Cowper-Symonds strength is one of the most widely used simple material models for strain rate dependent analysis. This model consists of a part for strain hardening and strain rate hardening. For the fit of strain rate hardening the tensile tests with strain rate 0.002 s^{-1} were performed. The model defines stress as [4, 5]:

$$Y = \left(A_0 + B \cdot \varepsilon_{pl}^{n}\right) \cdot \left[1 + \left(\frac{\dot{\varepsilon_{pl}}}{D}\right)^{\frac{1}{q}}\right]. \tag{4}$$

Where A_0 is quasi-static yield stress, B and n are strain hardening parameters, $\dot{\varepsilon}_{pl}$ is effective plastic strain rate, and D and q are strain rate hardening parameters.

From the quasi-static tensile test only the reference yield stress (Yref) was evaluated. The fit of the strain hardening parameters was done for each test and the parameters were averaged. Strain rate constants were fit from yield stress for each strain rate (Fig. 4). Material parameters are in Tab. 3.

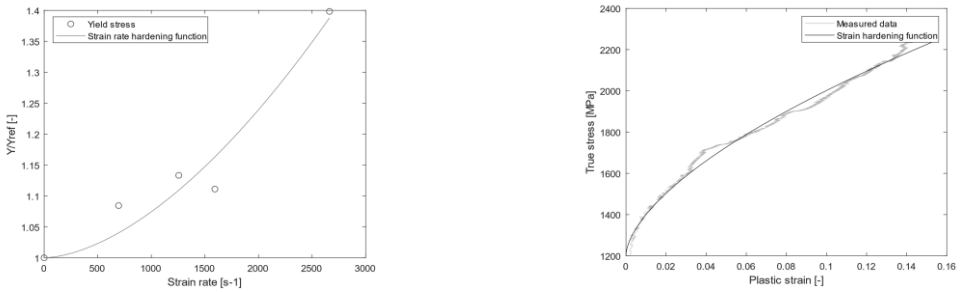

Fig. 4 Fitting of material parameters

Tab. 3 Cowper-Symonds material parameters

A_0 [MPa]	B [MPa]	n [-]	D [s^{-1}]	q [-]
900	4000	0.8	5376	0.759

FINITE ELEMENT ANALYSES

Simulation of the experiment with set material model was performed using Ansys Explicit solver [4]. The analyzes were done for each strain rate. The computational model was prepared according to the dimensions of the test device. The striker velocity was set according to the pressure in the gas gun. The stress strain curves of the experiment and the FEA were compared (Fig. 5).

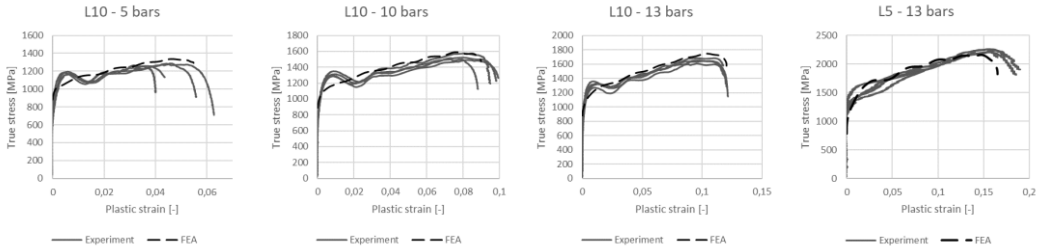

Fig. 5 Experiment and FEA comparison

CONCLUSION

In the paper is shown Split Hopkinson Pressure bar test of steel 42CrMo4+QT for computation analyses of race car crash test. The material was tested under impact loading with four different strain rates. With the measured data and added tensile test data, the coefficients of the Cowper-Symonds material model were found. With the use of Ansys Explicit solver, the computational analyzes were performed. The results from the analyzes and measurement were compared. It is obvious that the material model underestimated the stress just behind the yield stress for the strain rates 695 s^{-1} and 1256 s^{-1}. For the rest of the curves, the model follows measured data.

ACKNOWLEDGEMENT

This work has been supported by Specific Research „Experimental and Numerical Modeling for Solving Problems in Mechanics and Biomechanics“ (SP2024/037).

REFERENCES

[1] B. Hopkinson. X. A method of measuring the pressure produced in the detonation of high, explosives or by the impact of bullets. *Philosophical Transactions of the Royal Society of London. Series A*, Mathematical, Physical and Eng. Sci. **1914**, 213, 437-456. http://doi.org/10.1098/rsta.1914.0010

[2] H. Kolsky. An Investigation of the Mechanical Properties of Materials at Very High Rates of Loading. *Proceedings of the Physical Society. Section B* **1949**, 62, 676-700. http://dx.doi.org/10.1088/0370-1301/62/11/302

[3] R.W. Schafer. What Is a Savitzky-Golay Filter? [Lecture Notes] *IEEE Signal Processing Magazine* **2011**, 28 (4), 111-117. DOI: 10.1109/MSP.2011.941097

[4] Ansys Explicit Dynamics Analysis Guide. Southpointe, July 2022.

[5] G. Cowper, P. Symonds. Strain hardening and strain-rate effects in the impact loading of cantilever beams. Tech. Rep., Brown University Division of Applied Mathematics, 1957.

APPLIED MECHANICS 2024

April 17th – 19th, 2024
Hotel Toliar, Štrbské Pleso
Slovakia

ADDITIVE MANUFACTURING OF MULTIMATERIAL MEDICAL DEVICES (3D PRINTED ANKLE-FOOT-ORTHOSIS)

K. MENDOVÁ[1]*, O. ZOUFALÝ[2], P. RŮŽIČKA[3], R. SEDLÁČEK[4], M. DANIEL[5]

The aim of this research is to develop an innovative type of lower limb orthosis using 3D printing technology. Digital orthotics and intricate design capabilities are utilized to improve comfort, functionality, and aesthetics. The focus is on optimizing 3D printed ankle-foot orthoses (AFOs) to improve stability, gait pattern, and reduce muscle fatigue, specifically for children with cerebral palsy.

Keywords: additive manufacturing; AFO (ankle foot orthosis); mechanical testing; mechanical properties

INTRODUCTION

Ankle-foot orthoses (AFOs) are biomechanical devices applied externally to the lower limbs, aimed at stabilizing joints and enhancing the gait and physical functionality of the affected limb. Using digital orthotics and 3D printing technology, we aim to improve the comfort, functionality, aesthetics and usability of orthoses for children with cerebral palsy [1]. We use intricate designs to provide tailored solutions and incorporate modern principles into orthosis design. Multi-material 3D printing is transforming traditional manufacturing methods, resulting in increased functionality and stability. It enables the production of complex and functional parts with varying properties, textures, and colors in a single printing process. To fully utilize the potential of multi-material 3D printing, it is essential to have a thorough understanding of how material integration affects the desired properties and overall quality of orthoses.

[1] **Ing. Katarína Mendová**, Department of Mechanics, Biomechanics and Mechatronics, Faculty of Mechanical Engineering, Czech Technical University in Prague, Technická 4, Prague 6, Czech Republic; katarina.mendova@fs.cvut.cz
[2] **Ing. Ondřej Zoufalý**, Department of Mechanics, Biomechanics and Mechatronics, Faculty of Mechanical Engineering, Czech Technical University in Prague, Technická 4, Prague 6, Czech Republic; ondrej.zoufaly@fs.cvut.cz
[3] **Ing. Pavel Růžička, PhD.**, Department of Mechanics, Biomechanics and Mechatronics, Faculty of Mechanical Engineering, Czech Technical University in Prague, Technická 4, Prague 6, Czech Republic; pavel.ruzicka@fs.cvut.cz
[4] **doc. Ing. Radek Sedláček, Ph.D**, Department of Mechanics, Biomechanics and Mechatronics, Faculty of Mechanical Engineering, Czech Technical University in Prague, Technická 4, Prague 6, Czech Republic; radek.sedlacek@fs.cvut.cz
[5] **Prof. RNDr. Matej Daniel, Ph.D.**, Department of Mechanics, Biomechanics and Mechatronics, Faculty of Mechanical Engineering, Czech Technical University in Prague, Technická 4, Prague 6, Czech Republic; matej.daniel@cvut.cz

MANUFACTURING AND MECHANICAL TESTING OF MULTI-MATERIAL STRUCTURES

The possibility of integrating a metallic material into an additively manufactured polymer part was verified experimentally. The design of the experiment was inspired by a test procedure for testing the shear strength of bonded joints.

Sample preparation

The metal sample used was a flat part with dimensions of (114 x 25 x 2) mm produced by DMLS additive manufacturing in Ti6Al4V alloy, commonly used in medical technology, on the M2 machine (Concept Laser, now GE Additive). The polymer part was made using FDM technology on a Fortus 450mc machine (Stratasys). The design of the polymer part was also based on a flat prism (114 x 25 x 2) mm. The metal sample was inserted into the polymer structure during the additive manufacturing process. The overmold of polymer and metal was 25 mm long and the overmold area was 625 mm2. Two polymer materials were tested, namely: polycarbonate FDM PC-ISO (Stratasys), translucent, biocompatible, and polyamide FDM Nylon 12 (Stratasys), black (Fig. 1).

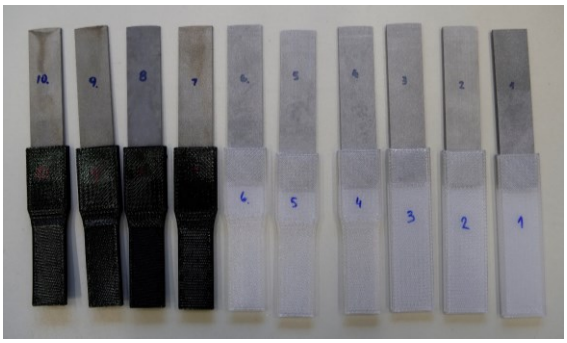

Fig. 1 Samples for shear strength test of Ti6Al4V - polymer interface

Mechanical testing

The MTS Minibionix test rig was used to test the strength of the bond between the Ti alloy and the polymer. The Ti alloy-polymer interface was subjected to shear stress during the tensile stress test. Controlled sliding was carried out at a constant rate of 1 mm/min for samples 1 to 7 and 5 mm/min for samples 8 to 10 until failure. The loading rate was increased for specimens 8 to 10 to ensure completion of the test within 1 minute.

DESIGN OF HIGH AFO

A prototype of high AFO was designed in Blender to serve patients with more severe forms of polio. The design was based on a low AFO model (Fig. 2 left), with added reinforcement to attach a spring to the orthosis. The design also includes space to accommodate the Achilles tendon. Perforations were added to reduce the weight of the ortosis, and holes were included for attaching fasteners. The high ortosis (Fig. 2 right) comprises a spring and a sleeve for attachment in the calf area. The sleeve has perforations to reduce weight and soften the structure. Reinforced areas with perforations are included for fastening the sleeve around the calf. A reinforcing structure is located at the rear of the sleeve to hold the spring, which can be printed in titanium and come in different shapes and stiffnesses.

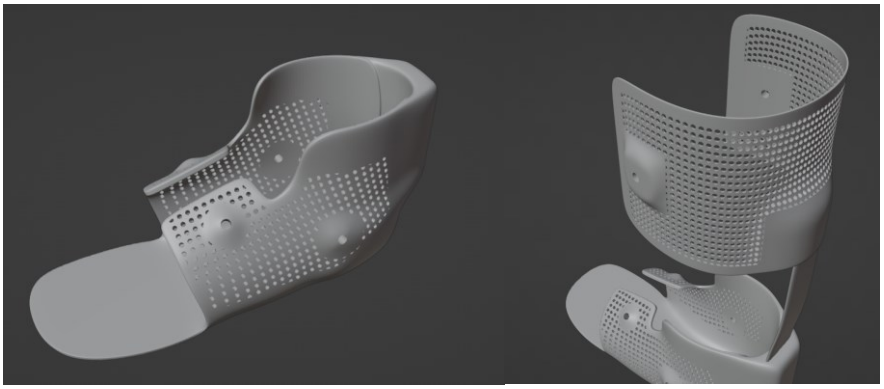

Fig. 2 Lower part of the high AFO (left), Sleeve and clamp for the spring for high AFO (right**)**

RESULTS

Tab. 1 Mechanical properties of tested materials

Material	Young´s modulus [GPa]	Tensile strength [MPa]
FDM PC-ISO	2,00	57
FDM Nylon 12	1,51	33
Ti6Al4V	114,80	1 085

Tab. 2 Maximum achieved force and shear stress between FDM PC - Ti6Al4V

Materials	**FDM PC-ISO (Stratasys) – Ti6Al4V**	
Sample	**Max. force achieved [N]**	**Max. shear stress [MPa]**
1	975,9	1,6
2	556,7	0,9
3	386,6	0,6
4	777,0	1,2
5	522,6	0,8
6	862,1	1,4
Average	**680,2**	**1,1**
Standard deviation	**226,4**	**0,4**
Standard deviation	**33,3 %**	**33,3 %**

Tab. 3 Maximum achieved force and shear stress between FDM Nylon 12 - Ti6Al4V

Materials	**FDM Nylon 12 (Stratasys) – Ti6Al4V**	
Sample	**Max .force achieved [N]**	**Max. shear stress [MPa]**
7	1 835,7	2,9
8	1 880,8	3,0
9	1 136,7	1,8
10	1 527,6	2,4
Average	**1 595,2**	**2,6**
Standard deviation	**343,6**	**0,5**
Standard deviation	**21,5 %**	**21,5 %**

Fig. 3 Prototype of high AFO orthosis with leg and calf casting

CONCLUSION

The complexity of 3D printed orthoses surpasses handmade AFO orthoses. We have now developed an automated process to create 3D models of AFOs exactly to measure. In the future, we plan to conduct gait analysis experiments involving both healthy children and children with cerebral palsy. Our goal is to assess changes in gait patterns in children with disabilities who transition from not wearing AFOs to wearing them, and thus improve their quality of life.

ACKNOWLEDGEMENT

The work has been supported by the grant project TM02000060 - Applied research on design principles and development of additive manufacturing of multimaterial medical devices.

REFERENCES

[1] E. Wright, S.A. DiBello. Principles of Ankle-Foot Orthosis Prescription in Ambulatory Bilateral Cerebral Palsy. *Physical Medicine and Rehabilitation Clinics of North America* **2020**, 31 (1), 69-89. ISSN 10479651

APPLIED MECHANICS 2024

April 17th – 19th, 2024
Hotel Toliar, Štrbské Pleso
Slovakia

COMPARISON OF THE INTERNAL DAMPING OF COMPOSITE SPECIMENS REINFORCED WITH KEVLAR FIBRES

P. MICHAL [1]*, M. VAŠKO[2], M. SAPIETA[3]

This paper deals with the comparison of the internal damping of a composite specimen reinforced with Kevlar fibres. The object of the experiment is to observe the changes in stiffness due to the changing internal structure of the specimen. The change in structure is provided by changing the orientation of the reinforcing Kevlar fibres in five configurations.

Keywords: Composite material; Kevlar fibres; dynamic properties; interface damping

INTRODUCTION

Composite materials are becoming an integral part of everyday life thanks to their unique properties, which find applications in almost all sectors, from technical to scientific, medical to sports. However, these properties can be influenced by a number of factors, including the material of the reinforcing fibres and their orientation.

Damping within composite materials has its own specific characteristics. The internal structure of the material and the subsequent distribution of physical fields within the material are the basis for the macrostructural response [1]. The main sources of internal damping are microplastic or viscoelastic phenomena at the interface between the matrix and the reinforcement, manifested in the form of relative displacements [2].

Interfacial damping results from frictional and adhesive interactions where vibration and mechanical energy dissipation occurs. This type of damping affects key properties of the composite, such as strength and damping capabilities, and can increase the material's resistance to fatigue damage. Influencing interface damping can be achieved by modifying the orientation and distribution of the reinforcing fibres, which fundamentally affects the vibration transmission behaviour of the composite. Adhesion at the interface, the presence of defects such as cracks, the overall microstructure, as well as the type and properties of the components and mechanical stresses are other factors that have a significant influence on interface damping [3].

[1] **Ing. Pavol Michal**, Department of Applied Mechanics, Faculty of Mechanical Engineering, University of Žilina, Univerzitná 8215/1, Žilina, Slovak republic; pavol.michal@fstroj.uniza.sk
[2] **doc. Ing. Milan Vaško, PhD.**, Department of Applied Mechanics, Faculty of Mechanical Engineering, University of Žilina, Univerzitná 8215/1, Žilina, Slovak republic; milan.vasko@fstroj.uniza.sk
[3] **Ing. Milan Sapieta, PhD.**, Department of Applied Mechanics, Faculty of Mechanical Engineering, University of Žilina, Univerzitná 8215/1, Žilina, Slovak republic; milan.sapieta@fstroj.uniza.sk

SAMPLE AND EXPERIMNET PREPARATION

A Markforged 3D printer, model Mark Two, was used to create the samples. This type of printer applies FFF (Fused Filament Fabrication) technology, which allows the precise deposition of reinforcing filaments of different materials in a selected arrangement. With this printing technique, we were able to set the specific orientation of the filaments in each sample, allowing us to assess what effect the different filament arrangements have on the damping properties of the specimen.

The specimens are made in two variations and five configurations of fibre arrangement. The first configuration has fibres arranged in the longitudinal direction (0°), the second configuration has fibres arranged at an angle of 45° to the longitudinal axis, the third configuration has fibres arranged in the transverse direction (90°), the fourth configuration has fibres arranged alternately at an angle of ±45°, and the fifth configuration has fibres arranged alternately in both the longitudinal and transverse directions (0°,90°). The first variant of the specimens is made without perimeter reinforcing fibres and the second variant of the specimens has two layers of reinforcement around the perimeter of the reinforcing layers.

In all configurations, the same external geometry and the same volume ratio of matrix to reinforcement of approximately 1:1 is maintained. The overall dimensions of the specimens are 320 mm in length, 20 mm in width,2.5 mm in thickness and the total number of printing layers is 25 of which 14 layers are reinforcement and 11 layers are matrix. The specific layout and orientation of the layers is shown in Table 1 and Table 2.

Tab. 1 Layout of specimen layers

Layer	Specimen	Number of layers
Matrix	Onyx	4
Reinforcement	Kevlar fiber	7
Matrix	Onyx	3
Reinforcement	Kevlar fiber	7
Matrix	Onyx	4

Tab. 2 Reinforcement configuration

Layer	Config. 1	Config. 2	Config. 3	Config. 4	Config. 5
Matrix	±45°	±45°	±45°	±45°	±45°
Reinforcement	0°	45°	90°	±45°	0°,90°
Matrix	±45°	±45°	±45°	±45°	±45°
Reinforcement	0°	45°	90°	±45°	0°,90°
Matrix	±45°	±45°	±45°	±45°	±45°

The experiment was performed by the impact method. An oscillation was built up using a dynamic hammer, and the response of the specimen was sensed with an accelerometer, from which the frequency response was subsequently determined. The analysed signal was processed in the BK Connect software, where several measurements were averaged. The resulting data was then exported to the MATLAB environment where calculations were performed to determine the damping coefficient.

ANALYSIS RESULTS

To calculate the internal damping coefficient, we used the 3dB droop method. Using this method, we arrived at the results from the frequency response graph (Fig. 1, Fig. 2) in a quick and easy way. In the MATLAB, we determined the first natural frequencies of each specimen using the following relations (1) and extracted from them the frequencies f1 and f2 located in the middle of the given peak. From the next equations, we determined the Q amplification factor and then the damping coefficient ζ.

The result of the experiment is a diagram of the frequency response of the material in which we analysed the first natural frequencies. For the specimens without perimeter reinforcement with fibre orientation of 45°, 90° and ±45°, the natural frequencies ranged from 30Hz to 32.5Hz and the specimens with fibre orientation of 0° and 0°,90° have natural frequency values of 72.5Hz and 65.5Hz (Fig. 1). For the specimens with perimeter reinforcement, the natural frequencies reached values ranging from 51Hz to 71.5Hz (Fig. 2).

By examining the damping results obtained from the MATLAB analysis, we found that the specimens without perimeter reinforcement have the highest damping coefficient values, except for the specimen with 0° fibre orientation. This is due to the lower proportion of longitudinal fibers compared to the specimen without perimeter fibre reinforcement. The highest damping coefficient (0.1311) was achieved by the specimen with 90° fibre orientation with the other specimens achieving significantly lower values. The specimens with 45° and ±45° reinforcement orientation achieved damping coefficient values of 0.0922 and 0.0821, respectively. And the lowest damping coefficient values were achieved by the specimens with 0° (0.0278) and 0°, 90° (0.0357) reinforcement orientation. The specimens with perimeter reinforcement have significantly lower variance of damping coefficient values than the specimens without perimeter reinforcement. For the specimens, the damping coefficient ranges from 0.0291to 0.0443. The maximum damping value is at a reinforcement orientation of ±45° and the minimum damping value is at a fibre orientation of 0°,90°. A detailed summary of the damping coefficient values is given in Table 3 and shown graphically in Figure 3.

$$\zeta = \frac{1}{2Q}, \quad Q = \frac{f_n}{\Delta f}, \quad \Delta f = f_1 - f_2 \tag{1}$$

where f_n is natural frequency, f_1, f_2 are frequencies extracted from the amplitude $\frac{A_{max}}{2}$

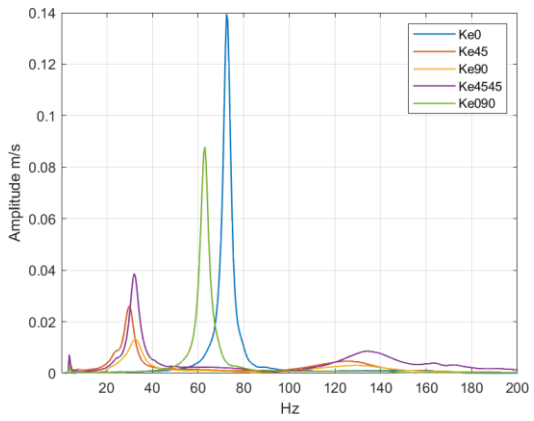

Fig. 1 Graph of frequency response without perimeter reinforcement

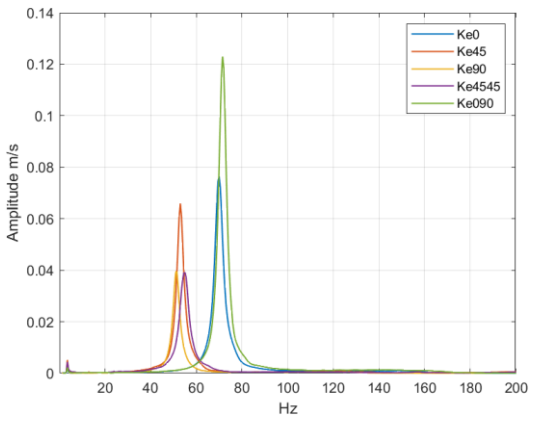

Fig. 2 Graph of frequency response with perimeter reinforcement

Tab. 3 Damping ratio ζ for different fibre orientations

Angle	0°	45°	90°	±45°	0°,90°
without perimeter reinforcement	0,0278	0,0922	0,1311	0,0821	0,0357
with perimeter reinforcement	0,0321	0,0354	0,0364	0,0443	0,0291

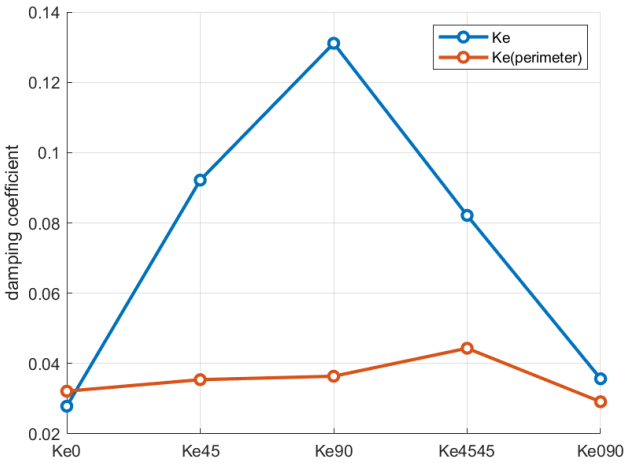

Fig. 3 Damping coefficient comparison

CONCLUSION

The experimental results show that changing the orientation of the reinforcing fibres in the composite material significantly affects the damping capabilities of the structure. We found that fibres oriented perpendicularly or at an angle of 45° with respect to the longitudinal direction exhibit higher damping capacity than fibres oriented in the longitudinal direction.

Further, we found that adding perimeter reinforcement and hence increasing the number of longitudinal fibres significantly reduces the overall damping and also reduces the difference in damping coefficient values between the different reinforcement configurations.

ACKNOWLEDGEMENT

The authors would like to thank their colleagues from the Department of Applied Mechanics at the Technical University of Ostrava for their cooperation in carrying out the experiments. This work has been supported by the grant project KEGA 005ŽU-4/2024.

REFERENCES

[1] V. Tita, J.D. Carvalho, J. Lirani. A procedure to estimate the dynamic damped behavior of fibre reinforced composite beams submitted to flexural vibrations. *Materials research* **2001**, 4 (4), 315-321.

[2] R. Greif, B. Hebert. Experimental techniques for dynamic characterization of composite materials. *Advances in Experimental Mechanics and Biomimetics* **1992**, AD-49/AMD-146, 83-97.

[3] T.H. Fay. Coulomb damping. *International Journal of Mathematical Education in Science and Technology* **2012**, 43 (7), 923-936. DOI: 10.1080/0020739X.2011.633624

APPLIED MECHANICS 2024

April 17th – 19th, 2024
Hotel Toliar, Štrbské Pleso
Slovakia

THE USE OF DATA DRIVEN EVOLUTIONARY ALGORITHMS FOR SAFE DESIGN OF INTEGRALLY WOUND COMPOSITE PRESSURE VESSEL

Z. PADOVEC[1]*, D. VONDRÁČEK[2], T. MAREŠ[3], N. CHAKRABORTI[4]

Presented work deals with the use of two data driven evolutionary algorithms. Evolutionary Deep Neural Nets (EvoDN2) which creates surrogate model of investigated problem - design of integrally wound composite pressure vessel for maximal pressure according to Hoffman strength criterion and minimize dimensions of end dome and failure indexes in the cylinder/dome joint and in dome itself. This problem leads to multi-criteria optimization with two design/variable functions and eleven objective/cost functions. Optimization itself was done with the use of Constrained Reference Vector Algorithm (cRVEA).

Keywords: pressure vessels; composite materials; optimization; filament winding; data-driven evolutionary algorithms

INTRODUCTION

Most studies dealing with optimal design of filament wound composite pressure vessel are focused only on its individual parts. There are studies aimed at finding the optimal shape of the end dome [1, 2], the optimal design of cylindrical part [3, 4] or the optimum design of junction area between cylindrical part and end dome [5, 6]. However, there may be some situations where the optimum of selected parameters is found (the optimal end dome shape is found, for example) but the resulting pressure vessel may still fail. This is because there is a lack of information about what is happening in the other important parts of the pressure vessel (the cylindrical part for example) which are not considered in such optimization processes. Therefore, it is essential to design a safe pressure vessel to consider all areas where the failure can potentially occur. However, this complex approach is not currently used in many pressure vessel optimization tasks. This work aims to eliminate this deficiency and elaborates a possible strategy of designing an optimal pressure vessel that will not

[1] **Ing. Zdeněk Padovec, Ph.D.**, Department of Mechanics, Biomechanics and Mechatronics, Faculty of Mechanical Engineering, CTU in Prague, Technická 4, Prague 6, Czech Republic; zdenek.padovec@fs.cvut.cz
[2] **Ing. Dominik Vondráček**, Department of Mechanics, Biomechanics and Mechatronics, Faculty of Mechanical Engineering, CTU in Prague, Technická 4, Prague 6, Czech Republic; dominik.vondracek@fs.cvut.cz
[3] **Doc. Ing. Tomáš Mareš, Ph.D.**, Department of Mechanics, Biomechanics and Mechatronics, Faculty of Mechanical Engineering, CTU in Prague, Technická 4, Prague 6, Czech Republic; tomas.mares@fs.cvut.cz
[4] **PhDr. Nirupam Chakraborti.**, Department of Mechanics, Biomechanics and Mechatronics, Faculty of Mechanical Engineering, CTU in Prague, Technická 4, Prague 6, Czech Republic; nirupam.chakraborti@fs.cvut.cz

fail. It is based upon authors' previous works [7, 8] that involved data-driven evolutionary multi-objective optimization [9] and further extends them.

DESCRIPTION OF THE PROBLEM

Filament wound composite pressure vessel of type IV was considered manufactured by means of filament winding, which is loaded with internal pressure and consists of cylindrical part and end dome as indicated in Fig. 1. The equator radius of the dome $R = 500$ mm and radius of polar opening $r_0 = 200$ mm was considered for all analyzed cases. The cylindrical part is used as main storage space of the pressure vessel, and it is manufactured from three layers - the balanced layer wound at winding angle $\pm\omega_0$ and two symmetrically placed monolayers wound at winding angle $\omega_1 = 90°$. The end dome itself is manufactured only from the balanced layer and is primarily used to seal the pressure vessel. As in the previous studies [7, 8], the elliptical shape of the end dome is considered here. This shape is defined by the radius at the equator R and size of the semi-minor axis x.

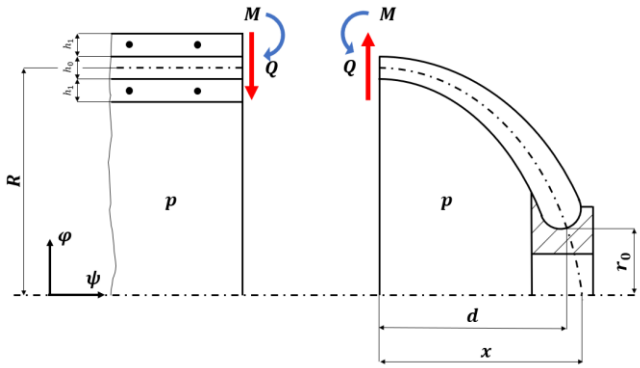

Fig. 1 Considered pressure vessel

The junction area is affected by internal shear force Q per unit length and internal bending moment M per unit length as shown in Fig. 1 which are causing additional membrane and bending stresses which are added to membrane stress caused by internal pressure. this superposition also defines the critical places in the junction as indicated in Fig. 2. In general, there are eight critical places in the junction: six in the cylindrical part and two in the end dome. The resulting stresses in each critical place are further used for failure index analysis. This analysis allows simple and fast determination of whether the analyzed place meets the selected strength criterion or not. If the value of the failure index in the analyzed place is lower than 1 then it will comply and if it is higher than 1, then the place will fail. All the failure indices in this study were computed using Hoffman's strength criterion which well reflects the real properties of the composite. The Hoffman's strength criterion can be expressed as

$$U = \frac{\sigma_L^2}{F_{Lt}\,F_{Lc}} + \frac{\sigma_T^2}{F_{Tt}\,F_{Tc}} - \frac{\sigma_L\,\sigma_T}{F_{Lt}\,F_{Lc}} + \frac{F_{Lc}-F_{Lt}}{F_{Lt}\,F_{Lc}}\,\sigma_L + \frac{F_{Tc}-F_{Tt}}{F_{Tt}\,F_{Tc}}\,\sigma_T + \frac{\tau_{LT}^2}{F_{LT}^2}., \tag{1}$$

where σ_L is stress in longitudinal direction, σ_T is the stress in the transversal direction, τ_{LT} is the shear stress, F_{Lt} is longitudinal tensile strength, F_{Lc} is longitudinal compressive strength, F_{Tt} is transversal tensile strength, F_{Tc} is transversal compressive strength and F_{LT} is shear failure strength along fibers.

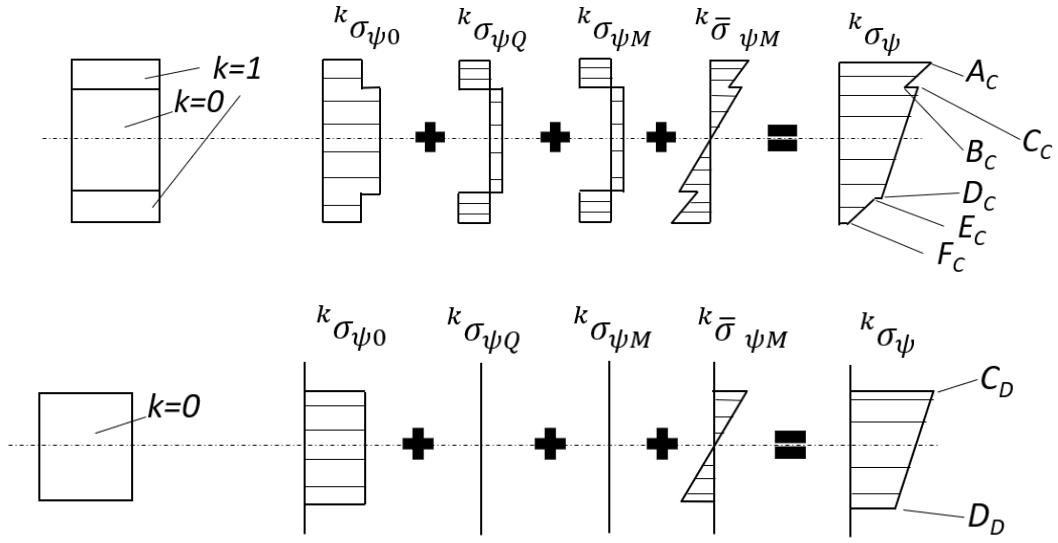

Fig. 2 The example of stress superposition

These eight critical places in the junction, however, do not ensure that the entire pressure vessel will not fail. It can still fail in some point along the meridian curve of the end dome itself. This phenomenon was observed and described in the authors' previous work [8]. For some material systems (especially for carbon-epoxy) it may happen that they will comply at all critical places in the junction, but the pressure vessel will fail somewhere along the meridian of the end dome. Therefore, an additional critical place on the end dome must be added.

OPTIMIZATION

There are nine places in total, which characterize the critical areas of the pressure vessel being analyzed here. If the Hoffman's failure index is lower than 1 in each of these nine places the pressure vessel will not fail. Although these failure indexes ensure that the pressure vessel will be safe, but they are not able to ensure that a pressure vessel designed this way will satisfy all the requirements of any technical applications, in terms of the requirements of the parameters like size of the vessel (especially the depth of the end dome), mass of the vessel or the magnitude of the internal pressure. Therefore, a constrained optimization involving these additional parameters needs to be done. These parameters were same as in the previous studies [7, 8] i.e., minimization depth of the end dome at the polar opening and maximization of the magnitude of internal pressure. The entire optimization task can be expressed mathematically as

$$f(x,p) = \begin{Bmatrix} \min d^2 \\ \min {}^{1}/_{p} \\ \min \mathrm{FI}_{1-8} \\ \min \mathrm{FI}_{\mathrm{dome}} \end{Bmatrix}, \tag{2}$$

where x is the semi-minor axis of the ellipse (see Fig. 1), p is the magnitude of internal pressure, d is the depth of the end dome at the polar opening (see Fig. 1), FI_{1-8} are failure indexes in the junction (see Fig. 2) and FI_{dome} is the maximal failure index along the meridian of the end dome.

Moreover, the sub-conditions were assigned to each objective/cost function. These sub-conditions can be expressed as

$$\begin{gathered} d^2 > 0 \\ {}^1/_p > 0 \\ \mathrm{FI}_{1-8} < 1 \\ \mathrm{FI}_{\mathrm{dome}} < 1 \end{gathered} \tag{3}$$

These sub-conditions make the task stricter, and it is obvious that solving this task with eleven objective functions is quite challenging. It required implementation of intelligent learning through Evolutionary Deep neural net algorithm (EvoDN2) [9] and many objective optimization using constrained Reference vector evolutionary algorithm (cRVEA) [9].

RESULTS AND DISCUSSIONS

The output from the cRVEA optimization module is a Pareto set of optimal solutions in which each member meets the set criteria of the task. They should be plotted in hyperspace with eleven dimensions in this case. However, such a display would not be very clear. Therefore, we chose to plot 2D graph for relationship between internal pressure and depth of the dome (Fig. 3) with numbers and next graph (Fig. 4) with failure indexes corresponding to each solution from Fig. 3. With this approach we can clearly see which solution has better or worse failure index. Plots were done for glass/epoxy system with material parameters from [7, 8].

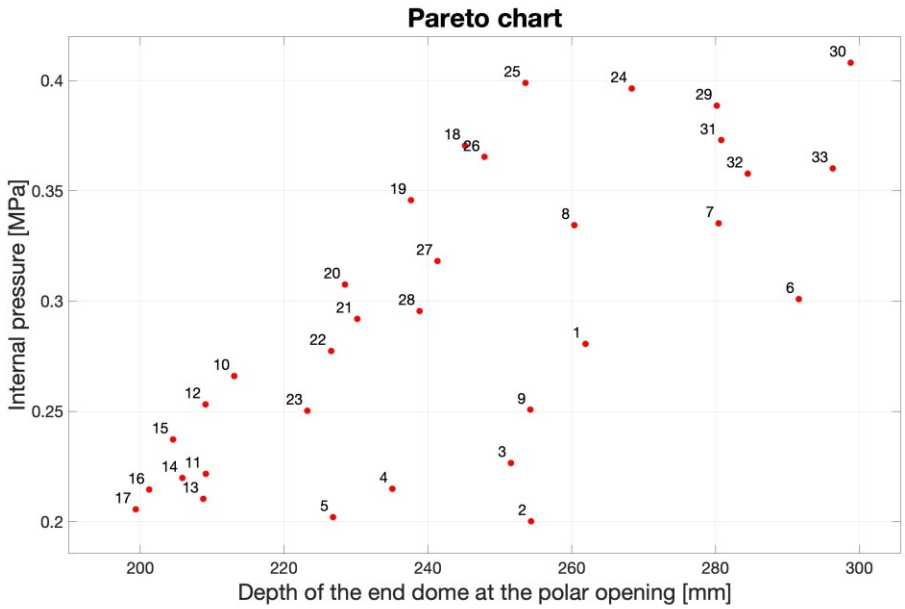

Fig. 3 Pareto chart for glass/epoxy system

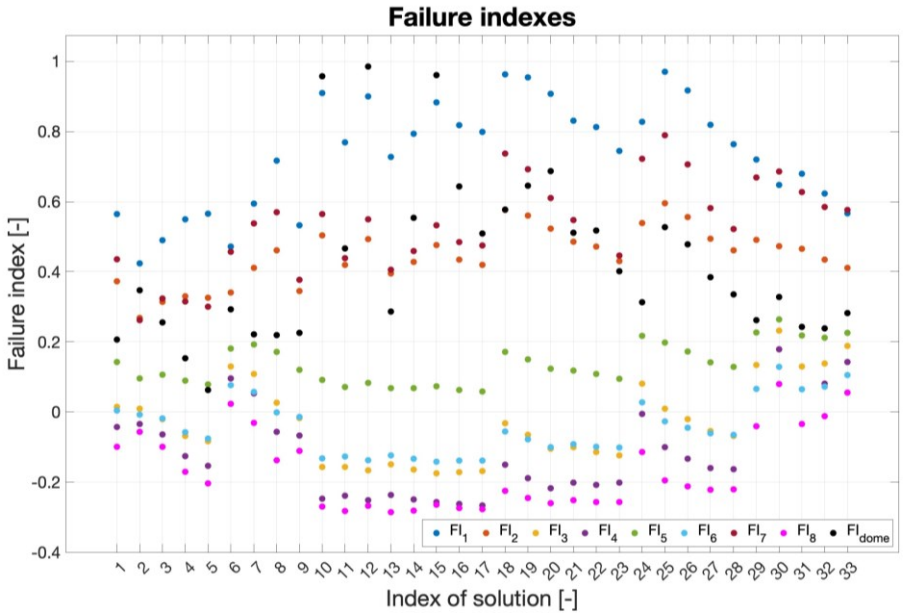

Fig. 4 Failure indexes for glass/epoxy system

The last thing to solve is to determine the optimum. This last step is probably the most complicated because the optimum needs to be chosen depending on the application where the pressure vessel is to be used or at possibilities of the producer and should be done by knowledgeable person. The magnitude of internal pressure has the priority for our purposes because the sub-conditions (see (3)) guarantee that Hoffman's failure indexes are below one. Therefore, the optimum solutions in both material systems were chosen primarily according to this parameter (see Fig. 3 and Fig. 4). These selected optimal solutions are shown with respect to the entire pressure vessel in Fig. 5.

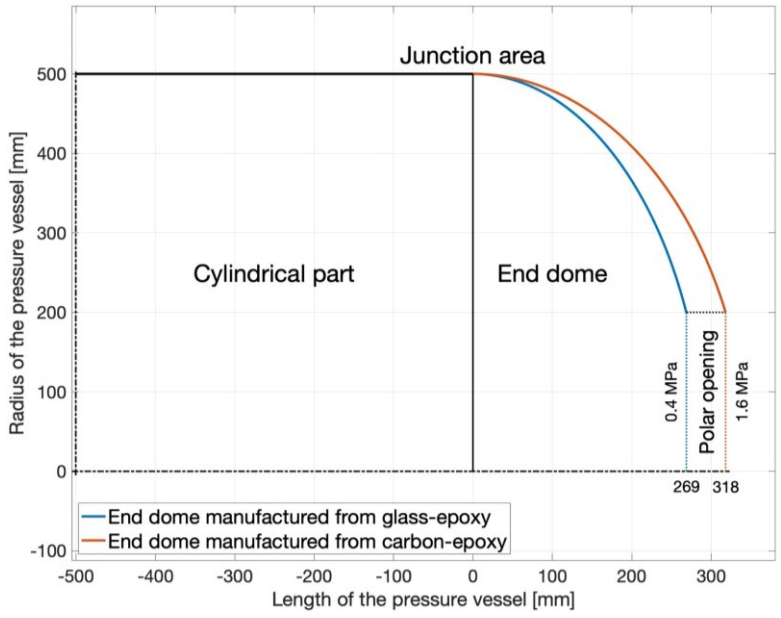

Fig. 5 Illustration of selected optimal solutions on entire pressure vessel

CONCLUSION

This study brings a completely new point of view to design of filament wound composite pressure vessels because the entire pressure vessel is considered during computation. It combines the conventional engineering approaches based on classic lamination theory and data driven evolutionary algorithms, which were used for optimization. The entire computation process was realized in MATLAB software. The optimization task was realized using EvoDN2 (creating surrogate models) and cRVEA (optimization algorithms) and was quite challenging because eleven objective/cost functions needed to be optimized. An output from the optimization are two plots - Pareto chart between depth of the end dome at polar opening and magnitude of internal pressure and chart of failure indexes. The Pareto chart gives a simple way for choosing the best compromise between these two objectives according to the needs of the designer. If the best solution is chosen the values of failure indexes can be easily found in the chart of failure indexes.

ACKNOWLEDGEMENT

This study received support from the Grant Agency of the Czech Technical University in Prague, under grant No. SGS24/123/OHK2/3T/12.

REFERENCES

[1] H. Fukunaga, M. Uemura. Optimum design of helically wound composite pressure vessels. *Composite Structures* **1983**, 1 (1), 31-49. DOI: 10.1016/0263-8223(83)90015-6

[2] M. Hojati, V.S. Ardebili, S.V. Hoa. Design of domes for polymeric composite pressure vessels. *Composite Engineering* **1995**, 5 (1), 51-59. DOI: 10.1016/0961-9526(95)93979-6

[3] C. Liu, Y. Shi. Design optimization for filament wound cylindrical composite internal pressure vessels considering process-induced residual stresses. *Composite Structures* **2020**, 235, 111755. DOI: 10.1016/j.compstruct.2019.111755

[4] J.H.S. Almeida Jr., et al. C. Liu, Y. Shi. Design, modeling, optimization, manufacturing and testing of variable-angle filament-wound cylinders. *Composites Part B: ENgineering* **2021**, 225, 109224. DOI: 10.1016/j.compositesb.2021.109224

[5] K. Jois, et. al. Numerical Analysis of Filament Wound Cylindrical Composite Pressure Vessels Accounting for Variable Dome Contour. *Journal of Composites Science* **2021**, 5 (2), 1-15. DOI: 10.3390/jcs5020056

[6] G. Park, C. Kim. Composite Layer Design Using Classical Laminate Theory for High Pressure Hydrogen Vessel (Type 4). *International Journal of Precision Engineering and Manufacturing* **2023**, 24, 571-583. DOI: 10.1007/s12541-022-00752-w

[7] D. Vondráček, Z. Padovec, T. Mareš, N. Chakraborti. Optimization of dome shape for filament wound pressure vessels using data-driven evolutionary algorithms. *Materials and Manufacturing Processes* **2023**, 38 (15), 1899-1910. DOI: 10.1080/10426914.2023.2187823

[8] D. Vondráček, Z. Padovec, T. Mareš, N. Chakraborti. Analysis and Optimization of Junction between Cylindrical Part and End Dome of Filament Wound Pressure Vessels Using Data Driven Evolutionary Algorithms. *Proceedings of Institution of Mechanical Engineers Part C: Journal of Mechanical Engineering Science.* **2023**, online first. DOI: 10.1177/09544062231191319

[9] N. Chakraborti. Data-driven Evolutionary Modeling in Materials Technology. CRC Press: Boca Raton, USA, 2022. ISBN 9781003201045

APPLIED MECHANICS 2024

April 17th – 19th, 2024
Hotel Toliar, Štrbské Pleso
Slovakia

REDUCTION OF MECHANICAL STRESS ON THE FORGING DIE IN THE DOVETAIL AREA

M. PAULEC[1]*, M. SÁGA[2], P. KOPAS[3]

Hot forging is frequently employed in mass production. Forging die failure most commonly occurs in the die cavity or the dovetail area of forging die. This article addresses the issue of reducing the load in the dovetail area of the die using geometrical modifications. In practice, the dovetail of the forging die fails due to mechanical cycles. The authors modify the radius on the dovetail in this paper to reduce the load in the die dovetail. The geometrical changes are compared using the Transvalor NxT 4.0 simulation software. The von-Mises equivalent stresses and von-Mises equivalent plastic strains are compared in the study. The results demonstrate that increasing the dovetail radius reduces the overall load in the dovetail area.

Keywords: Hot forging; Plastic deformation; Equivalent stress

INTRODUCTION

In the current era of technological advancement and exponential growth in industrial production, the demands for efficiency and durability in the tools used in forming processes have surged. Die forging, as one of the most widespread methods of forming, stands at the forefront of this revolution, where finding a balance between tool durability and economic efficiency presents a significant challenge. This article focuses on reducing mechanical stress on the forging die in the dovetail region, a critical segment that faces significant wear and fatigue damage [1].

Forging, historically rooted in artisanal manufacture, has evolved into a highly precise industrial process that necessitates high-quality tool steels, such as 56NiCrMoV7, known for its resistance to abrasive wear, plastic deformations, and fatigue damage. These attributes are crucial for the long lifespan of forging tools, which directly impacts the overall production costs and the affordability of forgings [2].

Understanding and modeling the plastic deformations and mechanical stresses that act on tools during forging is essential for their optimization. The application of the Finite Element Method

[1] **Ing. Michal Paulec**, Department of Applied Mechanics, Faculty of Mechanical Engineering, University of Žilina, Univerzitná 8215/1, Žilina, Slovak republic; Michal.Paulec@fstroj.uniza.sk
[2] **prof. Dr. Ing. Milan Sága**, Department of Applied Mechanics, Faculty of Mechanical Engineering, University of Žilina, Univerzitná 8215/1, Žilina, Slovak republic; Milan.Saga@fstroj.uniza.sk
[3] **Ing. Peter Kopas, PhD.**, Department of Applied Mechanics, Faculty of Mechanical Engineering, University of Žilina, Univerzitná 8215/1, Žilina, Slovak republic; Peter.Kopas@fstroj.uniza.sk

(FEM) allows for precise simulation and analysis of these dynamic processes, providing critical information necessary for the design of more durable and efficient forging dies [3].

This article contemplates a comprehensive strategy that encompasses not only material innovations but also advanced computational modeling methods to understand and minimize mechanical stress in the dovetail region of the forging die. Through this approach, we aim not only to extend the lifespan of forging tools but also to contribute to a more sustainable and economically viable production of forgings [4].

SIMULATION

Analysed forging die is used for the hot forging process. The production is realized by sets of two forging dies, namely the upper and lower die. The forging process consists of three phases: upsetting, preforging and finishing. Based on the company's experience, we have found that the lower forging die is the most stressed during the pre-forging operation. The most loaded part of the die is the preforging cavity. However, it is repaired during the forging process. Another heavily loaded area on the die is the dovetail under the pre-forging cavities. This area is not repaired during forging and therefore the initiation and growth of fatigue cracks is not controlled. For this reason, our analysis focuses on this part of the die. We simulate three variants of dies with a dovetail radius of R16, R20 and R25.

The simulation consists of two steps. In the first step, the pre-forging process is simulated, in which only the forged bar is deformable. The dies are perfectly rigid. During this step, the "Tool computation" function is enabled, which records the loads on the dies. In the second step, the load on the lower die is simulated. In this step, the die is deformable, and the die is clamped using forging wedges.

The software uses a viscoplastic "Hansel Spittel" computational model. The material model of the forged bar (steel C45) is imported from the libraries of the software "Transvalor Forge". The temperature of the forged bar is 1310 [°C]. Forging is carried out on a forging hammer. The machine specifications are given in Table 1. The percentage values of the ram strokes are given in Table 2. The thermal conductance between the materials is defined by the software as "Strong Interaction with Steel Dies". The friction between the forging dies and tools is defined as "Water+graphite" according to Coulomb's law. The geometry of the forged bar is generated in the simulation software (Figure. 1). The dimensions are D45x750 [mm]. The geometries of the forging dies were imported from the Catia V5 software in "stp" format. The geometries of the forging dies are shown in figures 2 and 3. The element types for meshing the geometry are triangles and tetrahedrons. The mesh width value is 2 [mm] for the billet and 20 [mm] for the dies.

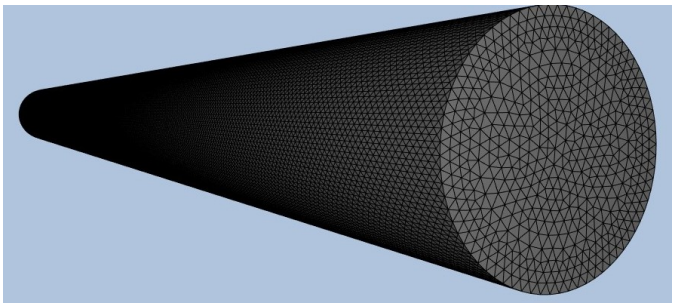

Fig. 1 Geometry of forging billet

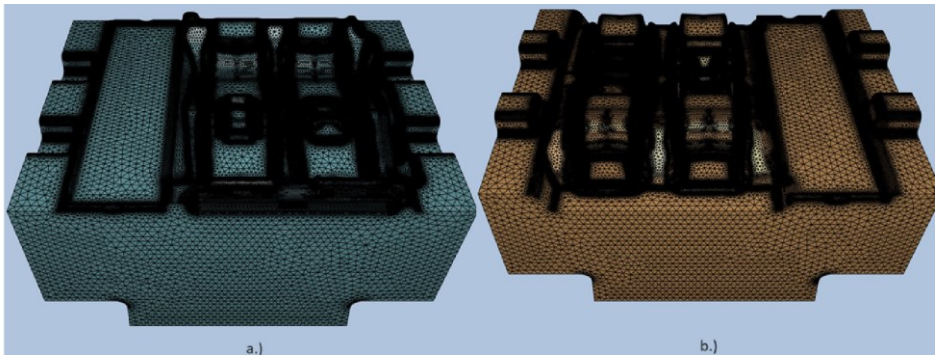

Fig. 2 Geometry of lower die (a) and upper die (b)

Tab. 1 Machine specification

Name	Value
Maximal energy of machine	100 [kJ]
Weight of ram	7100 [kg]

Tab. 2 Ram stroke percentage values for the pre-forging operation

Blow number [-]	1	2	3	4	5	6
Percentage [%]	10	15	15	15	25	35

In the second step, the material model of the die (tool steel 1.2714) is imported from the software libraries. The die is clamped using a geometry that represents the clamping in the machine's anvil block (fig.3). The friction between the die and the clamping geometry is set to "Bilateral sticking", which means that the nodes cannot move relative to each other. The temperature of the forging die is set to 250 [°C]. The temperature of the clamping geometry is 220 [°C]. The thermal conductivity between the die and the clamping geometry is defined by the software as "Strong Interaction with Steel Dies“.

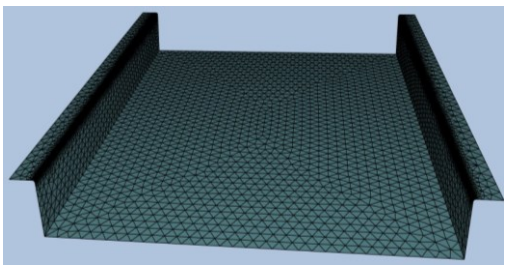

Fig. 3 Clamping geometry of forging die

RESULTS

The results show that the stress and plastic strain distributions are located at the ends of the dovetail. The maximum equivalent Von Mises stresses reach a value of 1900 [MPa]. The maximum equivalent Von Mises plastic strains reach a value of 0.1 [-]. The equivalent stresses exceed the ultimate strength values of 1600 [MPa]. Table 3 shows the values of the principal stresses and principal plastic strains. The values show that it is mainly a compressive load, and the values reach 200 [MPa]. From Table 3, the values of the equivalent Von-Mises stresses have decreased from 1912 [MPa] to 1624 [MPa] and equivalent Von-Mises plastic deformation have decreased from 0,1 to 0,065.

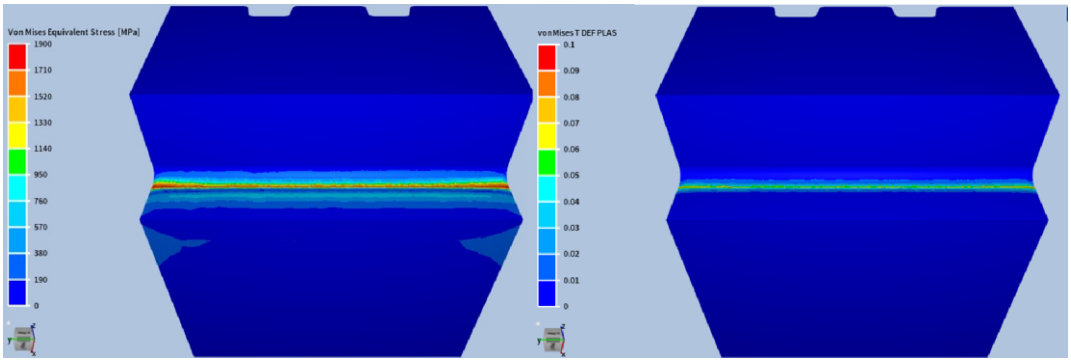

Fig. 4 Distributions of Von-Mises stress and plastic deformation

Tab. 3 Results of the stress-strain simulations

Value of radius	$\sigma_1\ [MPa]$	$\sigma_2\ [MPa]$	$\sigma_3\ [MPa]$	$\sigma_{VM}\ [MPa]$
R16	202,1	-45,185	-1850,21	1912,25
R20	189,5	25,152	-1652,89	1784,13
R25	175,5	-52,135	-1584,68,	1624,85
Value of radius	$\varepsilon_1\ [MPa]$	$\varepsilon_2\ [MPa]$	$\varepsilon_3\ [MPa]$	$\varepsilon_{VM}\ [MPa]$
R16	0,029	0,009	−0,066	0,1
R20	0,026	0,001	−0,052	0,08
R25	0,018	0,007	−0,043	0,065

CONCLUSION

In conclusion, this article elucidates significant findings on reducing mechanical load in the dovetail area of forging dies through geometrical modifications. Alterations to the dovetail radius have demonstrated a decrease in overall stress, offering considerable benefits in terms of tool longevity and cost-effectiveness. Utilizing the Transvalor NxT 4.0 simulation, optimal geometrical configurations were identified that minimize von-Mises equivalent stresses and plastic deformations, promoting more sustainable and economically advantageous forging production. This approach paves the way for further research and innovations in forging tool design and development.

REFERENCES

[1] CH. Sun, Y. Qin, G. Xiao, J. Zhang, J. Zhou. Research on the Hot Deformation Process of A100 Steel Based on High-Temperature Rheological Behavior and Microstructure. *Materials* **2024**, 17 (5), 2-3. DOI: https://doi.org/10.3390/ma17050991

[2] Y. Li, T. Xu, X. Cao, Z. Wu, J. Fan, CH. Hu, H. Dong. Morphology and Distribution of Primary Carbides in Forged Cr-Ni-Mo-V/Nb Steel. *Materials* **2024**, 17 (4), 3-4. DOI: https://doi.org/10.3390/ma17040867

[3] M. Eckert, M. Krbata, M. Kohutiar, M. Kuba. Hot deformation analysis of 100MnCrW4 tool steel. *Process. Struct. Integr.* **2024**, 43 (1), 318-323. DOI: https://doi.org/10.1016/j.prostr.2022.12.278

[4] Y. Liu, Z. Yin, J. Luo, C. Zhang, Y. Zhang. McTegart. Constitutive relationship and processing map of hot deformation in A100 steel. *High Temp. Mater. Proc.* ***2016***, 35 (1), 399-405. https://doi.org/10.1007/s11665-014-1012

APPLIED MECHANICS 2024

April 17th – 19th, 2024
Hotel Toliar, Štrbské Pleso
Slovakia

EFFECT OF ACTIVE MECHANICAL PROPERTIES ON INFLATION-EXTENSION BEHAVIOUR OF CYLINDRICAL TUBE

P. PELINKOVÁ[1]*, L. HORNÝ[2]

Human arteries are materials exhibiting nonlinear mechanical behaviour. In addition to the passive component, the arterial wall has an active component, which is smooth muscle. Smooth muscle contracts or relaxes according to the activation caused by sympathetic nervous system or chemical signals mediating mechanobiological reactions. Our aim is to study the effect of active behaviour on the mechanical response of arteries. In this paper, the concept of a computational model is presented that treats the carotid artery as a nonlinear anisotropic continuum described by a strain energy density that is divided into passive and active component. Using a numerical simulation based on an analytical approach, it is shown how the active behaviour can affect the response of the arterial wall to loading by internal pressure and axial prestretch.

Keywords: Smooth muscle; Contraction; Active behavior; Strain-energy density function; Constitutive model; Artery wall

INTRODUCTION

Arteries, like other soft biological tissues, exhibit complex mechanical behaviour, typically large non-linear elastic deformation [1, 2]. In contrast to connective tissues such as ligaments, arteries exhibit also active properties due to presence of smooth muscle cells (SMCs), which are important constituent of the tunica media [2-5]. Tunica media is the middle layer of an artery that, in addition to SMCs, consists of collagen fibres and elastic membranes [2]. The active component enables the blood vessels to respond to nerve stimuli.

Vascular SMCs have many roles, such as contraction and relaxation in the vascular wall through which they can change the diameter of the vessel at the arteriolar level to control local blood flow [6, 9]. Changes that are manifested at the level of arterioles as changes in cross-sectional area are observed more as changes in wall stiffness at the level of large arteries. Thus the contraction of SMCs leads to alterations that impact the distribution of stress and strain in the wall [7].

[1] **Ing. Pavla Pelinková**, Department of Mechanics, Biomechanics and Mechatronics, Faculty of Mechanical Engineering, Czech Technical University in Prague, Technická 4, Prague, Czech Republic; pavla.pelinkova@fs.cvut.cz

[2] **doc. Ing. Lukáš Horný, PhD.**, Department of Mechanics, Biomechanics and Mechatronics, Faculty of Mechanical Engineering, Czech Technical University in Prague, Technická 4, Prague, Czech Republic; lukas.horny@fs.cvut.cz

Constitutive models work with the idea of the artery as a purely passive structure have been extensively studied in recent decades. On the other hand, active properties are frequently neglected in computational models of the arterial mechanics, likely due to the complex coupling of mechanical and chemical processes [8]. Our goal is to build a mathematical model of a cylindrical tube, which will resemble an artery in its behaviour and will respect mechanical phenomena, such as large deformations, nonlinear passive response, and active behaviour [2].

METHODS

Concept of the model

Our model is based on the approach introduced by L. A. Taber in [4]. The artery wall is modelled as a hyperelastic incompressible material, which is treated as a homogeneous continuum consisting of a passive (subscript p) and an active (subscript a) component. Their contributions are in every material point summed according to the rule-of-mixtures such that $\varphi_a + \varphi_p = 1$. In order to include the active stress induced by muscle contraction into the model, an intermediate strain state is defined for the active component, which corresponds to the contracted yet unloaded muscle. For the passive component, as usual, only the stress-free (undeformed) and stressed (deformed) states are distinguished.

Kinematics of contraction

Three configurations of the active component are defined in the Fig. 1.

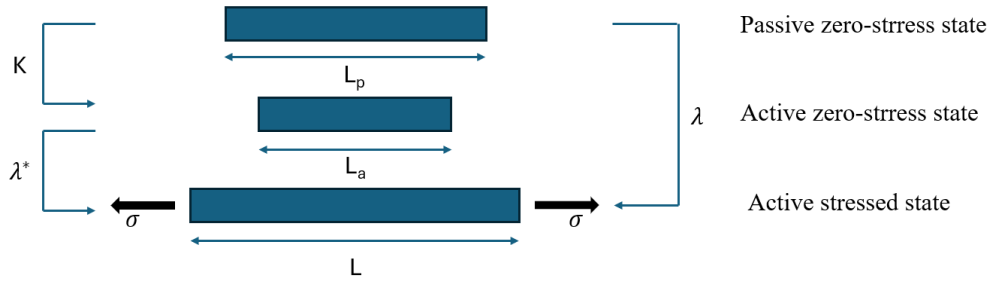

Fig. 1 Mechanical states of the active component, adopted from [4]

The λ means total stretch ratio, λ^* means elastic stretch ratio and K means contraction ratio. Contraction ratio K is defined as ratio between lengths L_p and L_a. K is often treated as a specified function of time. In our particular case, K is adopted to be a constant, because it has been assumed that the inflation of the tube is so fast that K does not change substantially within this time. Eq. (1) expresses the relation between λ, λ^* and K.

$$\lambda = K\lambda^* \tag{1}$$

Constitutive relations

Both the passive and active components of the arterial wall are modelled as hyperelastic. The total stress in the wall is given by the rule-of mixtures, which is expressed by Eqs. (2) to (4). Since we are dealing with a cylindrical arterial wall, the stress components are expressed in the cylindrical coordinate system with respect to the orthonormal basis and the physical components of the tensors are used. In order to maintain the uniformity of the cylindrical geometry, the absence of shear stresses and strains is assumed. It was assumed that the artery wall is incompressible material

[4-10]. This assumption causes that the hydrostatic stress component cannot be obtained by deriving the strain energy W so it is introduced separately by means of a multiplier p, which has to be determined from the force boundary condition.

$$\sigma_{rr} = \varphi_p \sigma_{rp} - p \tag{2}$$

$$\sigma_{\theta\theta} = \varphi_p \sigma_{\theta p} + \varphi_p \sigma_{\theta a} - p \tag{3}$$

$$\sigma_{zz} = \varphi_p \sigma_{zp} - p \tag{4}$$

Eq. (3) expresses the assumption that the active components representing the SMC are oriented only in the circumferential direction. Therefore, only the circumferential stress is composed of passive and active component. The axial and radial stresses correspond to the passive component only.

$$\sigma_{rp} = \frac{\partial W_p}{\partial \lambda_r} \qquad \sigma_{\theta p} = \frac{\partial W_p}{\partial \lambda_\theta} \qquad \sigma_{zp} = \frac{\partial W_p}{\partial \lambda_z} \qquad \sigma_{\theta a} = \frac{\partial W_a}{\partial \lambda^*} \tag{5}$$

Eqs. (5) express the fact that both components of the artery wall are considered as hyperelastic material and thus must be characterized by the strain energy density for the passive component W_p and for the active component W_a. Their specific forms are as follows.

$$W_p = \frac{c_0}{2}(I_c - 3) + \sum_{i=1}^{4} \frac{c_1^i}{4c_2^i}\left\{exp\left[\left[c_2^i (I_4^i - 1)^2\right]\right] - 1\right\} \tag{6}$$

$$W_a = \frac{c_a(t)}{\pi}\left[1 - \cos\pi\left(\frac{\lambda^* - 1}{\widehat{\lambda^*} - 1}\right)\right] \tag{7}$$

The model (6) was adopted from [11]. Here c_0, c_1^1, c_2^1, c_1^2, c_2^2, $c_1^{3,4}$, $c_2^{3,4}$ are material parameters and I_c is the first principal invariant of the right Cauchy-Green strain tensor. I_4^i (i = 1.4) are strain invariants corresponding to the material anisotropy. The model for active component, (7), was adopted from [4]. Here $\widehat{\lambda^*}$ denotes the maximum achievable value of λ^* and c_a is the time-varying active modulus that was assumed to be in the form Eq. (8).

$$c_a = \left[\frac{1 - K(t)}{1 - K_{min}}\right] c_{a,max} \tag{8}$$

Equilibrium equations

If we are not interested in the exact distribution of stresses and strains along the wall thickness, arteries can be modelled as thin-walled vessels [2, 4, 9, 11]. In this case, the balance of forces is expressed by Eqs. (9) to (11). Here r and h are deformed radius and thickness of the tube (reference dimensions are R and H). F_{red} is force required for axial pre-stretching of the tube and P is the internal pressure.

$$\sigma_{rr} = 0 \tag{9}$$

$$\sigma_{\theta\theta} = \frac{rP}{h} \tag{10}$$

$$\sigma_{zz} = \frac{F_{red}}{2\pi r h} + \frac{rP}{2h} \tag{11}$$

RESULTS

Tab. 1 shows constitutive model parameters that were used in our simulation. Parameters for passive component W_p were adopted from [11], specific values correspond to the left common carotid artery of 60 years old male donor. Based on the age of the donor, the axial prestretching force F_{red} was determined according to the prestretch data in [12].

Tab. 1 Model parameters and dimension of tube

c_0 $[kPa]$	$c_1^1[kPa]$	c_2^1	$c_1^2[kPa]$	c_2^2	$c_1^{3,4}[kPa]$	$c_2^{3,4}$	γ [°]
17.96	10.21	1.48	15.58	1.50	3.01	4.69	45.63
$c_{a,max}$ $[kPa]$	φ_a	φ_p	K	K_{min}	$\widehat{\lambda^*}$	R $[mm]$	H $[mm]$
300	0.4	0.6	0.8	0.5	2	4.45	1.36

Fig. 2 shows resulting inflation and extension response of the cylindrical tube representing the left common carotid artery. Red curves (Fig. 2A) show the behaviour in the circumferential direction, whereas blue curves (Fig. 2B) show the response in the axial direction. The solid line demonstrates only the passive behaviour of the tube without axial prestretch. The dotted line demonstrates the passive behaviour of the tube with initial axial pre-stretch $\lambda_Z^{ini} = 1.14$. Curves drawn with the diamonds correspond to a combination of passive and active behaviour of the tube with the initial axial prestretch $\lambda_Z^{ini} = 1.14$.

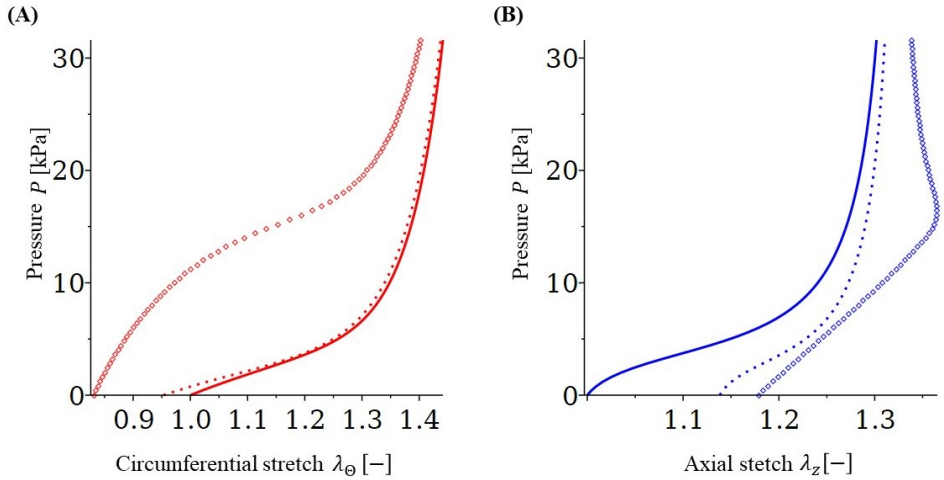

Fig. 2 Results of the inflation-extension simulation. (A) Longitudinal stretch versus pressure. (B) Circumferential stretch versus pressure. Purely passive responses without and with axial prestretching are indicated by solid and dotted curves, respectively. Symbols are used for passive + active behaviour of the initially prestretched artery.

CONCLUSION

Calculated results demonstrate that considering active component contribution significantly alters the inflation behaviour of the tube. rendering it more compliant in both directions compared to purely passive response. There is not only a change in stiffness in the circumferential direction, but also a change in axial response, even though the SMCs are oriented only in the circumferential

direction. This surprising result shows an interesting coupling between the active response and the anisotropy of the material. Our future work will focus on understanding this interaction in detail.

ACKNOWLEDGEMENT

The work has been supported by the grant project SGS22/149/OHK2/3T/12 “Research and development of applications and methods for diagnostic and therapeutic biomechanics”.

REFERENCES

[1] A. Agianniotis, A. Rachev, N. Stergiopulos. Active axial stress in mouse aorta. *Journal of Biomechanics* **2012**, 45, 1924-1927.

[2] J.-L. Gade. Mechanical Properties of Arteries, Identification and Application. Linköping University: LiU-Tryck, 2019. Linköping. ISBN 978-91-7685-011-4

[3] Z. Liu, R.A. Khalil. Evolving mechanisms of vascular smooth muscle contraction highlight key targets in vascular disease. *Biochemical Pharmacology* **2018**, 153, 91-122.

[4] L.A. Taber. Continuum Modeling in Mechanobiology. Washington University : Springer, 2020. ISBN 978-3-030-43207-2

[5] T. Tan, R. De Vita. A structural constitutive model for smooth muscle contraction in biological tissues. *International Journal of Non-Linear Mechanics* **2015**, 75, 46-53.

[6] T. Matsumoto, K. Nagayama. Tensile properties of vascular smooth muscle cells: Bridging vascular and cellular biomechanics. *Journal of Biomechanics* 2011, 45, 745-755.

[7] A. Rachev, K. Hayashi. Theoretical Study of the Effects of Vascular Smooth Muscle Contraction on Strain and Stress Distributions in Arteries. *Biomedical Engineering Society* **1999**, 27, 459-468.

[8] H. Chen. Microstructural constitutive model of active coronary media. *Biomaterials* **2013**, 34, 7575-7583.

[9] Y.C. Fung. Biomechanics, Mechanical Properties of Living Tissues. Second edition. University of California : Springer, 1993. ISBN 978-1-4419-3104-7

[10] M. Kroon. A constitutive model for smooth muscle including active tone and passive viscoelastic behaviour. *Mathematical Medicine and Biology* **2009**, 27, 129-155.

[11] A.V. Kamenskiy, Y.A. Dzenis, S.A.J. Kazmi, et al. Biaxial mechanical properties of the human thoracic and abdominal aorta, common carotid, subclavian, renal and common iliac arteries. *Biomech. Model Mechanobiol.* **2014**, 13, 1341–1359.

[12] L. Horný, T. Adámek, M. Kulvajtová. A comparison of age-related changes in axial prestretch in human carotid arteries and in human abdominal aorta. *Biomech. Model Mechanobiol.* **2017**, 16, 375–383.

APPLIED MECHANICS 2024

April 17th – 19th, 2024
Hotel Toliar, Štrbské Pleso
Slovakia

MODELLING OF MULTIAXIAL FATIGUE DAMAGE OF MACHINE ELEMENTS USING FEM

K. PIJÁKOVÁ[1]*, M. SÁGA[2], M. VAŠKO[3], Z. ŠAVRNOCH[4]

The development of MATLAB software for the analysis of fatigue damage to materials is a key step towards more accurate prediction of the service life of machine components subjected to cyclic loading. The research uses the Dang - Van, Findley and Von Mises hypothesis to calculate fatigue damage, with a key part being the generation of random load time functions and their application to models created using the finite element method (FEM). This approach allows efficient integration of the methodologies with visualization of the results directly on the FEA models, providing a detailed overview of the fatigue processes in materials.

Keywords: FEM; Matlab; Multiaxial fatigue; Dang-Van; Findley; Von Mises

INTRODUCTION

Currently, understanding and predicting the fatigue life of materials represents one of the greatest challenges in mechanical engineering. The development of advanced computing technologies and software is opening new avenues for more accurate and efficient modelling of the fatigue behaviour of materials. We are devoted to presenting advanced fatigue life calculation methodologies, with particular emphasis on multiaxial loading, which is a common phenomenon in many mechanical engineering applications.

In multiaxial loading, it is crucial to consider the different types of stresses acting on the material. The basic and widely used approaches include the Dang-Van method, the Findley criterion and the Von Misses hypothesis. Each of these methodologies offers unique perspectives on the fatigue problem and allows engineers to better understand and predict the fatigue life of components [1, 2].

[1] **Ing. Katarína Pijáková**, Department of Applied Mechanics, Faculty of Mechanical Engineering, University of Žilina, Univerzitná 8215/1, 010 26, Žilina, Slovakia; Katarina.Pijakova@fstroj.uniza.sk
[2] **prof. Dr. Ing. Milan Sága**, Department of Applied Mechanics, Faculty of Mechanical Engineering, University of Žilina, Univerzitná 8215/1, 010 26, Žilina, Slovakia; milan.saga@fstroj.uniza.sk
[3] **doc. Ing. Milan Vaško, PhD.**, Department of Applied Mechanics, Faculty of Mechanical Engineering, University of Žilina, Univerzitná 8215/1, 010 26, Žilina, Slovakia; milan.vasko@fstroj.uniza.sk
[4] **Ing. Zdenko Šavrnoch**, Department of Applied Mechanics, Faculty of Mechanical Engineering, University of Žilina, Univerzitná 8215/1, Žilina, Slovak republic; zdenko.savrnoch@fstroj.uniza.sk

Findley's modified method

Findley [3] assumed that the plane where a fatigue crack will grow is the one with the highest shear stress, leading to his definition of equivalent shear stress:

$$\tau_{FIN} = \tau_{max} + k \cdot \sigma_m \tag{1}$$

where k is a coefficient that takes the value of about 0,3 for a tough material. In the case where we have only a 1-axis alternating tension- pressure test, we can modify the previous relation assuming HMH as follows:

$$\sigma_{FIN} = \sqrt{3} \cdot \text{sign}\left(\frac{\sigma_1+\sigma_3}{2}\right) \cdot \frac{\sigma_1-\sigma_3}{2} + k \cdot \frac{\sigma_1+\sigma_3}{2} \tag{2}$$

We can already decompose such an equivalent stress by rain-flow decomposition. It is true that this approach is mainly suitable for proportional loading, but it also has its merits for non-proportional loading. As a disadvantage we can consider the choice of the coefficient k.

Dang-Van's modified method

Dang-Van [4,5] assumed the critical plane in which a fatigue crack starts to form is the plane with the largest shear stress and thus defined the equivalent shear stress in the form:

$$\tau_{DV} = \tau_{max} + k \cdot p_m = \frac{\sigma_1-\sigma_3}{2} + \left(\frac{\tau_c-\frac{\sigma_c}{2}}{\frac{\sigma_c}{\sqrt{3}}}\right) \cdot \left(\frac{\sigma_1+\sigma_2+\sigma_3}{3}\right) \tag{3}$$

where τ_c means the limit of fatigue for torsion, σ_c is the fatigue limit for axial tension - pressure, $\sigma_1, \sigma_2, \sigma_3$ are the principal stresses. If we consider that we only have a 1-axis alternating tension - pressure test, then we have to , again assuming HMH, modify the previous relation to the form:

$$\sigma_{DV} = \sqrt{3}\left|\text{sign}\left(\frac{\sigma_1+\sigma_3}{2}\right) \cdot \frac{\sigma_1-\sigma_3}{2} + \left(\frac{\tau_c-\frac{\sigma_c}{2}}{\frac{\sigma_c}{\sqrt{3}}}\right) \cdot \left(\frac{\sigma_1+\sigma_2+\sigma_3}{3}\right)\right| \tag{4}$$

after simplification of the following HMH adjustment:

$$\frac{\tau_c-\frac{\sigma_c}{2}}{\frac{\sigma_c}{\sqrt{3}}} \approx \frac{\tau_c-\frac{\sigma_c}{2}}{\frac{\sqrt{3}\tau_c}{3}} \approx 0{,}232 \tag{4}$$

the relationship will look as follows:

$$\sigma_{DV} = \sqrt{3}\left|\text{sign}\left(\frac{\sigma_1+\sigma_3}{2}\right) \cdot \frac{\sigma_1-\sigma_3}{2} + 0{,}232 \cdot \left(\frac{\sigma_1+\sigma_2+\sigma_3}{3}\right)\right| \tag{6}$$

We can decompose such equiavalent stresses by rain-flow decomposition into closed cycles. The approach is then more convenient for loads of proportional type.

TEST PROBLEM

In the meshing of this part we used 3D - SOLID elements, which have 4 nodes. The component was loaded with two forces that are randomly generated by normal distribution F1 -1000 ± 1200 N, in the Z-axis direction and F2 - 800 ± 500 N, in the X-axis direction.

Now follow the results of fatigue damage accumulation after 2000 x 32 cycles of operation, which means that the component was subjected to a stress of the form of 128 000 seconds, which is roughly 35.5 hours. The results are shown on the models for each of the criteria used to determine fatigue life Figs. 5-8. After the load was applied to the component, the following accumulation of fatigue damage was found according to the three hypotheses chosen.

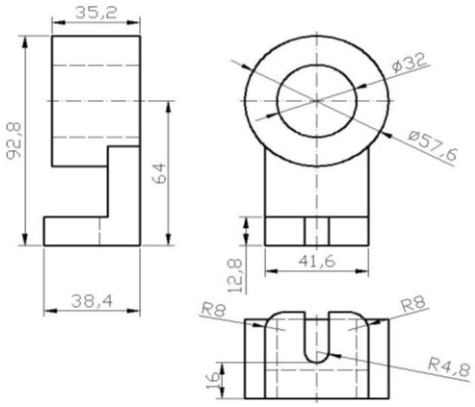

Fig. 1 Dimensions of the component

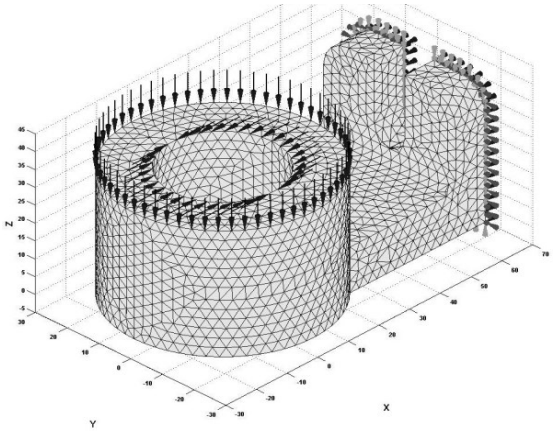

Fig. 2 3D model of the part with its meshing displayed in Matlab

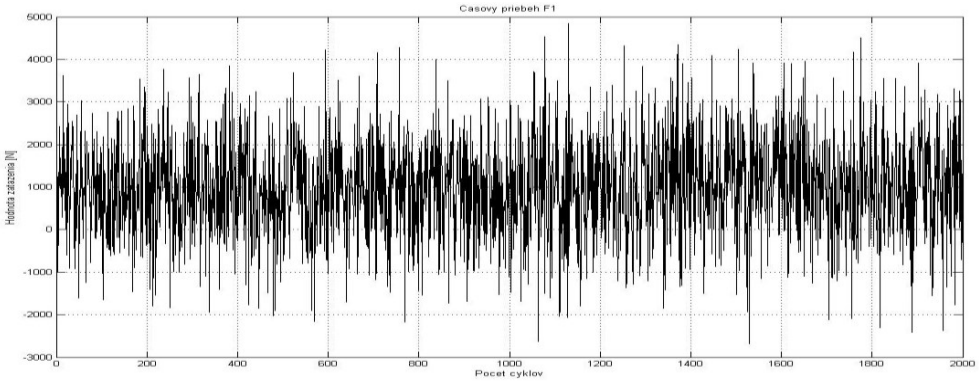

Fig. 3 Time course of the load force function F1

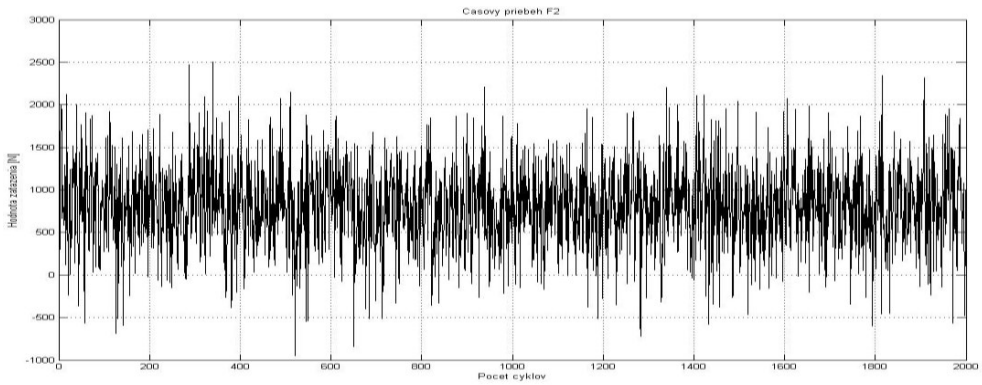

Fig. 4 Time course of the load force function F2

Tab. 1 Comparison of the results of the cumulative damage detected on the component

Applied method	Node with maximum damage	Maximum damage value
Dang - Van	272	$1.7049 \cdot 10^{-4}$
Findley	272	$3.8216 \cdot 10^{-4}$
Von Misses hypothesis	272	$1.8992 \cdot 10^{-4}$

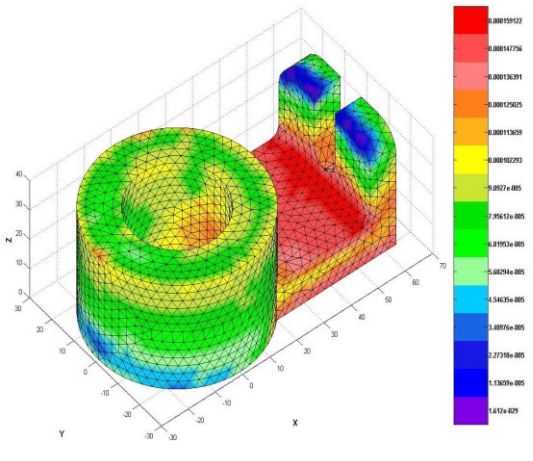

Fig. 5 Rendered damage according to the Dang-Van method (max. damage has a value of $1.7049 \cdot 10^{-4}$)

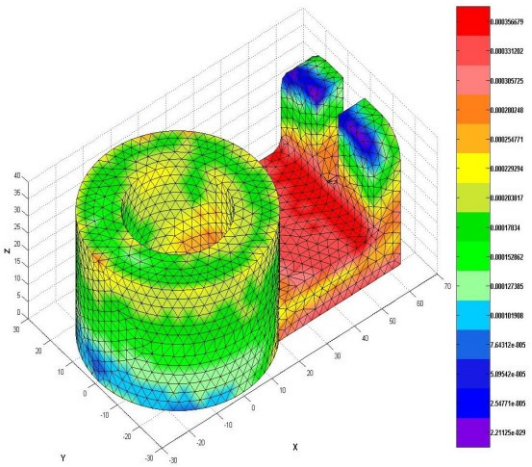

Fig. 6 Plotted Findley method damage (max. damage has value $3.8216 \cdot 10^{-4}$)

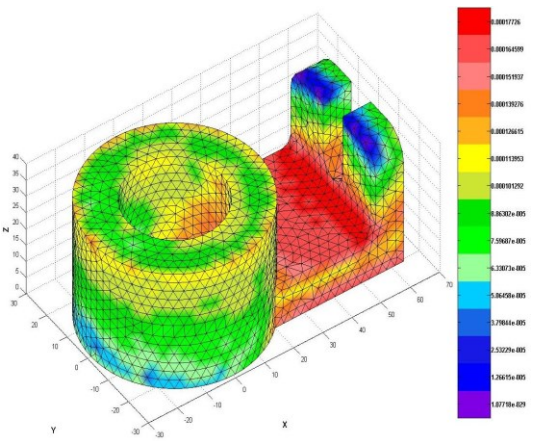

Fig. 7 Plotted damage according to the HMH-critical plane method (max. damage has a value of $1.8992 \cdot 10^{-4}$)

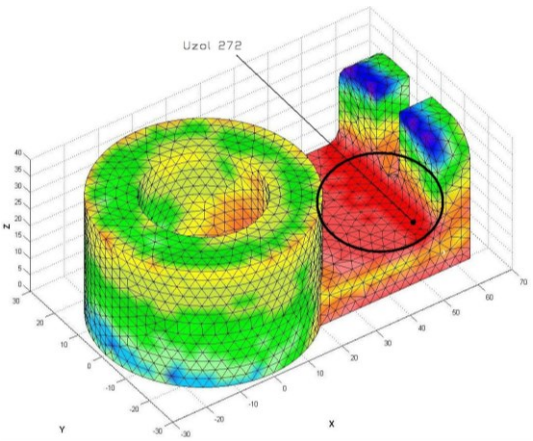

Fig. 8 Representation of the critical point and node where the maximum damage has been detected and where we expect the fatigue crack to initiate

As can be seen in Table 1, the results are very similar for the Dang-Van hypothesis and the Von Misses hypothesis. The following is the calculated mean and standard deviation from the obtained results: Mean $2.4752 \cdot 10^{-4}$, Standard deviation $1.1700 \cdot 10^{-4}$.

CONCLUSION

We have solved multiaxial loading on a finite-element model. We use the interconnection of MATLAB and ADINA software. We selected 2000 time steps for the loading forces, and the size of the load in each step was randomly generated in MATLAB with an appropriately chosen random distribution. Subsequently, a calculation was performed in ADINE, from which we obtained the stress components at each node for each time step. These stresses were used to calculate the cumulative fatigue damage according to the following hypotheses: the Dang - Van hypothesis, the Findley hypothesis and the Von Misses hypothesis. Finally, we compared the results, and in our case, after 64,000 cycles (which equates to roughly 35.56 hours of operation), very similar cumulative fatigue damage results came out.

ACKNOWLEDGEMENT

The work has been supported by the grant project VEGA no. 1/0423/23, KEGA no. 002ŽU-4/2023.

REFERENCES

[1] A Sága, M., Vavro, J., Kopecký, M. Počítačová analýza a syntéza mechanických sústav. ZUSI v Žiline, 2002. ISBN 80-968605-4-2

[2] M. Žmindák, I. Grajciar, J. Nozdrovický. Modelovanie a výpočty v metóde konečných prvkov, Diel I – Modelovanie v ANSYSe. Vedecko-technická spoločnosť pri Žilinskej univerzite, Žilina, 2004. ISBN 80-968823-5-X

[3] W.N. Findley. A theory for the effect of mean stress on fatigue of metals under combined torsion and axial load or bending. *J. Eng. Ind.* **1959**, 81 (4), 301–305. http://dx.doi.org/10.1115/1.4008327

[4] K. Dang Van, B. Griveau, O. Message. On a new multiaxial fatigue limit criterion: theory and applications. In: M.W. Brown, K.J. Miller (Eds.), EGF 3, Mechanical Engineering Publications, London, 1989, 479-496.

[5] K. Dang Van. Macro–micro approach in high-cycle multiaxial fatigue. In: D.L. McDowell, R. Ellis (Eds.), Advances in Multiaxial Fatigue, ASTM STP 1191, Philadelphia, 1993, 120-130.

APPLIED MECHANICS 2024

April 17th – 19th, 2024
Hotel Toliar, Štrbské Pleso
Slovakia

MODELING THE DYNAMICS OF A MOORING LINE USING SIMSCAPE MULTIBODY

O. PIROH[1]*, M. VAŠKO[1], L. JAKUBOVIČOVÁ[1], M. HANDRIK[1], J. MAJKO[1]

This theoretical study focuses on the development of a dynamic rope model using mathematical-physical modeling within the Simscape Multibody environment. Ropes are crucial components in systems subjected to dynamic forces (wind, currents), and their behavior directly impacts the stability and functionality of such systems. The mentioned software does not facilitate direct rope - loading simulation, necessitating the creation of a novel system. The fundamental concept of the finite element method, dividing the rope into individual elements, was employed to construct the model. However, instead of generating a finite element mesh, the rope itself was partitioned into a predefined number of elements interconnected by massless springs and dampers.

Keywords: Multibody dynamics; Simscape Multibody; rope; MATLAB; FEM

INTRODUCTION

Mooring lines represent critical components in various industries, including marine, oil and gas, and construction. Understanding their dynamic behavior under operational loads is crucial for determining the stability and lifespan of the entire system. Despite the significance of these aspects, previous research has not focused on creating a dynamic model using a combination of the finite element method and multi-body dynamics, as evidenced by the absence of relevant studies [1-3]. In response to this gap, our theoretical study presents a novel approach to creating a dynamic model of a mooring line. The new approach utilizes the fundamental principles of the finite element method and multi-body dynamics within the Simscape Multibody environment. The model developed in this manner, when defining the boundary conditions of operational loading, allows for the investigation of the motion of individual elements of the mooring line from both a kinematic and dynamic perspective. Through this approach, the authors aim to expand the understanding of complex dynamic and kinematic processes. Various methods are used to calculate the dynamics, such as static analysis, quasi-dynamic analysis, and dynamic analysis. In this case, the authors chose to use dynamic analysis, which considers the rope as a whole consisting of finite elements of concentrated mass and a spring-damper system. Such an analysis has the potential to describe the given system most accurately and reliably, as it includes all dynamic effects such as inertia, interaction with the seabed, etc. The finite element method divides the mooring line into multiple elements, and the

[1] **Ing. Ondrej Piroh**, **Assoc. Prof. Milan Vaško, PhD.**, **Ing. Lenka Jakubovičová, PhD.**, **Ing. Marián Handrik, PhD.**, **Ing. Jaroslav Majko, PhD.**, Department of Applied Mechanics, Faculty of Mechanical Engineering, University of Žilina, Univerzitná 8215/1, Žilina, Slovak republic; ondrej.piroh@fstroj.uniza.sk, milan.vasko@fstroj.uniza.sk, lenka.jakubovicova@fstroj.uniza.sk, marian.handrik@fstroj.uniza.sk, jaroslav.majko@fstroj.uniza.sk

accuracy of the calculation can be increased as the number of elements increases. The variables within each element are then described by interpolation functions, and the integrals are solved using numerical integration techniques. Examples of different solutions include the collocation [4], Galerkin [5, 6], and discontinuous Galerkin methods [7].

DEVELOPMENT OF A DYNAMIC MODEL

The dynamic model is created within the Simscape Multibody environment. This environment allows for the creation of a mathematical-physical model as well as excellent integration with the Simulink and MATLAB environments. The basic concept of the finite element method is used to create the model - dividing the rope into individual elements. However, in this case, a finite element mesh was not created, but the rope itself was divided into elements that are interconnected by massless springs and dampers.

To simulate the influence of the rope's weight and its inertial effects, cylindrical elements are created to describe the mass in each area. Each such cylinder has the diameter of the rope that would be physically used. These are perfectly rigid bodies with a uniform length. The mooring line has a parabolic shape (Fig. 1), which is specifically designed to minimize unwanted force concentrations and allow for an even distribution of load.

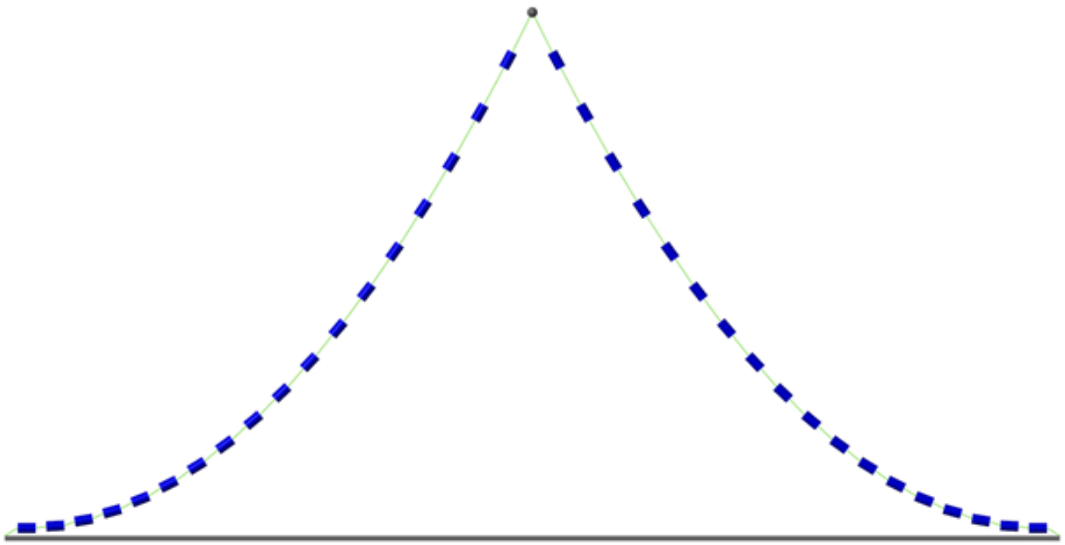

Fig. 1 Mooring line model

The rope is divided into 37 elements, including the central buoy. To achieve the mentioned parabolic shape, it is necessary to define the position of each element in the given axes. The Simscape Multibody environment works on the principle of moving the local coordinate system or possibly rotating it. Such a shift is provided by the Rigid Transform block based on the definition of the position relative to the global coordinate system.

Mooring line element model

Each mooring line element is formed by a joint that ensures the proper rotation and movement of the individual elements. This is a joint called a 6-DOF Joint. The joint allows for rotations and displacements in three axes, and therefore also for the calculation of these parameters. Within the internal mechanics, it allows for the setting of the equilibrium position as well as the spring stiffness

that holds the joint in a defined position and damping in a given axis [8]. In the figure (Fig. 2), the block is labeled with number 1.

To simulate movement in different environments (seawater, oil, ...), it is necessary to set the magnitude of the frictional force effect in all three axes. In the mentioned environment, it is possible to define the frictional force acting in the axial and radial directions. In the figure (Fig. 2), they are labeled with numbers 2 (frictional force in the axial direction) and 3 (frictional force in the radial direction).

Another element is an intangible rope that provides the connection between the individual elements. This is a combination of Belt - Belt-Cable end and Belt-Cable Properties blocks. This combination ensures proper connection while maintaining the mobility allowed by the joint. In the figure (Fig. 2), they are shown with numbers 4 (Belt - Cable End) and 5 (Belt - Cable Properties).

To apply the force acting in the sea current, the External Force and Torque block are used. The block allows for the definition of the forcing force directly on the solid element. In the figure (Fig. 2), this block is labeled with number 6.

The cylinders are modeled using the Cylindrical Solid block. In the figure (Fig. 2), it is labeled with number 7. This block describes a perfectly rigid body, allowing for the definition of basic properties such as mass or density.

The described model is created as a subsystem, whose outputs allow connection to individual blocks for determining position in space, defining force and contact with other elements and the seabed. The complete diagram of one element is shown in Figure (Fig. 2).

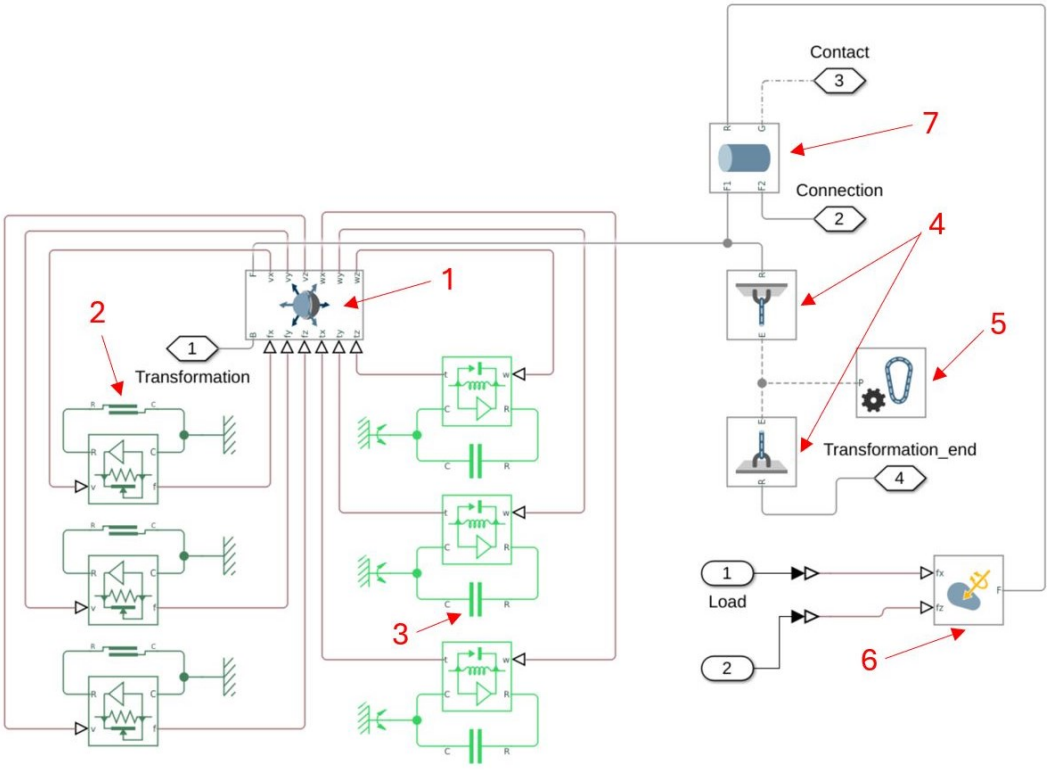

Fig. 2 Complete diagram of a single mooring line element

Mooring line motion simulation

The goal of numerical analysis is to determine the position of the buoy when the rope is loaded with a sinusoidal force. To achieve these goals, it is necessary to activate sensors that measure the position of the joint as well as its reaction force. Such measurement allows for obtaining information about the position and orientation in each plane. Figure 3 shows the course of the positions of the central buoy in two perpendicular planes. To obtain their values, the signals describing the position in the individual planes were added together.

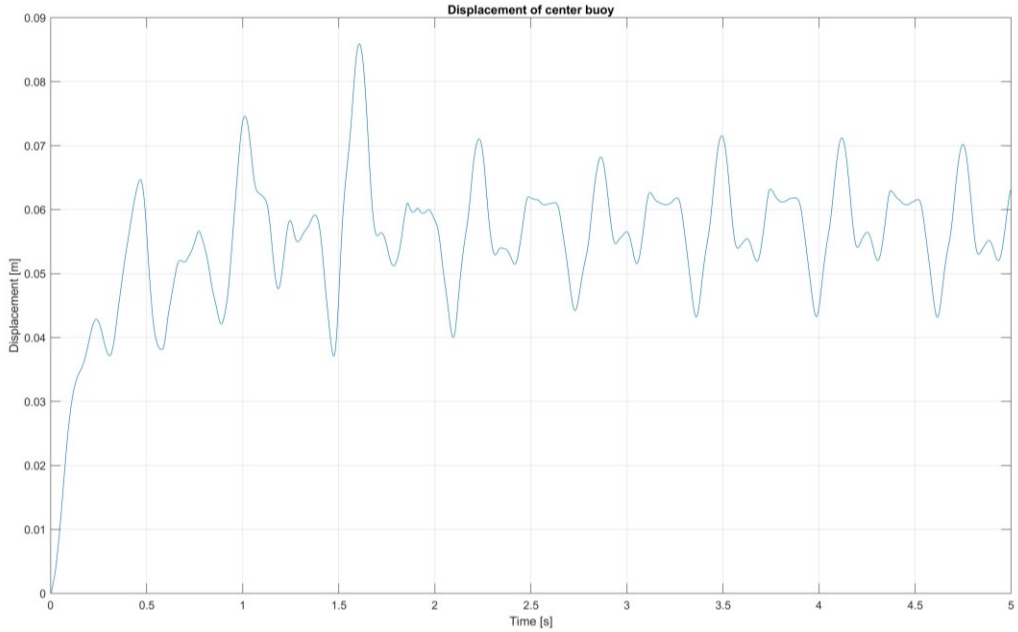

Fig. 3 Displacement trajectory of the central buoy over time

CONCLUSION

Simscape Multibody emerges as a powerful tool in the realm of multibody dynamics. It facilitates the modeling and simulation of complex systems with relatively favorable computational time. The presented model fulfills all crucial requirements for an adequate solution of the mooring rope's dynamic behavior. Since Simscape Multibody does not enable direct simulation of the rope as a whole, its discretization into elementary sections represented by blocks is necessary. These blocks accurately reflect the physical parameters and properties of the chosen ideal rope. Each rope element incorporates a rigid element characterizing its mass, as well as a frictional force acting during rotation and displacement and rope, blocks imparting the properties of a real rope to the element. As already demonstrated, numerical analysis of the dynamic model allows for gaining valuable insights into its behavior. Due to the described discretization, it is possible to obtain information about the position, velocity, acceleration, and reaction force in each element. Based on the time history of displacements, it is then possible to construct a comprehensive picture of the influence of the size, shape, and mass of individual mooring rope elements and their impact on the final motion.

ACKNOWLEDGEMENT

This work has been supported by the gran project KEGA 002ŽU-4/2023 and 005ŽU-4/2024.

REFERENCES

[1] J. Davidson, V.R. Ringwood. Mathematicall modelling of mooring systems for wave energy converters - A review. *Energies* **2017**, 10 (5), 666. https://doi.org/10.3390/en10050666

[2] B.Ch. Li, M. Chen, J. Choung. The quasi-static response of moored floating structures based on minimization of mechanical energy, *J. Mar. Sci. Eng.* **2021**, 9 (9), 960. https://doi.org/10.3390/jmse9090960

[3] F. Depalo, S. Wang, S. Xu, G.C. Soares. Design and analysis of mooring system for a wave energy converter. *J. Mar. Sci. Eng.* **2021**, 9 (7), 782. https://doi.org/10.3390/jmse9070782

[4] I. Chatjigeorgiou, S. Mavrakos. Comparison of numerical methods for predicting the dynamic behavior of mooring lines. In: Proceedings of the the Ninth International Offshore and Polar Engineering Conference, Brest, France, May 30 – June 4, 1999. https://onepetro.org/ISOPEIOPEC/proceedings-abstract/ISOPE99/All-ISOPE99/24914

[5] O.M. Aamo, T.I. Fossen. Finite element modelling of mooring lines. *Math. Comput. Simul.* **2000**, 53, 415-422. https://doi.org/10.1016/S0378-4754(00)00235-4

[6] O.M. Aamo, T.I. Fossen. Finite element modelling of moored vessels. *Math. Comput. Model. Dyn. Syst.* **2001**, 7, 47-75. https://doi.org/10.1076/mcmd.7.1.47.3632

[7] J. Palm, G.M. Paredes, C. Eskilsson, F.T. Pinto, L. Bergdahl. Simulation of mooring cable dynamics using a discontinuous Galerkin method. In: Proceedings of the 5th Int. Conference on Computational Methods in Marine Engineering, Hamburg, Germany, May 29–31, 2013. https://upcommons.upc.edu/handle/2117/333008

[8] MathWorks. 6-DOF Joint-Program. https://www.mathworks.com/help/sm/ref/6dofjoint.html

[9] MathWorks. Simscape Multibody documentation. https://www.mathworks.com/help/sm/

APPLIED MECHANICS 2024

April 17th – 19th, 2024
Hotel Toliar, Štrbské Pleso
Slovakia

NUMERICAL CALCULATION OF DEFORMATION, STRESS DISTRIBUTION AND LIFE-TIME ESTIMATION IN BURIED POLYMER PIPES UNDER VARIOUS CONDITIONS

J. PODUŠKA[1]*, R. GRATZA[2], L. TRÁVNÍČEK[3], P. HELEŠICOVÁ[4], L. NÁHLÍK[5], P. HUTAŘ[1]

Numerical simulations of buried polymer pipes are necessary for the investigation of their long-term behavior. The demanded parameters may include just stress and deformations or even fracture mechanical parameters. Even though calculation of the buried pipe deformation and other parameters is quite a simple task, it usually runs into a fundamental problem of obtaining the material data for the characterization of the soil. These are hard to find, difficult to measure and, in the rare case they are available, they tend to be very scattered. Models using such data are then impossible to verify. This contribution proposes a workaround for this problem by connecting the numerical simulations with the available standards for the design of buried polymer pipes. The method is presented in several examples.

Keywords: buried pipes; polymer pipes; soil loads; fracture mechanics; lifetime calculations

INTRODUCTION

Finite element method (FEM) simulations of polymer pipes under various loading conditions are an essential part of method for lifetime estimation of polymer pipes based on linear-elastic fracture mechanics [1]. Apart from saving time, the advantage of using a FEM model for the pipe lifetime estimation is the possibility to include different loading conditions and capture their influence. The influence of internal pressure, external pressure and bending was described in [2] and the influence of residual stress in the pipe wall was dealt with in [3]. There are also a few examples of works, where external pressure from soil was included in the model and its influence on the estimated lifetime was quantified [4, 5].

[1] **Ing. Jan Poduška, PhD.; Prof. Ing. Pavel Hutař, Ph.D.**, Institute of Physics of Materials, Czech Academy of Sciences, Žižkova 513/22, 616 00 Brno, Czech Republic; poduska@ipm.cz
[2] **Ing. Roman Gratza, PhD.**, Institute of Structural Mechanics, Faculty of Civil Engineering, Brno University of Technology, Veveří 331/95, 602 00 _Brno, Czech Republic; Roman.Gratza@vut.cz
[3] **Ing. Lukáš Trávníček, PhD.**, Department of Polymer Engineering and Science, Montanuniversität Leoben, 8700, Leoben, Austria; lukas.travnicek@uniloeben.ac.at
[4] **Bc. Petra Helešicová**, Institute of Solid Mechanics, Mechatronics and Biomechanics, Faculty of Mechanical Engineering, Brno University of Technology, Technická 2896, 61669 Brno, Czech Republic; helesicova@ipm.cz
[5] **Prof. Ing. Luboš Náhlík, PhD.**, CEITEC IPM, Žižkova 513/22, 616 00 Brno, Czech Republic; nahlik@ipm.cz

For the fracture-mechanics-based lifetime estimation of a buried pipe, it is important to calculate the stress in the pipe wall caused by the deformation of its cross section by the pressure of the surrounding soil. The standard way of FEM calculation is to model a pipe surrounded by a large bulk of soil and define the interaction between the pipe and soil using contact elements. The soil is divided into several zones with different material parameters to represent conditions (e.g. compaction, soil type, etc.) in different parts of the trench and around it. However, these models are accurate only if the stiffness properties of the pipe and soil are accurately known. Therefore, it is necessary to have a reliable source of soil parameters and a reliable method to verify the FEM model. Various standards for design of buried pipes, such as the German ATV DWVK A127 [6] or the Austrian ÖNORM B5012 [7] can serve as both. The combination of standard calculation and FEM model provides an easily verifiable way to calculate stress and deformation of a buried pipe.

METHOD FOR NUMERICAL SIMULATION OF A BURIED PIPE

The method presented combines the standard calculation (based on the ATV-DVWK A127) and numerical simulation. The numerical simulations take the important material parameters or loading parameters from the ATV calculation.

Standard calculation

Calculation procedure based on the ATV-DVWK A127 standard was used as a referential model for the comparison with the FEM models. Its principle is the determination of soil pressure distribution acting on a buried pipe. the soil around the pipe in a trench is divided into 4 different zones with different parameters (compaction degree and modulus):

- **Zone 1**: the backfill zone; the original soil from the site, that was dug out to make the trench, is returned in this zone after pipe installation.
- **Zone 2**: the bedding zone; zone around the pipe, where often sand or well-graded gravel is used instead of the original soil to protect the pipe.
- **Zone 3**: original undisturbed soil next to the trench.
- **Zone 4**: undisturbed soil under the trench, the stiffest soil.

See scheme of the trench and the principle of the ATV calculation in Fig. 1.

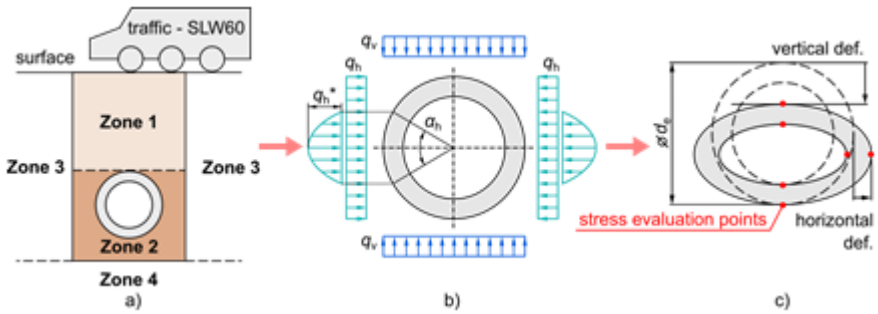

Fig. 1 Principle of ATV calculation method: a) the trench is represented by 4 different zones with different parameters, road traffic loads on the surface are included; b) soil pressure distribution on the pipe is calculated; c) deformation and stress are evaluated.

FEM models

Two different FEM models were created for the numerical simulation:

- **2D pressure model** – simple 2D model in plain strain that represents the situation from Fig.1(b), the linear pressures *q* are taken from the ATV calculation.

- **2D full model** – this is a larger 2D model that represents the situation from Fig. 1(a). A large portion of the soil is modelled around the pipe. The model is loaded by gravity and pressure from traffic. The soil is represented by a linear-elastic material model whose parameters are taken from the ATV standard.

Four different load cases are presented here to show the behavior of the model and the influence of traffic and quality of the embedding soil on the deformation of a buried pipe. The model pipe is a polyethylene (long term modulus 275 MPa, Poisson ratio of 0.33) pipe with the outer diameter d_o of 90 mm and the wall thickness s of 8.2 mm. The pipe is placed in a trench with the depth of 3.0 m and width of 1.0 m, there is no friction between the refill soil and trench walls. Varying parameters of the load cases are the following:

- **Case 1** – heavy traffic on the surface, the soil in zone 2 around the pipe is the same as the refill soil – soil category *G3* (cohesive mixed soils consisting of silt and gravel), 90% Proctor density, low stiffness.
- **Case 2** – no traffic on the surface, the soil in zone 2 around the pipe is the same as the refill soil – soil category *G3* (cohesive mixed soils consisting of silt and gravel), 90% Proctor density, low stiffness.
- **Case 3** – heavy traffic on the surface, the soil in zone 2 around the pipe is category *G2* (slightly cohesive soils – mostly gravel), 92% Proctor density, higher stiffness.
- **Case 4** – no traffic on the surface, the soil in zone 2 around the pipe is category *G2* (slightly cohesive soils – mostly gravel), 92% Proctor density, higher stiffness.

RESULTS

The most important parameters to evaluate from the models are the vertical deformation of the pipe (i.e. compression) and the tangential stress on the inside and outside of the pipe, which is the most important in case of crack initiation. The vertical deformation of the pipe in the 4 load cases is shown in Fig. 2.

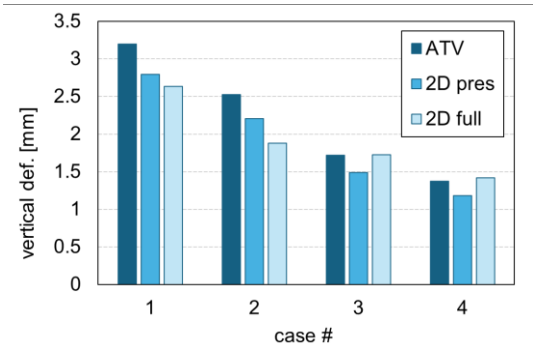

Fig. 2 Vertical deformation of the considered pipe (d_e = 90 mm, s = 8.2 mm) in 4 load cases.

The influence of the traffic load in the depth of 3.0 m is not very distinctive – it accounts for les than 1 mm change in deformation. The change in the bedding zone soil towards stiffer type, however, helps the pipe quite significantly, because it can take more of the load. In terms of stresses, this results in lowering the local maxima/minima of tangential stress by approximately 1 MPa – see Fig. 3.

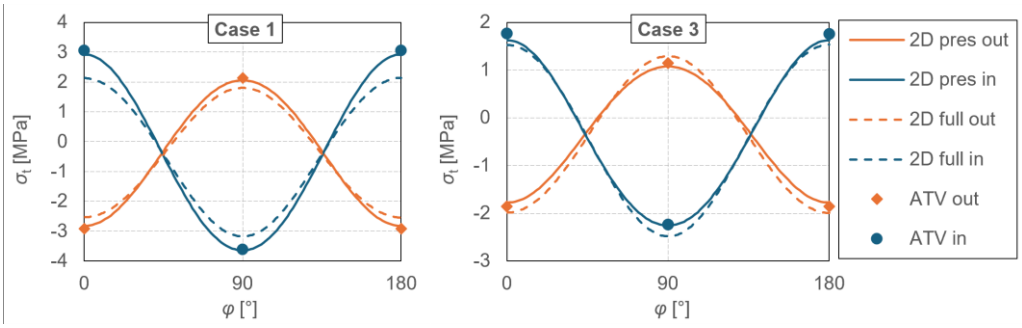

Fig. 3 Plots of tangential stress in the buried pipe in case 1 and 3 that differ in the zone 2 soil type.

The discrepancies in the deformation values can be attributed to the differences in the approach to calculation. The approach of the ATV is uses basic beam theory in plane stress whereas the FEM models assume plain strain, which is considered more accurate.

CONCLUSION

The presented method to calculate the deformation and stress in a buried pipe using a combination of standard and FEM proved as reliable. The agreement between the different models in various load cases is good, which means that this method can be used for more complicated cases such as analyses of buried pipes with cracks or pipes loaded by stones present in the soil. Such cases cannot be calculated by the standard but the parameters from the standard can be used as input for those. Also, the verification of the method for 3D models is going to be finished shortly.

ACKNOWLEDGEMENT

The research has been conducted in cooperation with Polymer Competence Center Leoben GmbH (PCCL, Austria) within the framework of the COMET-program of the Federal Ministry for Climate Action, Environment, Energy, Mobility, Innovation and Technology and the Federal Ministry for Digital and Economic Affairs with contributions by the Chair of Material Science and Testing of Polymers at Montanuniversität Leoben. The PCCL is funded by the Austrian Government and the State Governments of Styria, Lower Austria and Upper Austria.

REFERENCES

[1] A. Frank, et al. Fracture Mechanics Lifetime Prediction of Polyethylene Pipes. *Journal of Pipeline Systems Engineering and Practice* **2019**, 10 (1), 1-14.

[2] P. Hutař, et al. A numerical methodology for lifetime estimation of HDPE pressure pipes. *Engineering Fracture Mechanics* **2011**, 78 (17), 3049-3058.

[3] J. Poduška, et al. Residual stress in polyethylene pipes. *Polymer Testing* **2016**, 54, 288-295.

[4] J.W. Wee, S.Y. Park, B.H. Choi. Modeling and application of discontinuous slow crack growth behaviors of high-density polyethylene pipe with various geometries and loading conditions. *Engineering Fracture Mechanics* **2020**, 236 (July), 107205.

[5] J. Poduška, et al. Lifetime Calculation of Soil-Loaded Non-Pressure Polymer Pipes. *Key Engineering Materials* **2019**, 827, 141-146.

[6] ATV–DVWK–A 127: Statische Berechnung von Abwasserkanälen und -leitungen, 2000.

[7] ÖNORM B 5012: Statische Berechnung erdverlegter Rohrleitungen für die Wasserversorgung und die Abwasser-Entsorgung, 2008.

APPLIED MECHANICS 2024

April 17th – 19th, 2024
Hotel Toliar, Štrbské Pleso
Slovakia

COMPUTATIONAL ANALYSIS OF HYDRODYNAMIC LUBRICATION BEHAVIOR IN A PIN-ON-DISC TEST RIG

P. POLACH[1]*, J. RENDL[2], L. SMOLÍK[3], M. OMASTA[4], P. ŠPERKA[5], M. HAJŽMAN[6]

Hydrodynamic lubrication plays a crucial role in various mechanical setups, facilitating smooth contact between moving parts and stationary elements. This paper deals with the underlying mathematical models governing this process, exploring their significance and applications. We present the potential of computational modeling in the context of pin-on-disc setup, as a powerful tool for designing and conducting controlled experiments with precision. Additionally, we briefly introduce insights into an experimental test rig tailored specifically for studying hydrodynamic lubrication, outlining its design. Through numerical simulations, practical results are obtained that not only validate the developed models but also offer valuable insights into lubrication dynamics in technical practice.

Keywords: Tribology; Hydrodynamic lubrication; Surface contact; Numerical simulations; Pin-on-disc

INTRODUCTION

This paper deals with basic mathematical models of hydrodynamic contact lubrication, which can be used to investigate the significance and applications of these contacts. The pin-on-disc method is presented as a suitable tool for conducting tribology experiments. A combination of computational techniques and experimental approaches contributes to a better understanding of the behavior of hydrodynamically lubricated contacts.

Hydrodynamic lubrication is essential in numerous mechanical configurations involving interactions between moving components and stationary elements. These are, for example, journal

[1] **Assoc. Prof. Dr. Ing. Pavel Polach**, New Technologies for the Information Society, Faculty of Applied Sciences, University of West Bohemia, Technická 8, Plzeň, Czech Republic; ppolach@ntis.zcu.cz
[2] **Ing. Jan Rendl, Ph.D.**, New Technologies for the Information Society, Faculty of Applied Sciences, University of West Bohemia, Technická 8, Plzeň, Czech Republic; rendlj@ntis.zcu.cz
[3] **Ing. Luboš Smolík, Ph.D.**, New Technologies for the Information Society, Faculty of Applied Sciences, University of West Bohemia, Technická 8, Plzeň, Czech Republic; carlist@ntis.zcu.cz
[4] **Ing. Milan Omasta, Ph.D.**, Department of Tribology, Faculty of Mechanical Engineering, Brno University of Technology, Technická 2896/2, Brno, Czech Republic; milan.omasta@vut.cz
[5] **Ing. Petr Šperka, Ph.D.**, Department of Tribology, Faculty of Mechanical Engineering, Brno University of Technology, Technická 2896/2, Brno, Czech Republic; petr.sperka@vut.cz
[6] **Assoc. Prof. Ing. Michal Hajžman, Ph.D.**, Department of Mechanics, Faculty of Applied Sciences, University of West Bohemia, Technická 8, Plzeň, Czech Republic; mhajzman@kme.zcu.cz

and thrust bearings, piston rings, and thrust washers and seals. Low friction, high load-carrying capacity, and long service life are the main advantages of these contacts. It is obvious that based on the positive properties of this type of contact and their wide applicability in technical practice, it is important to study them in detail and look for ways to further improve their properties.

One of the most important directions in improving the properties of hydrodynamically lubricated contacts is surface microtexturing. The first mention of the favorable impact of surface texturing dates back to the 1960s by Hamilton [1]. Targeted surface treatments provide a range of advantages. Dimples on the surface can facilitate lubricant retention, trap wear particles, and reduce surface contact area and adhesion levels. In the hydrodynamic regime, these dimples can increase the bearing capacity due to local cavitation with asymmetric pressure distribution or inertia-related effects [2, 3].

Another way to enhance the tribological performance of hydrodynamically lubricated contacts is to replace the conventional no-slip boundary condition with a slip boundary condition. This approach is inspired by the effect of superhydrophobic surfaces. Practically, inducing limited slip can be achieved by applying chemicals or PVD (physical vapor deposition) coating [4]. Such modifications completely change fluid flow dynamics and pressure generation.

It has been discovered that even thermal effects can have a significant influence on the behavior of a lubricated contact [5]. Another mechanism that can have a positive impact is the viscosity wedge effect [6]. This phenomenon arises from the variations in liquid viscosity across the contact area and contributes to the generation of additional contact pressure [7].

As mentioned, improving the tribological performance of hydrodynamically lubricated contacts is influenced by various parameters. Given the complexity of the system and the importance of understanding the local behavior of the contact, a thorough insight into related phenomena is highly desirable. The pin-on-disc laboratory experimental setup is a widely utilized technique in tribological research. Through this approach, essential tribological parameters such as transmitted forces, oil film height, temperature, etc., can be investigated and documented. Subsequently, it is appropriate to develop mathematical models for simulating the experimental measurements conducted and to validate these models based on the measurement results. Once the mathematical models are validated, an analysis of possibilities to enhance the properties of the lubricated contact can be conducted.

HYDRODYNAMIC FLOW IN LUBRICATED CONTACTS

The most common approaches to simulate hydrodynamic lubrication in contacts depend on a numerical solution of the Reynolds equation [2], which describes the flow of a viscous lubricant in a thin gap. The Reynolds equation is a partial differential equation that can be obtained by simplifying the general Navier-Stokes (conservation of momentum) equations and combining them with the continuity equation (conservation of mass).

Assuming incompressible flow, and uniform viscosity and density in the film, the Navier-Stokes equations can be simplified into the following form [8]

$$\frac{\partial \mathbf{u}}{\partial t} + (\mathbf{u} \cdot \nabla)\mathbf{u} = \nu_0 \nabla^2 \mathbf{u} - \frac{\nabla p}{\rho_0} + \mathbf{g}, \tag{1}$$

where $\mathbf{u}$ is the velocity vector, ν_0, ρ_0 are the fluid kinematic viscosity and density, respectively, $\mathbf{g}$ includes external sources and ∇ is the vector differential operator. The inertia terms on the left-hand side make the Navier-Stokes equations nonlinear. The first term on the right represents viscous forces.

If the viscous and pressure terms dominate over inertia effects, the steady-state solution of Eq. (1) can be obtained by solving the Stokes equations [8]:

$$\mu_0 \nabla^2 \mathbf{u} - \nabla p + \rho_0 \mathbf{g} = \mathbf{0} \quad \text{and} \quad \boldsymbol{\nabla} \cdot \mathbf{u} = \mathbf{0}, \tag{2}$$

where $\mu_0 = \nu_0 \rho_0$ is the dynamic viscosity. To solve Eqs. (1) and (2) one must define boundary conditions.

The dimension of Eqs. (1) and (2) can be reduced by applying some boundary conditions. More specifically, the assumption of no slip at the top and bottom surfaces of the film allows the expression of the fluid velocity profile across the height of the film, i.e. in the z-direction. For example, if the velocity of the bottom surface is v_x and of the top surface is fixed, then the velocity profile is

$$u_x = \frac{z^2 - z\,h}{2\,\mu} \frac{\partial p}{\partial x} + v_x \left(1 - \frac{z}{h}\right), \tag{4}$$

where h is the film height at the point given by coordinates x and y. An analogous relation holds also for u_y. After substituting Eq. (4) into the continuity equation and integrating for z, one obtains a bulk flow in the x direction. The bulk flow can be further substituted into the Navier-Stokes (1) or Stokes (2) equations. A new partial differential equation called the Reynolds equation, is obtained by doing so (and also by neglecting body forces, inertia terms, and the variation of pressure across the fluid film). For hydrodynamic lubrication in a pin-on-disc tribometer, this equation takes the form [9]

$$\frac{\partial}{\partial x}\left(\frac{h^3}{12\,\mu}\frac{\partial p}{\partial x}\right) + \frac{\partial}{\partial y}\left(\frac{h^3}{12\,\mu}\frac{\partial p}{\partial y}\right) = \frac{\partial (v_x\,h)}{2\,\partial x} + \frac{\partial (v_y\,h)}{2\,\partial y} + \frac{\partial h}{\partial t}. \tag{6}$$

where the last (squeeze) term can be neglected if the steady-state solution is needed. This equation is the foundation of the classical lubrication theory. By solving this equation with appropriate boundary and geometric conditions, one may obtain pressure distribution and either film thickness $h = h(x, y)$ or load capacity. These parameters are the most important in lubrication theory because the pressure indicates how much force is transmitted through the contact, while the film thickness indicates a lubrication regime in which the contact is operating.

The Reynolds equation is often solved by the finite difference method [9], but the finite element and volume methods are also common [2].

PIN-ON-DISC METHOD

The pin-on-disc experimental setup involves a small pin interfacing with a rotating disc. An experimental approach developed at the Department of Tribology Brno University of Technology, which employs optical methods, was used to study the film thickness, the load-carrying capacity of the contacts, and, in the case of a textured surface, the influence of the various shapes, locations, and geometry of texture (in this case the dimples). The experimental test rig is extensively described in [10]. Scheme and real experimental test rig you can see in Fig. 1.

A series of experiments were carried out on the pin-on-disc test rig with various geometric configurations (inclination) and various operating parameters (disc load and speed). These experiments were conducted using both pins without textures and pins with different texture parameters. Initially, experiments were conducted with pins without textures to validate the initial experimental results against numerical simulations. Subsequently, the first set of experiments with textured pins was aimed at defining the suitable range for evaluating the effect of surface texturing. The subsequent phase was aimed at the explanation of the effect of surface texturing on lubricant film thickness, and friction. For each pin, minimum film thickness and friction force were evaluated as a function of normal force and speed, and compared with results obtained from smooth surfaces.

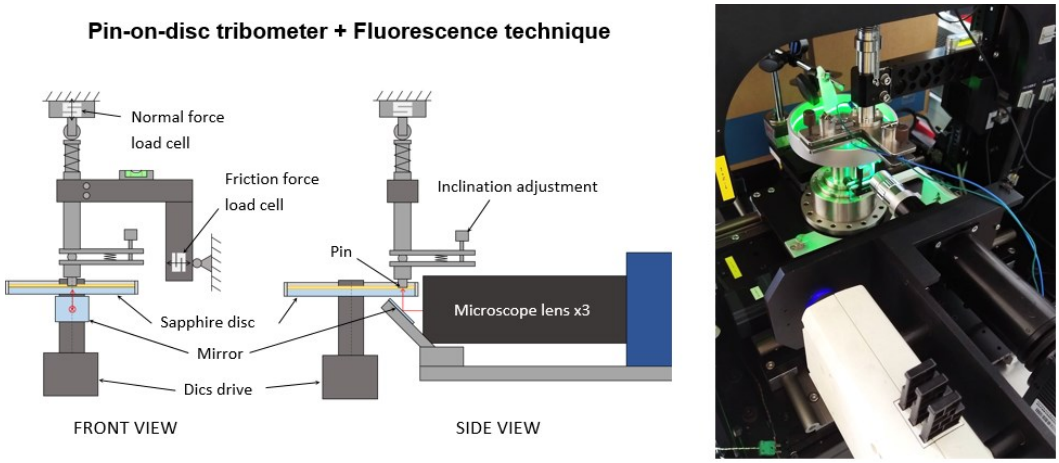

Fig. 1 Scheme and real experimental rig

The experimental results were compared with numerical simulations to validate the techniques and to discuss possible deviations. A numerical model of the pin-on-disc was developed and analysed. The operation conditions and study cases were stated based on the geometry of the proposed experimental test rig and various pin geometries. Two approaches were employed to study hydrodynamic lubrication between the pin and disc. Initially, a thin oil film approximation based on the Reynolds theory was utilized. This approach sufficiently describes the lubrication of smooth pins, but it is inefficient for textured surfaces. Subsequently, a pin-on-disc CFD (based on Navies-Stokes equations) model was used to validate the obtained results for a smooth pin and to analyze textured surfaces. The film height, rotation speed, pin inclination, hydrodynamic force, and friction force were studied for smooth pins.

The pin, with a diameter of 5.2 mm, was located on the disc at a radial center-to-center distance of 60 mm. The operating disc speed was 150 rpm. The isoviscous approximation defined by 186.9 mPa·s (operating temperature 300 K) and constant pin inclination angle 12 mm were supposed for the numerical simulations. Fig. 2 shows the comparison of the vertical hydrodynamic force calculated for both approaches employing the Reynolds and Navier-Stokes equations and vertical applied load during the experiments for various minimum film heights (thickness). Typical pressure distribution along the pin section and various minimum thicknesses is depicted in Fig. 3. The figure also contains the planar colormap of one chosen simulation case to depict the pressure distribution on the pin surface. Measured friction force in the pin-on-disc contact and evaluated from the simulations employing the Navier-Stokes equations are compared in Fig. 4. The discrepancies between the experimental and numerical results of the hydrodynamic and friction force may be caused mainly by isoviscous approximation in the numerical simulation contrary to the thermal effect present in the experiments and the constant pin inclination in the experiments is not perfectly achieved due to potential vibrations during the operation.

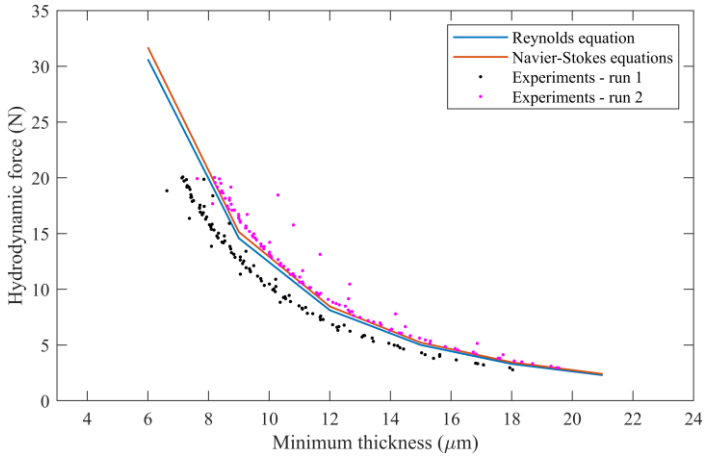

Fig. 2 Comparison between experimentally measured and calculated hydrodynamic force

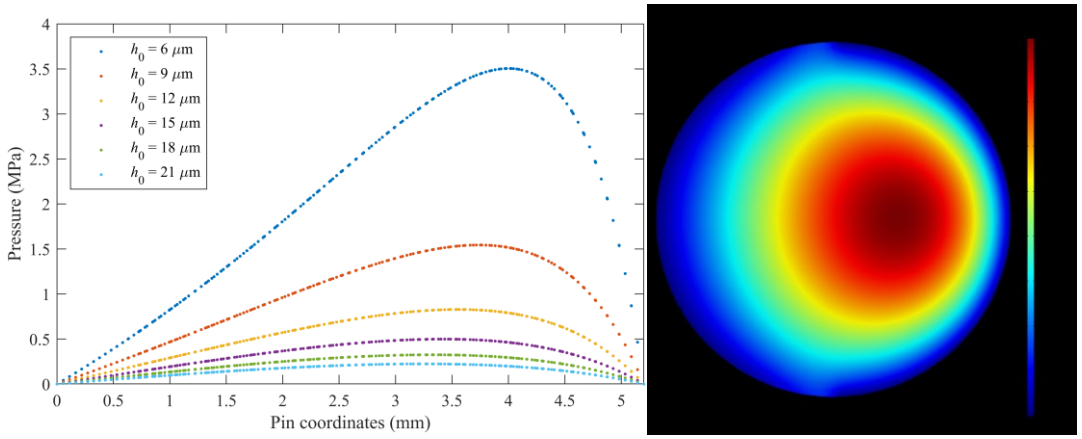

Fig. 3 Calculation of pressure along the pin diameter for various lubricant film thicknesses, and pressure distribution on the pin surface for a lubricant film thickness of 12 μm (based on Navier-Stokes equations)

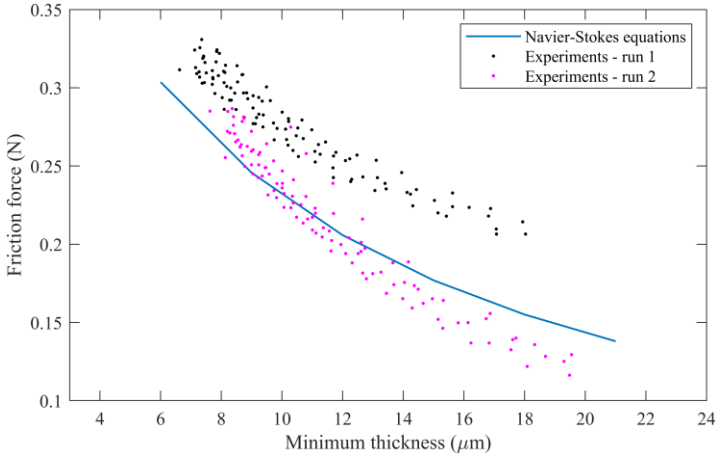

Fig. 4 Comparison between experimentally measured and calculated friction force within the lubricant film

CONCLUSION

This paper deals with basic mathematical models of hydrodynamic contact lubrication, which can be used to investigate the significance and applications of these contacts. The pin-on-disc method as a suitable tool for conducting tribology experiments is briefly introduced. By combining theoretical frameworks, computational techniques, and experimental approaches, we aim to advance the understanding of hydrodynamic lubrication and promote advances in engineering and related fields.

ACKNOWLEDGEMENT

This research work was supported by the Czech Science Foundation project 22-29874S "Thermohydrodynamic effects of boundary slip and surface texturing in sliding contacts". Chosen simulations were performed in the AVL Excite software which is available in the framework of the University Partnership Program of AVL List GmbH, and whose usage is greatly acknowledged.

REFERENCES

[1] D.B. Hamilton, J.A. Walowit, C.M. Allen. A Theory of Lubrication by Microirregularities. *Journal of Basic Engineering* **1966**, 88 (1), 177-185. DOI: 10.1115/1.3645799

[2] D. Gropper, L. Wang, T.J. Harvey. Hydrodynamic lubrication of textured surfaces: A review of modeling techniques and key findings. *Tribology International* **2016**, 94, 509-529. DOI: 10.1016/j.triboint.2015.10.009

[3] P. Lu, R.J.K. Wood. Tribological performance of surface texturing in mechanical applications – review. *Surface Topography: Metrology and Properties* **2020**, 8 (4), paper 043001. DOI: 10.1088/2051-672X/abb6d0

[4] J.H. Choo, R.P. Glovnea, A.K. Forrest, H.A. Spikes. A Low Friction Bearing Based on Liquid Slip at the Wall. *Journal of Tribology* **2007**, 129 (3), 611-620. DOI: 10.1115/1.2736704

[5] S. Cupillard, S. Glavatskih, M.J. Cervantes. 3D thermohydrodynamic analysis of a textured slider. *Tribology International* **2009**, 42 (10), 1487-1495. DOI: 10.1016/j.triboint.2009.05.021

[6] A. Cameron. Hydrodynamic Lubrication of Rotating Disks in Pure Sliding. A New Type of Oil Film Formation. *Journal of Institution of Petroleum* **1951**, 37, 471-486.

[7] X. Meng, M.M. Khonsari. Viscosity wedge effect of dimpled surfaces considering cavitation effect. *Tribology International* **2018**, 122, 58-66. DOI:10.1016/j.triboint.2018.02.011

[8] D.J. Acheson. Elementary Fluid Dynamics. Oxford University Press : Oxford, 1990. ISBN 978-0-19-859679-0

[9] Y. Hori. Hydrodynamic Lubrication. Springer-Verlag: Tokyo, Japan, 2006. ISBN 978-4-431-27898-6

[10] M. Hajžman, J. Rendl, L. Smolík, M. Omasta, P. Šperka. Methodology for the computational analysis of hydrodynamic lubrication in pin-on-disc experiments. Editors: I. Zolotarev, L. Pešek, M. S. Kozień, Proceedings of the International Colloquium DYMAMESI 2023 Cracow (Poland), Cracow University of Technology, 2023, 31-34. ISBN 978-80-87012-85-7

APPLIED MECHANICS 2024

April 17th – 19th, 2024
Hotel Toliar, Štrbské Pleso
Slovakia

MEASUREMENT OF RESIDUAL STRESS PROFILE USING MODIFIED SLOTTING METHOD AND NUMERICAL MODELLING

J. RAKUŠAN[1]*, P. DLHÝ[2], P. HUTAŘ[3], M. JAMBOR[4]

The residual stress measurement by relaxation is often linked with the complete destruction of the measuring sample. However, preserving the sample is very important in many cases. There are other non-destructive residual stress measurement methods. However, they are often expensive or cannot be performed. Therefore, attaching the strain gauge and cutting the specimen may be the only reasonable choice for residual stress measurement. This contribution deals with residual stress measurement by the modified slotting method. Modifying the slotting method allows the determination of the residual stress profile through the whole specimen width. It also preserves enough material to manufacture the specimen for, e.g., fatigue crack growth rate testing.

Keywords: Residual stresses; experimental measurement; finite element modelling

INTRODUCTION

Many different methods are used for residual stress measurement, such as destructive, semi-destructive and non-destructive. Relaxation techniques are often associated with partial or complete destruction of the sample. The semi-destructive method may be used when preserving samples for further analysis, such as fatigue life or crack growth rate measurement is required. Residual stresses are often variable, so sometimes the same sample on which the residual stresses were measured is wanted to be analysed further.

The residual stress can also be measured using non-destructive methods, but these methods can be expensive. Using a semi-destructive method combines the advantages of the destructive method (relatively easy to measure) and preserves the sample for further analyses.

This contribution deals with the residual stress determination by the modified slotting method. The modification allows the determination of residual stress through the whole width of the measured sample.

[1] **Bc. Jakub Rakušan**, Institute of Physics of Materials CAS, v. v. i., Žižkova 513/22, Brno, Czech Republic; rakusan@ipm.cz
[2] **Ing. Pavol Dlhý, PhD.**, Institute of Physics of Materials CAS, v. v. i., Žižkova 513/22, Brno, Czech Republic; dlhy@ipm.cz
[3] **Prof. Ing. Pavel Hutař, PhD.**, Institute of Physics of Materials CAS, v. v. i., Žižkova 513/22, Brno, Czech Republic; hutar@ipm.cz
[4] **Ing. Michal Jambor, PhD.**, Institute of Physics of Materials CAS, v. v. i., Žižkova 513/22, Brno, Czech Republic; jambor@ipm.cz

The measured samples are manufactured directly from the induction hardened railway axles. Fig. 1 a) shows a schematic illustration of one sample position in the axle. Mainly the axial residual stress is preserved after the sample cut out. Due to the specimen geometry, the tangential residual stress is relaxed. The residual stress as mentioned before is dominant in one direction (axial), allowing a presumption of uniaxial state of stress. Consequently, strain gauges can be attached in a single direction. Fig. 1 b). shows the direction and position of attached strain gauges schematically.

Before the experiment, it was necessary to verify the functionality of the method, for which the finite element method (FEM) was used. The slot parameters, width, and depth were chosen based on an FEM study. Chosen width, and depth are 6 mm and 2 mm, respectively.

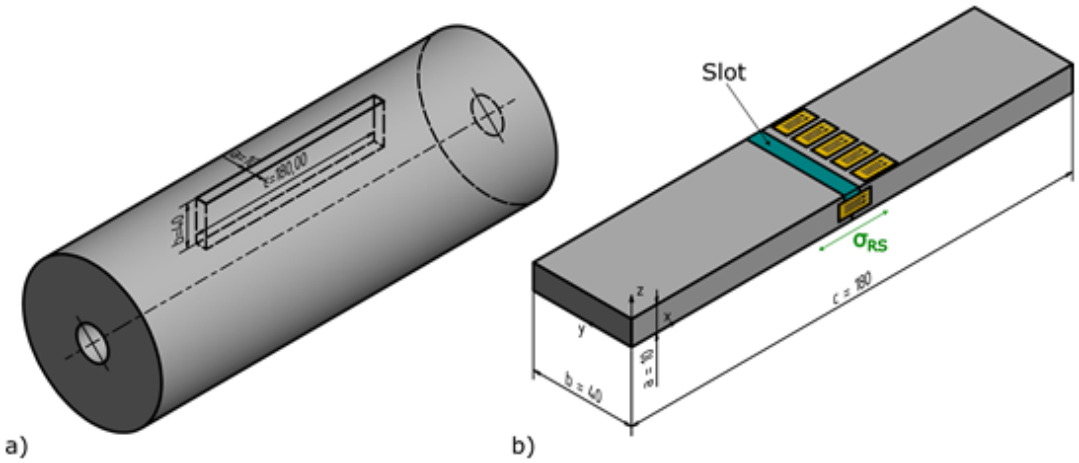

Fig. 1 a) schematic illustration of the sample position in the axle; b) Geometry of the sample

METHODOLOGY AND RESIDUAL STRESS MEASUREMENT

Two samples were measured (called sample A and sample B). Samples were manufactured from the same railway axle with spacing of 120° around the circumference of the axle. Fig. 2 shows the procedure scheme for residual stress determination. By the slot manufacturing, the strain was released and measured by the strain gauges. After the measurement, data were post-processed. Postprocessing was necessary to check the effect of residual stress release on the measured data and to detect and adjust any anomalies in measured strain after the experiment. Next, the simulation of redistribution of residual stresses was made as the first step. The second step, the slot was added into the FEM model and residual stresses were partially released. From areas, where strain gauges were attached, mean values of measured strains were obtained. Measured strain was calculated as difference between the first step (model of the intact specimen without the slot removal) and the second step (model with the slot removed). After determining the values of strains and stresses using FEM analysis, measured and FEM results data were compared. If the sum of the errors, which has been defined as: $error = \sum \frac{\varepsilon_{meas} - \varepsilon_{calc,i}}{\varepsilon_{meas}}$, was less than 1%, than the final result is obtained. In case where the sum of the errors is more, the residual stresses implemented to FEM model are changed by using the difference between measured and FEM obtained strains. The FEM simulation runs again until the error is less than 1%. The residual stress is determined iteratively because it is an inverse problem.

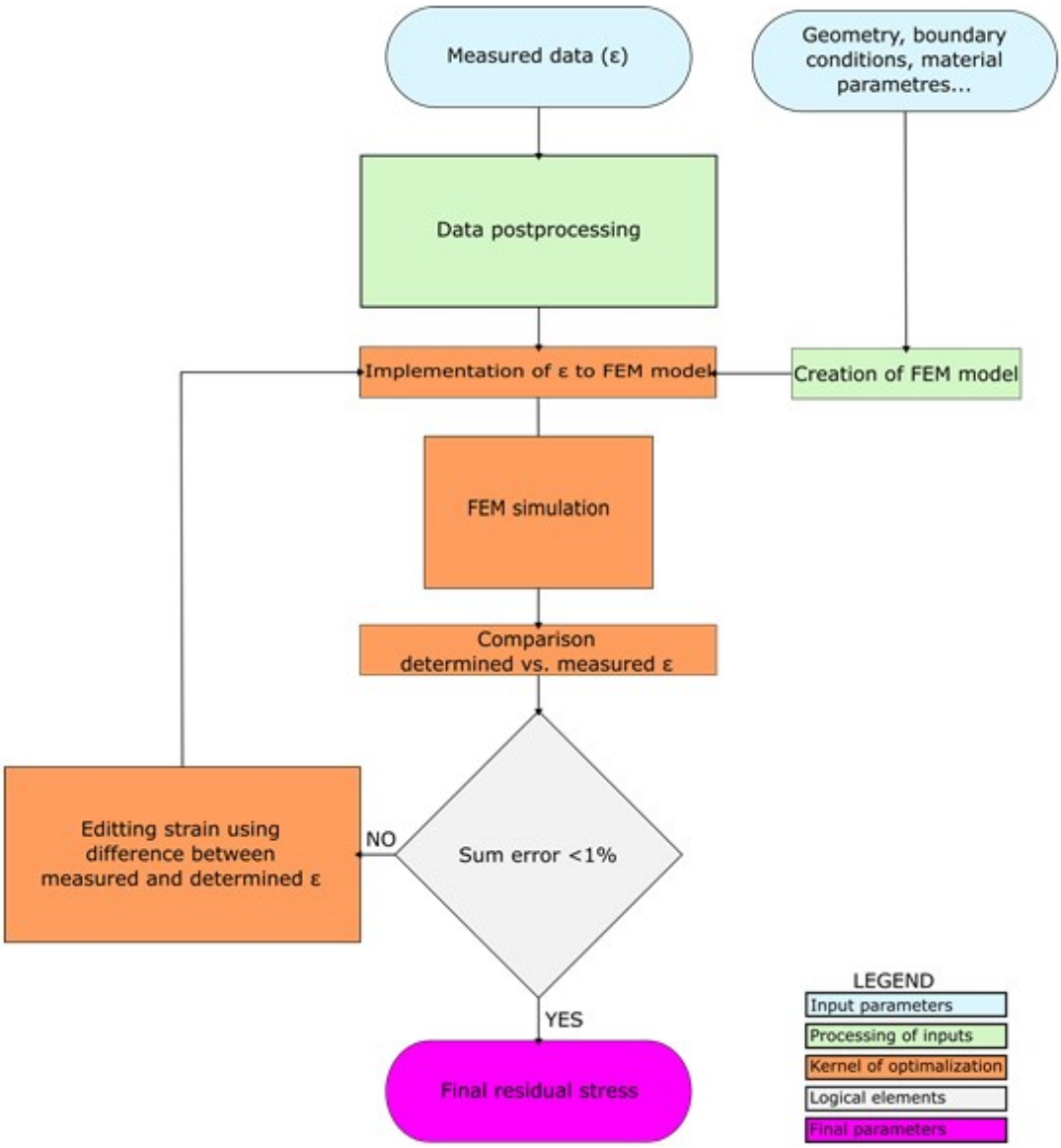

Fig. 2 Scheme of residual stress determination

RESULTS OF RESIDUAL STRESS MEASUREMENT

Residual stresses were determined using scheme (Fig. 2) above for both samples (A, B). Fig. 3 shows residual stresses determined on both samples. On the horizontal axis we can see distance from the external surface of the original railway axle (y axis in Fig. 1 b)) and the vertical axis describes magnitude of the determined residual stress in axial direction (x axis in Fig. 1 b)). The residual stress had sinus waveform. Near the external surface, residual stress is around $+25\ MPa$. With increasing distance from the external surface residual stress is decreasing to $-120\ MPa$ and then it rises to $20\ mm$ depth to its total maximum of $+210\ MPa$. After reaching maximum residual stress decreases back to the negative values up to total minimum $-220\ MPa$ at the depth of $40\ mm$.

Fig. 3 shows determined residual stress profile. Measured points are marked as crosses and pink spline show interpolation of mean values of stresses in each point. The measurement variance is adequate for the utilized measurement chain and the experience of the experimenters.

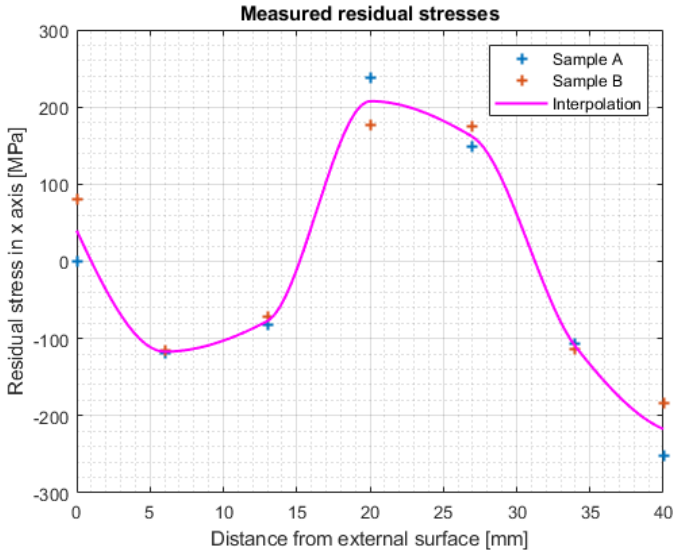

Fig. 3 Measured residual stresses

CONCLUSION

The developed methodology is capable of residual stress determination only with the partial destruction of the samples. By measuring the residual stresses with a modified slotting method, the magnitudes and directions of the residual stresses can be obtained relatively quickly. Knowledge of residual stress distribution helps properly describe the sample's behaviour during crack growth rate measurements.

ACKNOWLEDGEMENT

This research has been supported by grant No. CK03000060 "Advanced design methodology of railway axles for safe and efficient operation" of The Technology Agency of the Czech Republic and the equipment and the base of research infrastructure IPMinfra were used during the research activities.

REFERENCES

[1] G.S. Schajer. Practical Residual Stress Measurement Methods. Chichester, UK: John Wiley & Sons, Ltd, 2013. ISBN 9781118402832

[2] M. Vlk, L. Houfek, P. Hlavoň, P. Krejčí, V. Kotek, J. Klement. Experimentální mechanika. VUTIUM, Brno, CZ, 2003.

[3] M.D. Olson, B.T Watanabe, T.A Wong et al. Near Surface Residual Stress Measurement Using Slotting. *Exp. Mech*. **2022**, 62, 1401-1410. https://doi.org/10.1007/s11340-022-00858-2

[4] F. Haiyang, B. Pan, R. Kang. Recent progress of residual stress measurement methods: A review. *Chinese Journal of Aeronautics* **2021**, 34 (2), 54-78. DOI: https://doi.org/10.1016/j.cja.2019.10.010

APPLIED MECHANICS 2024

April 17th – 19th, 2024
Hotel Toliar, Štrbské Pleso
Slovakia

DRIVE SELECTION FOR CRAWLER MOBILE ROBOT

J. RDUCH[1], P. JURECZKO[2]

The article describes the process of selecting a drive for a prototype of an electric universal crawler platform. At the beginning, the goals and assumptions of the project were specified. Then the concept of the vehicle in question was shown. The main part of the work presents the process of calculating the required engine power. The obtained results were compared with another method of determining the power of a tracked vehicle. Based on those values, specific commercially available components were selected. The last part presents a working prototype based on previous calculations. The tests then allowed for the formulation of conclusions.

Keywords: Tracked; Crawler; Electric; Drive

INTRODUCTION

Modern industrial plants are characterized by a high degree of automation and robotization. Therefore, they use various types of mobile devices on a large scale. They are most often found as transport vehicles in warehouses, cooperating with other infrastructure elements such as conveyors. Often, these are also autonomous vehicles (AGVs) that eliminate humans from the operator role. This allows you to reduce costs and increase efficiency.

Mobile robots equipped with a frame are used, among others, by sappers. This makes it possible to operate in dangerous situations without endangering human life. After installing an appropriate manipulator, it is possible to perform work in situations where a classic industrial robot is impossible to use due to its range.

Remotely controlled vehicles are also becoming increasingly popular as platforms for weapons assembly. Examples of such solutions are TALON SWORDS robots or Perkun anti-aircraft units.

PROJECT ASSUMPTIONS

The drive is selected for a specific platform with the following parameters:

- Length – 0,85 m
- Body width– 530 mm

[1] **Jacek Rduch, MSc. Eng.**, Department of Theoretical and Applied Mechanics, Faculty of Mechanical Engineering, Silesian University of Technology, Konarskiego 18 A Street, Gliwice 44-100, Poland; jacek150497@o2.pl
[2] **Pawel Jureczko, PhD. Eng.**, Department of Theoretical and Applied Mechanics, Faculty of Mechanical Engineering, Silesian University of Technology, Konarskiego 18 A Street, Gliwice 44-100, Poland; pawel.jureczko@polsl.pl

- Running system consisting of two rubber tracks in size 180x72x36
- Weight of frame and tracks 135 kg

Assumptions and goals to be achieved were also formulated:

- Maximum ground slope 15%
- Acceleration 1 m/s^2
- Maximum speed 5 km/h
- Load capacity 100 kg

DRIVE SELECTION

The most important element when selecting the parameters of the drive system is to determine all the resistances that the vehicle will have to overcome. The key factor influencing this is the weight of the device. The mass of the drive unit with other components was estimated at 100 kg and was added to the already known mass of the frame and tracks. After taking into account the lifting capacity and rounding up, the vehicle weight was 350 kg.

Determining the friction force requires knowledge of the friction coefficient. Roads in poor condition or cobblestones were considered to be the surface on which the vehicle will move, which corresponds to a coefficient value of 0.05 [1].

Calculations

The calculations began with drawing the forces acting on the vehicle while climbing the assumed hill (Fig. 1). The angle α is 10° and the diameter of the drive wheel is 0.293 m.

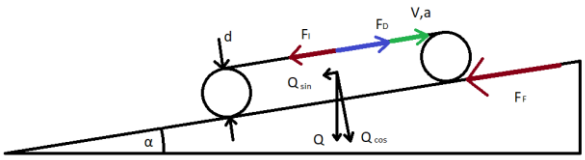

Fig. 1 Forces acting on the vehicle

First, the components of the gravitational force acting parallel and perpendicular to the ground were determined.

$$Q_{cos} = m \cdot G \cdot \cos\frac{\alpha \cdot \pi}{180} = 3381 \text{ N} \quad (1)$$

$$Q_{sin} = m \cdot G \cdot \sin\frac{\alpha \cdot \pi}{180} = 596 \text{ N} \quad (2)$$

m – vehicle weight [kg],

G – force of gravity = 9,81 N,

α – elevation angle [°].

On this basis, the friction force was determined (Eq. (3)) and then, after taking into account the acceleration, the inertia force was determined (Eq. (4)).

$$F_F = Q_{cos} \cdot f = 169 \text{ N} \quad (3)$$

$$F_I = m \cdot a = 350 \text{ N} \quad (4)$$

f – friction coefficient,

a – acceleration.

The total resistance force of the movement was calculated as the sum of the individual resistances (Eq. (5)).

$$F_I = Q_{sin} \cdot F_F \cdot F_I = 1115 \text{ N} \tag{5}$$

When turning a tracked vehicle, the friction between the tracks and the ground plays a very important role. The analysis of this situation began again with a sketch with marked forces (Fig. 2). The worst case was considered, i.e. rotation around its own axis.

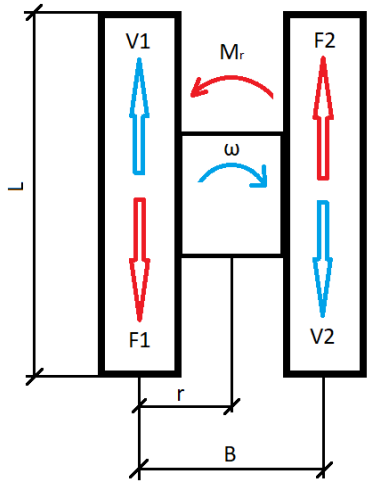

Fig. 2 Forces acting during turning

First, the turning resistance was determined (Eq. (6)) assuming a resistance coefficient μ_{smax} of 0.9 corresponding to a dry dirt road [1].

$$\mu_s = \frac{\mu_{smax}}{0{,}92+0{,}15 \cdot \frac{r}{B}} = 0.905 \tag{6}$$

Then, the track resistance forces were determined (Eq. (7,8)). The difference between them is due to being on a hill.

$$F1 = \frac{\mu_s \cdot m \cdot G \cdot L}{4 \cdot B} \cdot \cos\left(\frac{\alpha \cdot \pi}{180}\right) + \frac{Q_{sin}}{2} + \frac{F_F}{2} = 1285.33 \text{ N} \tag{7}$$

$$F2 = \frac{\mu_s \cdot m \cdot G \cdot L}{4 \cdot B} \cdot \cos\left(\frac{\alpha \cdot \pi}{180}\right) - \frac{Q_{sin}}{2} + \frac{F_F}{2} = 689.10 \text{ N} \tag{8}$$

The calculated forces must be overcome by the motors. Therefore, the required torque of one of them was calculated (Eq. (9)), taking into account the radius of the drive wheel r = 0.1465 m.

$$M = \frac{F1+F2}{2} \cdot r = 144.63 \text{ Nm} \tag{9}$$

Due to the need to obtain such a high torque, it was decided to use a worm gear, which additionally provides self-locking. The rotational speed of the output shaft was determined (Eq. (10)) based on the assumed vehicle speed V=1.39 m/s.

$$n = \frac{V \cdot 60}{2 \cdot \pi \cdot r} = 90.5 \text{ rpm} \tag{10}$$

From the obtained values, the power of a single drive was calculated (Eq (11)).

$$P = \frac{M}{\omega} = 1.37 \text{ kW} \tag{11}$$

The results were compared with the values obtained using Eq. (13). Previously, the unit power P_u had to be determined using Eq. (12). The calculations assumed an efficiency of the drive system n_m of 0.6 and an overload index Δ of 1.8 [1].

$$P_u = \frac{f+\frac{\alpha}{100}}{270 \cdot n_m \cdot (0.95-0.005 \cdot V)} \cdot 1000 \cdot V \cdot \frac{1}{36} = 7.55 \text{ kW/t} \quad (12)$$

$$P = \frac{P_u \cdot m}{2000} \cdot \Delta = 1.31 \text{ kW} \quad (13)$$

Elements selection

When selecting specific components, the required power was assumed to be approximately 40% higher than that designated to overcome resistances not previously taken into account, resulting from, among others, inaccuracies in manufacturing, assembly or track tension. Due to the high power, it was decided to use a 60V power supply, which will reduce the current in accordance with Eq. 14 [2].

$$P = U \cdot I \quad (14)$$

Analyzing the available drives, a gear motor was selected consisting of a brushless motor with a power of 2.2 kW and a RVM90 worm gear with a gear ratio of i = 30.

PROTOTYPE

The selected drives were installed in the vehicle prototype. Completion of the project also allowed us to verify the assumed weight of the vehicle, which ultimately amounted to 320 kg. Tests carried out in various conditions showed the correct selection of drive elements.

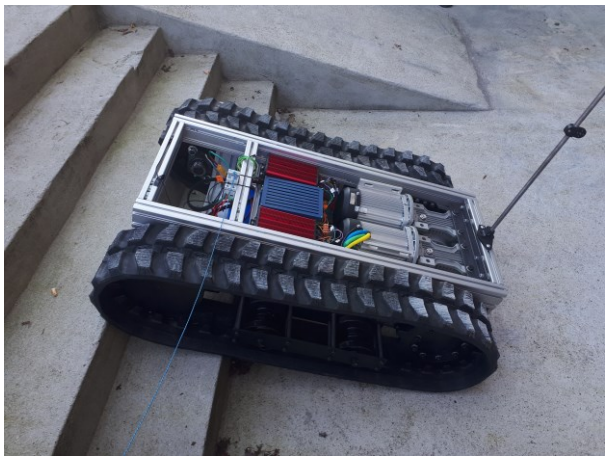

Fig. 3 Prototype during tests

CONCLUSION

Both methods gave similar results. The use of a formula taken from the literature required the estimation of I coefficients, which resulted in a value that was 5% lower. Tests of the built prototype confirmed the correctness of the calculations. The solutions offered by manufacturers allow the selection of components close enough to those required to ensure proper operation.

REFERENCES

[1] Z. Burdziński. Teoria ruchu pojazdu gąsienicowego. WKŁ : Warszawa, Poland, 1972.

[2] J. Osiowski, J. Szabatin. Podstawy teorii obwodów Tom 1. PWN : Warszawa, Poland, 2016. ISBN 9788301187217

APPLIED MECHANICS 2024

April 17th – 19th, 2024
Hotel Toliar, Štrbské Pleso
Slovakia

SOLVER ANALYSIS FOR A ROTARY MACHINE MODEL IN MSC.ADAMS

Z. ŠAVRNOCH[1]*, A. SAPIETOVÁ[2], V. DEKÝŠ[3], K. PIJÁKOVÁ[4]

Successful simulation of rotary machine dynamics heavily relies on selecting a numerical solver appropriate for the model's characteristics. This study investigates the performance of various solvers within MSC.ADAMS for a rotary machine model. The model incorporates flexible elements, realistic bearing representations, and potential nonlinearities arising from component interactions. Comparative analysis is conducted between implicit (GSTIFF) and explicit (HHT) solvers, considering their accuracy, computational efficiency, and stability. Key findings explore how factors such as stiffness variations, dynamic loading, and contact forces influence solver choice. The study concludes with recommendations for optimal solver selection strategies in ADAMS, enhancing simulation reliability and efficiency for rotary machine design analysis.

Keywords: Adams View; Rotordynamics; Solver; Jeffcott rotor; GSTIFF; HHT

INTRODUCTION

Rotary machines are essential components across countless industries, powering diverse applications from manufacturing equipment to transportation systems. Accurate and efficient simulation of their dynamic behavior is crucial for robust design, performance analysis, and troubleshooting. Numerical modeling programs like MSC.ADAMS facilitate such simulations, offering a range of solvers to computationally solve a system's equations of motion.

Selecting the most suitable solver is important for achieving reliable simulation results. The choice depends heavily on the model's characteristics. While implicit solvers often demonstrate superior accuracy for stiff systems, explicit solvers can excel in terms of computational efficiency and stability under certain conditions [1, 3]. Rotary machine models may exhibit significant nonlinearities due to component interactions, such as those within bearings, flexible bodies or contact phenomena, further complicating solver selection [2].

This study aims to provide clarity in solver selection for rotary machine simulations within MSC.ADAMS. Specifically, it investigates the performance of implicit (GSTIFF) and explicit (HHT)

[1] **Ing. Zdenko Šavrnoch**, Department of Applied Mechanics, Faculty of Mechanical Engineering, University of Žilina, Univerzitná 8215/1, Žilina, Slovak republic; zdenko.savrnoch@fstroj.uniza.sk
[2] **Prof. Ing. Alžbeta Sapietová, PhD.**, Department of Applied Mechanics, Faculty of Mechanical Engineering, University of Žilina, Univerzitná 8215/1, Žilina, Slovak republic; alzbeta.sapietova@fstroj.uniza.sk
[3] **doc. Ing. Vladimír Dekýš, CSc.**, Department of Applied Mechanics, Faculty of Mechanical Engineering, University of Žilina, Univerzitná 8215/1, Žilina, Slovak republic; vladimir.dekys@fstroj.uniza.sk
[4] **Ing. Katarína Pijáková**, Department of Applied Mechanics, Faculty of Mechanical Engineering, University of Žilina, Univerzitná 8215/1, Žilina, Slovak republic; katarina.pijakova@fstroj.uniza.sk

solvers with identical conditions. Model complexity and solver performance metrics are considered to offer practical recommendations for enhancing simulation accuracy and efficiency in rotary machine design analysis.

MODEL DESCRIPTION

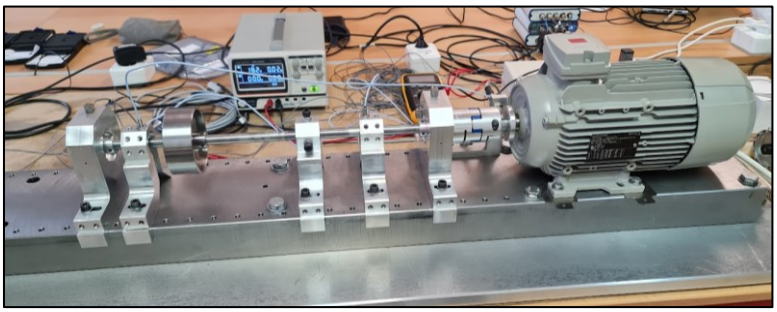

Fig. 1 Real representation of an analyzed model - Rotorkit TU Ostrava

This study utilizes a Laval/Jeffcott rotor model to investigate solver performance in MSC.ADAMS View. Key model components and their characteristics are as follows:

1. Shaft: The shaft (ϕ15-L550) is modeled as a uniform rod with a circular cross-section. It is represented as a flexible body using the View Flex function in Adams software. Material of the shaft is steel, which is specified from the Adams material library. The Young's modulus of the steel is 207 GPa, the Poisson's ratio is 0.29, and the density is 7801 kg/m^3.
2. Rigid Disk: A mass imbalance is introduced by a single rigid disk mounted on the flexible shaft at a distance equal to 1/4 of the bearing distance. The disk's mass is 1.41 kg, and its moments of inertia around the x, y, and z axes are Ixx = 1980.0672 kg·mm^2, Iyy = 1123.5965 kg·mm^2 and Izz = 1123.579 kg·mm^2.
3. Bearings: Shaft is supported by two SKF 61805 deep groove ball bearings with C0 clearance. Bearings are modeled with Adams Bearings Plugin (Machinery toolbox) as detailed representations, incorporating their stiffness, potential nonlinearities, and realistic contact behavior.
4. Shaft shackles: Aluminium elements between bearings and shaft acting like a shaft adapter.

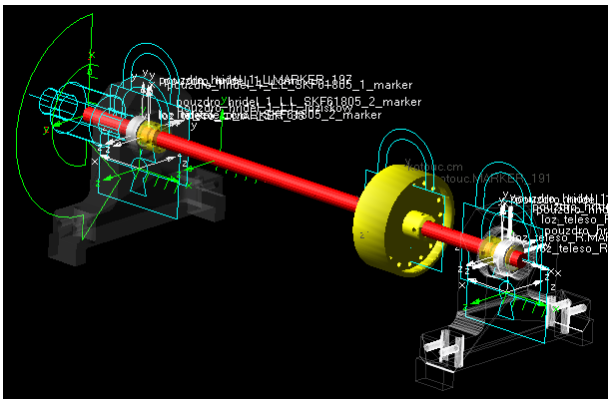

Fig. 2 Numerical model analyzed in Adams View

SOLVER DESCRIPTION

In terms of numerical analysis, two solvers/integrators can be used for the evaluated model: GSTIFF and HHT. According to the Adams Solver User Guide, both are recommended, yet they employ different calculation methods and rely on the model's elements [3].

GSTIFF Solver

An implicit solver designed for stiff systems where simulation speed may be less crucial than high accuracy. GSTIFF is the most widely used and tested integrator in Adams. It offers two formulations:

- I3: Prioritizes displacement errors, suitable for most numerically stiff models. Computationally more efficient but may be less accurate for velocities and accelerations compared to SI2.
- SI2: Emphasizes velocity errors, making it valuable where precise velocities or high-frequency oscillations are important. More accurate for velocities and accelerations but computationally slower than I3 [4].

HHT Solver

An explicit solver known for its computational efficiency and stability at small time steps. It might exhibit less accuracy for high-frequency oscillations compared to GSTIFF.

The HHT integrator is based on the method proposed by H.M. Hilber, T.J.R. Hughes, and R.L. Taylor [5]. The method is widely used in the structural dynamics community for the numerical integration of second order ordinary differential equations that are obtained at the end of finite element discretization.

RESULTS

Numerical simulation was performed for the balanced system and for the system with 3 grams of unbalanced mass which is roughly 0.2 % of the disk mass. Simulation time was 20 s with step size 0.0001 and angular acceleration 50 rad/s^2. For a better contrast, two more solvers are added to comparison, namely Newmark (Explicit/Implicit) and HASTIFF (Implicit). Following set of graphs shows the translational displacement of the left bearing marker representing the bearing center of gravity.

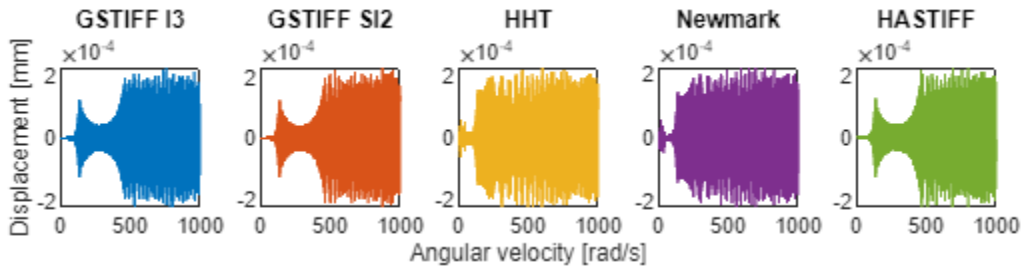

Fig. 3 Simulation results of different solvers depicting the vertical translational displacement (y-axis) – balanced system

Explicit solvers struggle in accurately capturing stabilization phenomena beyond the first critical angular velocity in rotor system. The dynamic behavior during and after stabilization phases might require even smaller time steps. Bearings are inherently nonlinear. The accuracy and stability of each solver can be strongly influenced by how well they handle nonlinear effects as the system interacts with higher rotational velocities.

Following sets of graphs represent translational velocity of the same bearing marker along y-axis for the system with unbalanced mass.

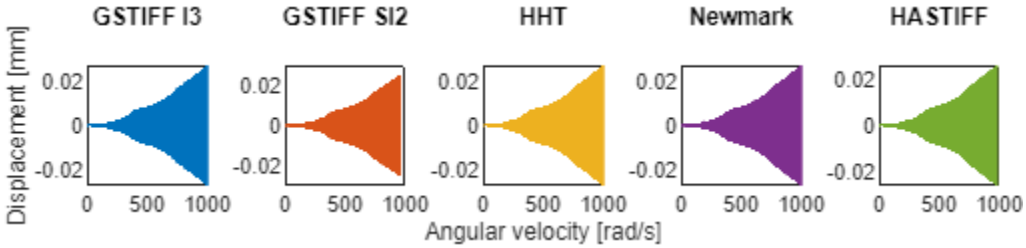

Fig. 4 Simulation results of different solvers depicting the vertical translational displacement (y-axis) – unbalanced system

The small imbalance might keep rotor system primarily within a linear response regime. Under this condition, the differences between explicit and implicit solvers become less visible, what can explain the similar results.

CONCLUSION

The objective of this paper was to assess and compare the performance of the most widely used and recommended integrators/solvers available in Adams View software. The primary focus was on achieving accurate results with stability while minimizing computational time.

To answer which has a higher impact on the system, the nonlinearity inherited from detailed bearings or the (linear) deformation of the shaft, the nonlinear effects from the bearings likely dominate. Explicit solvers like HHT struggle to capture the high-frequency oscillations after the first critical speed, leading to numerical errors. As such, there's no single "best" solver for this application. All solvers involve trade-offs, and the most suitable solver must be chosen according to the specific simulation goals and model characteristics. If simulations requiring numerous iterations or very small time-steps might benefit from HHT's efficiency. If precise velocities, accelerations, or high-frequency responses are crucial, GSTIFF (particularly SI2) may be necessary.

ACKNOWLEDGEMENT

This article has been supported by the grant project 01/0753/24 VEGA and 011/ŽU-4/2022 KEGA.

REFERENCES

[1] A. Sapietová, V. Dekýš, L. Jakubovičová, P. Novák, and M. Sapieta. Dynamika riešená v programoch Matlab a MSC.ADAMS. Žilina : Žilinská univerzita, 2023. ISBN 9788055419565

[2] M. Byrtus, M. Hajžman, V. Zeman. Dynamika rotujících soustav. Západočeská univerzita v Plzni, 2010. ISBN 978-80-7043-953-1

[3] ADAMS Solver User Guide for Adams 2023.4 by Hexagon. Product documentation.

[4] K.E Brenan, S.I. Campbell, L.R. Petzold. Numerical Solution of Initial Value Problems in Differential-Algebraic Equations. Classics in Applied Mathematics, 1996. ISBN: 0-89871-353-6

[5] H.M. Hilber, T.J.R. Hughes, R.L. Taylor. Improved numerical dissipation for time integration algorithms in structural dynamics. *Earthquake Eng. and Struct. Dynamics* **1977**, 5 (283292).

APPLIED MECHANICS 2024

April 17th – 19th, 2024
Hotel Toliar, Štrbské Pleso
Slovakia

EXPERIMENTS WITH MULTI DEGREES OF FREEDOM SYSTEMS OF ACTIVE RESONATORS

Z. ŠIKA[1]*, K. KRAUS[2]

The contribution is devoted to experiments with multi degrees of freedom active absorber demonstrators. The active absorber demonstrators are tuned to approach the ideal of a dynamically isotropic absorbing mechanical system with one multiple eigenfrequency. The goal of the researched devices is the ability to eliminate spatially complex vibration of the primary system. Active control is realized using a several voice-coil actuators with optical position sensing of the absorber mechanism leg lengths. The set of distributed 1 DOF absorbers as well as one compact 3 DOF mechanism are tested. The main problem is a complex nonlinear character of friction and damping whose identification, simulation and on-line elimination is investigated in order to create ideal absorbers by feedback control.

Keywords: Active vibration absorber; System of multiple active absorbers; Compact active absorbing mechanism; Unifrequency absorbing system; Identification and elimination of nonlinear passive resistances

INTRODUCTION

Active vibration reduction by various methods is among the intensively developing areas of mechatronics of various types of machines and other technical systems [1]. One of the important methods of active vibration reduction is active vibration absorption. This is an alternative to the well-known passive absorption, in which passive elements such as masses, springs and dampers are supplemented by actuators, which can be voice-coils, piezo-actuators and others. The fundamental advantage of the active version of absorption is the significantly wider adaptability of interventions and the overall improvement of the possibilities of influencing the behavior of the primary system whose vibration are to be reduced.

The long time developed unique concept of active vibration absorption creates a so-called delayed resonator [2], which by delaying the measured quantities, such as e.g. acceleration of the absorbing mass [3], and using it for an actuator feedback creates a resonator that appears ideal

[1] **prof. Ing. Zbyněk Šika, PhD.**, Department of Mechanics, Biomechanics and Mechatronics, Faculty of Mechanical Engineering, Czech Technical University in Prague, Technická 4, 160 00 Praha 6, Czech republic; Zbynek.Sika@fs.cvut.cz

[2] **Ing. Karel Kraus**, Department of Mechanics, Biomechanics and Mechatronics, Faculty of Mechanical Engineering, Czech Technical University in Prague, Technická 4, 160 00 Praha 6, Czech republic; Karel.Kraus@fs.cvut.cz

(without damping) and can be adaptively tuned to the required frequency. One of recent generalization of the delayed resonator idea is the concept of dynamically isotropic (unifrequency) compact planar [4] or spatial [5] absorption mechanisms for eliminating geometrically complex vibration. Paper [6] develops the concept of using a compact absorber with three degrees of freedom for absorbing the vibrations of a robot moving in the workspace. The presented contribution is devoted to experiments with absorber demonstrators, on the one hand a system of four distributed 1DOF absorbers and on the other hand a compact 3DOF absorber forming a planar mechanism. The main problem with existing demonstrators are the non-linear dissipative forces, which are difficult to eliminate.

IDENTIFICATION AND ELIMINATION OF NON-LINEAR PASSIVE RESISTANCES FOR DISTRIBUTED SET OF 1-DOF ABSORBERS

The goal of 1-DOF absorbers set development was to get close to ideal absorbers by the active control. For the given implementation of the absorbers on the demonstrator (see Fig. 1), this was not successfully achieved using the delayed resonator concept, apparently due to the significantly non-linear frictional forces in the linear bearings.

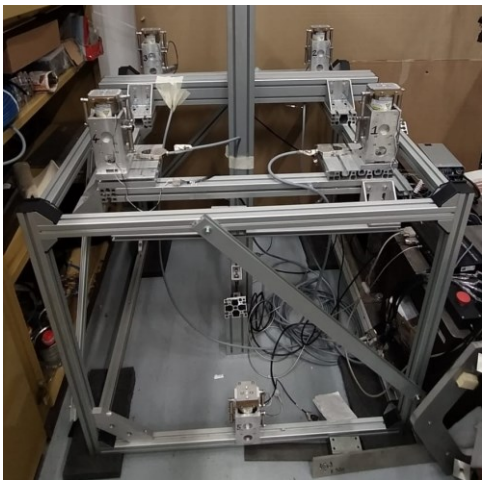

a) Realization of flexible primary structure demonstrator

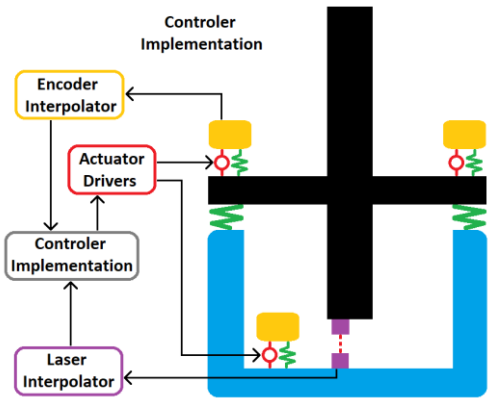

b) Scheme of sensing and actuation in

Fig. 1 Experimental demonstrator with four distributed 1-DoF absorbers.

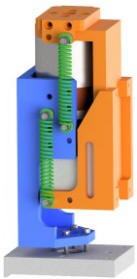

a) Design of absorber

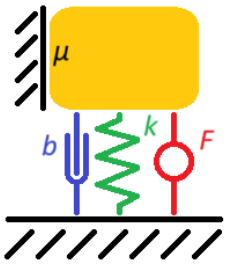

b) Mechanical scheme of reality

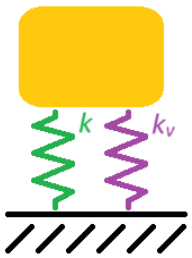

c) Target of active corrections

Fig. 2 Design of 1 DOF absorber and concept of active realization of ideal absorber

These nonlinearities stood out significantly when trying to identify passive effects and were therefore also included in the compensation algorithm. The active control of voice-coils was

therefore adapted to maximum elimination of identified nonlinear passive resistances (Fig. 2) modeled as a nonlinear function of relative position and velocity evaluated using the accurate on-line optical position measurements parallel with the voice-coils. At the same time, the passive stiffness values of the absorbers springs were also corrected by the active vice-coil forces. The example of achieved experimental results for harmonic disturbance signal is shown in Fig. 3. The first red line corresponds to the moment when the correction on-line algorithms of the absorbers are turned on, and the second when the disturbance signal is turned off.

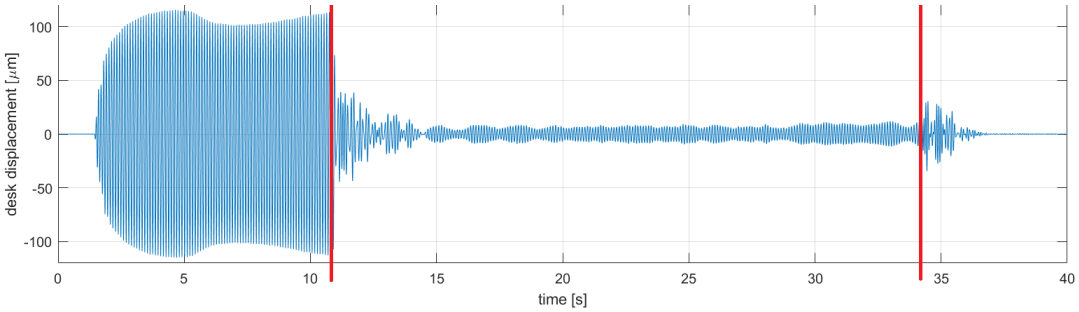

Fig. 3 Example of suppression of demonstrator primary structure vibration measured by laser interferometer

IDENTIFICATION OF NON-LINEAR PASSIVE RESISTANCES FOR COMPACT PLANAR 3-DOF ABSORBER WITH FOUR VOICE-COILS

An even more complicated situation with nonlinear frictional phenomena occurred in the case of a compact planar absorber demonstrator with 3 degrees of freedom (Fig. 4 a)) and four voice-coils (Fig. 4 b)), one voice coil each in the left and right parallel legs and two voice coils in the middle leg perpendicular to the other two. The methods of identification and subsequent elimination of passive effects in controllers relatively successfully used for distributed 1 DOF absorbers proved to be insufficient here. The reason is probably the interaction of passive resistances in individual sliding lines and their combination with passive resistances during relative rotational motions. As can be seen from the measurements in Fig. 5, there is a noticeable slip-stick effect and big differences in step responses of individual legs. The more complex dissipation models [7-8] were tried to identify passive resistances. Especially some versions of the LuGre friction model seems to be relatively successful.

a) Mechanical scheme of absorber b) Realization of demonstrator

Fig. 4 Experimental demonstrator of compact planar 3-DOF absorber with four voice-coils

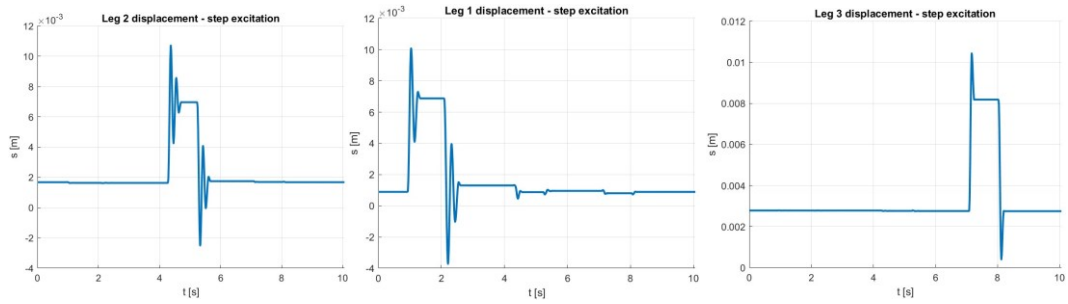

a) Response of leg 1 (left) b) Response of leg 2 (middle) c) Response of leg 3 (right)

Fig. 5 Step responses of particular 3-DOF absorber legs for friction effects identifiaction

As is well known, the LuGre model introduces an internal phenomenological dynamic model for micromechanics with additional state variables and several coefficients. The coefficients of models for particular LuGre friction forces were identified by optimization of the whole absorber mechanical model in comparison with measured reality. Despite the significant improvement of most identification results, in some of the tested regimes the agreement with reality was not sufficient (Fig. 6). To further improve the identification and the resulting behavior of the absorber, the procedure of combining LuGre models with the use of neural networks was once proposed, and above all, the design of a new version of the 3 DOF demonstrator with better properties was approached.

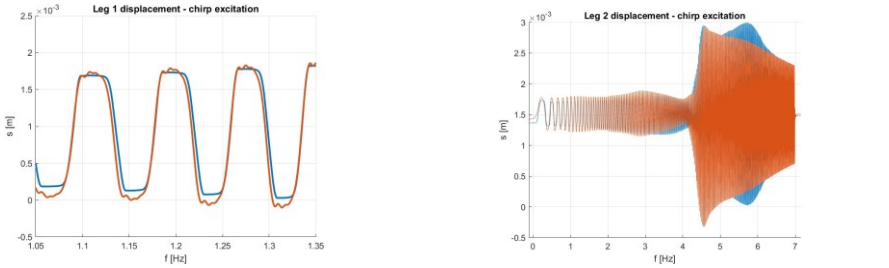

a) Detail of Leg 1 motion comparison b) Leg 2 motion comparison for chirp excitation

Fig. 6 Examples of comparison of real motion (blue) and model motion (red) for LuGre friction model

ACKNOWLEDGEMENT

The work has been co-funded by the Europen Union under the project “Robotics and advanced industrial production” (reg. no. CZ.02.01.01/00/22 008/0004590) and the grant project “Identification and compensation of imperfections and friction effects in joints of mechatronic systems” No. 23-07280S of the Czech Science Foundation.

REFERENCES

[1] A. Preumont. Vibration Control of Active Structures: An Introduction. Springer International Publishing, 2018, 246. http://dx.doi.org/10.1007/978-3-319-72296-2

[2] N. Olgac, B. Holm-Hansen. A novel active vibration absorption technique: Delayed resonator. *J. Sound Vib.* **1994**, 176 (1), 93-104. http://dx.doi.org/10.1006/jsvi.1994.1360

[3] T. Vyhlídal, N. Olgac, V. Kučera. Delayed resonator with acceleration feedback – complete stability analysis by spectral methods and vibration absorber design. *J. Sound Vib.* **2014**, 333 (25), 6781-6795. http://dx.doi.org/10.1016/j.jsv.2014.08.002

[4] Z. Šika, T. Vyhlídal, Z. Neusser. Two-dimensional delayed resonator for entire vibration absorption. *J. Sound Vib.* **2021**, 500 (116010). http://dx.doi.org/10.1016/j.jsv.2021.116010

[5] Z. Šika, J. Krivošej, T. Vyhlídal. Three dimensional delayed resonator of Stewart platform type for entire absorption of fully spatial vibration. *J. Sound Vib.* **2024**, 576, (118290). http://dx.doi.org/10.1016/j.jsv.2023.118154

[6] K. Kraus, Z. Šika, P. Beneš, J. Krivošej, T. Vyhlídal. Mechatronic robot arm with active vibration absorbers. *J. Vib. Control* **2020**, 26 (13–14), 1145-1156. http://dx.doi.org/10.1177/1077546320918488

[7] S. Huang, W. Liang. Intelligent Friction Compensation: A Review. *IEEE/ASME Ttransactions on Mechatronics* **2019**, 24 (4), 1763-1774. http://dx.doi.org/10.1109/TMECH.2019.2916665

[8] G. Rill, T. Schaeffer, M. Schuderer. LuGre or not LuGre. *Multibody System Dynamics* **2023**, 60, 191-218. http://dx.doi.org/10.1007/s11044-023-09909-5

APPLIED MECHANICS 2024

April 17th – 19th, 2024
Hotel Toliar, Štrbské Pleso
Slovakia

APPLICATION AND VALIDATION OF A HIGH ORDER NEURAL NETWORKS BASED RIEMANN SOLVER FOR 1D EULER EQUATIONS

A. TATER[1]*, P. KOVÁŘ[2], J. FÜRST[3]

The Riemann solver holds a key position in most computational fluid dynamics (CFD) codes, crucial for simulating compressible flows. The time to obtain the exact solution of the Riemann problem for ideal fluids is high because of the complexity of the model. Consequently, approximate Riemann solvers are preferred over exact ones to mitigate this complexity. This contribution describes application and validation of state-of-the-art Riemann solver, which very accurately approximates the behaviour of an exact Riemann solver needing only a fraction of the exact solver's computational time. This is achieved by employing a specific type of neural networks. This new approximate Riemann solver is implemented in classical Godunov's scheme and validated on the well-known Sod's shock tube problem with promising results in terms of accuracy and time efficiency.

Keywords: Finite volume method; Approximative Riemann solvers; Higher order neural networks; 1D Euler equations; Sod's shock tube

INTRODUCTION

The Riemann problem holds a crucial position in the realm of computational fluid dynamics (CFD), particularly within finite volume methods (FVM). It tackles the fundamental challenge of solving hyperbolic partial differential equations that govern the inviscid compressible fluid flow.

In essence, the Riemann problem [1] delves into understanding how fluids behave at the interface between two distinct states. It serves as a pivotal test case for grasping how discontinuities, shocks, and rarefactions propagate through the fluid medium. A Riemann solver's task is to determine the fluxes of conserved quantities across the interfaces between adjacent computational cells which arise from the Godunov's scheme [2].

Exact Riemann solvers solve the Riemann problem by using an iterative method. Although they provide precise results, exact solvers are computationally expensive and often impractical for complex flow scenarios due to their high computational cost. Thus, approximate Riemann solvers, such as the HLLC [3] or AUSM+up [4] numerical fluxes, that aim to approximate the solution of

[1] **Ing. Adam Tater**, Department of Technical Mathematics, Center of Aviation and Space Research, Faculty of Mechanical Engineering, Czech Technical University in Prague; adam.tater@fs.cvut.cz
[2] **Ing. Patrik Kovář**, Department of Technical Mathematics, Center of Aviation and Space Research, Faculty of Mechanical Engineering, Czech Technical University in Prague
[3] **Prof. Ing. Jiří Fürst, PhD.**, Department of Technical Mathematics, Faculty of Mechanical Engineering, Czech Technical University in Prague

the Riemann problem using simplified models or assumptions are used. These solvers strike a balance between accuracy and computational efficiency, making them widely used in practice for simulating a broad range of fluid flows.

Another state-of-the-art approach involves approximating the exact Riemann solver using artificial neural networks, which can offer more accurate solutions than standard approximative solvers. Additionally, the evaluation of the numeric flux can be much faster using this approach. This approach is implemented into Godunov's scheme and tested on Sod's shock tube problem [5].

GOVERNING EQUATIONS

A set of partial differential equations presented below is a fundamental set of equations in fluid dynamics. Mathematically, the equations consist of three coupled partial differential equations, governing the time-evolution of density, momentum, and total energy along the spatial dimension. These equations serve as the basis for modelling of compressible fluid flows in aerodynamics.

Under the assumption of continuum, the above-mentioned system of conservation laws [6], usually named Euler equations, can be written as

$$\frac{\partial \rho}{\partial t} + \frac{\partial (\rho u)}{\partial x} = 0, \tag{1}$$

$$\frac{\partial (\rho u)}{\partial t} + \frac{\partial (\rho u^2)}{\partial x} + \frac{\partial p}{\partial x} = 0, \tag{2}$$

$$\frac{\partial (\rho E)}{\partial t} + \frac{\partial}{\partial x}\big((\rho E + p)u\big) = 0, \tag{3}$$

where ρ denotes density, u is velocity, p is pressure and E is the total energy. Furthermore, x and t are space coordinate and time, respectively. The system can be rewritten into the vector form as

$$\frac{\partial \mathbf{W}}{\partial t} + \frac{\partial \mathbf{F}}{\partial x} = 0, \text{ where } \mathbf{W} = \begin{pmatrix} \rho \\ \rho u \\ \rho E \end{pmatrix} \text{ and } \mathbf{F} = \begin{pmatrix} \rho u \\ \rho u^2 + p \\ (\rho E + p)u \end{pmatrix}. \tag{4}$$

To close the system, the equation of state needs to be employed. In this case, the equation of ideal gas [7], where γ denotes heat capacity ratio, is used in following form

$$p = (\gamma - 1)\left(\rho E - \frac{1}{2}\rho u^2\right). \tag{5}$$

METHODS

The entire methodology consists of the Godunov's scheme and the corresponding Riemann solver predicting the numerical flux which is used. The new approximative Riemann solver under investigation is constructed as shallow higher order neural network [8] with three neurons in the first layer and three output neurons, i.e., single net for coupled problem. Training data set was obtained from exact Riemann solver using the methodology described in [1], where the whole topic of the Riemann problem and its solutions, both exact and approximate, is well described.

Godunov's scheme

The Godunov method is a powerful numerical technique employed to solve the 1D Euler equations. In this method, the fluid flow is discretized into a series of grid cells, and the solution is evolved in time through a sequence of time steps. At each cell interface, the method computes the numerical fluxes of conserved quantities using a Riemann solver to accurately model the flow behaviour between neighbouring cells. Mathematically, it can be derived from system (4) by integrating it over one cell i and introducing an average value of variables $\mathbf{W}_i$ for each cell at cell centres x_i as

$$\Delta x \frac{\partial \mathbf{W}_i}{\partial t} + \int_{x_{i-\frac{1}{2}}}^{x_{i+\frac{1}{2}}} \frac{\partial \mathbf{F}}{\partial x} dx = 0, \text{ where } \Delta x = x_{i+\frac{1}{2}} - x_{i-\frac{1}{2}} \tag{6}$$

denotes volume of a cell i. By the application of the divergence theorem on the volume integral, it is possible to obtain a semi-discrete scheme as

$$\frac{\partial \mathbf{W}_i}{\partial t} + \frac{1}{\Delta x}\left(\mathbf{F}_{i+\frac{1}{2}} - \mathbf{F}_{i-\frac{1}{2}}\right) = 0, \text{ where } \mathbf{F}_{i+\frac{1}{2}} \text{ and } \mathbf{F}_{i-\frac{1}{2}} \text{ are fluxes at cell faces.} \tag{7}$$

These fluxes are evaluated by specific Riemann solver. Finally, time derivative is discretised by forward Euler method and after some manipulation, the discrete scheme can be written as

$$\mathbf{W}_i^{n+1} = \mathbf{W}_i^n - \frac{\Delta t}{\Delta x}\left(\mathbf{F}_{i+\frac{1}{2}} - \mathbf{F}_{i-\frac{1}{2}}\right), \text{ where } \Delta t \text{ is a time step.} \tag{8}$$

Resulting Godunov's scheme is first order accurate in space and time.

RESULTS

The Sod's shock tube problem [5] serves as a benchmark to evaluate the precision of computational fluid dynamics codes, particularly Riemann solvers. Originating from Sod's thorough examination in 1978, this test entails a one-dimensional Riemann problem featuring specified parameters for the left and right states of an ideal gas with $\gamma = 1.4$, these states are listed in Tab. 1.

Tab. 1 Initial conditions for Sod's shock tube problem.

Variable	ρ [kg·m^{-3}]	p [Pa]	u [m·s^{-1}]
Left state	1	1	0
Right state	0.125	0.1	0

The time evolution of this problem can be described by solving the Euler equations. Numerical resolution of this scenario allows for testing against an analytical solution, providing insights into the accuracy of a code in capturing and resolving shocks and contact discontinuities, as well as reproducing the accurate density profile of the rarefaction wave.

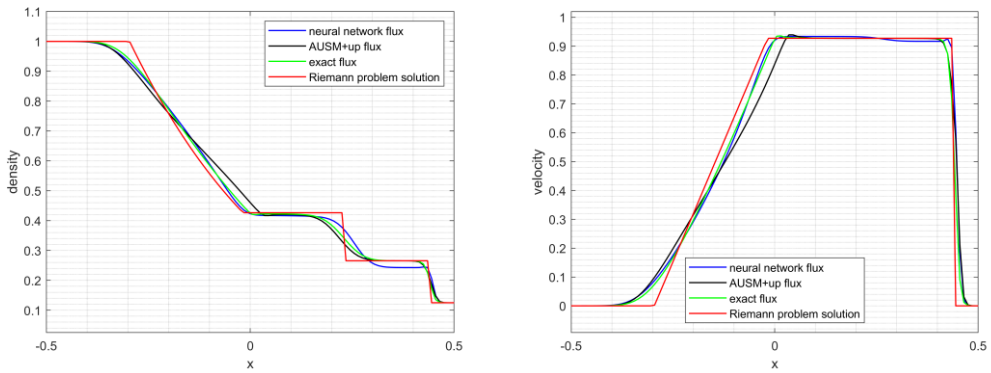

Fig. 1 Sod's shock tube: (left) density comparison; (right) velocity comparison.

Numerical solutions obtained from Godunov's method, which were held until $t = 0.25$ s was reached on mesh consisting of 100 cells, are shown in Fig. 1. Neural network flux was compared with well-known AUSM+up [4] flux and exact flux [1] as well as with the real Riemann problem solution. Neural network flux shows very good agreement in case of velocity. On the other hand, it

predicts quite poorly density in region between contact discontinuity and shock wave. To evaluate the error in density prediction, an error was introduced as

$$\delta = \frac{\sum_i^n \left|\rho_i^{\text{Riemann}} - \rho_i^{\text{numerical}}\right|}{n}, \text{ where } n \text{ is the number of cells in mesh.} \quad (9)$$

Comparison of performance and accuracy results for each tested flux is listed in Tab. 2.

Tab. 2 Comparison of achieved computation times and deviations from the real solution.

Flux	Neural network	AUSM+up	Exact
Computational time [s]	0.471	0.373	2.474
δ [kg·m-3]	0.0203	0.0233	0.0157

CONCLUSION

The newly developed neural network approximate Riemann solver was implemented into Godunov's method and tested by solving the Sod's shock tube problem and compared with classical AUSM+up approximate flux and exact flux. It was found that it gives promising results in terms of accuracy and time efficiency. Therefore, it is appropriate to continue developing this idea.

ACKNOWLEDGEMENT

This work was supported by the grant agency of the Czech Technical University in Prague, grant No. SGS22/148/OHK2/3T/12.

The authors would also like to thank for the support from the ESIF, EU Operational Programme Research, Development and Education, and from the Center of Advanced Aerospace Technology (CZ.02.1.01/0.0/0.0/16019/0000826), Faculty of Mechanical Engineering, Czech Technical University in Prague.

REFERENCES

[1] E.F. Toro. Riemann solvers and numerical methods for fluid dynamics: a practical introduction. Springer Science & Business Media, 2013.

[2] S.K. Godunov. A Difference Scheme for Numerical Solution of Discontinuous Solution of Hydrodynamic Equations. *Mat. Sbornik* **1959**, 47, 271-306.

[3] E.F. Toro, M. Spruce, W. Speares. Restoration of the contact surface in the HLL-Riemann solver. *Shock waves* **1994**, 4, 25-34.

[4] M.S. Liou. A sequel to AUSM, Part II: AUSM+-up for all speeds. *Journal of computational physics* **2006**, 214 (1), 137-170.

[5] G.A. Sod. A Survey of Several Finite Difference Methods for Systems of Nonlinear Hyperbolic Conservation Laws. *J. Comput. Phys.* **1978**, 27 (1), 1-32.

[6] R.J. LeVeque. Finite volume methods for hyperbolic problems. Vol. 31. Cambridge university press, 2002.

[7] E. Clapeyron. Mémoire sur la puissance motrice de la chaleur. *Journal de l'École Polytechnique* **1835**, XIV, 153-190.

[8] M.M. Gupta, I. Bukovsky, N. Homma, A. Solo, Z.G. Hou. Fundamentals of higher order neural networks for modeling and simulation. In: Artificial Higher Order Neural Networks for Modeling and Simulation, IGI Global, 103-133, 2013.

APPLIED MECHANICS 2024

April 17th – 19th, 2024
Hotel Toliar, Štrbské Pleso
Slovakia

WHICH THRESHOLD IS DECISIVE FOR FATIGUE CRACK PROPAGATION OF SEMI-ELLIPTICAL SURFACE CRACKS?

D. TICHOŇ[1]*, T. VOJTEK[2], P. POKORNÝ[3], P. HUTAŘ[4]

Fatigue crack propagation (FCP) data including the threshold regime were experimentally obtained for semi-elliptical surface cracks in non-standard dog bone specimens. Dog bone specimens were manufactured from corroding structural steel S275. Artificial semi-elliptical defects were produced on the surface of each specimen with the depth of circa 1.7 mm and width on the free surface of 4 mm. Load shedding technique was used to decrease the load level until the crack was arrested in the threshold regime for load ratio R = 0.1. Parameters influencing the threshold value were maintained constant during tests. Non-standard experimental-numerical methodology was applied to correctly estimate the FCP thresholds.

Keywords: semi-elliptical surface crack; dog bone specimen; corroding steel S275; fatigue crack propagation; non-standard threshold estimation

INTRODUCTION

In engineering practice, the safety-relevant components must undergo a close periodic monitoring for a presence of crack-like imperfections, which arise a potential risk of a fatigue failure. Optimal inspection periodicity is set with respect to the residual fatigue life estimation, which is affected by several phenomena, such as the size of postulated crack or the fatigue crack propagation (FCP) threshold, $K_{max,th}$ (or ΔK_{th}), that even for a small crack decides whether it propagates or not. The $K_{max,th}$ refers to the threshold of the linear elastic fracture mechanics, meaning that this concept is not reliable for cracks smaller than a certain size related to grain size. For longer cracks, the FCP threshold is composed of the intrinsic part known as the effective threshold, $\Delta K_{eff,th}$, and the remaining part given by crack closures. These mechanisms develop over the crack length and exhibit transient behaviour until the crack can be considered as long.

[1] **Ing. Dušan Tichoň**, Institute of Physics of Materials Czech Academy of Sciences, Zizkova 513/22, Brno, Czech Republic; Institute of Applied Mechanics Brno, Ltd., Resslova 972/3, Brno, Czech Republic; tichon@ipm.cz
[2] **Ing. Tomáš Vojtek, PhD.**, Institute of Physics of Materials Czech Academy of Sciences, Zizkova 513/22, Brno, Czech Republic; vojtek@ipm.cz
[3] **Ing. Pavel Pokorný, PhD.**, Institute of Physics of Materials Czech Academy of Sciences, Zizkova 513/22, Brno, Czech Republic; pokorny@ipm.cz
[4] **Prof. Ing. Pavel Hutař, PhD.**, Institute of Physics of Materials Czech Academy of Sciences, Zizkova 513/22, Brno, Czech Republic; hutar@ipm.cz

However, the study of the FCP thresholds is surrounded by many unanswered questions and unresolved issues. To mention a few, it is difficult to determine the crack size limit of so-called physically or mechanically short cracks, where crack closures become fully developed. In addition, the term crack length itself is quite misleading since it was introduced within the analytical 2D solutions. When considering a crack with the real crack front shape, e.g. semi-elliptical, it is possible to determine several crack lengths – in the inner direction or on the free surface.

Another major task is to deal with the transferability of crack propagation data from standard laboratory specimens (like C(T) and M(T) with straight crack front) to non-standard ones, or better, to real components. The FCP data are commonly one-to-one transferred to other specimens, which is usually not valid in the near-threshold and lower Paris regime. The influence of several phenomena deteriorates the transferability, for instance the crack geometry and size, specimen thickness [1], load ratio, load history, loading frequency, or air humidity [2].

The situation is even worse for cracks with real crack front shape, e.g. semi-elliptical, and for non-standard specimens. The FCP data are generally missing and the effect of beforementioned aspects is rather unknown. However, in order to clarify some ambiguities regarding the FCP data transfer to cracks with real crack front shape, it is first necessary to unify the definition of decisive crack growth direction and the corresponding threshold value related to the preservation of the integrity of a component. In the case of C(T) or M(T) specimens, the threshold value is commonly evaluated from the data calibrated and observed on the surface of the specimen, where the variance of stress intensity factor (SIF) along the relative straight arrested crack front can be neglected. In contrast to standard specimens, dog bone specimens with surface semi-elliptical crack may exhibit different crack growth behaviour, meaning the crack still propagating on the surface is arrested in the inner direction. Therefore, the correct estimation of the decisive threshold value is an important step in the investigation of potential data transfer, which is under the debate for decades.

EXPERIMENTAL MEASUREMENT OF CRACK PROPAGATION DATA

The non-standard dog bone specimen was manufactured from the standard structural corroding steel S275. Specimen thickness was $t = 10$ mm, the width of the narrowed part containing the crack was $W = 45$ mm, width of clamped part $W_2 = 60$ mm, radius $R = 80$ mm and the total length was $L = 250$ mm, see Fig. 1a. To observe the fatigue crack propagation (FCP), artificial semi-elliptical defect was created into the surface of dog bone specimen by electric sparkling method with depth of 1.79 mm and the width on the free surface of circa 4 mm.

The specimen was cyclically loaded on resonant machine Zwick Vibrophore 250 (with the maximum possible force of 250 kN). The loading frequency depended on the total system stiffness composed of parts given by a machine and by prepared specimen and reached approximately 120 Hz. The experimental setup is depicted in Fig. 1b. Experimental measurements were performed under practically constant environmental conditions (relative air humidity of 30% at 21 °C).

Load shedding measurement technique was used to deliberately decrease the load until the crack was arrested in the threshold regime. Firstly, the crack depth of 1 mm was reached. Afterwards, the load was decreased after each crack length increment of circa 0.1 mm. The test was performed for load ratio $R = 0.1$. The FCP was observed on the specimen surface on both sides from the centre of the specimen optically by the CCD camera uEye UI-2280SE-M-G.

As soon as the specimen was broken, fracture surfaces were observed on optical stereomicroscope Olympus SZX10 with adjusted camera Promicra 3-3CP. Due to differences in the local oxide debris production, the semi-elliptical crack sill propagating on the free surface was arrested in the inner direction. Therefore, the FCP threshold estimated on the basis of the

experiment is only valid close to the free surface of the specimen but not for the inner crack growth direction, which is the shortest crack path to endanger the structural integrity of the component. Thus, it was necessary to determine the crack front shape when crack arrest occurred for the inner point, see the red line in Fig. 3a, where the typical darker layers of oxidation products are visible on the fracture surface.

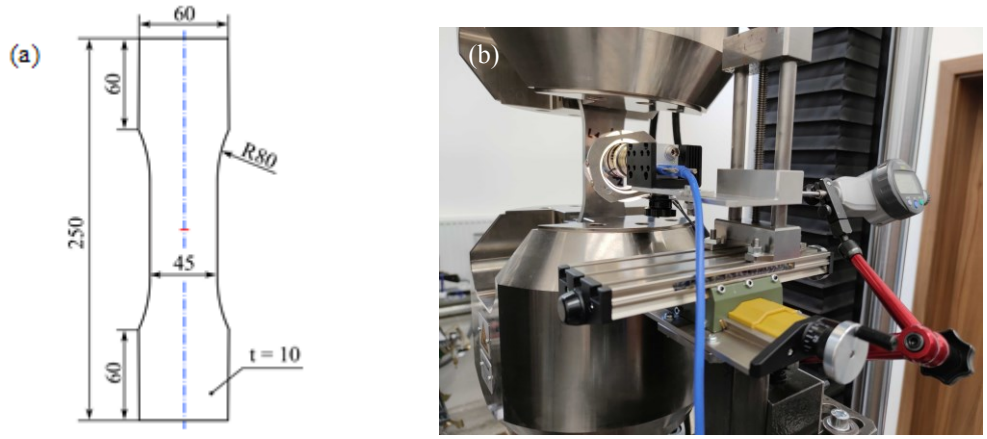

Fig. 1 Schematic of dog bone specimen with created semi-elliptical defect position (a), experimental setup (b)

NUMERICAL ESTIMATION OF CRACK PROPAGATION THRESHOLD

To correctly evaluate the fatigue crack propagation (FCP) threshold, 3-D finite element numerical model of dog bone specimen was created. Only one plane of symmetry was applied. Semi-elliptical surface crack was created in the centre of the model on the symmetry plane. The numerical model is depicted in Fig. 2. The crack front shape for a moment when crack was arrested in the inner direction and the final arrested crack front were obtained from digitalized fracture surface and were imported into the numerical model.

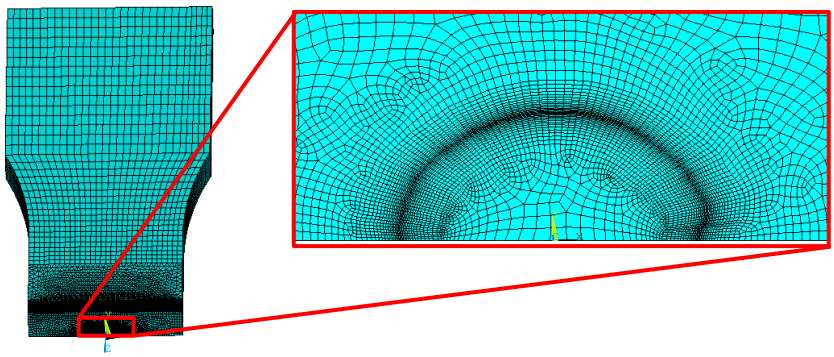

Fig. 2 Created 3-D numerical finite element model with detail of modelled real crack front in the moment of crack arrest in the inner crack growth direction

Along the crack front, 100 elements were created to monitor the stress intensity factor (SIF) caused by the loading mode I, K_I. It was calculated as the average of 8^{th} to 10^{th} contour. Therefore, fine mesh of linear SOLID185 elements was created in the vicinity of the modelled crack. In the remaining part of the numerical model no strict rules for meshing were applied. Linear elastic material model was considered with corresponding parameters: modulus of elasticity $E = 207$ GPa and Poisson's ratio $\mu = 0.3$.

The maximum force load corresponding to the experiment was distributed to all nodes comprised in the volume part that was clamped in the hydraulic device. For a moment of crack arrest in the inner direction, the maximum force was $F_{max} = 37.467$ kN and for the final arrested crack front $F_{max} = 32.33$ kN, respectively. The SIFs along the crack front shapes (blue and red line in Fig. 3a) are depicted in Fig. 3b.

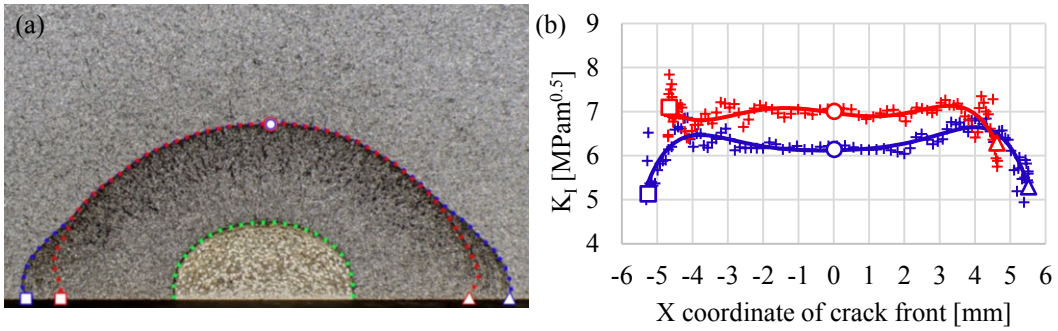

Fig. 3 The typical fracture surface with marked lines, green – initial notch, red – crack arrested in the inner direction, blue – final crack front (a), SIF evolution along the crack fronts (b)

CONCLUSION

The proposed non-standard experimental-numerical methodology for fatigue crack propagation (FCP) threshold estimation offers correct evaluation of the threshold value of semi-elliptical surface crack propagating in the inner crack growth direction, which leads to the shortest residual lifetime until the fatigue failure. The FCP threshold for the inner point ($X = 0$ in the Fig. 3b) differed from 7.06 MPam$^{0.5}$ in the moment of the crack arrest for the inner point (red line in Fig. 3a) to 6.22 MPam$^{0.5}$ in the case of the final arrested crack front (blue line in Fig. 3a). The threshold for the point on the free surface was even lower, specifically 5.19 MPam$^{0.5}$.

Despite the drop by only 12% in the threshold value for the inner point of the final arrested crack, it may significantly influence the estimated residual fatigue life, especially in applications where the majority of the loading spectrum lies in the near-threshold regime. The latter is common, for instance, in the loading of railway axles. On the other hand, evaluating the FCP threshold from the specimen surface, which is not the decisive in the matter of fatigue failure, seems to be too conservative (drop by 26.5%) and corresponding predictions unusable.

ACKNOWLEDGEMENT

This work was financially supported by the Czech Science Foundation in the frame of the project No. 22-28283S. The work was also supported by the Brno University of Technology through the project FSI-S-23–8240.

REFERENCES

[1] T. Vojtek, et al. Classically determined effective ΔK fails to quantify crack growth rates. *Theoretical and Applied Fracture Mechanics* **2020**, 108 (102608). DOI: 10.1016/j.tafmec.2020.102608

[2] T. Vojtek, P. Pokorný, I. Kuběna, L. Náhlík, R. Fajkoš, P. Hutař. Quantitative dependence of oxide-induced crack closure on air humidity for railway axle steel. *Int. J. Fatigue* **2019**, 123, 213-224. DOI: 10.1016/j.ijfatigue.2019.02.019

APPLIED MECHANICS 2024

April 17th – 19th, 2024
Hotel Toliar, Štrbské Pleso
Slovakia

EXPERIMENTAL AND NORMATIVE APPROACH TO DETERMINING THE SERVICE LIFE OF WELDED JOINTS

A. TOŠKOVÁ[1]*, M. FUSEK[2]

The contribution deals with the determination of the service life of multiaxially loaded welded joints in the area of low-cycle fatigue. Jiang criterion, which combines several principles of low-cycle material fatigue criteria, will be discussed in more detail. Furthermore, the possibilities of determining the service life of welded joints according to normative approaches will be discussed in comparison with the experimental results of biaxial fatigue tests of a circumferential welded joint.

Keywords: Welding; fatigue; life prediction; multiaxial loading; experimental verification

INTRODUCTION

Fatigue is one of the fundamental problems in material mechanics. In determining the life of a notched component, the problem is more complex than that of conventional smooth specimens. This paper outlines possible approaches to service life determination and takes a closer look at a selected normative approach, the results of which are compared with experimental data.

LIFE PREDICTION OF MULTI-AXIALLY LOADED COMPONENT

Material fatigue is a process of material degradation due to repeated loading. However, many machine components are loaded multiaxially, where the material is loaded in several directions simultaneously. For multi-axially loaded components, service life must be determined using fatigue criteria. Fatigue criteria tend to be divided into three categories in the field of low cycle fatigue according to the approach used to determine life. The effective strain approach is based on the Manson-Coffin equation. The most widely used critical plane approaches include the Brown-Miller criterion (see [1]), its Kandil modification, the Wang-Brown criterion and the Fatemi-Socie criterion. The most well-known energy criterion is the Smith-Watson-Topfer criterion (see [2]). Another criterion, which differs in principle from the above-mentioned ones, is the Jiang criterion (see [3]) or its modification (see [4]).

[1] **Ing. Anna Tošková**, Department of Applied Mechanics, Faculty of Mechanical Engineering, VSB - Technical University of Ostrava, 17. listopadu 2172/15, Ostrava - Poruba, Czech Republic; anna.toskova@vsb.cz

[2] **doc. Ing. Martin Fusek Ph.D.**, Department of Applied Mechanics, Faculty of Mechanical Engineering, VSB - Technical University of Ostrava, 17. listopadu 2172/15, Ostrava - Poruba, Czech Republic; martin.fusek@vsb.cz

WELDED JOINT LIFE PREDICTION

There are several ways to predict the service life of welded joints. In general, these predictions can be classified into three categories, namely:

1. Assessment according to standards (e.g. Eurocode 3, International Institute of Welding).
2. Assessment based on special methodologies (e.g. Volvo methodology, FEMFAT methodology).
3. Assessment based on in-house fatigue testing.

The first group includes the standard EN 1993-1-9, the so-called Eurocode 3 (see [5]) and the set of recommendations issued by the International Institute of Welding (IIW), see more in [6].

International Institute of Welding Standard

The IIW standard provides fatigue resistance data in the form of SN curves or crack growth curves, the fatigue design is then based on the stress range or stress intensity factor range. The fatigue design approaches are based on nominal stress, hot-spot stress and effective notch stress, as well as fracture mechanics and component testing approaches and subsequent work with experimental data. This methodology is not recommended for low-cycle fatigue where the nominal stress is greater than one and a half times the yield strength of the material.

The fatigue design of classified structural details and welded joints is based on a range of nominal stresses – normal or shear. Separate SN curves are provided to assess the normal or shear stress range. The mathematical description of the fatigue curves is as follows for normal and shear stress respectively

$$N = \frac{C}{\Delta\sigma^m}, \text{resp.} N = \frac{C}{\Delta\tau^m}, \tag{1}$$

where $\Delta\sigma$ or $\Delta\tau$ is the normal or shear stress range, C is the fatigue constant, m represents the slope of the fatigue curves and N is the number of cycles Each SN fatigue strength curve is defined by the characteristic fatigue strength of the structural detail in MPa at $2 \cdot 10^6$ cycles. This value is the fatigue class (FAT class). The slope of the SN curves for details considered on the basis of normal stresses is $m = 3$, the fatigue limit corresponds to $N = 10^7$ cycles. The slope of the SN curves for details considered under shear stresses is $m = 5$, the fatigue limit corresponds to $N = 10^8$ cycles.

DETERMINATION OF THE SERVICE LIFE OF THE SELECTED WELDED JOINT

Experimentally and according to IIW, the service life of the butt circumferential welded joint was determined. The service life was evaluated at five levels of strain amplitude for symmetrical tensile and compressive loading.

Determination of Service Life according to the IIW Approach of Nominal Stress

Five strain amplitudes at a constant strain rate were chosen, from which the values of the nominal stresses for cracking in the weld toe were determined. For the slope $m = 3$, the FAT curve of the given structural detail was compiled, from which the number of cycles to fracture was subtracted. The weld is not considered to be non-destructively tested. The construction detail then falls under FAT 36. The base metal falls under FAT 160, which does not cross FAT 36 in any way. The determined service lives are listed in the table Tab. 1.

Experimental Verification of Service Life

Strain-controlled fatigue tests were performed in symmetrical tension and compression for five selected values of the strain amplitude. Fatigue tests were performed on specimens with one type I circumferential butt weld. The full penetration weld is single-layer and not modified in any way after welding. The weld is made using the fusion welding method (MAG). The base metal is S235, the filler metal is G3Si1. The used specimen is shown in Fig. 1.

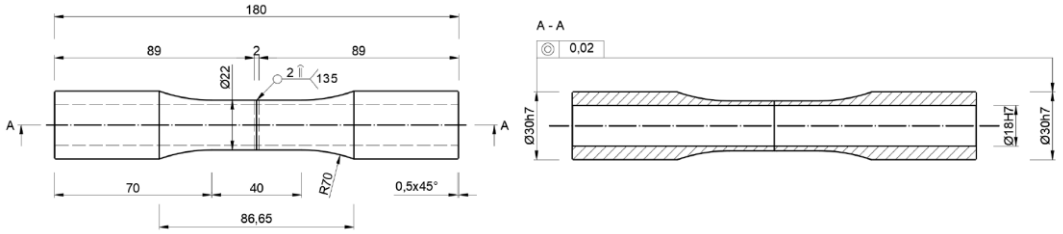

Fig. 1 Testing specimen

Fatigue tests were performed with the LabControl 100kN/1000Nm testing machine. The termination criterion was set as a 20% drop in force or torque amplitude. The determined service lives are listed in the table Tab. 1.

Comparison of Service Life Prediction according to IIW and Experiment

In the table Tab. 1 shows the actual number of cycles N_f with the estimated number of cycles according to IIW $N_{f\,IIW}$ for a given nominal strain amplitude $\varepsilon_{a,n}$ and quotient $k = \frac{N_f}{N_{f\,IIW}}$.

Tab. 1 Comparison of service life prediction according to IIW and experiment

$\varepsilon_{a,n}$ [-]	N_f [-]	$N_{f\,IIW}$ [-]	k [-]
0,0043	941	14	67,2
0,0030	2 085	43	48,5
0,0017	10 290	238	43,2
0,0010	30 525	1 139	26,8
0,0006	228 032	5 277	43,2

According to the limitation of the applicability of the IIW standard, the prediction is not suitable for the first three $\varepsilon_{a,n}$ due to the large nominal stresses in relation to the value of yield strength, which was determined by the certificate to be 315 MPa. Even so, it is obvious that the actual service life is significantly higher than that estimated by IIW.

Determination of the Basquin and Manson-Coffin Fatigue Parameters using the Neuber Correction

As compressive tensile tests had already been performed, it was possible to predict the service life of the welded joint loaded with torsion. The fatigue parameters for the Manson-Coffin criterion were obtained from the output data of the tension and compression tests, and the torsional stress parameters were obtained by conversion, from which the shear strain γ_a were subsequently determined for the given level of service life.

However, since there is a notch in the specimen that forms the welded joint, the stress and strain at the root of the notch was determined based on Neuber correction:

$$\sigma \cdot \varepsilon = \sigma_{FEM} \cdot \varepsilon_{FEM} \cdot \frac{\beta}{\alpha}. \quad (2)$$

In Eq. 2 σ and ε corresponds stress and strain at the root of the notch, σ_{FEM} and ε_{FEM} is the stress and strain found from a static simulation using a linear FEM model. The $\frac{\beta}{\alpha}$ ratio is the ratio of the fatigue notch factor and theoretical stress concentration factor.

For the Neuber correction, the Ramberg-Osgood model was fitted using cyclic stress strain curve using nominal strain amplitude and stress amplitude values from stabilized half-life hysteresis loops.

$$\varepsilon_a = \frac{\sigma_a}{E} + \left(\frac{\sigma_a}{K}\right)^n \quad (3)$$

The constants in Eq. 3 were determined as $K = 805{,}1$ MPa, $n = 7{,}3282$ and $E = 217\,101$ MPa. To determine the geometry of the weld, the cross-sectional dimensions of the weld were measured using a VHX-7000 digital microscope. FEM analysis of the axisymmetric linear model ($E = 204\,967$ MPa, $\mu = 0{,}3$) of the cross section of the weld was performed to determine the stress and strain at the notch root σ_{FEM} and ε_{FEM} (see Fig. 2 and Fig. 3). From the simulation, the stress gradient necessary to establish the $\frac{\beta}{\alpha}$ ratio was determined. According to [7] the ratio $\frac{\beta}{\alpha} = 0{,}7336$ was determined.

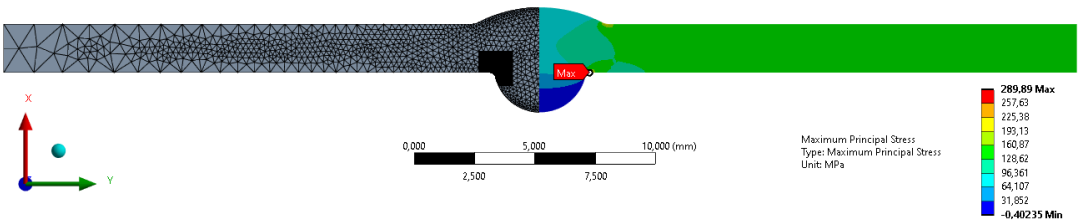

Fig. 2 Axisymmetric FEM model, stress distribution

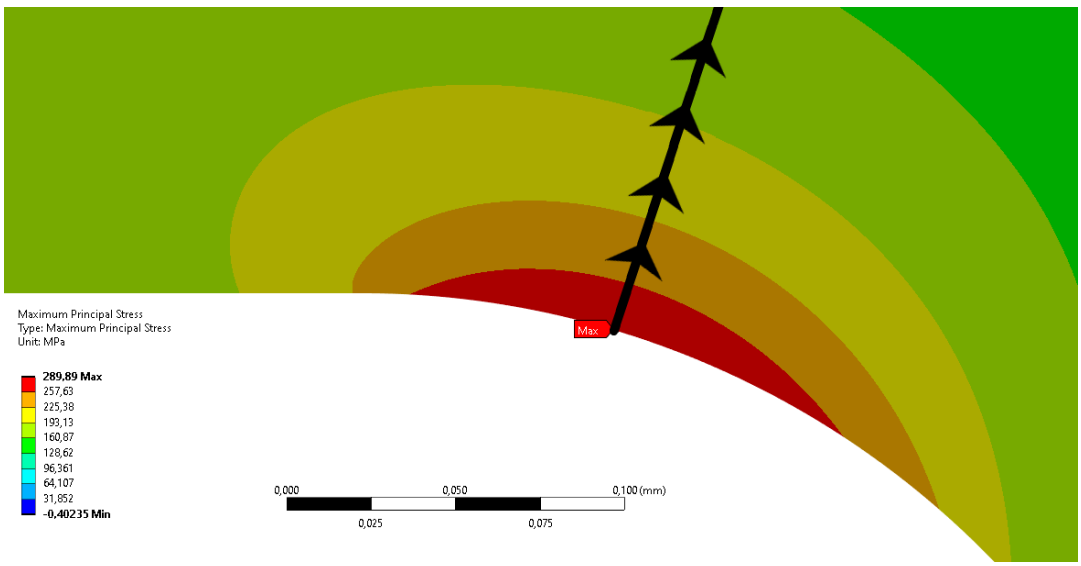

Fig. 3 Normal stress at the root of the notch with direction to determine the stress gradient

In the table Tab. 2 the uncorrected and corrected fatigue parameters are summarized. These parameters include not only the influence of the material, but also the shape of the notch itself. These are therefore the fatigue parameters belonging to the given component. In the picture Fig. 4 the Neuber correction is shown.

Tab. 2 The Basquin and Manson-Coffin fatigue parameters (uncorrected and corrected)

Fatigue Parameter	Uncorrected	Corrected
E [MPa]	217 101	217 101
$\sigma_f{}'$ [MPa]	1 521,8	1401,1
$\varepsilon_f{}'$ [-]	1,2123	57,9963
b [-]	-0,1794	-0,1369
c [-]	-0,8025	-1,0030

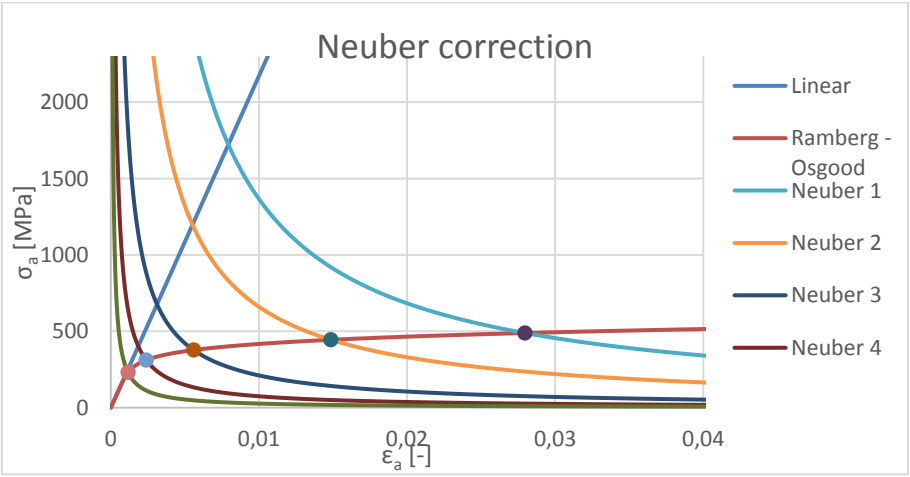

Fig. 4 Neuber correction

In the table Tab. 3, the actual number of cycles N_f, the estimated uncorrected number of cycles $N_{f,nc}$, the relative error between N_f and $N_{f,nc}$, the estimated corrected number of cycles $N_{f,c}$ and the relative error between N_f and $N_{f,c}$.

Tab. 3 Comparison of number of cycles to fracture (actual, uncorrected and corrected)

N_f [-]	$N_{f,nc}$ [-]	Error [%]	$N_{f,c}$ [-]	Error [%]
941	2 754	193	1 116	19
2 085	4 073	95	2 209	6
10 290	9 471	8	7 200	30
30 525	42 239	38	29 046	5
228 032	437 761	92	273 477	20

Except for the third test, the predictive ability was significantly improved for all specimens.

From the corrected fatigue parameters, the Manson-Coffin fatigue parameters for torsional stress were determined, from which the shear strain amplitudes $\gamma_{a,nc}$ for the given service life levels $N_{f\gamma}$ were determined by a similar method (see Tab. 4). These determined values will then be verified experimentally.

Tab. 4 Service life prediction for specified shear strain amplitudes (corrected and uncorrected)

$N_{f\gamma}$ [-]	$\gamma_{a,c}$ [°]	$\gamma_{a,nc}$ [°]
1 400 000	0,07247	0,06280
1 540 000	0,07138	0,06191
1 680 000	0,07041	0,06111
1 820 000	0,06954	0,06040
1 960 000	0,06874	0,05974

CONCLUSION

The paper discussed the determination of the service life of a selected welded joint subjected to deformation at five levels of the strain amplitude. The estimate was made according to [6] with experimental verification. According to the limitation of the applicability of the IIW standard, the prediction is not suitable for the first three values of $\varepsilon_{a,n}$. Even so, it is obvious that the actual service life is significantly higher than that estimated by IIW, which means that this approach is very conservative. Furthermore, the contribution dealt with determining the fatigue parameters of the Manson-Coffin equation. In this way, from already performed tests in symmetrical tension and compression, the shear strain amplitudes were determined for future experimental verification. The experimental data will then be used to set up Jiang prediction model, where a certain process zone will be determined for stress evaluation using a combination of linear elastic fracture mechanics and nonlinear fracture mechanics.

ACKNOWLEDGEMENT

This work has been supported by Specific Research „Experimental and Numerical Modeling for Solving Problems in Mechanics and Biomechanics“(SP2024/037).

REFERENCES

[1] M.W. Brown, K.J. Miller. A theory for fatigue failure under multiaxial stress-strain conditions. *Proceedings of the Institution of Mechanical engineers* **1973**, 187 (1), 745-755.

[2] K.N. Smith. A stress-strain function for the fatigue of metals. *Journal of materials* **1970**, 5, 767-778.

[3] Y.-Y. Jiang. A fatigue criterion for general multiaxial loading. *Fatigue & fracture of engineering materials & structures* **2000**, 23 (1), 19-32.

[4] M. Fusek, R. Halama, D. Lickova. Two modifications of Jiang criterion for constant amplitude multiaxial loading of AA2124-T851 and SS316L. *Continuum Mechanics and Thermodynamics* **2020**, 1-17.

[5] A. Nussbaumer, L. Borges, L. Davaine. Fatigue design of steel and composite structures: Eurocode 3: Design of steel structures, part 1-9 fatigue; Eurocode 4: Design of composite steel and concrete structures. John Wiley & Sons, 2012.

[6] A. Hobbacher. IIW Recommendations for fatigue design of welded joints and components, Doc. IIW-1823. *WRC Bulletin* **2008**, 520.

[7] E. Haibach. FKM - Guideline: Analytical strength assessment of components in mechanical engineering. *Germany, Frankfurt/Main: Forschungskuratorium Maschinenebau,* 2003.

APPLIED MECHANICS 2024

April 17th – 19th, 2024
Hotel Toliar, Štrbské Pleso
Slovakia

ROM OF CFD SIMULATIONS: APPLICATION FOR A PART OF BATTERY

M. M. ULIČNÝ[1]*, M. BAŤA[2], G. GÁLIK[3], J. PAULECH[4], Š. BERTA[5], A. ÜRGE[6]

A Reduced Order Model (ROM) is a simplified representation of a complex system, designed to provide a computationally more efficient alternative. In the context of Computational Fluid Dynamics (CFD), creating a reduced order model allows for faster simulations while retaining the essential information about the fluid dynamics. This paper is directed to an application for a chosen part of battery pack.

Keywords: battery; ANSYS; ROM; CFD

INTRODUCTION

Batteries are electrochemical devices that convert chemical energy stored in solid reactants into electrical energy, which later powers various systems [1]. To achieve higher power outputs, batteries are usually combined into units called battery packs, which are capable of supplying enough power for larger systems such as an electric car.

There can be several problems with these designs, one of the most significant being the inhomogeneous degradation of the individual batteries in the pack, leading to degradation of the power unit performance or compromising safe operation.

This work reflects on a research project at our department that uses detailed and system simulations to address precisely this complex problem of non-uniform battery pack degradation, where it ultimately links detailed Computational Fluid Dynamics (CFD) simulations to a system

[1] **Ing. Michal Miloslav Uličný**, Department of Applied Mechanics and Mechatronics, Institute of Automotive Mechatronics, Faculty of Electrical Engineering and Information Technology, Slovak University of Technology in Bratislava. Ilkovičova 3, Bratislava, Slovak Republic; michal.ulicny@stuba.sk
[2] **Ing. Martin Baťa**, Department of Applied Mechanics and Mechatronics, Institute of Automotive Mechatronics, Faculty of Electrical Engineering and Information Technology, Slovak University of Technology in Bratislava. Ilkovičova 3, Bratislava, Slovak Republic; martin.bata@stuba.sk
[3] **Ing. Gabriel Gálik, PhD.**, Department of Applied Mechanics and Mechatronics, Institute of Automotive Mechatronics, Faculty of Electrical Engineering and Information Technology, Slovak University of Technology in Bratislava. Ilkovičova 3, Bratislava, Slovak Republic; gabriel.galik@stuba.sk
[4] **Ing. Juraj Paulech, PhD.**, Department of Applied Mechanics and Mechatronics, Institute of Automotive Mechatronics, Faculty of Electrical Engineering and Information Technology, Slovak University of Technology in Bratislava. Ilkovičova 3, Bratislava, Slovak Republic; juraj.paulech@stuba.sk
[5] **Ing. Šimon Berta**, Department of Applied Mechanics and Mechatronics, Institute of Automotive Mechatronics, Faculty of Electrical Engineering and Information Technology, Slovak University of Technology in Bratislava. Ilkovičova 3, Bratislava, Slovak Republic; simon.berta@stuba.sk
[6] **Ing. Andrej Ürge**, Department of Applied Mechanics and Mechatronics, Institute of Automotive Mechatronics, Faculty of Electrical Engineering and Information Technology, Slovak University of Technology in Bratislava. Ilkovičova 3, Bratislava, Slovak Republic; andrej.urge@stuba.sk

model of the battery pack by simplifying the numerical CFD model into a so-called Reduced Order Model (ROM) component, which is later implemented in a system architecture. Various computational software from ANSYS were used to produce these models and simulations, namely ANSYS Fluent for CFD simulations, ANSYS Twin Builder for system simulations and ANSYS ROM Builder for the creation of the ROM model itself. Used version of all these software was 2023 R2 [2].

STATIC ROM

There are several mathematical methods that are used to reduce complex models, the method used by ANSYS ROM Builder for static ROM is called Singular Value Decomposition (SVD). The logic of this method works on the principle described in Eq. (1) [3]:

$$\boldsymbol{X} = \boldsymbol{U} \cdot \boldsymbol{\Sigma} \cdot \boldsymbol{V}^{*} \tag{1}$$

Where the left side represents a matrix $\boldsymbol{X}$ consisting of the learning data (snapshots, one snapshot is basically one simulation) in which each column represents the values of each snapshot so the values of observed outputs. On the right side matrix $\boldsymbol{U}$ represents unitary matrix with left singular vectors also called modes. Number of modes determines whether accurate representation of data is obtained in ROM so it has to be chosen correctly but does not have to too large since the first vectors contribute the most to influencing the outcome and last vectors have zero value (they are sorted by influence, this is where the reduction happens). Later, a number of verification points is selected to evaluate the error of the results of the reduced model compared to the original model. Matrix $\boldsymbol{\Sigma}$ represents diagonal matrix which consists of singular values and matrix $\boldsymbol{V}^{*}$ represents unitary matrix with right singular vectors [4].

INVESTIGATED PART

The subject of investigation is a battery pack consisting of 15 batteries and three meandering cooling channels in which water flows as a cooling medium, this system is shown in Fig. 1:

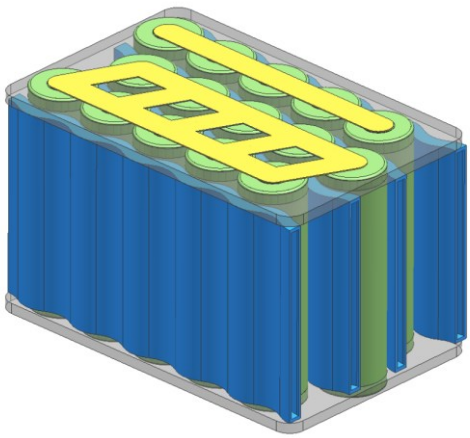

Fig. 1 Investigated battery pack

However, the whole battery pack as a whole is too demanding for CFD computation if it has to interact with the other components in the system model in real time, so it was necessary to create a reduced model of the pack, specifically of a selected region, which is also in Fig. 2 (ROMs will be copied next to each other in the system model):

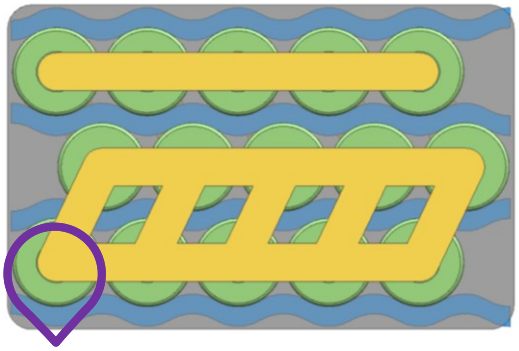

Fig. 2 Selected region for ROM

The concept behind the simulation is that the electrical quantities of the batteries are temperature dependent, therefore these blocks representing the individual batteries receive information about their temperature from the CFD simulation and in turn provide information about the generated power as input to the CFD simulation.

Meshed version of 3D model of the investigated part which consists of a single battery, sliced region of cooling channel and water can be seen below in Fig. 3:

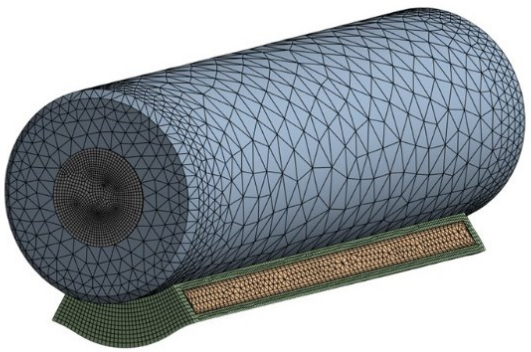

Fig. 3 Mesh of a selected region of the battery pack

DESIGN OF EXPERIMENT AND RESULTS

In the design of experiment (DoE), the mass flow and water temperature at the beginning of the cooling channel section and the battery power are considered as inputs to the ROM. The temperatures at the end of the cooling channel section and the average temperature of the battery are considered as outputs. The range of mass flow is considered from 0 to 0.02 kg/s, the range of inlet temperature from 270 to 360 K and the power from 0 to 10.5 W. A total number of samples (snapshots) from 100 to 150 were selected in which the ranges of input variables were distributed according to the optimal space-filling design method. After DoE calculation, the number of modes was found to achieve the best results set to 20 and the number of verification points to 20. Here, the results from first analysis with 100 snapshots, 20 modes and 15 verification points achieved the errors shown in Tab. 1 according to the evaluation methods also shown in the table (for each method, the best achievable value is 0 %).

Tab. 1 Values of errors in the first DoE

Method	Learning points value [%]	Verification points value [%]
Global Relative Norm2 Error	0.1174	1.9683
Average Relative Norm2 Error	0.076157	0.83047

After further experiments, it was confirmed that increasing the number of snapshots and verification points increases the quality of the ROM model, which can be seen in the evaluated error percentages. The experiment with 150 snapshots, 20 modes and 20 verification points seemed to be the most advantageous DoE, as it achieved the best ratings for low percentage error, but at the same time it did not use as much data. This is shown in Tab. 2.

Tab. 2 Values of errors in the best DoE

Method	Learning points value [%]	Verification points value [%]
Global Relative Norm2 Error	0.00054099	1.8197
Average Relative Norm2 Error	0.00041464	0.56221

CONCLUSION

After introducing and analyzing the main issue of this paper, the investigated problem regarding the degradation of battery systems based on inhomogeneous thermal load during operation, software tools used for detailed and system simulation were also introduced. However, the core of the work lies in the proposal of an approach to investigate this problem and its solution, this work specifically addresses the reduction of a complex 3D CFD model of a battery pack consisting of 15 batteries to a ROM due to which it will also be possible to compute thermal analyses of such a complex system in real time (in integration in a system model with other components). For this, a certain part of the geometric model was selected, whose reduction is sufficient. But most importantly, a suitable number of modes and verification points was found to achieve a sufficient ROM, whose errors, found using the Global Relative Norm2 Error and Average Relative Norm2 Error methods, reached values relatively close to 0 %.

ACKNOWLEDGEMENT

This work was supported by the project of the internal FEI STU call Innovative batteries and battery systems for e-mobility applications (BATSYS).

REFERENCES

[1] V.S. Bagotsky, A.M. Skundin, Y.M. Volfkovich. Electrochemical Power Sources: Batteries, Fuel Cells, and Supercapacitors. The ECS Series of Texts and Monographs. Wiley, 2015. ISBN 9781118460238

[2] Ansys® Academic Research, Release 23.2

[3] S.L. Brunton, J.N. Kutz. Data-Driven Science and Engineering. Cambridge University Press, 2019. ISBN 9781108380690

[4] ANSYS RomDocs RomBuilder, 2023 R2, Section 1.2.2

APPLIED MECHANICS 2024

April 17th – 19th, 2024
Hotel Toliar, Štrbské Pleso
Slovakia

ANALYSIS OF THE MECHANICAL PROPERTIES OF NANOFIBROUS SURGICAL SUTURES

M. VOPÁLKOVÁ[1]*, T. SUCHÝ[2], R. SEDLÁČEK[3], D. LUKÁŠ[4], J. MIKULE[5]

In this work, we investigated the mechanical properties of a novel nanofibrous suture composed of polycaprolactone monofilament core and polycaprolactone AC electrospun nanofibrous cover. Our intention was to investigate the mechanical properties with regard to the application of this suture as a chirurgical suturing material for wound closing. We focused on changes in tensile properties during suture cultivation in two types of media (pH 7.2 and pH 8.9 simulating healthy and chronic wounds, respectively) and with or without 2.5N static load which simulates the load in a sutured surface wound.

Keywords: suture; nanofibers; mechanical properties

INTRODUCTION

Since ancient times, mankind has been looking for effective ways to treat injuries, and one of the oldest and most important procedures is the use of sutures. The treatment of injuries by sutures dates back to ancient times, with the earliest surviving mention found in the Edwin Smith surgical papyrus from 3,500 BC. Additional references to suturing wounds can be found in Charaka's Samhita, a treatise dated to about 1,000 BC, which also discusses alternative methods such as the use of ant claws for wound closure. Susrata's Samhita, dating back to about 600 BC, further elaborates on the use of various sewing materials, including sutures made from horsehair or animal sinews, demonstrating the longstanding practice of wound suturing across different cultures. Additionally, evidence of sutures has been discovered in Egyptian mummies, indicating its widespread use in ancient civilizations [1, 2].

Despite its ancient origins, wound suturing continues to undergo development and research, particularly in the realm of suturing materials. One such advancement is the development of

[1] **Bc. Marika Vopálková**, Department of Mechanics, Biomechanics and Mechatronics, Faculty of Mechanical Engineering, Czech Technical University in Prague, Technická 4, Prague, Czech republic; marika.vopalkova@fs.cvut.cz
[2] **doc. Ing. Tomáš Suchý, PhD.,** Institute of Rock Structure and Mechanics of The Czech Academy of Sciences, v. v. i., V Holešovičkách 94/41, Prague, Czech republic; suchy@irsm.cas.cz
[3] **doc. Ing. Radek Sedláček, PhD.**, Department of Mechanics, Biomechanics and Mechatronics, Faculty of Mechanical Engineering, Czech Technical University in Prague, Technická 4, Prague, Czech republic; radek.sedlacek@fs.cvut.cz
[4] **prof. RNDr. David Lukáš, CSc.**, Department of Chemistry, Faculty of Science, Humanities and Education, Technical University of Liberec, Studentská 5, Liberec, Czech Republic; david.lukas@tul.cz
[5] **Ing. Jaroslav Mikule**, Department of Chemistry, Faculty of Science, Humanities and Education, Technical University of Liberec, Studentská 5, Liberec, Czech Republic; jaroslav.mikule@tul.cz

nanofibrous sutures, made possible through a production method known as AC electrospinning. These sutures aim to mimic the structure of the extracellular matrix, potentially reducing inflammation within the body. Given that the extracellular matrix primarily consists of nano and microfiber structures, the use of nanofibrous sutures holds promise for enhancing patient comfort and promoting healing [3].

Understanding and evaluating the properties of these novel sutures, including mechanical properties and biocompatibility, is crucial for their successful application. By gaining insights into the behavior of nanofiber sutures, researchers can contribute to the ongoing development of improved suture materials, ultimately advancing patient care and outcomes.

MATERIALS AND METHODS

The focus of this study is primarily to characterize and evaluate the mechanical properties of the tested nanofibrous sutures under simulated wound conditions. Specifically, four types of sutures were examined: two kinds with a monofilament core and a nanofibrous shell (core: monofilament, polycaprolactone, RWTH Aachen; packaging: nanofiber, polycaprolactone, AC electrospinning, TUL) varying in pulling speed of the central suture, in the case of suture A this speed was 20 $m.min^{-1}$. and in the case of suture B it was 30 $m.min^{-1}$, a standalone central monofilament M, and, for comparison with commonly used degradable suturing materials, the Monolac suture K (monofilament, Glycolide-ε-Caprolactone, EP 2, Chirana T. Injecta, s.r.o.) was selected.

In terms of mechanical properties, we assessed characteristics relevant to the use as suturing material. We focused on tensile properties (following the guidelines of standard ČSN EN ISO 2062 [4], using winding jaws with a free length of 250 mm, crossbar speed of 250 $mm.min^{-1}$, and the universal testing machine Inspekt 100kN; force sensor AST, KAF 1kN) after cultivation in the specified media for up to 14 days.

For cultivation purposes, two types of media were utilized aiming at mimicking a healthy wound (pH 7.2, phosphate buffer saline) and a chronic wound (pH 9, borate and acetate-carbonate buffer). Both media were kept at 37 °C. Sutures were cultured both without load and under static load (2.5 N, representing the lower limit of forces exerted on stitches during sewing [5, 6]) to account for sample handling. All materials were tested also in a dry and hydrated (1 hour) state for comparative purposes.

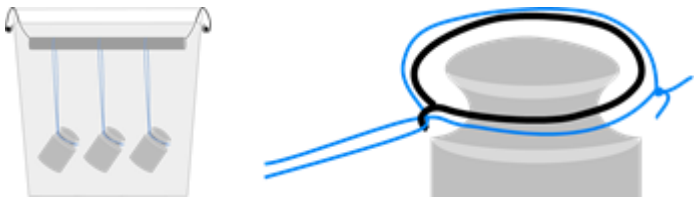

Fig. 1 Suture cultivation scheme and weight tying scheme

From the point of view of statistical evaluation of the measured data due to the violation of normality in some groups of data (Shapiro-Wilk, α=0.05), the match of variances was evaluated by Levene's test (α=0.05) and the agreement of the distribution was tested using nonparametric Mann-Whitney tests (α=0.05, Bonferroni correction).

RESULTS

This paper discusses the first results of the experiment. First, a comparison of four types of sutures and then comparison of the degradation of one of the examined suture with the control suture (Suture A) in the medium simulating a chronic wound (Medium c) and finally the development of the measured properties during cultivation on the example of one of the examined suture (Suture A).

Here we present, the maximum forces and the corresponding engineering strain. When comparing the nanofibrous sutures (A, B) and monofilament (M) with the control suture (K), it is evident that in the dry state, the standard sutures achieves both higher maximum forces (more than twice) and higher engineering strains. It has also been shown that the nanofibrous shell has no effect on the maximum achieved force, as the shell does not carry any load, but the shell has an impact on the engineering strain. Probably the friction between the shell and the central monofilament seems to cause less engineering strain than with the monofilament itself as you can see on Fig. 2.

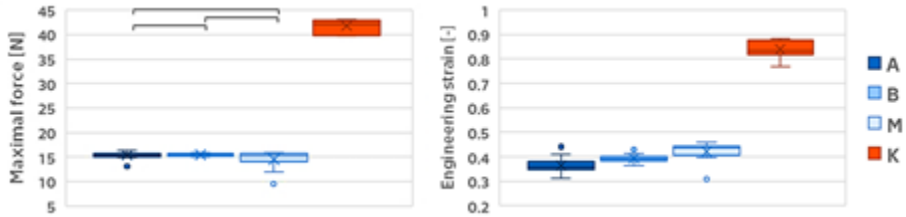

Fig. 2 Graphs of measured tensile characteristics of all examined sutures under dry conditions (n=7 - 18, $p<0.05$, Mann-Whitney test, the pairs without statistically significant differences are marked with connectors)

When comparing the control suture and the type A sutures (cultivation in a medium simulating a chronic wound, without static load), it can be seen that both in terms of maximum force and engineering strain, the control suture has a faster degradation process than the type A suture (the maximum achieved strength has practically not changed and the engineering strain has only increased between the zero and seventh day, which is probably mainly related to the complete hydration of the suture.

Interesting phenomena have also been observed in the cultivation of sutures in medium. First, with just an hour of hydration, the measured engineering strain increased significantly, probably due to a reduction in friction between the nanofiber shell and the central monofilament. An interesting effect was also observed in sutures loaded with static load. With these sutures, we have seen an increase in the maximum forces and at the same time a decrease in the engineering strain compared to freely cultivated sutures, these observed phenomena point to a phenomenon called stretching (uniaxially stretched polymer chains lead to higher stiffness and strength in the direction of the stretched chains) [7].

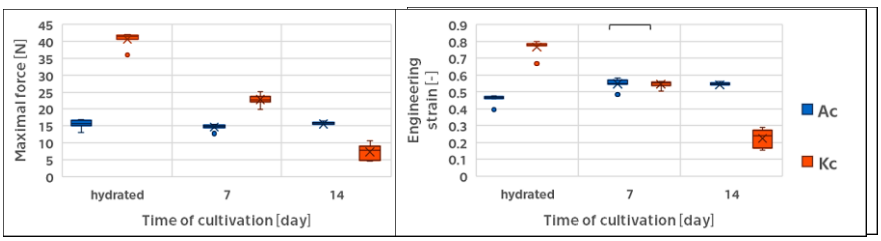

Fig. 3 Graphs comparing control suture and suture A in medium with pH 9 without weight loading (n=7, $\alpha=0.05$, Mann-Whitney, the pairs without statistically significant differences are marked with connectors)

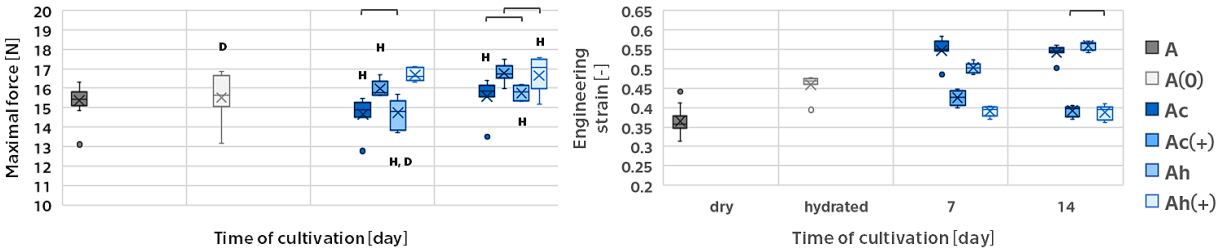

Fig. 4 Graphs of tensile properties during the cultivation of type A suture (Ac medium with PH 9, Ah medium with pH 7.2, (+) static load) ($n \geq 7$, α=0.05, Mann-Whitney, the pairs without statistically significant differences are marked with connectors, with dry marked by D, with hydrated marked with H)

CONCLUSION

In our study, we explored the mechanical characteristics of nanofiber sutures. Our findings reveal that tensile properties are primarily impacted by the suture's core, while the cladding affects elongation and offers protection against degradation in the medium. Additionally, hydration and cultivation load influence the measured results. Notably, the tested nanofiber sutures exhibited slower degradation compared to the control suture, along with lower initial maximum forces and engineering strain. These conclusions induce a framework for further improvement of the developed suture and further research, especially with regard to other mechanical properties such as bending properties, friction properties, creep behaviour of the suture as a whole, but also the behaviour of the wrap as such under mechanical load.

ACKNOWLEDGEMENT

This research work was supported by the Grant Agency of the Czech Technical University in Prague SGS22/149/OHK2/3T/12.

REFERENCES

[1] J. Rose, F. Tuma. Sutures And Needles. *StatPearls* [online]. Treasure Island (FL): StatPearls Publishing, 2022 [cit. 2023-04-13]. 30969713. https://pubmed.ncbi.nlm.nih.gov/30969713/

[2] C.C. Snyder. On the history of the suture. *Plastic and Reconstructive Surgery* **1976**, 58 (4), 401. ISSN 0032-1052.

[3] R. Rošic, P. Kocbek, J. Pelipenko, J. Kristl, S. Baumgartner. Nanofibers and their biomedical use. *Acta Pharmaceutica* **2013**, 63 (3), 295-304. DOI: 10.2478/acph-2013-0024

[4] ČSN EN ISO 2062. Textilie - Nitě na návinech: Zjišťování pevnosti a tažnosti jednotlivých nití při přetrhu pomocí přístroje s konstantní rychlostí prodloužení (CRE). Praha : Úřad pro technickou normalizaci, metrologii a státní zkušebnictví, 2010.

[5] N. Marsidi, S. Vermeulen, T. Horeman, R. Genders. Measuring Forces in Suture Techniques for Wound Closure. *Journal of Surgical Research* **2020**, 255, 135-143. DOI: 10.1016/j.jss.2020.05.033

[6] B.R. Austin, R.A. Henderson. Buried Tension Sutures: Force-Tension Comparisons of Pulley, Double Butterfly. *Mattress, and Simple Interrupted Suture Patterns. Veterinary Surgery* **2006**, 35 (1), 43-48. DOI: 10.1111/j.1532-950X.2005.00110.x

[7] M.R. Mackley. Polymer processing: the physics of stretching chains. *Physics in Technology* **1978**, 9 (1), 13-19. DOI: 10.1088/0305-4624/9/1/I03

APPLIED MECHANICS 2024

April 17th – 19th, 2024
Hotel Toliar, Štrbské Pleso
Slovakia

SMART MATERIAL IS NOT NECESSARILY GENIOUS

L. ZACH[1]*, V. KRALÍK[1]

This paper introduces some ideas about how the nature could be inspiring for biomechanical solutions. The application of new material structures inspired by nature is wide-ranging, due to additive technology even implantology but also in traditional mechanical applications where new smart solutions are needed to achieve all kinds of savings.

Keywords: biomimetics; additive technology; implantology; biomechanics; finite element method

INTRODUCTION

Biomimetics is an interdisciplinary branch of science where the biological tissues are studied by the engineers and the scientists with the aim to invent or to innovate new material structures and innovative products. A nature offers many material structures that have been optimized by billions of years of evolution and are worth inspiration and study. In general, the nature prefers the “additive technologies” when it comes to build a mass. The nature also prefers continuously (gradually) changing mechanical properties and composite structures. These features are rarely found in the engineering materials due to the difficulties in conventional manufacturing technologies. Nature's imagination often goes beyond our technical capabilities. However, the development of 3D printing represents a significant advance for the field of biomimetic materials. It is thus possible to combine 3D structures and materials "endlessly" to find suitable solutions, e.g. for optimally rigid and flexible, biocompatible, absorbable, biodegradable, etc. structures. Not genious solutions but definitely smart, nonetheless, inspired by nature, made by machines.

BIOMECHANICS AND BIOMIMETICS

The essence of all engineering devices is the material. In biomechanics, the term artificial is often used - e.g., artificial replacement - although this is not related to the material but to a manufacturing that is not "in-vivo". However, implantology has always been about one thing, and that is to replace the non-functional with the functional. And for a long time, the living with the non-living. Even today, despite to the possibility of implanting living tissues, the development of artificial implants is a challenge, and living nature is an endless inspiration. So-called biomimetic materials are then created in the laboratory as a result of the successful study of living tissues.

[1] **Ing. Lukáš Zach, PhD.**, **Ing. Vlastimil Králík, PhD.**, Department of Mechanics, Biomechanics and Mechatronics, Faculty of Mechanical Engineering, Czech Technical University in Prague, Technická 4, Praha, Czech republic; lukas.zach@fs.cvut.cz, vlastimil.kralik@fs.cvut.cz

The sophistically structured and lightweight bone as a bio-composite is replaced in artificial replacements by an unnaturally compact and rigid structure that affects other surrounding parts. And the same is true for many other implants. However, bone is by nature not only a load-bearing element, but also a flexible one. Or, another example, the dental ligament, which is actually a natural shock absorber that prevents damage to the tooth when biting down on anything hard.

An inherent property of living tissues is also their degradability. Printing from environmentally friendly materials is therefore another benefit that the development of 3D printing brings with it.

The typical methodology used in biomimetics is shown in Figure 1, where in the first step is the idea initiated by researcher (knows the solution) or technologist (knows the problem) and the goal is the invention.

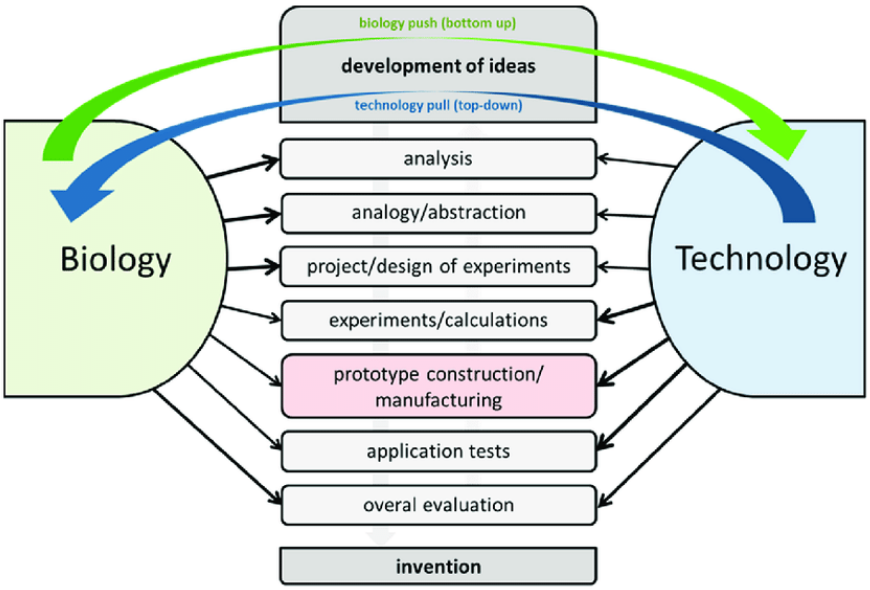

Fig. 1 Simplified chart of a biomimetic development process [1]

An abstraction process, meaning an extraction and a generalization of principles found in a biological model, is one of the most important steps, but also one of the most difficult steps in a biomimetic project. A prerequisite for the abstraction is to separate important influencing factors from irrelevant influencing factors for a given effect and then determine a type of a relationship that exists between the influencing factors.

Gradient structures – wooden bio-composites

To characterize a live matter incl. wooden material as a homogenous material is always tricky. The wood fits the definition of a fiber (bio-)composite. A strength and stiffness of the matter depends on the orientation of "building blocks" and loads. It causes the wood act as a different material when loaded by a pressure force, tensile force, bending moment, etc. [2-4] Although the material is purely anisotropic, a simplification is made to describe it as orthotropic or even isotropic material.

A good example of two different woods is a liana and a bamboo [5]. When plotting a graph of a modulus of elasticity as a function of a radial position (see Figure 2), there is clearly demonstrated the reversed behaviour of both woods. These quite simple structures can be called gradient structures, which can be mathematically modelled and inspiring for new engineering solutions, since the gradient of the modulus of elasticity can positively influence the stress distribution while

bending. The inspiration by these bio-composite could bring new gradient material structures with optimized (evenly distributed) stress distribution throughout the cross-section.

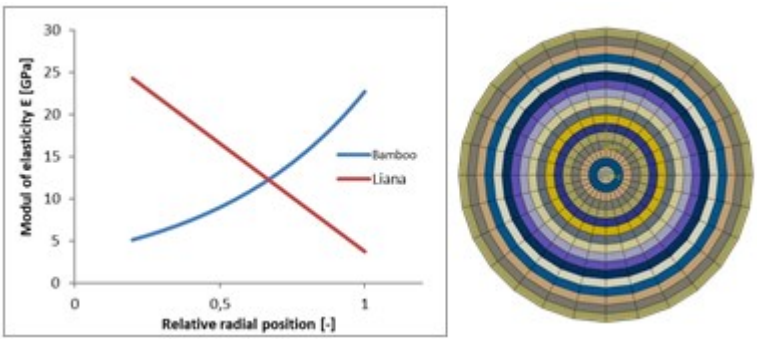

Fig. 2 Graph of relationship of modulus of elasticity as a function of a radial position [5].

For the simulation of both wooden structures by FEM to show their advantages, two models with 17 layers of gradient modulus of elasticity have been prepared. The liana and the bamboo were modelled as beams 100 mm long and 17 mm in diameter. The results of gradient structures have been compared to constant moduli models (E = 13.9 GPa for the bamboo and E = 14.02 GPa for the liana). See the Fig. 3 to understand better the influence of gradient structures on the properties.

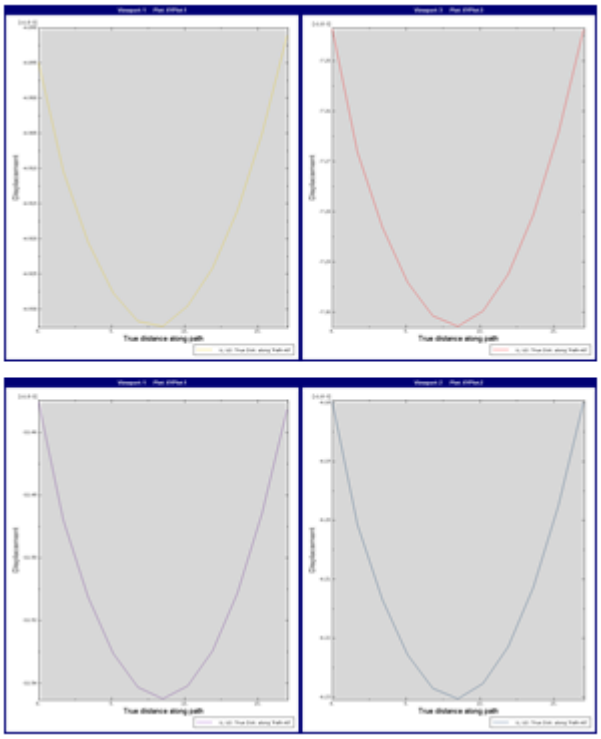

Fig. 3 Results of displacements for a gradient bamboo compared to constants material (above) and gradient liana compered to constant material.

These graphs of displacements are comparing the gradient structure with the constant moduli materials (let's say the average materials). For example, the reduction of displacement of 33% while bending the bamboo-like gradient compared to constant structure is evident, inversely for the liana. We can observe the influence of gradient structure also on the stress distribution and the maxima.

Other structures

Bone like structure could be another type of material, for example the femur, is especially tailored with its anisotropic behaviour to withstand force impacts like running jumping or walking and keeps the bone itself light weight. This behaviour is possible to be replicated using additive manufacturing technologies. This structure is also shockproof where the impacts coming from effects like a falling or a hitting a hard obstacle. Another advantage of the live tissue is a healing effect. Where the bone can be recovered, the implant or another product can fail.

If these impacts happen more often, nature has the solution. For example, a periodontal ligament is a perfect shock absorber and prevents a tooth from being destroyed when a mammal accidently bites into a very hard object [6]. All these bio-composite materials are providing the strength and stiffness. Better outcomes of bio-inspired materials and structures can be reached mainly by:

1. Appropriate material choice;
2. Appropriate combination of materials;
3. Available technology.

CONCLUSION

There are many inspirations in the nature for development of the new smart materials and structures. Fortunately, there is also more and more technologies for (re-)producing such as additive and electroforming technologies or an electrolytic plating.

The deep study of the natural materials is crucial. Where the nature has the self-repairing mechanisms, the engineering material must undergo all necessary tests end experiments.

ACKNOWLEDGEMENT

This work is support by special grants of the Department of Mechanics, Biomechanics and Mechatronics, Faculty of Mechanical Engineering, Czech Technical University.

REFERENCES

[1] Verein Deutscher Ingenieure (VDI). Guideline 6220: Biomimetics, Conception and strategy; Differences between Biomimetic and Conventional Method/Products; VDI: Düsseldorf, Germany, 2012.

[2] P. Horáček, L. Gandelová, J. Šlezingerová. Nauka o dřevě. B.m. : Mendelova zemědělská a lesnická univerzita, 1996. ISBN 80-7157-194-6

[3] F.P. Kollmann, W.A. Cote, Jr. Principles of Wood Science and Technology - I Solid Wood. B.m. : Springer-Verlag Berlin Heidelberg, 1968. ISBN 978-3-642-87928-9

[4] A. Požgaj, D. Covanec, S. Kurjatko, M. Babiak. Štruktúra a vlastnosti dreva. Bratislava : PRÍRODA, a.s., 1993. ISBN 80-07-00600-1

[5] V. Králík, L. Vojtěch. Kompozitní vrstvené biomimetické struktury. [Research Report] Praha : CTU FME, Dept. of Mech., Biomech. and Mechatr., 2020. Report No. 12105/20/46.

[6] M.R. Hien. Soft tissue structural assessment using mechanical measurements. [Doctoral thesis] Edinburgh : Heriot Watt University, 2010.

APPLIED MECHANICS 2024

April 17th – 19th, 2024
Hotel Toliar, Štrbské Pleso
Slovakia

IDENTIFICATION OF FRICTION SIMULATION MODEL PARAMETERS

J. ZAVŘEL[1]*, Z. ŠIKA[2]

The friction model plays a fundamental role in mechanics. Correctly determined model parameters then influence the behaviour of the whole mechanical system. Tabular values of the friction coefficient for Coulomb friction model are not accurate and sufficient. Obtaining other possible parameters for more complex mathematical models (e.g. LuGre model) is then very difficult or highly variable depending on the specific problem. The only possibility is to obtain the parameters experimentally. This is especially true for unknown combinations of materials. In order to obtain objective model parameters, an experimental device has been constructed that allows to evaluate model parameters under different conditions and to identify parameters of more complex mathematical models.

Keywords: friction; LuGre; Coulomb, Stribeck; slip-stick

INTRODUCTION

In every mechanism, mechatronic product, in robotics and in static systems too, passive effects play an important role. In the vast majority of cases, it is sufficient to model them in the simplest way, namely by a Coulomb's law [1]. In this case, the passive effect is equal to the product of the normal force and the friction coefficient. The static coefficient of friction is therefore for adhesion and the dynamic coefficient for passive effects in motion. Usually, uniform motion and a corresponding coefficient independent on the relative velocity of the bodies are considered. Such a description can be used with sufficient accuracy for the design of mechanisms and their dimensioning. For the description of the dynamics of mechanisms, however, these considerations are no longer sufficient. These simple relations are then no longer consistent with real motion when simulating behaviour in terms of dynamics.

However, it is necessary to distinguish between static state and motion. This divides the coefficients of friction into static and dynamic (kinematic - Coulomb) coefficients of friction [2].

[1] **Ing. Jan Zavřel, PhD.**, Department of Mechanics, Biomechanics and Mechatronics, Faculty of Mechanical Engineering, Czech Technical University in Prague, Technická 4, Praha 6, Czech Republic; Jan.Zavrel@fs.cvut.cz
[2] **prof. Ing. Zbyněk Šika, PhD.**, Department of Mechanics, Biomechanics and Mechatronics, Faculty of Mechanical Engineering, Czech Technical University in Prague, Technická 4, Praha 6, Czech Republic; Zbynek.Sika@fs.cvut.cz

The static passive force is given by an equation

$$F_c = \mu_s |N| \tag{1}$$

and the dynamic friction force like

$$F_k = \mu_k |N|, \tag{2}$$

where $|N|$ is the magnitude of normal force, μ_s the static coefficient and μ_k is the dynamic force coefficient.

Models describing more complex phenomena are then used for dynamics problems. One of them is the Stribeck's effect [2].

The Stribeck effect $G(v, N)$ is defined by the equation

$$G(v, N) = F_s + (F_s - F_c) e^{-\left|\frac{v}{\vartheta}\right|^{\alpha}}, \tag{3}$$

where v is the relative velocity, ϑ the Stribeck velocity and α coefficient of the Stribeck curve shape. The parameter α can vary from 0.5 to 2. The Stribeck's curve thus includes both static and dynamic friction effects.

More complex description of the effect is by the LuGre mathematical model with newly introduced state variable z. The model is based on the deformation of the bristles at the contact surface between the bodies (Fig. 1). The state variable z describes their deformation.

$$\dot{z} = v - z \frac{\sigma_0 |v|}{G(v,N)}. \tag{4}$$

The resulting passive effect F is then given by the resulting equation

$$F = \sigma_0 z + \sigma_1 \dot{z} + \sigma_2 v, \tag{5}$$

where σ_0 is the bristle stiffness, σ_1 is the bristle damping and σ_2 is the viscosity coefficient.

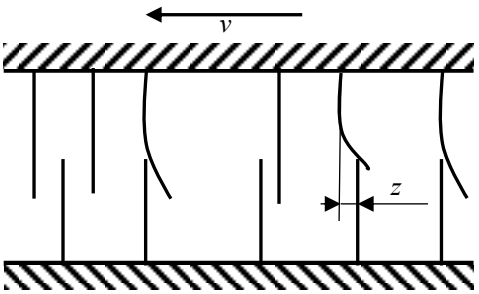

Fig. 1 Deformation of bristles in the LuGre model

Although this model is more complex, it contains many parameters. Obtaining precise specific parameters is very difficult and their values are usually not constant. Some parameters, such as the shape of the Stribeck's curve or the damping and stiffness of the bristles, cannot be generally determined. The parameters are also dependent on the magnitude of the normal force [3]. It makes the coefficient determination difficult.

DETERMINATION OF THE COEFFICIENTS

The coefficients for the friction models can be obtained from tabulated values for different material combinations and their machining and current condition. However, these are only approximate values, which are often very different from the actual task or experiment. Usually only static and dynamic coefficients can be usually found. For this reason, it is advisable to find out the coefficients

experimentally [4]. This is especially necessary for combinations of materials for which tabular values are not given. The correct choice of the mathematical description of friction effect is crucial to the behaviour of the simulation model [5].

In the LuGre model, the setting of the bristles stiffness is crucial. Low bristle stiffness in the model often results in a simulation similar to the low-load experiment. High values are then closer to the Stribeck's curve [4]. Experimentally measured data can be used to obtain correct friction model values by using a simulation model based on the same problem [1].

EXPERIMENTAL RESULTS

An experimental device was built to obtain the coefficients of the friction models (Fig. 2). It is designed to obtain the coefficients of friction of the materials of the moving mass (carriage) on the ground plate. The device consists of a sliding part which is moved by a motor and an attached carriage. The weight of the carriage can varry by adding weight, because there is the possible dependence of the coefficients on the normal force. The motion of both the carriage and the drive is recorded together with the force at their connection. The time record is further used to identify the coefficients needed for the correct adjustment of the mathematical friction model.

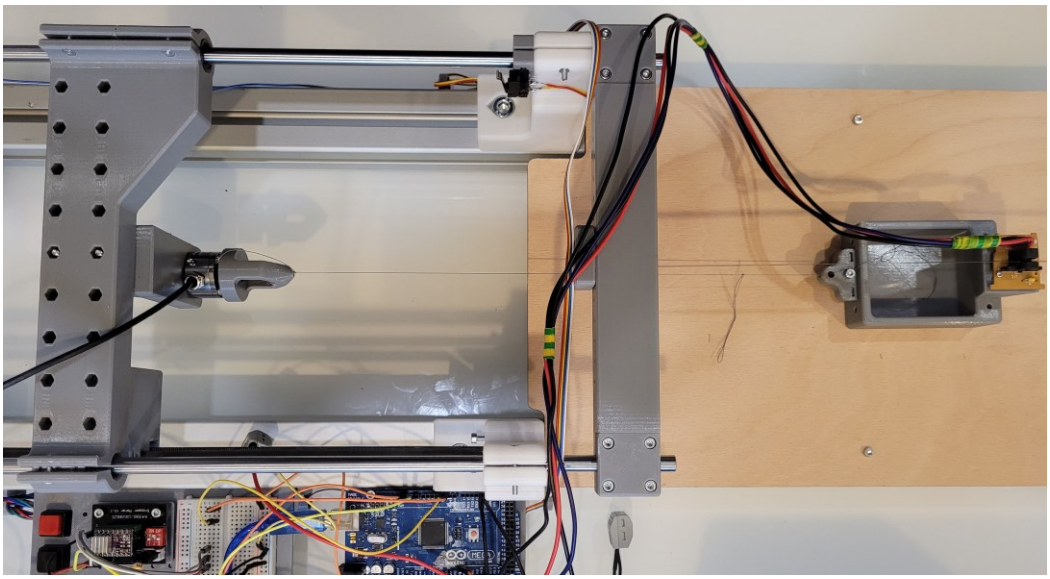

Fig. 2 Experimental device for measurement of friction coefficient

The basic parameters of the models are the coefficients for static and dynamic friction. The static coefficient of friction can be obtained by increasing the force acting on the carriage and measuring its displacement. At the moment when the carriage starts to move, a force has been reached the point from which the static coefficient of friction can be determined. However, it is a good idea to take the measurement with the spring in place, as the transition from static to moving is very quick (Fig. 3a). The dynamic coefficient of friction, on the other hand, is determined at uniform steady motion. For this measurement, it is advisable to have a rigid (very stiff) connection when pulling the carriage. However, the slip-stick effect can, and does, affect the measurement. This effect causes vibrations and the dynamic coefficient must be evaluated on the basis of the average value of the recording (Fig. 3b). An example of the slip-stick effect is shown in Fig. 3c. The slip-stick effect is a natural continuation of the movement when pulling the carriage. When the carriage is pulled from

the static state, it will move and come to a stop. This motion is repeated. As can be seen in Fig. 3c, the poor repeatability of the experiment must be included in the uncertainty of the identified coefficient.

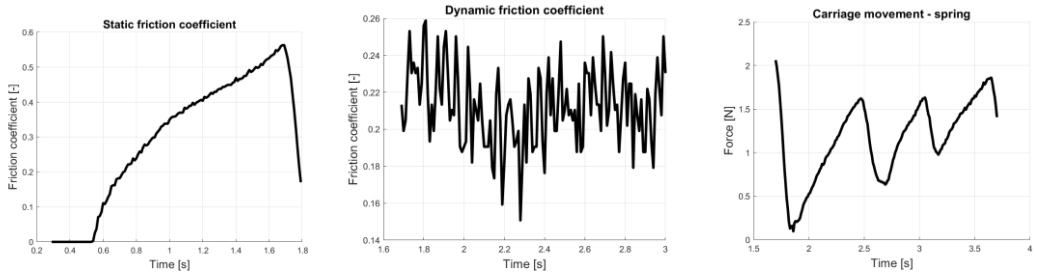

a) b) c)

Fig. 3 Time record of the measurement: a) static coefficient, b) dynamic coefficient, c) slip-stick effect

CONCLUSION

The simulation of dynamic systems is highly dependent on the accurate setting of the coefficients. This is also related to their accurate determination. The evaluation of the coefficients should ideally be carried out under conditions under which the system to be modelled will also be operated. The ideal case is to measure the data on the resulting system and find the parameters on the friction simulation model according to these data [1].

ACKNOWLEDGEMENT

The work has been supported by the project "Identification and compensation of imperfections and friction effects in joints of mechatronic systems" No. 23-07280S of the Czech Science Foundation.

REFERENCES

[1] J. Zavřel, Z. Šika, M. Hajžman. Experimental identification of friction model parameters for selected materials In: Proceedings of computational mechanics 2023. Plzeň : University of West Bohemia, 2023, 221-222. ISBN 978-80-261-1177-1

[2] H. Yanada, Y. Sekikawa. Modeling of dynamic behaviors of friction. *Mechatronics* **2008**, 18 (7), 330-339. ISSN 0957-4158, https://doi.org/10.1016/j.mechatronics.2008.02.002

[3] T. Piatkowski. Dahl and LuGre dynamic friction models - The analysis of selected properties. *Mechanism and Machine Theory* **2014**, 73, 91-100. ISSN 0094-114X, https://doi.org/10.1016/j.mechmachtheory.2013.10.009

[4] L. Pešek, M. Hajžman, L. Půst, V. Zeman, M. Byrtus a J. Brůha. Experimental and numerical investigation of friction element dissipative effects in blade shrouding. *Nonlinear Dynamics* **2015**, 79 (3), 1711-1726.

[5] F. Marques, P. Flores, J.C. Pimenta Claro, H.M. Lankarani. A survey and comparison of several friction force models for dynamic analysis of multibody mechanical systems. *Nonlinear Dynamics* **2016**, 86, 1407-1443.

APPLIED MECHANICS 2024

April 17th – 19th, 2024
Hotel Toliar, Štrbské Pleso
Slovakia

CREATING A SHOULDER MODEL WITH RESPECT TO PASSIVE SCAPULOHUMERAL RHYTHM

O. ZOUFALÝ[1]*, M. DANIEL[2]

Creating a musculoskeletal model of the shoulder joint for biomechanical calculations is a complex process that involves a combination of anatomical knowledge, kinematic data, muscle forces, and mathematical muscle models. One of the challenges while creating model of the shoulder joint is a movement of the scapula. The goal is to make a musculoskeletal that reproduces the motion and function of scapula, clavicula and humerus. With knowledge of scapula movement, we can estimate pathological movement or changes in scapula movement after invasive procedures.

Keywords: Muscle modelling; Shoulder joint; Scapulohumeral rhythm; Hill's muscle model; Scapula movement

INTRODUCTION

Shoulder is a biomechanically complex system that is comprised of interconnected elements, including bones (clavicle, scapula), muscles and ligaments. Scapulohumeral rhythm is a synchronization between humeral elevation, clavicular rotation, and upward rotation of scapula. In the literature the upward rotation of scapula is measured during passive and active humeral elevation. The aim of this study is to evaluate the influence of passive non-linear muscle response on Scapulohumeral rhythm.

METHODS

A 2D dimensional model of shoulder was adopted for simplicity. Bones and muscles geometries were obtained from 3D OpenSim model [1]. A reduction method was used to represent two main muscle groups: Scapulohumeral group and Scapulothoracic group.

Scapulohumeral group mainly consists of rotator cuff muscles, abductors, and adductors of humerus. Musculus teres major and Musculus subscapularis were chosen as a representative adductor of Scapulohumeral group. Scapulothoracic mainly consists of muscles fixing and

[1] **Ing. Ondřej Zoufalý**, Department of Mechanics, Biomechanics and Mechatronics, Faculty of Mechanical Engineering, Czech Technical University in Prague, Technicka 4, Praha 6, Czech Republic; ondrej.zoufaly@fs.cvut.cz
[2] **Prof. RNDr. Matej Daniel, Ph.D.**, Department of Mechanics, Biomechanics and Mechatronics, Faculty of Mechanical Engineering, Czech Technical University in Prague, Technicka 4, Praha 6, Czech Republic; matej.daniel@cvut.cz

stabilizing scapula, Musculus rhomboideus major and minor was taken to represent muscles whose function is downward rotation of scapula.

The center of rotation for the glenohumeral joint was defined at the center of the humeral head. The center of rotation for the scapulothoracic joint was approximated based on previous study [2].

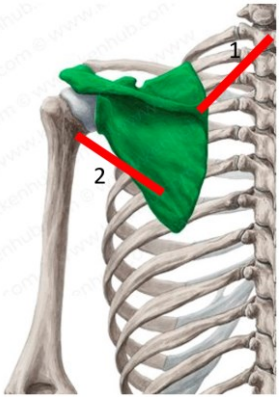

Fig. 1 A model of upper limb with two muscle groups representing teres major and subscapularis muscle (number 2 in the figure) and musculus rhomboideus major and minor (number 1 in the figure)

For the muscle a Hill-type muscle model was used. Hill-type model consists of muscle contractile element in series with elastic spring representing tendon and in parallel with elastic spring representing passive properties of muscle. Muscle force depends on muscle length and contraction velocity. Muscle can produce maximal force at its optimal length and the force decreases when lengthening or shortening. When muscle is stretched above its optimal length, the muscle produces passive force which is not dependent on muscle activation. Force-velocity relationship describes active muscle force during contraction. Muscle force decreases with increasing shortening velocity and vice versa. During isometric contraction the muscle produces maximum isometric force when fully activated.

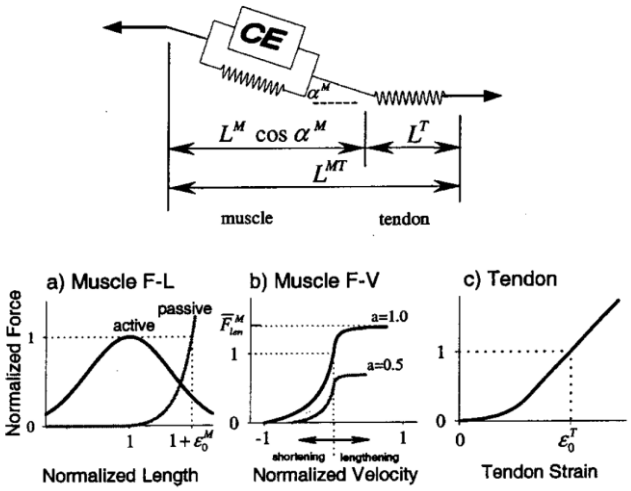

Fig. 2 A Hill-type model describing musculo-tendon mechanics. a) Active and passive force-length relationships. b) Force-velocity relationship for different activation level. c) Tendon force-length velocity which was omitted in this study [3]

In this study only passive properties of the muscle were considered. Muscle passive force is described as follows [3]:

$$\bar{F}^{PE}\left(\bar{l}^{M}\right) = \frac{e^{\frac{k^{PE}\left(\bar{l}^{M}-1\right)}{\epsilon_0^M}-1}}{e^{k^{PE}}-1} F_0 \tag{1}$$

Where $\epsilon_0^M = 0.5 - 0.6$ is the passive muscle strain due to maximum isometric force, $k^{PE} = 5$ is the shape factor of the exponential function and F_0 is maximal isometric force.

The principle of minimum potential energy was used to estimate scapular rotation for a given humeral elevation angle. The principle assumes that the scapula adopts a position that minimizes the total potential of the system, that is the total potential energy stored in the muscles. The potential energy of the muscle was calculated as follows:

$$U_m = \int_{l0}^{l_m} F_m(F_0, l_0, \phi_s, \phi_h) dl \tag{2}$$

Where l_0 is the optimal length of the muscle, l_m is muscle length and F_m is passive force of a muscle, ϕ_s and ϕ_h are angles of the scapula and humerus, respectively. Total potential energy of the system U_C is defined as:

$$\frac{\partial U_C}{\partial \phi_s} = 0 \tag{3}$$

Optimal length of muscles l_0 was estimated as the length of muscle in resting position of upper limb, i.e. when ϕ_s and ϕ_h are equal to zero.

RESULTS

Scapulohumeral rhythm was calculated for different ratios of maximum isometric forces F_0. The results were compared to experimental data of passive scapulohumeral rhythm from previous studies [4-8].

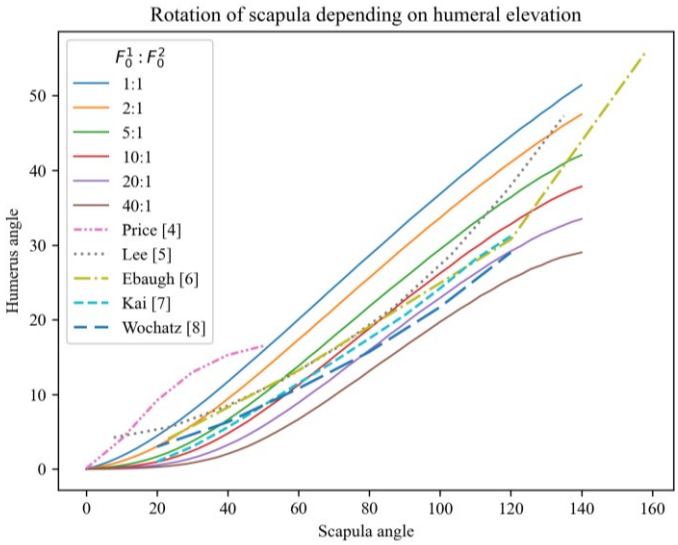

Fig. 3 Rotation of scapula during humeral elevation for different force ratios of muscle groups (F_0^1 and F_0^2 are maximum isometric forces of muscle groups 1 and 2, respectively)

If both muscle groups have approximately the same strength, the motion of scapula is excessive. If the scapulothoracic muscle group is 5-10 times stronger, the model simulates the experimentally measured movement well. When the scapulothoracic muscles are too strong, then the range of scapula movement is low compared to experimental data.

Although the model is planar and simple, it can capture the behavior of scapula during humeral elevation. It can also be seen how the scapula movement changes during different muscle configurations and muscle parameters. It can be useful when analyzing pathological states etc.

CONCLUSION

In this study we showed that we can approximately simulate scapulohumeral rhythm during passive humeral elevation using passive properties of muscle. It can be useful to predict changes in scapula movement after surgeries or during pathologies in the musculoskeletal system of the upper limb.

In the future work we will deal with scapulohumeral rhythm during active humeral rhythm with respect to stability of glenohumeral joint.

ACKNOWLEDGEMENT

The work on this paper was supported by the Czech Science Foundation grant GA23-06920S.

REFERENCES

[1] W. Wu, P.V.S. Lee, A.L. Bryant, M. Galea, D.C. Ackland. Subject-specific musculoskeletal modeling in the evaluation of shoulder muscle and joint function. *J. Biomech.* **2016**, 49 (15), 3626-3634. DOI: 10.1016/j.jbiomech.2016.09.025

[2] F.C. Forte, M.P. de Castro, J.M. de Toledo, D.C. Ribeiro, J.F. Loss. Scapular kinematics and scapulohumeral rhythm during resisted shoulder abduction--implications for clinical practice. *Phys. Ther. Sport* **2009**, 10 (3), 105-111. DOI: https://doi.org/10.1016/j.ptsp.2009.05.005

[3] D.G. Thelen. Adjustment of muscle mechanics model parameters to simulate dynamic contractions in older adults. *J. Biomech. Eng.* **2020**, 125 (1), 70-77. DOI: https://doi.org/10.1115/1.1531112.

[4] C.I.M. Price, P. Franklin, H. Rodgers, R. Curless, G. Johnson. Active and passive scapulohumeral movement in healthy persons: a comparison. *Arch. Phys. Med. Rehabil.* **2000**, 81 (1), 28-31. DOI: 10.1016/s0003-9993(00)90217-x

[5] B. Lee, D. Kim, Y. Jang, H. Jin. Three-dimensional in vivo scapular kinematics and scapulohumeral rhythm: a comparison between active and passive motion. *J. Shoulder Elbow Surg.* **2020**, 29 (1), 185-194. DOI: 10.1016/j.jse.2019.05.036

[6] D.D. Ebaugh, P.W. McClure, A.R. Karduna. Three-dimensional scapulothoracic motion during active and passive arm elevation. *Clinical Biomechanics* **2005**, 20, 700-709. DOI: 10.1016/j.clinbiomech.2005.03.008

[7] Y. Kai, M. Gotoh, K. Takei. Analysis of scapular kinematics during active and passive arm elevation. *J. Phys. Ther. Sci.* **2016**, 28 (6), 1876-1882. DOI: 10.1589/jpts.28.1876

[8] M. Wochatz, S. Rabe, T. Engel, S. Mueller, F. Mayer. Scapular kinematics during unloaded and maximal loaded isokinetic concentric and eccentric shoulder flexion and extension movements. *J. Electromyogr. Kinesiol.* **2021**, 57. DOI: 10.1016/j.jelekin.2021.102517

APPLIED MECHANICS 2024

April 17th – 19th, 2024
Hotel Toliar, Štrbské Pleso
Slovakia

POSSIBILITIES OF VIBRATION ENERGY REDISTRIBUTION IN MECHANICAL DRIVES USING PNEUMATIC FLEXIBLE TUNERS

L. ŽUĽOVÁ[1]*, R. GREGA[2], M. KAČÍR[3]

Mechanical oscillation in mechanical drive systems and mechanisms, rotors, supporting structures or vehicles is based on constant transformation of energy. Part of this mechanical energy is converted into unwanted vibrations. The current trend of redistribution this vibration is targeted energy transfer connected to secondary system, where it is absorbed in an irreversible way. Systems of targeted energy transfer are parts of structures with defined construction and properties. Under certain construct conditions, pneumatic flexible tuners can be used in mechanical systems such as TET systems.

Keywords: Nonlinear Energy Sink; Targeted Energy Transfer; Pneumatic flexible tuners

INTRODUCTION

In mechanical drives, during their operation, unwanted torsional vibrations arise, which can be reduced by various available methods and procedures, such as self-frequency control, changing the stiffness and damping of the system, isolators and vibration dampers. These elements are referred to be as dynamic vibration dampers, absorbers, pendulum vibration absorbers and other various dynamic elements. Many of these elements are designed as linear systems that are effective only in a narrow band frequency range and tuned to a specific frequency. However, nowadays many machines and devices operate in broadband frequencies (Fig. 1) and therefore it is necessary to apply such dynamic members to machine drives, whose characteristics and properties would allow of intentional nonlinearities in their design approaches in order to obtain the advantages of nonlinear systems [1, 2]. Precisely the characteristics and properties of pneumatic flexible tuners, during their tuning, could act as members with non-linear curves. The aim of the article is to demonstrate their suitability as TET systems.

[1] **Ing. Lucia ŽUĽOVÁ,** Department of Engineering for Design of Machines and Transport Equipment, Faculty of Mechanical Engineering, Technical University of Košice, Letná 9, Košice, Slovak republic; lucia.zulova@tuke.sk
[2] **prof. Ing. Robert GREGA, PhD.**, Department of Engineering for Design of Machines and Transport Equipment, Faculty of Mechanical Engineering, Technical University of Košice, Letná 9, Košice, Slovak republic; robert.grega@tuke.sk
[3] **Ing. Matúš KAČÍR**, Department of Engineering for Design of Machines and Transport Equipment, Faculty of Mechanical Engineering, Technical University of Košice, Letná 9, Košice, Slovak republic; matus.kacir@tuke.sk

On the basis of these studies, nonlinear systems are developed to be effective in wide band frequency with the ability to effectively act as Nonlinear Energy Sinks – NES (Fig. 2) [2-4].

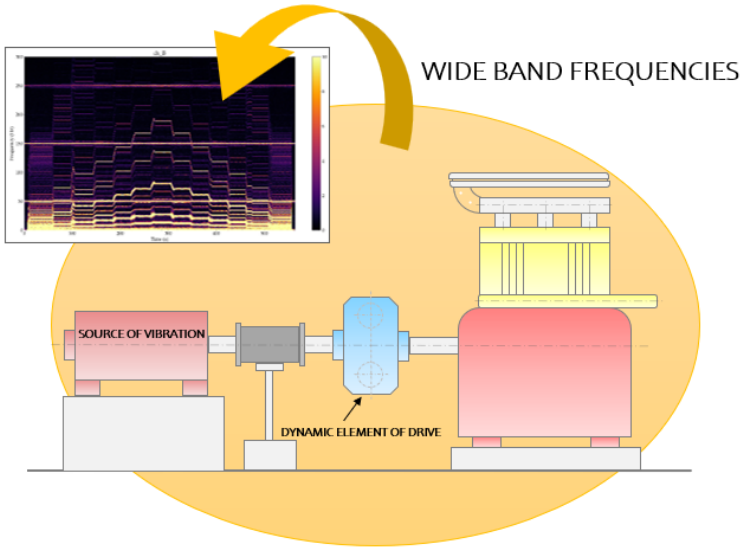

Fig. 1 Example of mechanical drive operating in wide band frequencies

Properly designed NESs can passively absorb energy from linear subsystem. Directing this energy from a linear part of the system to the non-linear part is called non-linear energy distribution, which means the possibility of distribution of vibrational energy using the effect of resonance and non-linear stiffness, which will allow the creation of resonance with any linear sub-system. Targeted redistribution of vibration energy using resonance is called non-linear Targeted Energy Transfer (TET) [5, 6].

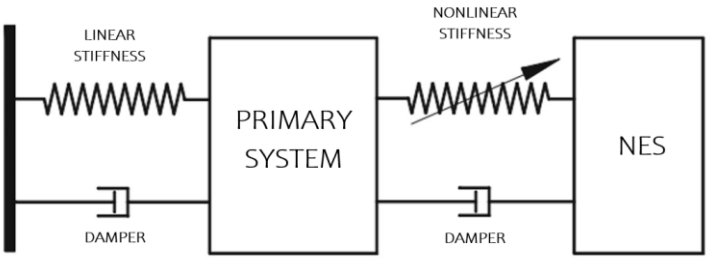

Fig. 2 Scheme of a nonlinear energy absorber [3]

TARGETED ENERGY TRANSFER (TET)

The aim of TET systems is a process of energy transfer from the primary structure to the attached dynamic system in an irreversible manner and results in nonlinear interactions caused by the nonlinear coupling of the NES to the system, leading to efficient passive energy transfer. Mechanical drives are thus protected from destructive vibration amplitudes by passive transfer and dissipation of unwanted energy induced into such systems [6, 7].

However, even for structural modes with wide band frequencies, nonlinear energy interactions can occur in nonlinear systems due to one or more internal resonances. Unlike linear dampers, which operate in a narrow band frequency, the general behavior of linear systems is substantially

changed by nonlinear connections. This is a consequence of the fact that the nonlinear coupling has frequency and energy dependence [8], which causes the ability to operate nonlinearly at a wide band frequency energy regime in the transmission and dissipation of energy through multiple resonant traps in linear systems. These non-linear connections are called NES as mentioned above. Consequently, the NES is considered as a structural passive vibration control device [2].

An effective TET should meet the following criteria from the NES:

- energy should be transferred to the NES in a one-way, irreversible way (i.e. minimal energy should be pumped back into the primary structure),
- fast transfer and dissipation of a large amount of energy from the primary system,
- TET should occur in a wide range and different types of impulsive arousal conditions,
- the secondary (added) mass should be relatively light compared to the primary construction of the system,
- the efficiency of the TET process should be adapted to the dynamically changing parameters of the system [2].

Practical application of TET systems

The use of TET systems is currently used in many engineering industries where torsional vibrations occur. One of these sectors is automotive industry, where the reduction of torsional vibrations in engine has the effect of extending the life of its parts, improving performance as well as reducing engine noise. The part of the drive in which it is possible to change the dynamic properties in order to reduce torsional vibrations is the dual-mass flywheel (DMF). However, the high requirements for the elimination of drive vibrations can no longer be satisfactorily eliminated using conventional DMF.

An innovation for the effective elimination of unwanted torsional vibrations of the engine is a DMF with centrifugal pendulum dampers. Centrifugal pendulum dampers are an additional functional unit in a DMF, which contains pendulum masses on a secondary mass (Fig. 3). The springs used in the primary mass absorb the relevant vibrations, while the remaining engine speed irregularities are effectively eliminated by the pendulum masses.

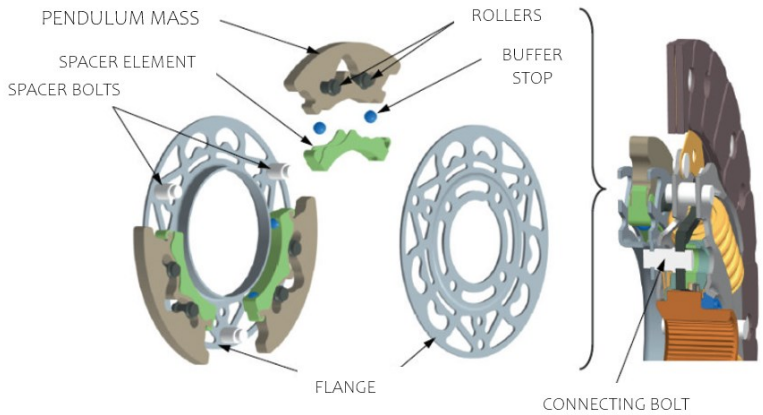

Fig. 3 Dual-mass flywheel with pendulum centrifugal damper

The pendulum masses are arranged at 90° intervals and dimensioned so that they can swing freely in the direction of rotation. The mass of the pendulum masses (Fig. 4) and the curved radius of the carrier track are precisely matched to the torsional vibration or behavior of motor so that they oscillate in opposition to the torsional vibration of motor. By this opposing effect of the pendulum

force, disturbing torsional vibrations of the engine in front of the gearbox are very effectively reduced.

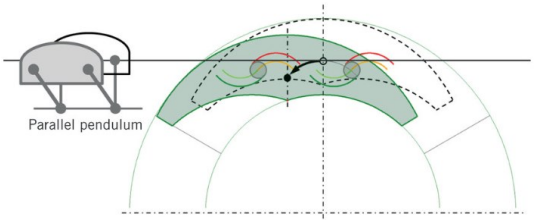

Fig. 4 Pendulum masses [7]

APPLICATION OF PNEUMATIC FLEXIBLE TUNER

The aim of appropriate tuning of a torsional oscillating mechanical drive is the elimination of unwanted vibrations created in drive. One of the options for tuning the mechanical drive is the application of a pneumatic flexible tuner, specifically a pneumatic flexible coupling (Fig. 5), which is developed at the Department of Engineering for Design of Machines and Transport Equipment, Faculty of Mechanical Engineering of Technical University in Košice, which is dedicated to the development, research and application of pneumatic flexible torsional couplings in mechanical drives.

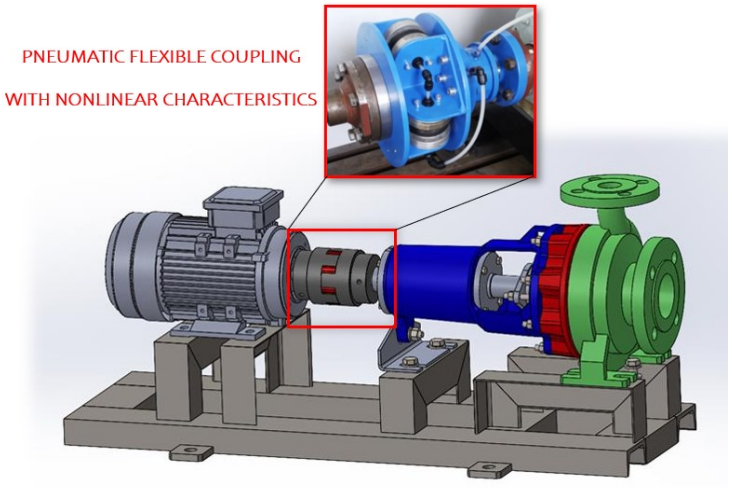

Fig. 5 Application of a pneumatic flexible coupling in drive instead of a conventional coupling

The basic characteristic of pneumatic flexible couplings is a compression space located between the driving and driven parts of the coupling. The compression space is made up of one or more pneumatic-elastic elements, which may or may not be interconnected. The pneumatic-elastic element is filled with a gaseous medium (most often air). The construction and principle of the function of pneumatic couplings allows to achieve a wide variability of their strength and operational properties, which is one of their exceptional properties [9]. In the case of a suitably tuned pneumatic tuner to the required values of torsional stiffness, it would be possible to achieve courses of dynamic components similar to the course of the characteristics of a non-linear system, which could have the function of a TET system after additional design solutions. A pneumatic spring element designed in this way would be able to absorb the dangerous torsional vibrations that would be absorbed in it. Figure 5 shows a mechanical drive with a conventional coupling as an

example, which after replacing it with a pneumatic flexible coupling, could act as a mechanical drive with a TET system.

CONCLUSION

As can be seen, the increasing demands for the smooth operation of machines and devices with mechanical drives with the lowest possible values of torsional vibrations is a worldwide trend that brings challenges in the research and development of dampers and tuners. The increased need to reduce torsional vibrations brings with it ever new possibilities of using long-used dampers and torsional vibration tuners, but with implemented new elements of non-linear systems that take advantage of their advantages.

From the above-mentioned possibilities of applying nonlinear systems in practice, we can conclude that nonlinear systems applied in mechanical systems have a justified function of targeted reduction of unwanted vibrations arising during their operations. Solutions for damping vibrations designed before the introduction of NES and TET are effective, but their use is limited to certain working frequencies, and thus they do not have as wide range of possibilities as the use of systems with nonlinear properties. Another great advantage of these NES and TET systems is their structural simplicity and versatile use of different types for a specific mechanical system with changing dynamic properties.

ACKNOWLEDGEMENT

The work has been supported by the grant project KEGA: 037 TUKE-04/2024, KEGA: 044 TUKE-4/2024 and VEGA 1/0224/23.

REFERENCES

[1] R. Grega, J. Krajnak, L. Žuľová, M. Kačír, P. Kaššay, M. Urbanský. Innovative solution of torsional vibration reduction by application of pneumatic tuner in shipping piston devices. *Journal of Marine Science and Engineering* **2023**, 11 (2), 261.

[2] A.S. Saeed, R.A. Nasar, M.A. Al-Shudeifat. A review on nonlinear energy sinks: designs, analysis and applications of impact and rotary types. *Nonlinear Dynamics* **2022**, 1-37.

[3] Y.S. Lee, G. Kerschen, A.F. Vakakis, P. Panagopoulos, L. Bergman, D.M. McFarland. Complicated dynamics of a linear oscillator with a light, essentially nonlinear attachment. *Phys. D Nonlinear Phenom.* **2005**, 204, 41-69. https://doi.org/10.1016/j.physd.2005.03.014

[4] M. Pfabe, Ch. Woernle. Reduction of Periodic Torsional Vibration using Centrifugal Pendulum Vibration Absorbers. *PAMM* **2009**, 9, 285-286. DOI: 10.1002/pamm.200910116

[5] X.J. Jing, A.F. Vakakis. Exploring nonlinear benefits in engineering, *Mechanical Systems and Signal Processing* **2019**, 125, 1-3. DOI: https://doi.org/10.1016/j.ymssp.2019.01.059

[6] H. Ding, L.Q. Chen. Designs, analysis, and applications of nonlinear energy sinks. *Nonlinear Dyn*. **2020**, 100, 3061-3107. https://doi.org/10.1007/s11071-020-05724-1

[7] M. Hässler, A.D. Kooy, R. Welter, V. Lichtenwald. Clutch Disc With Centrifugal Pendulum Absorber. *Auto Tech Review* **2016**. 5, 26-31. DOI: 10.1365/s40112-016-1118-7

[8] R. Grega, I. Grega. Zjednodušené metódy analýzy pre nelineárne pohonné systémy. In: Transfer inovácií 42/2020, 2020.

[9] P. Kaššay, R. Grega, M. Urbanský, J. Krajňák, M. Kačír, L. Žuľová. Novel Design of Variable Stiffness Pneumatic Flexible Shaft Coupling: Determining the Mathematical-Physical Model and Potential Benefits. *Machines* **2023**, 12 (1), 28 p.

APPLIED MECHANICS 2024

April 17th – 19th, 2024
Hotel Toliar, Štrbské Pleso
Slovakia

MATLAB-ADINA COUPLING FOR FINITE ELEMENT ANALYSIS

M. HANDRIK[1]*, M. VAŠKO[1], J. MAJKO[1], O. PIROH[1]

This paper explores the possibilities of coupling the MATLAB and ADINA software packages. MATLAB serves as the control software, where data is prepared for processing in ADINA for solving the mechanics of continua problems using the finite element method. The information exchange and collaboration between these two software packages will be demonstrated by the example of creating a topology optimization module. The ADINA program does not support the solution of optimization tasks.

Keywords: Adina; MATLAB; finite element analysis; topology optimization; mechanics of continua

INTRODUCTION

Users of commercial software often find themselves lacking certain functionalities within the software. Commercial software may include programming tools for creating additional functionalities, but these options are often limited to a specific area of the software's functionality. In finite element analysis software, this is typically the ability to define new material types or new element types. Modification of other functionalities is practically impossible.

One solution is to couple the MATLAB program with the given commercial software. The missing functionality can be created in the MATLAB environment, thus extending the capabilities of the commercial software. This paper will focus on coupling the MATLAB program and the Adina program for finite element calculations and will create a module for topology optimization. The procedure is applied to a specific software Adina from the field of finite element calculations, and the used procedure can be applied to any other software that meets the basic requirements:

- Running the program from the command line with the input file in the form of a text file. The input file contains all the data necessary to solve the given task, and often the input file contains a sequence of commands necessary to solve the given task.
- Running the solution of the given task from the command line.
- Running the program from the command line with the input file in the form of a text file to export results from the given program. Again, it is most convenient for us if the input file is a sequence of commands for processing and exporting results from the given program.

[1] **Ing. Marian Handrik, PhD.**, **Assoc. Prof. Milan Vaško, PhD.**, **Ing. Jaroslav Majko, PhD.**, **Ing. Ondrej Piroh**, Department of Applied Mechanics, Faculty of Mechanical Engineering, University of Žilina, Univerzitná 8215/1, Žilina, Slovak republic; marian.handrik@fstroj.uniza.sk, milan.vasko@fstroj.uniza.sk, jaroslav.majko@fstroj.uniza.sk, ondrej.piroh@fstroj.uniza.sk

Most finite element analysis programs allow the program to be run from the command line and have their language - commands for creating models. The existence of a language with commands for creating models is due to the historical and long-term development of this group of software packages. Some of the finite element analysis software packages have been under development for over 40 years. In the beginning, the existence of a language with commands was one of the main options for creating models. The coupling of the Adina and MATLAB programs will be carried out in the environment of operating systems with the Linux kernel. In the case of using MS Windows operating systems, minor adjustments are required: setting the PATH variable to the directory with the aui and adina executable files, changing the parameters in the command line for these programs, and changing / to \ in the commands for creating the path to the files.

CONTROLLING ADINA CALCULATIONS FROM THE MATLAB ENVIRONMENT

When controlling calculations in an external program, such as Adina from MATLAB, data exchange needs to be ensured through files. In this case, these will be text files. Working with binary files is more complex, and it is also more difficult to determine the data structure of such a file.

The flow diagram of instructions and data flows when coupling MATLAB and Adina programs is shown in Figure 1. File types are indicated in black. These files typically have the same names and different extensions, and some files may have different names. Program names are shown in azure, as they are called in the system when they are run. Blue arrows show data flows, i.e. which program creates or reads which file. Red arrows show instructions, for running the given program from the MATLAB environment using the system function. Parameters must be defined when running - instructions on how to run the given program.

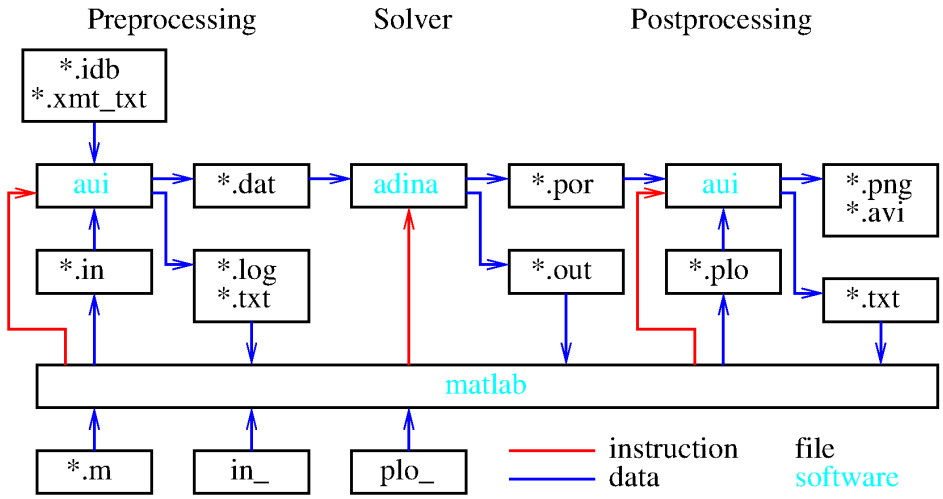

Fig. 1 Instruction and data flow diagram

The instruction and data flow diagram illustrates files categorized by file extension type. The meaning and content of each file type are as follows:

- .m: These are MATLAB scripts and functions. They may contain data required for problem-solving, such as material characteristics, the number of time steps to be solved, the name of the model or task being solved, and other parameters. These files also contain a sequence of

commands for solving a specific task, which may include built-in MATLAB functions used for the task.

- .in: These are input text files for the Adina AUI program. They contain a sequence of commands that create the computational model for the task being solved in Adina. When the file is loaded into Adina AUI, the individual commands are interpreted sequentially in the order they are written in the file. Changing command parameters modifies the model being created and the conditions for interpreting subsequent commands. The sequential calling of commands can be relatively time-consuming but allows for a complete change of the model being created.
- .idb and. xmt_txt: The *.idb input file is a binary file - a database of the task being solved. This file stores information about the model at the time the file was saved and does not contain information about how the model was created. It is possible to modify some model parameters, such as time functions, time steps, linear and nonlinear solver settings, and load values. However, it is not possible to modify the following model properties: geometry - must be recreated, element type - mesh must be deleted and recreated, etc. The *.xmt_txt is a text file containing the geometry in Parasolid format. This file is created if the Adina-M module is used, and the model is saved in the binary database format *.idb.
- in_: These files are created from the *.in file and represent a modified model in the form of a template. The file uses parameters in the commands for creating the model in Adina AUI. The file is used for the repeated creation of .in files. Parameters are written to the file, and the contents of the template in the *in_ are copied.
- .log: These files contain the output of the Adina AUI program generated by redirecting the standard output and error output of the Adina AUI program. The output of the Adina AUI program is the program's response to interpreting the commands in the *.in. If a command is interpreted correctly, the command is written to the output. If a command is not written correctly or an error occurs during its interpretation, the command and warnings or error messages for the command are included. This file is used, if necessary, to check the correctness of the computational model creation and the generation of the *.dat file.
- .txt: These are text files containing output information from the Adina AUI program. The output may include, for example, information about the finite element mesh, node points, geometry, the number of faces on a body, and other information related to model creation. The files may also contain analysis results from the Adina program, such as nodal stresses, element stresses, node point coordinates and displacements, mass, frequencies, and others.
- .dat: This is a text file containing information about the computational model created in the Adina AUI program. The file is an input file for solving the computational model in the Adina program. The file content structure is complex and cannot be used to modify the computational model.
- .por: This is a binary file containing analysis results for the computational model in the Adina program. The file is loaded into the Adina AUI program after switching to the analysis results display mode. The file also stores information about the applied boundary conditions. The file does not contain all types of results; some are calculated only when required for display or output, such as equivalent stresses, principal stresses, and others.
- .out: These are text files created by the Adina program and contain information about the progress of the problem-solving process. The file is created during problem-solving and can be used to monitor the progress of the calculation, convergence of the calculation, or to track problems during problem-solving. After the calculation is finished, the Adina program's termination status is written to the file, indicating successful completion of the task or

termination due to an error. The *.out file is used to check for error-free operation after the Adina program has finished.

- .plo: These contain a sequence of commands for processing results in the Adina AUI program after switching to the results processing mode. In the file, we use a command to load the corresponding *.por file, define the file names for the outputs in *.txt format, and specify which results to output to these files. This file type can also be used to load an analysis results model from a *.por file, and further results calculated in the MATLAB program can be written to this file. Writing the results obtained by processing in the MATLAB program allows these results to be displayed in the Adina AUI program and visualized in the geometric model.
- .plo_: This is a template for creating *.plo files and is used similarly to the *in_ template.
- .png and .avi: These are image and animation files from the visualization of results in the Adina AUI program.

When creating a computational algorithm and its implementation in the MATLAB program, it is not necessary to use all the above file types or Adina program modules. The use of these files depends on the interdependencies and the need for information exchange between the MATLAB and Adina programs.

A significant advantage is the ability to create parametric models within the software being used. The Adina AUI program has this capability implemented. Conversely, if the program does not allow for the creation of parametric models, the implementation of algorithms themselves becomes more complex but still possible. An independent function in MATLAB must be created to enable the generation of parametric models. For such a function, we will implement parameter substitution for a numerical value, inserting the numerical value into the correct location. The function will sequentially read the input file in text format. In each line, the parameter identifier must be searched for, for example, the $ character, and then the text following this character must be identified. After identifying the parameter character and parameter text, substitution for the parameter's numerical value is performed. In the last step, the loaded and modified text is written to a new file. We have used the $ character as the parameter identifier. If this character is used in the input file for the controlled program, we must choose another identifier, possibly a combination of characters, as the parameter identifier.

TOPOLOGICAL OPTIMIZATION

Topological optimization is a specific type of optimization problem. In this problem, a standard design variable is not defined in the form of a scalar value or a vector of design variable values, and therefore classical optimization algorithms cannot be used. We will demonstrate the principle and implementation of topological optimization with the coupling of MATLAB and Adina programs on the task of minimizing weight under the constraint of not exceeding the maximum allowable stress value in the structure.

To begin, let's define the fundamental concepts that will allow us to explain the principle of topological optimization:

- Set of admissible solutions α, or solution space: This represents the set of all points within the domain where a solution to the topological optimization problem is assumed.
- Sets of fixed points β_i: These are sets or spaces of points that must be present in every sub-set of potential solutions.
- Sets of possible solutions to the optimization problem γ_i: Each set γ_i is a subset of the admissible set α and must contain all fixed-point sets β_i.

The relationships between the defined sets are illustrated in Figure 2. All sets of possible solutions must be subsets of the admissible solution set $\{\gamma_1, \gamma_2, \dots, \gamma_n\} \in \alpha$ for the problem. Additionally, all fixed-point sets must be subset of every possible solution $\{\beta_1, \beta_2, \dots, \beta_n\} \in \gamma_i$.

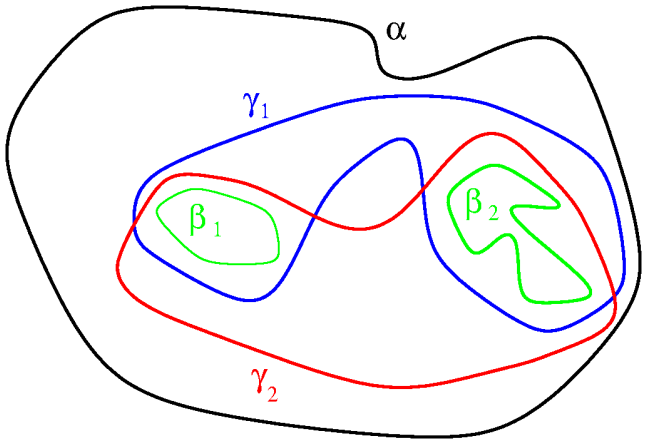

Fig. 2 Sets in topological optimization

If we translate the previous definitions of sets into a language that mechanical engineers understand, then:

- The set of feasible solutions α is a piece of material, for example a cuboid with dimensions 300x100x20 as shown in Figure 3.
- The sets of fixed points β_i are holes for pins to connect to other parts of the structure. From a construction point of view, we must maintain the diameter and spacing of the holes shown in Figure 3.
- The set of possible solutions to the optimization problem – the set γ_i – is any shape of a tie rod that can be made from such a piece of material, where the shape is completely arbitrary but must include holes for connection to other parts of the structure. There is an infinite number of possible solutions to the problem. Based on the defined conditions in the optimization process, we select one of the possible solutions that meets the prescribed conditions. The resulting solution shape may depend on the method of solving the optimization problem and the settings of the method used to solve the topological optimization.

It is impossible to describe the arbitrary shape of any structure using mathematical functions. The description of the surface of the body - a possible solution is unknown, therefore, we cannot use the method of parametric optimization. On the other hand, we will perform stress-strain analysis using the finite element method. In the finite element method, we must discretize the model, i.e. divide the body into a finite element mesh. In our case, we divide the set of admissible solutions α into subsets α_1, α_2, ... α_n – finite elements. Then some subsets α_i – finite elements belong to the set of fixed points β and must be in any possible solution of the task. In our example in Figure 3, these will be finite elements generated on the surface of the holes. The union of all subsets α_i must give us the set α, $\sum_n \quad \alpha_i = \alpha$. If we make a union of only some subsets αi, we get the set of a possible solution of the optimization task – the set γ_i. So, if we consider using only some elements, we get a possible solution to the optimization task.

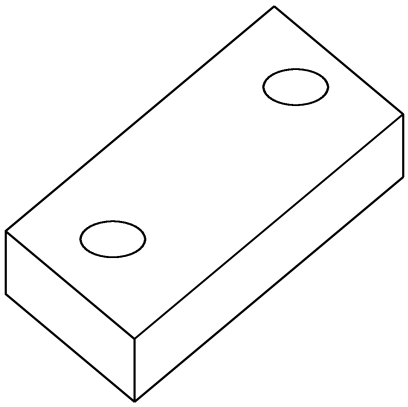

Fig. 3 Set in topology optimization on a real body

Solving a topology optimization problem in the finite element method is straightforward. It involves turning on and off certain groups of elements to obtain various possible solutions for the design geometry of the optimized structure.

We have explained the basic concepts and the fundamental principle of topology optimization, which involves turning on and off finite elements in the computational model. In the iterative process of topology optimization, we will use a material replacement procedure, replacing material with a significantly softer one. After completion - after convergence of the topology optimization task, we will perform the transfer of elements to a new group of elements with a softer material. Performing the calculation with the transferred elements allows us to obtain results on the optimized model and display the optimized shape of the component geometry after topology optimization.

For topology optimization tasks, several algorithms can be constructed based on different strategies for selecting suitable candidates for deactivation. We will present an algorithm based on comparing the equivalent stress state in the elements of the structure:

1. Create an optimized structure model in Adina AUI. Define a material softer than the last material in the order and another last group of elements for deactivated elements.
2. Choose the basic parameters of the optimization process. The number of elements to be deactivated in the model in one iteration is determined as a percentage of the number of activated elements. We also define the number of elements that will be returned to the model and will be activated in one iteration. Their number is chosen similarly to the number of deactivated elements. This is the number of elements that we switch from the deactivated state to the activated state. We define the minimum number of elements to be moved from the activated state to the deactivated state, this number will be the convergence criterion. We define the maximum allowable stress in the structure.
3. Load the computational model into Adina AUI, and obtain information about the number of element groups, the number of created material models, and the geometry included in the EXCLUDE zone.
4. In the next step, we create a selection of elements based on the geometry in the EXCLUDE zone, then we obtain information about the material assigned to the individual groups of elements and a list of all elements included in the individual groups.
5. We test the convergence of the computational algorithm. The convergence criterion is the condition: that the number of elements that can be reassigned to the deactivated group falls below a defined value. If the task has converged, we proceed to step 13.
6. Create a new input file to generate a computational model in Adina AUI with the current state of activated and deactivated elements.

7. In Adina AUI, load the model modified for activated and deactivated elements and create a *.dat file for Adina.
8. Perform stress analysis in Adina and output the stress values in the elements to a text file.
9. Load the stresses from the files and sort them from smallest to largest.
10. Determine the maximum stress value. If the maximum allowable stress value in the structure is exceeded, reduce the number of elements that can be reassigned to another group. Return to the previous step of the iterative procedure and use the information about activated and deactivated elements from the previous iteration step.
11. Select a defined number of elements with the lowest stress value in the activated group and reassign them to the deactivated group. Similarly, select the elements to be reassigned from the deactivated state to the activated state. In this case, we select the elements with the highest stress value on the deactivated elements.
12. Return to step 5.
13. If the computational task has converged to a solution, create a new input file for Adina AUI, in which the elements with a softer material - deactivated elements, are reassigned to the last group of elements - for deactivated elements. Perform the calculation for the model modified in this way, then we can display the optimized structure shape in the results analysis by not displaying the last group of elements.

Creating a computational model for topology optimization and its solution by implementing algorithms in MATLAB and Adina will begin with the creation of a basic geometric model and defining the computational model in Adina AUI. The computational task model in Adina AUI will be created as a file of type *.in, which contains a sequence of commands for the Adina AUI program. When creating the model, we will create the softest material last in order and a group of elements for disabled elements, this group of elements will be created last - with the last serial number. In the input file, we will define a zone called EXCLUDE, which will include all geometric elements that are to form the solid geometry. The created computational model is a simplified model of a bearing housing for mounting a wheelset to the chassis frame of a railway vehicle.

In the Adina AUI program, the created model is read from the model.in file and saved in the form of a binary file *model.idb. This automatically creates a geometry file in the Parasolid format *model.xmt_txt. In the task of topological optimization, neither the geometry nor other parameters related to the geometry, boundary conditions, contact, finite element mesh, or other defined properties are changed. For this reason, the model can be saved in the form of a binary file, which also stores the created finite element mesh. Loading the binary model file, including the finite element mesh, is significantly less time-consuming than generating the finite element mesh on the created geometry.

The second strong argument for using a binary model file is that when using free meshing, a different finite element mesh may be created with each meshing. However, we need the same mesh to be used in the model throughout the topological optimization task. If we have the same finite element mesh throughout the topological optimization task, we can load the mesh parameters at the beginning and process them before starting the actual topological optimization iteration process.

In topological optimization, we will work with several text files generated by the Adina AUI program. We will show the format of the files, the way data is store in these files, and the significance of the data in the topological optimization process.

The first type of file we will work with is the file named model_TSTEP.txt. This file will store information about the number of load cases to be solved. The file has the format:

```
ADINA: AUI version 23.00.00.306, 29 June 2023:  *** NO HEADING DEFINED ***
 Licensed from Bentley Systems, Inc.
 Listing of timestep DEFAULT :

    No.Steps     Timestep size
      10     0.1000000000000E+01

 *** End of list.
```

The file contains a header with eight lines. We need to read these lines, but we do not need the information stored in them. On the following line, two numbers are stored: the first is the number of steps and the second is the step size. The listing is called with the LIST TIMESTEP DEFAULT command.

The second type of file we will work with is named model_NEG.txt. This file will contain information about the elements used in the model. The file has the format:

```
ADINA: AUI version 23.00.00.306, 29 June 2023:  *** NO HEADING DEFINED ***
 Licensed from Bentley Systems, Inc.
        Element group labels:

             1
             2

 *** End of list.
```

The file contains a header with seven lines. These lines are followed by the names of the element groups. By default, a sequential number of the element group is given after the name. The listing is called with the LIST EGROUP command.

The third type of file we will work with is named model_NMAT.txt. This file will contain information about the number of defined material models. The file has the format:

```
ADINA: AUI version 23.00.00.306, 29 June 2023:  *** NO HEADING DEFINED ***
 Licensed from Bentley Systems, Inc.
       Material label:    Type:

            1       Elastic
            2       Elastic

 *** End of list.
```

The file contains a header with seven lines. This is followed by information about the material number and material type. We only need the information about the material number. The listing is called with the LIST MATERIAL command.

The next type of file we will work with is named model_EXC.txt. This file will contain information about the EXCLUDE zone, which is information about the geometric entities on which the fixed finite element mesh elements are located. Fixed finite element mesh elements must always be turned on. The file has this format:

```
ADINA: AUI version 23.00.00.306, 29 June 2023:  *** NO HEADING DEFINED ***
 Licensed from Bentley Systems, Inc.
 Listing of zone EXCLUDE

    Include nodes attached to elements = no
    Include attached geometry        = no
```

```
   Include elements attached to nodes = yes

   Geometry faces 1 to 3 of geometry body 1
   Geometry faces 6 to 7 of geometry body 1
   Geometry face 10 of geometry body 1
   Geometry faces 13 to 15 of geometry body 1
   Geometry face 22 of geometry body 1
   Geometry face 24 of geometry body 1
   Geometry face 27 of geometry body 1
   Geometry faces 31 to 34 of geometry body 1
   Geometry faces 39 to 42 of geometry body 1
   Geometry body 2

*** End of list.
```

The file contains an eleven-line header, followed by lines with information about points, lines, edges, surfaces, faces, volumes, and bodies that are included in the EXCLUDE zone. Based on this information, we will obtain the element numbers that belong to the group of fixed elements. The listing is called with the LIST ZONE NAME=EXCLUDE command.

The next type of file we will use will be named model_EG_N.txt, where N is the sequential number of the element group. We must perform the listing of the element group properties for each element group. The file format is as follows:

```
ADINA: AUI version 23.00.00.306, 29 June 2023:  *** NO HEADING DEFINED ***
 Licensed from Bentley Systems, Inc.
 Listing of element group         1

 Type          = THREEDSOLID
 DISPLACEMENTS   = large
 STRAINS       = default
 MATERIAL      =         1
 RSINT         = default
 TINT          = default
 RESULTS       = stresses
 DEGEN         = default
 FORMULATION     = default
 STRESSREFERENCE = global
 INITIALSTRAIN   = none
 FRACTURE      = no
 CMASS         = default
 STRAIN-FIELD    =         0
 UL-FORMULATION  = default
 LVUS1         =         0
 LVUS2         =         0
 SED           = no
 RUPTURE       = ADINA
 INCOMPATIBLE-MOD= default
 TIME-OFFSET     =  0.0000000000000E+00
 WTMC          =  0.1000000000000E+01
 OPTION        = None
 PRINT         = default
 SAVE          = default
 TBIRTH        =  0.0000000000000E+00
 TDEATH        =  0.0000000000000E+00
 TMC-MATERIAL    =         1
 RUPTURE-LABEL   =         0
 EM            = no
 JOULE         = no
 BOLT-NUMBER     =         0
 BOLT-PLANE      =         0
 BOLT-LOAD       =  0.0000000000000E+00
```

```
BOLT-TOL      = 0.0000000000000E+00
DESCRIPTION   = NONE

*** End of list.
```

The file header has seven lines, followed by information about the settings for the given group of elements. For us, the important line is the one with the keyword MATERIAL, followed by the default material group for the given group of elements. The listing is called with the LIST EGROUP FIRST=N command, where N is the number of the desired group of elements.

The listing of elements belonging to the group of fixed elements will be in a file named model_EFIX.txt. The listing of elements that must always be turned on must be done in two steps:

1. Create a selection of elements for each type of geometric entity.
2. Merge the created selections into a single final selection.

To define the selection, we will use the ELEMENTSET command, which will create selections for the types of geometric entities, as well as merge all selections into one final selection. The file format is as follows:

```
ADINA: AUI version 23.00.00.306, 29 June 2023:  *** NO HEADING DEFINED ***
 Licensed from Bentley Systems, Inc.
 Listing of Elementset        4

 GROUP       =       0
     El    Group
   1727456       1
   1840576       1
   1867056       1
.
.
.
    517400       2
    517401       2
    517402       2
 DESCRIPTION   =NONE

 *** End of list.
```

The file contains a nine-line header, followed by lines with the element number and the element group number. The listing is called using the LIST ELEMENTSET command.

In the next file, we will get information about the elements in the given group of elements. The listing file will have the name model_EDATA_N.txt, where N is the sequential number of the element group. The listing of elements must be done for each group of elements. The file has the format:

```
ADINA: AUI version 23.00.00.306, 29 June 2023:  *** NO HEADING DEFINED ***
 Licensed from Bentley Systems, Inc.

      Element nodal connectivity for:

      Substructure       0 / Element Group       1 / Type THREEDSOLID

      Element      N1      N2      N3      N4      N5
               N6      N7      N8      N9     N10
              N11     N12     N13     N14     N15
              N16     N17     N18     N19     N20
              N21     N22     N23     N24     N25
              N26     N27

         1  1266690  1266967  1266691  1266698
```

```
         2  1266690  1266967  1266698  1266535
         3  1317344  1363823  1363816  1325130
.
.
.
      5760343  2056354  1825588  1400591  2079447
      5760344  1200833  1200247  1844234  1402523
      5760345  2079442  1400687  2079444  2079076

*** End of list.
```

The file contains a seventeen-line header, followed by a data structure that contains one line for each element. The line contains the element number, followed by four-node numbers that form the element. For the topological optimization task, we need the element numbers. The listing is called with the LIST ENODES GROPU=N command, where N is the number of the desired element group.

The penultimate type of file we will work with when reading data is the model_S_T.txt results file. In this case, we will read a file containing unsmoothed equivalent stresses according to HMH. The number T denotes the load step in the topological optimization iteration. In this case, the stress listing is performed at the integration points of the elements. The file format is as follows:

```
ADINA: AUI version 23.00.00.306, 39 June 2023:  *** NO HEADING DEFINED ***
 Licensed from Bentley Systems, Inc.
 Finite element program ADINA, response DEFAULT (type load-step):
 Listing for zone WHOLE_MODEL:
 Element field variables are evaluated using RST interpolation.
                 EFFECTIVE
     POINT         STRESS

 Time 1.00000E+01

 Element 1 of element group 1

 Int point 1         2.02906E+00

 Element 2 of element group 1

 Int point 1         1.93223E+00

 Element 3 of element group 1

 Int point 1         1.07052E+01
.
.
.
 Element 517400 of element group 2

 Int point 1         5.18198E-02

 Element 517401 of element group 2

 Int point 1         4.03404E-01

 Element 517402 of element group 2

 Int point 1         4.52963E-02


*** End of list.
```

The file contains a thirteen-line file header, followed by information about the element number and the element group to which it belongs. This is followed by a blank line and information about the integration point and the equivalent stress value. This information is repeated for all elements in all element groups.

The last type of file is the structural weight output file. The output will be in the model_M.txt file. File format:

```
ADINA: AUI version 23.00.00.306, 8 March 2024:  *** NO HEADING DEFINED ***
Licensed from Bentley Systems, Inc.
Finite element program ADINA, response LATEST (type load-step):
Scanning for absolute maximum in zone WHOLE_MODEL:
Variable MASS:

 6.86368E+01, location-independent

*** End of list.
```

The file again contains a header, nine lines in total, followed by a data section. This section contains the mass. Mass is not a parameter needed to control topological optimization. We will only use it to express progress in optimization.

We can start creating the computational model in Matlab. We will create a startup script main.m and an optimization function topopt.m.

We will first create a startup script main.m, in which we will define the parameters for controlling the topological optimization task. This will be followed by starting the timer and calling the function for topological optimization. The solution time of the task, the resulting weight, and the percentage change in weight will be printed. The created model of the solved task has almost 6,000,000 elements. At the beginning of the iteration process, 10% of the enabled elements will be turned off and 2% of the disabled elements will be turned on. If the maximum allowable stress value is exceeded, this ratio will be reduced to 1/2 of the value until the number of disabled elements is less than 0.2% of the number of enabled elements.

```
% Startovaci subor pre topologicku optimalizaciu
model = "model";       % Nazov riesenej ulohy
Smax = 150;            % Maximalne dovolene napatie.
Eout = 0.10;           % Podiel elementov, ktory sa bude vypinat na zaciatku
Ein = 0.02;            % Podiel elementov, ktory sa bude zapinat na zaciatku
Emin = 0.002;          % Minimalny podiel elementov so zmenou
tic;
[mass, frac] = topopt("model", Smax, Eout, Ein, Emin);
fprintf("\nCas riesenia topologickej optimalizacie: %1.0f sekund.\n", toc);
fprintf("Vysledna hmotnost %1.3f, zmena hmotnosti o %1.0f%%.\n", mass, frac);
```

The topological optimization algorithm will be created in the topopt.m file. We will start by creating the function header with the function's return values and input variables defined. We will then continue with a brief function description and the creation of some variables. These variables need to be initialized, as the way they are used in the algorithm requires them to exist at the time they are used.

```
function [mass, frac] = topopt(model, Smax, Eout, Ein, Emin)
% funkcia pre topologicku optimalizaciu v programe Adina
% mass - vysledna hmotnost konstrukcie
% frac - podiel vypnutych elementov
% model - nazov riesenej ulohy, modelu v programe Adina
% Smax - maximalne dovolene napatie v konstrukcii podla HMH
% Eout - podiel elementov z celkoveho poctu, ktory sa vypina
```

```
% Ein - podiel elementov z celkoveho poctu, ktory sa zapina
% Emin - minimalny podiel elelemntov ktory sa vypina
  n = 0;                    % pocitadlo iteracii
  point = [];               % body v exclude
  line = [];                % ciary v exclude
  edge = [];                % hrany v exclude
  surface = [];             % plochy v exclude
  face = [];                % povrchy v exclude
  volume = [];              % objemy v exclude
  body = [];                % telesa v exclude
  elem = [];                % maatica elementov
  status = zeros([], "uint8");  % stav elementov zapnute, vypnute, pevne
  index = zeros([], "uint32");  % poradie uzlov pri zoradeni podla napati
  itmass = [];              % hmotnost pre kazdu iteraciu
  mass=0;
  frac=0;
```

As the first step of the algorithm, we will create the input file model_topopt.in, which will contain a sequence of commands to print out the model parameters in the first print phase. We will extract information about the time steps, the number of defined load states, information about the number of defined element groups, and determine the number of created material groups. Finally, we will extract information about the geometric elements included in the EXCLUDE zone, which is a fixed geometry zone, and geometric elements with boundary conditions, constraints, contact, and the like are included in this zone.

```
fprintf("Nacitanie modelu a jeho analyza .... ");
fout = fopen(sprintf("%s/%s_topopt.in", pwd(), model), "w");
fprintf(fout, "*\n");
fprintf(fout, "DATABASE OPEN FILE=,\n");
fprintf(fout, "'%s/%s.idb',\n", pwd(), model);
fprintf(fout, "     PERMFILE=,\n");
fprintf(fout, "'%s/%s.idb',\n", pwd(), model);
fprintf(fout, "     PROMPT=NO\n");
fprintf(fout, "*\n");
fprintf(fout, "FILELIST OPTION=FILE FILE=,\n");
fprintf(fout, "'%s/%s_TSTEP.txt'\n", pwd(), model);
fprintf(fout, "*\n");
fprintf(fout, "LIST TIMESTEP DEFAULT\n");
fprintf(fout, "*\n");
fprintf(fout, "FILELIST OPTION=FILE FILE=,\n");
fprintf(fout, "'%s/%s_NEG.txt'\n", pwd(), model);
fprintf(fout, "*\n");
fprintf(fout, "LIST EGROUP\n");
fprintf(fout, "*\n");
fprintf(fout, "FILELIST OPTION=FILE FILE=,\n");
fprintf(fout, "'%s/%s_NMAT.txt'\n", pwd(), model);
fprintf(fout, "*\n");
fprintf(fout, "LIST MATERIAL\n");
fprintf(fout, "*\n");
fprintf(fout, "FILELIST OPTION=FILE FILE=,\n");
fprintf(fout, "'%s/%s_EXC.txt'\n", pwd(), model);
fprintf(fout, "*\n");
fprintf(fout, "LIST ZONE NAME=EXCLUDE\n");
fprintf(fout, "*\n");
fprintf(fout, "EXIT SAVE=NO PROMPT=NO IMEDIATE=YES\n");
fclose(fout);
```

In the next step, we will run the Adina AUI program with the created input file, while also testing the correctness of the program's execution.

```
while 1
  system(sprintf("aui -cmd -m 16GB -t 16 -s %s_topopt.in > %s_topopt.log 2>&1", model, model));

  if isfile(sprintf("%s_TSTEP.txt", model)) && isfile(sprintf("%s_NEG.txt", model)) && ...
      isfile(sprintf("%s_NMAT.txt", model)) && isfile(sprintf("%s_EXC.txt", model))
    break;
  else
    pause(5*rand(1));
  end
end
```

We will gradually load the information from the files and store it in variables: time for the time values in the individual calculation steps - load states, eg for the element group numbers, and mat for the serial numbers of the created material groups.

```
fin = fopen(sprintf("%s/%s_TSTEP.txt", pwd(), model), "r");
for k = 1 : 8
  fgetl(fin);
end
data = fscanf(fin, " %d %f\n", [2, inf])';
fclose(fin);
time = data(2) : data(2) : data(1)*data(2);
fin = fopen(sprintf("%s/%s_NEG.txt", pwd(), model), "r");
for k = 1 : 7
  fgetl(fin);
end
eg = fscanf(fin, " %d\n", [1, inf])';
fclose(fin);
fin = fopen(sprintf("%s/%s_NMAT.txt", pwd(), model), "r");
for k = 1 : 7
  fgetl(fin);
end
mat = fscanf(fin, " %d %*s\n", [1, inf])';
fclose(fin);
```

Parsing the model_ECX.txt file is a significantly more complex task. This file stores information about the geometric elements on which fixed elements will be applied. The file contains eleven header lines, which we will read but do not need the information stored in the header. Following the header lines are lines with information that we need to identify based on the text in these lines. The text may contain a record for a single geometric element or for a group of geometric elements in each range.

For geometric elements of type edge, and face, we must also identify the body - point whose edges or faces are listed. Geometric points, lines, and surfaces have global numbering, while each body - point has its own numbering system. In total, up to six different types of geometric elements can be written, but not all types may be present. We also do not know how many times a given type of geometric element will be used when writing to the file. For this reason, we need to use a different approach when reading information from this file. After reading the header, we will use a while loop with a test for the end of the file using the feof function, which will allow us to read the entire file. Next, we will read one line from the file, and we will try to read this line using the sscanf function, where the format string allows us to distinguish between the text and the numbers in the record. If the text in the analyzed line is of the same format as the format string, the sscanf function will return the read numbers in the data variable and the number of read numbers in the nc variable. Otherwise, the number of read numbers is zero. Finally, we will test the value in the nc variable and write the read data to the appropriate variable if necessary.

```
fin = fopen(sprintf("%s/%s_EXC.txt", pwd(), model), "r");
for k = 1 : 11
  fgetl(fin);
end
while ~feof(fin)
  str = fgetl(fin);
  [data, nc] = sscanf(str, " Geometry point %d", [1, 1]);
  if nc == 1
    point = [point; data];
  end
  [data, nc] = sscanf(str, " Geometry points %d to %d", [2, 1]);
  if nc == 2
    point = [point; (data(1) : data(2))'];
  end
  [data, nc] = sscanf(str, " Geometry line %d", [1, 1]);
  if nc == 1
    line = [line; data];
  end
  [data, nc] = sscanf(str, " Geometry lines %d to %d", [2, 1]);
  if nc == 2
    line = [line; (data(1) : data(2))'];
  end
  [data, nc] = sscanf(str, " Geometry edge %d of geometry body %d", [2, 1]);
  if nc == 2
    edge = [edge; data(1) data(2)];
  end
  [data, nc] = sscanf(str, " Geometry edges %d to %d of geometry body %d", [3, 1]);
  if nc == 3
    edge = [edge; [(data(1) : data(2))' (data(3)*ones(1, data(2)-data(1)+1))']];
  end
  [data, nc] = sscanf(str, " Geometry surface %d", [1, 1]);
  if nc == 1
    surface = [surface; data];
  end
  [data, nc] = sscanf(str, " Geometry surfaces %d to %d", [2, 1]);
  if nc == 2
    surface = [surface; (data(1) : data(2))'];
  end
  [data, nc] = sscanf(str, " Geometry face %d of geometry body %d", [2, 1]);
  if nc == 2
    face = [face; data(1) data(2)];
  end
  [data, nc] = sscanf(str, " Geometry faces %d to %d of geometry body %d", [3, 1]);
  if nc == 3
    face = [face; [(data(1) : data(2))' (data(3)*ones(1, data(2)-data(1)+1))']];
  end
  [data, nc] = sscanf(str, " Geometry volume %d", [1, 1]);
  if nc == 1
    volume = [volume; data];
  end
  [data, nc] = sscanf(str, " Geometry volumes %d to %d", [2, 1]);
  if nc == 2
    volume = [volume; (data(1) : data(2))'];
  end
  [data, nc] = sscanf(str, " Geometry body %d", [1, 1]);
  if nc == 1
    body = [body; data];
  end
  [data, nc] = sscanf(str, " Geometry bodies %d to %d", [2, 1]);
  if nc == 2
    body = [body; (data(1) : data(2))'];
  end
```

```
end
```

The second in-order printout of information about the created computational model in the Adina AUI program follows. This printout is dependent on the values read from the first printout, and therefore we need to use two separate printouts of model data. We implement the printout of the properties of all element groups. This is followed by a group of commands to create a selection of elements based on the given type of geometric entity. Next, the last selection with number one is created, which is formed by merging all previous non-zero printouts. We print information about the elements in all element groups. The last printout is a list of element numbers and the element group to which the given element belongs for the created selection of fixed elements.

```
fout = fopen(sprintf("%s/%s_topopt.in", pwd(), model), "w");
fprintf(fout, "*\n");
fprintf(fout, "DATABASE OPEN FILE=,\n");
fprintf(fout, "'%s/%s.idb',\n", pwd(), model);
fprintf(fout, "     PERMFILE=,\n");
fprintf(fout, "'%s/%s.idb',\n", pwd(), model);
fprintf(fout, "     PROMPT=NO\n");
for k = 1 : size(eg)
  fprintf(fout, "*\n");
  fprintf(fout, "FILELIST OPTION=FILE FILE=,\n");
  fprintf(fout, "'%s/%s_EG_%d.txt'\n", pwd(), model, eg(k));
  fprintf(fout, "*\n");
  fprintf(fout, "LIST EGROUP FIRTS=%d\n", eg(k));
end
if ~isempty(point)
  fprintf(fout, "*\n");
  fprintf(fout, "ELEMENTSET NAME=2 ALL-EXT=NO GROUP=0 DESCRIPT='NONE' OPTION=POINTS,\n");
  fprintf(fout, "     ZONE='' TARGET=0 APPEND=NO DISTANCE=0.00000000000000,\n");
  fprintf(fout, "     GEOM-DEF=YES\n");
  fprintf(fout, "@CLEAR\n");
  for k = 1 : size(point, 1)
    fprintf(fout, "%d 0\n", point(k, 1));
  end
  fprintf(fout, "@\n");
end
if ~isempty(line)
  fprintf(fout, "*\n");
  fprintf(fout, "ELEMENTSET NAME=3 ALL-EXT=NO GROUP=0 DESCRIPT='NONE' OPTION=LINE-EDGE,\n");
  fprintf(fout, "     ZONE='' TARGET=0 APPEND=NO DISTANCE=0.00000000000000,\n");
  fprintf(fout, "     GEOM-DEF=YES\n");
  fprintf(fout, "@CLEAR\n");
  for k = 1 : size(line, 1)
    fprintf(fout, "%d 0\n", line(k, 1));
  end
  fprintf(fout, "@\n");
end
if ~isempty(edge)
  fprintf(fout, "*\n");
  fprintf(fout, "ELEMENTSET NAME=4 ALL-EXT=NO GROUP=0 DESCRIPT='NONE' OPTION=LINE-EDGE,\n");
  fprintf(fout, "     ZONE='' TARGET=0 APPEND=NO DISTANCE=0.00000000000000,\n");
  fprintf(fout, "     GEOM-DEF=YES\n");
  fprintf(fout, "@CLEAR\n");
  for k = 1 : size(edge, 1)
    fprintf(fout, "%d %d\n", edge(k, 1), edge(k, 2));
  end
  fprintf(fout, "@\n");
end
if ~isempty(surface)
  fprintf(fout, "*\n");
```

```
  fprintf(fout, "ELEMENTSET NAME=5 ALL-EXT=NO GROUP=0 DESCRIPT='NONE' OPTION=SURFACE-FA,\n");
  fprintf(fout, "     ZONE='' TARGET=0 APPEND=NO DISTANCE=0.00000000000000,\n");
  fprintf(fout, "     GEOM-DEF=YES\n");
  fprintf(fout, "@CLEAR\n");
  for k = 1 : size(surface, 1)
    fprintf(fout, "%d 0\n", surface(k, 1));
  end
  fprintf(fout, "@\n");
end
if ~isempty(face)
  fprintf(fout, "*\n");
  fprintf(fout, "ELEMENTSET NAME=6 ALL-EXT=NO GROUP=0 DESCRIPT='NONE' OPTION=SURFACE-FA,\n");
  fprintf(fout, "     ZONE='' TARGET=0 APPEND=NO DISTANCE=0.00000000000000,\n");
  fprintf(fout, "     GEOM-DEF=YES\n");
  fprintf(fout, "@CLEAR\n");
  for k = 1 : size(face, 1)
    fprintf(fout, "%d %d\n", face(k, 1), face(k, 2));
  end
  fprintf(fout, "@\n");
end
if ~isempty(volume)
  fprintf(fout, "*\n");
  fprintf(fout, "ELEMENTSET NAME=7 ALL-EXT=NO GROUP=0 DESCRIPT='NONE' OPTION=VOLUME,\n");
  fprintf(fout, "     ZONE='' TARGET=0 APPEND=NO DISTANCE=0.00000000000000,\n");
  fprintf(fout, "     GEOM-DEF=YES\n");
  fprintf(fout, "@CLEAR\n");
  for k = 1 : size(volume, 1)
    fprintf(fout, "%d 0\n", volume(k, 1));
  end
  fprintf(fout, "@\n");
end
if ~isempty(body)
  fprintf(fout, "*\n");
  fprintf(fout, "ELEMENTSET NAME=8 ALL-EXT=NO GROUP=0 DESCRIPT='NONE' OPTION=BODY,\n");
  fprintf(fout, "     ZONE='' TARGET=0 APPEND=NO DISTANCE=0.00000000000000,\n");
  fprintf(fout, "     GEOM-DEF=YES\n");
  fprintf(fout, "@CLEAR\n");
  for k = 1 : size(body, 1)
    fprintf(fout, "%d 0\n", body(k, 1));
  end
  fprintf(fout, "@\n");
end
fprintf(fout, "*\n");
fprintf(fout, "ELEMENTSET NAME=1 ALL-EXT=NO GROUP=0 DESCRIPT='NONE' OPTION=MERGE,\n");
fprintf(fout, "     ZONE='' TARGET=0 APPEND=NO DISTANCE=0.00000000000000,\n");
fprintf(fout, "     GEOM-DEF=YES\n");
fprintf(fout, "@CLEAR\n");
if ~isempty(point)
  fprintf(fout, "2 0\n");
end
if ~isempty(line)
  fprintf(fout, "3 0\n");
end
if ~isempty(edge)
  fprintf(fout, "4 0\n");
end
if ~isempty(surface)
  fprintf(fout, "5 0\n");
end
if ~isempty(face)
  fprintf(fout, "6 0\n");
end
```

```
if ~isempty(volume)
  fprintf(fout, "7 0\n");
end
if ~isempty(body)
  fprintf(fout, "8 0\n");
end
fprintf(fout, "@\n");
for k = 1 : size(eg, 1)
  fprintf(fout, "*\n");
  fprintf(fout, "FILELIST OPTION=FILE FILE=,\n");
  fprintf(fout, "'%s/%s_EDATA_%d.txt'\n", pwd(), model, eg(k, 1));
  fprintf(fout, "*\n");
  fprintf(fout, "LIST ENODES GROUP=%d\n", eg(k, 1));
end
fprintf(fout, "*\n");
fprintf(fout, "FILELIST OPTION=FILE FILE=,\n");
fprintf(fout, "'%s/%s_EFIX.txt'\n", pwd(), model);
fprintf(fout, "*\n");
fprintf(fout, "LIST ELEMENTSET 1\n");
fprintf(fout, "*\n");
fprintf(fout, "EXIT SAVE=NO PROMPT=NO IMEDIATE=YES\n");
fclose(fout);
```

In the next step, we will run the Adina AUI program with the created input file, while also testing the correctness of the program's execution.

```
while 1
  system(sprintf("aui -cmd -m 16GB -t 16 -s %s_topopt.in > %s_topopt.log 2>&1", model, model));

  if isfile(sprintf("%s_EFIX.txt", model))
    break;
  else
    pause(5*rand(1));
  end
end
```

The algorithm continues by loading data from the created files. We will start by reading the model_EG_N.txt file, where N is the serial number of the element group. In this file, we test for the occurrence of the word MATERIAL. If such a line is identified, the serial number of the material is loaded and added to the second column of the eg variable. This is followed by a test to check if the last defined element group has the last created material assigned. For the algorithm to function correctly, we need the last material in order to be defined as a soft material and the last element group as a group with a default soft material.

```
for k = 1 : size(eg, 1)
  fin = fopen(sprintf("%s/%s_EG_%d.txt", pwd(), model, eg(k, 1)), "r");
  for p = 1 : 7
   fgetl(fin);
  end
  while ~feof(fin)
    str = fgetl(fin);
    [data, nc] = sscanf(str, " MATERIAL = %d", [1, 1]);
    if nc == 1
      eg(k, 2) = data;
    end
  end
end
if eg(end, 2) ~= mat(end)
  printf("ERROR: Poslena skupina elementov EG_%d nema priradeny posedny material %d!", eg(end, 1), mat(end));
  return
```

```
end
```

We continue by reading the information about the element number and the element group to which it belongs. This information is inserted into the first and second columns of the elem matrix, respectively. In the third column, we insert the information about the serial number of the material predefined for the given element-element group.

We proceed by reading the elements belonging to the fixed element group, which cannot be turned off during the optimization process.

```
for k = 1 : size(eg, 1)
  fin = fopen(sprintf("%s/%s_EDATA_%d.txt", pwd(), model, eg(k, 1)), "r");
  for p = 1 : 17
    fgetl(fin);
  end
  data = fscanf(fin, " %d %d %d %d %d\n", [5, inf])';
  fclose(fin);
  if ~isempty(data)
    elem = [elem; [(data(:,1)) (eg(k, 1)*ones(size(data, 1), 1)) ...
      (eg(k, 2)*ones(size(data, 1), 1))]];
  end
end
fin = fopen(sprintf("%s/%s_EFIX.txt", pwd(), model), "r");
for k = 1 : 9
  fgetl(fin);
end
data = fscanf(fin, " %d %d\n", [2, inf])';
fclose(fin);
```

The first column of the status variable is filled with ones, and the number of rows is equal to the total number of elements in all element groups. All elements are stored in the elem variable. The status variable will be used to identify the state of the elements, which can be: 0 - turned off element, 1 - turned on element, 2 - fixed element. For each iteration of the topology optimization algorithm, we will use the column whose index is equal to the iteration number. This format of the status variable allows us to easily return to the state of the previous iteration of the topology optimization algorithm.

The Adina AUI program creates a printout of elements by sorting them from lowest to highest number in each element group and sorting the element groups by order number. In this format, the data is stored in the data variable, into which we have read the elements with the fixed element property. In the elem variable, we have the elements sorted in the same way. If the data in these two variables is sorted in this way, then we can use a simplified method of searching for identical element numbers in the same element group to assign fixed element properties to the status variable.

```
status = ones(size(elem, 1),1);
p = 1;
for k = 1 : size(elem, 1)
  if elem(k, 1) == data(p, 1) && elem(k, 2) == data(p, 2)
    status(k, 1) = 2;
    p = p + 1;
    if p > size(data, 1)
      break;
    end
  end
end
fprintf("OK\n\n");
```

We define the number of elements to be turned off, the number of elements to be turned on, and the minimum number of elements to be turned off as the convergence criterion.

The following is a while loop with a test for convergence of the iterative process of the topology optimization task.

```
nout = round(Eout * sum(status(:, 1) == 1));
nin= round(Ein * sum(status(:, 1) == 0));
nmin = round(Emin * sum(status(:, 1) == 1));
while nout > nmin
  % nastavenie poradoveho cisla iteracii
  n = n +1;
  tstart = tic();
```

We update the values of the number of elements to be turned off, the number of elements to be turned on, and the minimum number of elements to be changed to the off state for testing the convergence of the iterative process of the topology optimization task. This is followed by a printout of information about the iteration parameters.

```
  nout = round(Eout * sum(status(:, n) == 1));
  nin = round(Ein * sum(status(:, n) == 0));
  nmin = round(Emin * sum(status(:, n) == 1));
  fprintf("Iteracia: %d, zapnute elementy %1.2f%% \n", n, 100*sum(status(:, n) >= 1)/size(status, 1));
  fprintf("     pocet => zapnutych: %8d  vypnutych: %8d  pevnych: %8d\n",...
        sum(status(:, n) == 1), sum(status(:, n) == 0), sum(status(:, n) == 2 ));
  fprintf("     zmena => zapnutych: %8d  vypnutych: %8d  Eout: %f  Emin: %f\n",...
         nout, nin, Eout, Emin);
```

We open the model_topopt.in file for writing and write commands to read the database of the model of the solved task in a binary file. We write information about the material group used for the given element according to the value in the status variable. These commands turn elements on or off in the current model.

```
  fout = fopen(sprintf("%s/%s_topopt.in", pwd(), model), "w");
  fprintf(fout, "*\n");
  fprintf(fout, "DATABASE OPEN FILE=,\n");
  fprintf(fout, "'%s/%s.idb',\n", pwd(), model);
  fprintf(fout, "     PERMFILE=,\n");
  fprintf(fout, "'%s/%s.idb',\n", pwd(), model);
  fprintf(fout, "     PROMPT=NO\n");
  for k = 1 : size(eg, 1)
    fprintf(fout, "*\n");
    fprintf(fout, "EDATA SUBSTRUC=0 GROUP=%d UNDEFINE=IGNORE\n", eg(k, 1));
    fprintf(fout, "@CLEAR\n");
    for p = 1 : size(elem, 1)
      if elem(p, 2) == eg(k, 1) && status(p, n) == 0
        fprintf(fout, "%d %d 0  'DEFAULT'  'DEFAULT' 0 0 0 0 0 -1\n", elem(p, 1), eg(end, 2));
      end
      if elem(p, 2) == eg(k, 1) && status(p, n) > 0
        fprintf(fout, "%d %d 0  'DEFAULT'  'DEFAULT' 0 0 0 0 0 -1\n", elem(p, 1), elem(p, 3));
      end
    end
    fprintf(fout, "@\n");
  end
  fprintf(fout, "*\n");
  fprintf(fout, "ADINA OPTIMIZE=YES FILE=,\n");
  fprintf(fout, "'%s/%s_topopt.dat',\n", pwd(), model);
  fprintf(fout, "     FIXBOUND=YES OVERWRIT=YES\n");
  fprintf(fout, "*\n");
  fprintf(fout, "EXIT SAVE=NO PROMPT=NO IMEDIATE=YES\n");
  fclose(fout);
```

In the next step, we run the Adina AUI program with the created input file, while also testing the correctness of the program's execution. We run the solution of the task in the Adina program, while also testing the correctness of the program's execution.

```
while 1
  system(sprintf("aui -cmd -m 16GB -t 16 -s %s_topopt.in > %s_topopt.log 2>&1", model, model));
  str = sprintf("%s/%s_topopt.log", pwd(), model);
  fin = fopen(str, "r");
  out = false;
  while ~feof(fin)
    line = fgetl(fin);
    if contains(line, "successfully created")
      out = true;
    end
  end
  fclose(fin);
  if out
    break;
  else
    pause(5*rand(1));
  end
end
while 1
  system(sprintf("adina -m 16GB -M 32GB -t 16 %s_topopt >> %s_topopt.log 2>&1", model, model));
  str = sprintf("%s/%s_topopt.out", pwd(), model);
  fin = fopen(str, "r");
  out = false;
  while ~feof(fin)
    line = fgetl(fin);
    if contains(line, "Solution successful")
      out = true;
    end
  end
  fclose(fin);
  if(out)
    break;
  else
    pause(5*rand(1));
  end
end
```

Once the solution of the task has been obtained in the Adina program, the equivalent stresses are printed out for all load and loaded states of the structure. We then rerun the Adina AUI program with the created input file, while also testing the correctness of the program's execution.

```
fout = fopen(sprintf("%s/%s_topopt.plo", pwd(), model), "w");
fprintf(fout, "*\n");
fprintf(fout, "LOADPORTHOLE OPERATIO=CREATE FILE='%s/%s_topopt.por',\n", pwd(), model);
fprintf(fout, "    TAPERECO=0 DUMPFORM=NO PRESCAN=NO RANGE=ALL,\n");
fprintf(fout, "    TIMESTAR=0.00000000000000 TIMEEND=0.00000000000000 STEPSTAR=0,\n");
fprintf(fout, "    STEPEND=0 STEPINCR=1 ZOOM-MOD=0 INITIAL-=AUTOMATIC CPSTART=1,\n");
fprintf(fout, "    CPEND=0 SEQFILE=SINGLE MULTIFIL=10\n");
for k = time
  fprintf(fout, "*\n");
  fprintf(fout, "FILELIST OPTION=FILE FILE='%s/%s_S_%d.txt'\n", pwd(), model, k);
  fprintf(fout, "*\n");
  fprintf(fout, "RESPONSE LOAD-STEP NAME=DEFAULT TIME=%f SEQUENC=MAIN\n", k);
  fprintf(fout, "*\n");
  fprintf(fout, "ZONELIST ZONENAME=WHOLE_MODEL RESULTGR=DEFAULT SMOOTHIN=NONE,\n");
  fprintf(fout, "    RESULTCO=DEFAULT RESPOPTI=RESPONSE RESPONSE=DEFAULT,\n");
  fprintf(fout, "    RESPRANG=DEFAULT VARIABLE=EFFECTIVE_STRESS\n");
```

```
end
fprintf(fout, "*\n");
fprintf(fout, "FILELIST OPTION=FILE FILE='%s/%s_M.txt'\n", pwd(), model);
fprintf(fout, "*\n");
fprintf(fout, "ZONEMAX ZONENAME=WHOLE_MODEL TYPE=ABSMAX NUMBER=1 RESULTGR=DEFAULT,\n");
fprintf(fout, "     SMOOTHIN=DEFAULT RESULTCO=DEFAULT RESPOPTI=RESPONSE,\n");
fprintf(fout, "     RESPONSE=LATEST RESPRANG=DEFAULT VARIABLE=MASS\n");
fprintf(fout, "*\n");
fprintf(fout, "EXIT SAVE=NO IMEDIATE=YES PROMPT=NO\n");
fclose(fout);
while 1
  system(sprintf("aui -cmd -plot -m 16GB -t 16 -s %s_topopt.plo >> %s_topopt.log 2>&1", model, model));
  if isfile(sprintf("%s_M.txt", model))
    break;
  end
end
```

We load the stress values into the stress variable, where each row represents an element in the finite element mesh. The column index is equal to the load case number.

```
stress = zeros(size(elem, 1), time(end));
for k = time
  fin = fopen(sprintf("%s/%s_S_%d.txt", pwd(), model, k), "r");
  for p = 1 : 12
    fgetl(fin);
  end
  data = fscanf(fin, " Element %d of element group %d\n\n Int point 1 %f\n", [3, inf])';
  fclose(fin);
  stress(:, k) = data(:, 3);
end
fin = fopen(sprintf("%s/%s_M.txt", pwd(), model), "r");
for p = 1 : 9
  fgetl(fin);
end
data = fscanf(fin, " %f, location-independent\n", [1, 1])';
fclose(fin);
itmass(n) = data;
```

Before further processing the stress analysis results, we need to determine a representative stress value for each element. We currently have stress values for each load case. The representative stress value for each element is the maximum stress value from all load cases. This value determines the effectiveness of the given element in the structure. We store the maximum stress value for all elements in the stress variable. These values form one column. The second command creates numbers in the first column with order from 1 to the total number of elements in the structure. This number is the index number in the elem and status matrices.

```
stress = max(stress, [], 2);
stress = [(1:size(stress, 1))' stress];
```

A check is then performed to see if the maximum stress value in the entire model has exceeded the maximum allowable stress. If this value is exceeded in the first iteration step, the base model – the model from which the topology optimization process starts – is poorly designed and the topology optimization process is terminated.

If the maximum stress value in the model is higher than the maximum allowable stress in the structure in an iteration step other than the first, a large amount of material has been removed from the structure and too many elements have been turned off. In this case, we change the values of the proportions of elements to be turned off and turned on and return to the previous iteration step. We

create a new model for the same iteration in which there will be a smaller number of elements turned off.

```
if max(stress(:, 2)) > Smax && n == 1
  fprintf("V zakladnom modeli je prekrocena hodnota maximaleho dovoleneho napatia!\n");
  return;
elseif max(stress(:, 2)) > Smax
  Eout = Eout / 2;
  Ein = Ein / 2;
  % opakovanie iteracie
  n = n - 1;
end
```

The stress matrix is then sorted according to the stress value in the second column. When sorting from smallest to largest stress, the entire row is manipulated, including the ordinal number in the first column. In this way, we retain the information about where the element with the given stress value is in the elem and status matrices. The element ordinal numbers - indices are written to the index matrix.

```
stress = sortrows(stress, 2);
index(:, n) = stress(:, 1);
```

A new n+1 column is then created in the status variable. We define temporary variables cout and cin to count the currently changed number of elements for the next iteration. In the for loop for all elements, by increasing the index k, we move to the element with a higher stress value, and by decreasing the index end+1-k, we move from the element with the highest stress value to the element with a lower stress value.

We test whether the currently changed number of elements from the state on to the state off, the value cout is less than the maximum number of elements that can be turned off, and we also test whether the given element is on. If both conditions are met, we can turn off the given element, assign the value 0 to the variable status in the row according to the value of index - which is the ordinal number of the element to column n+1 - and increase the value of cout by one. We set that the given element will be turned off in the next iteration.

Similarly, we test the value cin for the current change from off to on and whether the given element is off. If the condition is met, we can turn on the given element. Turning on the element in the next iteration is implemented by writing the value 1 to the corresponding row of the status matrix according to the value of the index, again writing it in column n+1.

In the last test, we check whether we have already changed the maximum number of elements from the state on to off and from off to on. If this condition is met, we use the break command to exit the for loop.

```
status(:, n+1) = status(:, n);
cout = 0;
cin = 0;
for k = 1 : size(elem, 1)
  if cout < nout && status(index(k, n), n) == 1
    status(index(k, n), n+1) = 0;
    cout = cout + 1;
  end
  if cin < nin && status(index(end+1-k, n), n) == 0
    status(index(end+1-k, n), n+1) = 1;
    cin = cin + 1;
  end
  if cout >= nout && cin >= nin
    break
```

```
    end
  end
```

The current structure weight and the maximum stress value in the given iteration are written to the terminal. The solution time for the current iteration of the topology optimization process is also printed.

All generated files are then deleted to ensure that new files must be created in the new iteration and that the iteration process will function correctly.

```
  fprintf("    hmotnost: %f  maximalne napatie: %f  cas riesenia: %1.0f sekund\n",...
       itmass(n), max(stress(:, 2)), toc(tstart));
  delete(sprintf("%s_topopt.*", model));
  delete(sprintf("%s_S_*.txt", model));
  delete(sprintf("%s_M.txt", model));
end
```

The created topology optimization iteration algorithm is guaranteed to converge, and after the iteration procedure is completed, a solution to the optimization problem is obtained.

The following group of commands creates a modified model based on the last iteration with a combination of turned-on and turned-off elements in this iteration. In this created model, the reassignment of turned-off elements to the last group of elements will be used to turn off the elements. The last group of elements is a group with a softer material.

Before creating the final model with the result of the topology optimization task, we delete all files that were created during the optimization process.

We create an input file for the Adina AUI program called model_topopt.in, which will contain a sequence of commands to create the optimized model.

```
delete(sprintf("%s_*.*", model));
fout = fopen(sprintf("%s/%s_topopt.in", pwd(), model), "w");
fprintf(fout, "*\n");
fprintf(fout, "DATABASE OPEN FILE=,\n");
fprintf(fout, "'%s/%s.idb',\n", pwd(), model);
fprintf(fout, "    PERMFILE=,\n");
fprintf(fout, "'%s/%s.idb',\n", pwd(), model);
fprintf(fout, "    PROMPT=NO\n");
```

The ELMOVE command is then used to reassign the element to the given group of elements. In a for loop for all elements in the model, we test the value in the status variable in the last iteration. If the element is turned off, we reassign it. This procedure reassigns all turned-off elements to the last group of elements. This is followed by a pair of commands to save the model database for the program solving the computational task in the Adina program. The last command is to terminate the Adina AUI program.

```
fprintf(fout, "*\n");
fprintf(fout, "ELMOVE FROM=0 TO=%d OPTION=ELEM EXPAND=0 DELETE-E=YES\n", eg(end, 1));
fprintf(fout, "@CLEAR\n");
for k = 1 : size(elem, 1)
  if status(k, n) == 0
    fprintf(fout, "%d %d\n", elem(k, 1), elem(k, 2));
  end
end
fprintf(fout, "@\n");
fprintf(fout, "*\n");
fprintf(fout, "ADINA OPTIMIZE=YES FILE=,\n");
fprintf(fout, "'%s/%s_topopt.dat',\n", pwd(), model);
fprintf(fout, "    FIXBOUND=YES OVERWRIT=YES\n");
```

```
  fprintf(fout, "*\n");
  fprintf(fout, "EXIT SAVE=NO PROMPT=NO IMEDIATE=YES\n");
  fclose(fout);
```

The Adina AUI program is then restarted with the created input file, and the program's correct operation is tested. The modified data model is then solved, and as always, the solution is tested for correctness.

```
  while 1
    system(sprintf("aui -cmd -m 16GB -t 16 -s %s_topopt.in > %s_topopt.log 2>&1", model, model));
    str = sprintf("%s/%s_topopt.log", pwd(), model);
    fin = fopen(str, "r");
    out = false;
    while ~feof(fin)
      line = fgetl(fin);
      if contains(line, "successfully created")
        out = true;
      end
    end
    fclose(fin);
    if out
      break;
    else
      pause(5*rand(1));
    end
  end
  while 1
    system(sprintf("adina -m 16GB -M 32GB -t 16 %s_topopt >> %s_topopt.log 2>&1", model, model));
    str = sprintf("%s/%s_topopt.out", pwd(), model);
    fin = fopen(str, "r");
    out = false;
    while ~feof(fin)
      line = fgetl(fin);
      if contains(line, "Solution successful")
        out = true;
      end
    end
    fclose(fin);
    if(out)
      break;
    else
      pause(5*rand(1));
    end
  end
  mass = itmass(end);
  frac = 100 * (itmass(1) - itmass(end)) / itmass(1);
end
```

During the solution of the topology optimization task, the following information is displayed on the MATLAB command line.

```
Nacitanie modelu a jeho analyza .... OK

Iteracia: 1, zapnute elementy 100.00%
    pocet => zapnutych:  3712403  vypnutych:       0  pevnych:   197061
    zmena => zapnutych:   371240  vypnutych:       0  Eout: 0.100000  Emin: 0.002000
    hmotnost: 68.939600  maximalne napatie: 72.404200  cas riesenia: 3828 sekund
Iteracia: 2, zapnute elementy 90.50%
    pocet => zapnutych:  3341163  vypnutych:   371240  pevnych:   197061
    zmena => zapnutych:   367528  vypnutych:    8167  Eout: 0.110000  Emin: 0.002000
    hmotnost: 68.939600  maximalne napatie: 171.807000  cas riesenia: 4157 sekund
Iteracia: 2, zapnute elementy 90.60%
```

pocet => zapnutych: 3344875 vypnutych: 367528 pevnych: 197061
zmena => zapnutych: 183968 vypnutych: 4043 Eout: 0.055000 Emin: 0.002000
hmotnost: 61.278700 maximalne napatie: 77.907100 cas riesenia: 4021 sekund
Iteracia: 3, zapnute elementy 86.00%
pocet => zapnutych: 3164950 vypnutych: 547453 pevnych: 197061
zmena => zapnutych: 191479 vypnutych: 6624 Eout: 0.060500 Emin: 0.002000
hmotnost: 61.278700 maximalne napatie: 291.147000 cas riesenia: 4314 sekund
Iteracia: 3, zapnute elementy 85.87%
pocet => zapnutych: 3160020 vypnutych: 552383 pevnych: 197061
zmena => zapnutych: 95591 vypnutych: 3342 Eout: 0.030250 Emin: 0.002000
hmotnost: 61.278700 maximalne napatie: 270.027000 cas riesenia: 4477 sekund
Iteracia: 3, zapnute elementy 88.24%
pocet => zapnutych: 3252626 vypnutych: 459777 pevnych: 197061
zmena => zapnutych: 49196 vypnutych: 1391 Eout: 0.015125 Emin: 0.002000
hmotnost: 59.826800 maximalne napatie: 78.107500 cas riesenia: 3969 sekund
Iteracia: 4, zapnute elementy 87.02%
pocet => zapnutych: 3204821 vypnutych: 507582 pevnych: 197061
zmena => zapnutych: 53320 vypnutych: 1689 Eout: 0.016638 Emin: 0.002000
hmotnost: 58.943700 maximalne napatie: 78.414200 cas riesenia: 3940 sekund
Iteracia: 5, zapnute elementy 85.70%
pocet => zapnutych: 3153190 vypnutych: 559213 pevnych: 197061
zmena => zapnutych: 57707 vypnutych: 2047 Eout: 0.018301 Emin: 0.002000
hmotnost: 58.943700 maximalne napatie: 239.149000 cas riesenia: 4031 sekund
Iteracia: 5, zapnute elementy 85.59%
pocet => zapnutych: 3149161 vypnutych: 563242 pevnych: 197061
zmena => zapnutych: 28817 vypnutych: 1031 Eout: 0.009151 Emin: 0.002000
hmotnost: 58.943700 maximalne napatie: 239.148000 cas riesenia: 4129 sekund
Iteracia: 5, zapnute elementy 86.31%
pocet => zapnutych: 3177035 vypnutych: 535368 pevnych: 197061
zmena => zapnutych: 14536 vypnutych: 490 Eout: 0.004575 Emin: 0.002000
hmotnost: 58.382700 maximalne napatie: 78.586600 cas riesenia: 4025 sekund
Iteracia: 6, zapnute elementy 85.95%
pocet => zapnutych: 3162989 vypnutych: 549414 pevnych: 197061
zmena => zapnutych: 15919 vypnutych: 553 Eout: 0.005033 Emin: 0.002000
hmotnost: 58.105900 maximalne napatie: 78.726800 cas riesenia: 4031 sekund
Iteracia: 7, zapnute elementy 85.55%
pocet => zapnutych: 3147623 vypnutych: 564780 pevnych: 197061
zmena => zapnutych: 17426 vypnutych: 625 Eout: 0.005536 Emin: 0.002000
hmotnost: 57.830200 maximalne napatie: 78.910700 cas riesenia: 4076 sekund
Iteracia: 8, zapnute elementy 85.12%
pocet => zapnutych: 3130822 vypnutych: 581581 pevnych: 197061
zmena => zapnutych: 19066 vypnutych: 708 Eout: 0.006090 Emin: 0.002000
hmotnost: 57.521000 maximalne napatie: 79.093700 cas riesenia: 4170 sekund
Iteracia: 9, zapnute elementy 84.65%
pocet => zapnutych: 3112464 vypnutych: 599939 pevnych: 197061
zmena => zapnutych: 20850 vypnutych: 804 Eout: 0.006699 Emin: 0.002000
hmotnost: 57.163500 maximalne napatie: 79.251700 cas riesenia: 4213 sekund
Iteracia: 10, zapnute elementy 84.14%
pocet => zapnutych: 3092418 vypnutych: 619985 pevnych: 197061
zmena => zapnutych: 22787 vypnutych: 914 Eout: 0.007369 Emin: 0.002000
hmotnost: 56.762400 maximalne napatie: 79.465000 cas riesenia: 4187 sekund
Iteracia: 11, zapnute elementy 83.58%
pocet => zapnutych: 3070545 vypnutych: 641858 pevnych: 197061
zmena => zapnutych: 24888 vypnutych: 1041 Eout: 0.008105 Emin: 0.002000
hmotnost: 56.323000 maximalne napatie: 79.659500 cas riesenia: 4212 sekund
Iteracia: 12, zapnute elementy 82.97%
pocet => zapnutych: 3046698 vypnutych: 665705 pevnych: 197061
zmena => zapnutych: 27164 vypnutych: 1187 Eout: 0.008916 Emin: 0.002000
hmotnost: 55.833500 maximalne napatie: 79.891500 cas riesenia: 4243 sekund
Iteracia: 13, zapnute elementy 82.31%
pocet => zapnutych: 3020721 vypnutych: 691682 pevnych: 197061
zmena => zapnutych: 29626 vypnutych: 1357 Eout: 0.009808 Emin: 0.002000

hmotnost: 55.301000 maximalne napatie: 80.163800 cas riesenia: 4277 sekund
Iteracia: 14, zapnute elementy 81.58%
pocet => zapnutych: 2992452 vypnutych: 719951 pevnych: 197061
zmena => zapnutych: 32284 vypnutych: 1553 Eout: 0.010788 Emin: 0.002000
hmotnost: 54.719200 maximalne napatie: 80.485500 cas riesenia: 4194 sekund
Iteracia: 15, zapnute elementy 80.80%
pocet => zapnutych: 2961721 vypnutych: 750682 pevnych: 197061
zmena => zapnutych: 35147 vypnutych: 1782 Eout: 0.011867 Emin: 0.002000
hmotnost: 54.085700 maximalne napatie: 80.847400 cas riesenia: 4203 sekund
Iteracia: 16, zapnute elementy 79.94%
pocet => zapnutych: 2928356 vypnutych: 784047 pevnych: 197061
zmena => zapnutych: 38226 vypnutych: 2047 Eout: 0.013054 Emin: 0.002000
hmotnost: 53.389600 maximalne napatie: 81.246200 cas riesenia: 4429 sekund
Iteracia: 17, zapnute elementy 79.02%
pocet => zapnutych: 2892177 vypnutych: 820226 pevnych: 197061
zmena => zapnutych: 41530 vypnutych: 2356 Eout: 0.014359 Emin: 0.002000
hmotnost: 52.662000 maximalne napatie: 81.681200 cas riesenia: 4332 sekund
Iteracia: 18, zapnute elementy 78.02%
pocet => zapnutych: 2853003 vypnutych: 859400 pevnych: 197061
zmena => zapnutych: 45064 vypnutych: 2715 Eout: 0.015795 Emin: 0.002000
hmotnost: 51.861900 maximalne napatie: 82.084300 cas riesenia: 4352 sekund
Iteracia: 19, zapnute elementy 76.93%
pocet => zapnutych: 2810654 vypnutych: 901749 pevnych: 197061
zmena => zapnutych: 48834 vypnutych: 3134 Eout: 0.017375 Emin: 0.002000
hmotnost: 51.003400 maximalne napatie: 82.719200 cas riesenia: 4624 sekund
Iteracia: 20, zapnute elementy 75.77%
pocet => zapnutych: 2764954 vypnutych: 947449 pevnych: 197061
zmena => zapnutych: 52844 vypnutych: 3622 Eout: 0.019112 Emin: 0.002000
hmotnost: 50.061800 maximalne napatie: 83.511500 cas riesenia: 4445 sekund
Iteracia: 21, zapnute elementy 74.51%
pocet => zapnutych: 2715732 vypnutych: 996671 pevnych: 197061
zmena => zapnutych: 57094 vypnutych: 4191 Eout: 0.021023 Emin: 0.002000
hmotnost: 49.057500 maximalne napatie: 84.300300 cas riesenia: 4666 sekund
Iteracia: 22, zapnute elementy 73.15%
pocet => zapnutych: 2662829 vypnutych: 1049574 pevnych: 197061
zmena => zapnutych: 61580 vypnutych: 4854 Eout: 0.023126 Emin: 0.002000
hmotnost: 47.958600 maximalne napatie: 85.316100 cas riesenia: 4882 sekund
Iteracia: 23, zapnute elementy 71.70%
pocet => zapnutych: 2606103 vypnutych: 1106300 pevnych: 197061
zmena => zapnutych: 66295 vypnutych: 5628 Eout: 0.025438 Emin: 0.002000
hmotnost: 46.746700 maximalne napatie: 86.586500 cas riesenia: 4788 sekund
Iteracia: 24, zapnute elementy 70.15%
pocet => zapnutych: 2545436 vypnutych: 1166967 pevnych: 197061
zmena => zapnutych: 71227 vypnutych: 6531 Eout: 0.027982 Emin: 0.002000
hmotnost: 45.463400 maximalne napatie: 87.754700 cas riesenia: 4680 sekund
Iteracia: 25, zapnute elementy 68.50%
pocet => zapnutych: 2480740 vypnutych: 1231663 pevnych: 197061
zmena => zapnutych: 76358 vypnutych: 7582 Eout: 0.030780 Emin: 0.002000
hmotnost: 44.070300 maximalne napatie: 89.259900 cas riesenia: 4887 sekund
Iteracia: 26, zapnute elementy 66.74%
pocet => zapnutych: 2411964 vypnutych: 1300439 pevnych: 197061
zmena => zapnutych: 81665 vypnutych: 8806 Eout: 0.033858 Emin: 0.002000
hmotnost: 42.612800 maximalne napatie: 91.104500 cas riesenia: 4973 sekund
Iteracia: 27, zapnute elementy 64.87%
pocet => zapnutych: 2339105 vypnutych: 1373298 pevnych: 197061
zmena => zapnutych: 87118 vypnutych: 10230 Eout: 0.037244 Emin: 0.002000
hmotnost: 41.062400 maximalne napatie: 93.197700 cas riesenia: 5044 sekund
Iteracia: 28, zapnute elementy 62.91%
pocet => zapnutych: 2262217 vypnutych: 1450186 pevnych: 197061
zmena => zapnutych: 92680 vypnutych: 11882 Eout: 0.040969 Emin: 0.002000
hmotnost: 39.442400 maximalne napatie: 95.654800 cas riesenia: 5182 sekund
Iteracia: 29, zapnute elementy 60.84%

pocet => zapnutych: 2181419 vypnutych: 1530984 pevnych: 197061
zmena => zapnutych: 98307 vypnutych: 13799 Eout: 0.045066 Emin: 0.002000
hmotnost: 37.786900 maximalne napatie: 98.261000 cas riesenia: 5185 sekund
Iteracia: 30, zapnute elementy 58.68%
pocet => zapnutych: 2096911 vypnutych: 1615492 pevnych: 197061
zmena => zapnutych: 103948 vypnutych: 16017 Eout: 0.049572 Emin: 0.002000
hmotnost: 36.171500 maximalne napatie: 100.881000 cas riesenia: 5144 sekund
Iteracia: 31, zapnute elementy 56.43%
pocet => zapnutych: 2008980 vypnutych: 1703423 pevnych: 197061
zmena => zapnutych: 109548 vypnutych: 18577 Eout: 0.054529 Emin: 0.002000
hmotnost: 34.438900 maximalne napatie: 103.844000 cas riesenia: 5137 sekund
Iteracia: 32, zapnute elementy 54.10%
pocet => zapnutych: 1918009 vypnutych: 1794394 pevnych: 197061
zmena => zapnutych: 115047 vypnutych: 21526 Eout: 0.059982 Emin: 0.002000
hmotnost: 32.747800 maximalne napatie: 107.288000 cas riesenia: 5539 sekund
Iteracia: 33, zapnute elementy 51.71%
pocet => zapnutych: 1824488 vypnutych: 1887915 pevnych: 197061
zmena => zapnutych: 120381 vypnutych: 24913 Eout: 0.065981 Emin: 0.002000
hmotnost: 31.088200 maximalne napatie: 110.576000 cas riesenia: 5301 sekund
Iteracia: 34, zapnute elementy 49.27%
pocet => zapnutych: 1729020 vypnutych: 1983383 pevnych: 197061
zmena => zapnutych: 125490 vypnutych: 28790 Eout: 0.072579 Emin: 0.002000
hmotnost: 29.447200 maximalne napatie: 114.914000 cas riesenia: 5421 sekund
Iteracia: 35, zapnute elementy 46.79%
pocet => zapnutych: 1632320 vypnutych: 2080083 pevnych: 197061
zmena => zapnutych: 130319 vypnutych: 33213 Eout: 0.079836 Emin: 0.002000
hmotnost: 29.447200 maximalne napatie: 156.437000 cas riesenia: 5416 sekund
Iteracia: 35, zapnute elementy 46.78%
pocet => zapnutych: 1631914 vypnutych: 2080489 pevnych: 197061
zmena => zapnutych: 65143 vypnutych: 16610 Eout: 0.039918 Emin: 0.002000
hmotnost: 29.447200 maximalne napatie: 156.427000 cas riesenia: 5402 sekund
Iteracia: 35, zapnute elementy 48.03%
pocet => zapnutych: 1680487 vypnutych: 2031916 pevnych: 197061
zmena => zapnutych: 33541 vypnutych: 8111 Eout: 0.019959 Emin: 0.002000
hmotnost: 28.720900 maximalne napatie: 115.464000 cas riesenia: 5212 sekund
Iteracia: 36, zapnute elementy 47.38%
pocet => zapnutych: 1655057 vypnutych: 2057346 pevnych: 197061
zmena => zapnutych: 36337 vypnutych: 9034 Eout: 0.021955 Emin: 0.002000
hmotnost: 28.289400 maximalne napatie: 115.549000 cas riesenia: 5643 sekund
Iteracia: 37, zapnute elementy 46.68%
pocet => zapnutych: 1627754 vypnutych: 2084649 pevnych: 197061
zmena => zapnutych: 39311 vypnutych: 10069 Eout: 0.024151 Emin: 0.002000
hmotnost: 27.862300 maximalne napatie: 117.612000 cas riesenia: 5732 sekund
Iteracia: 38, zapnute elementy 45.93%
pocet => zapnutych: 1598512 vypnutych: 2113891 pevnych: 197061
zmena => zapnutych: 42465 vypnutych: 11231 Eout: 0.026566 Emin: 0.002000
hmotnost: 27.418000 maximalne napatie: 119.720000 cas riesenia: 6188 sekund
Iteracia: 39, zapnute elementy 45.13%
pocet => zapnutych: 1567278 vypnutych: 2145125 pevnych: 197061
zmena => zapnutych: 45799 vypnutych: 12537 Eout: 0.029222 Emin: 0.002000
hmotnost: 26.951800 maximalne napatie: 120.827000 cas riesenia: 6011 sekund
Iteracia: 40, zapnute elementy 44.28%
pocet => zapnutych: 1534016 vypnutych: 2178387 pevnych: 197061
zmena => zapnutych: 49310 vypnutych: 14005 Eout: 0.032144 Emin: 0.002000
hmotnost: 26.438000 maximalne napatie: 122.458000 cas riesenia: 5965 sekund
Iteracia: 41, zapnute elementy 43.38%
pocet => zapnutych: 1498711 vypnutych: 2213692 pevnych: 197061
zmena => zapnutych: 52993 vypnutych: 15655 Eout: 0.035359 Emin: 0.002000
hmotnost: 25.886200 maximalne napatie: 123.849000 cas riesenia: 5862 sekund
Iteracia: 42, zapnute elementy 42.42%
pocet => zapnutych: 1461373 vypnutych: 2251030 pevnych: 197061
zmena => zapnutych: 56840 vypnutych: 17511 Eout: 0.038895 Emin: 0.002000

hmotnost: 25.267000 maximalne napatie: 125.676000 cas riesenia: 6264 sekund
Iteracia: 43, zapnute elementy 41.42%
pocet => zapnutych: 1422044 vypnutych: 2290359 pevnych: 197061
zmena => zapnutych: 60841 vypnutych: 19598 Eout: 0.042784 Emin: 0.002000
hmotnost: 24.646500 maximalne napatie: 127.179000 cas riesenia: 5865 sekund
Iteracia: 44, zapnute elementy 40.36%
pocet => zapnutych: 1380801 vypnutych: 2331602 pevnych: 197061
zmena => zapnutych: 64984 vypnutych: 21946 Eout: 0.047063 Emin: 0.002000
hmotnost: 23.990300 maximalne napatie: 128.983000 cas riesenia: 5990 sekund
Iteracia: 45, zapnute elementy 39.26%
pocet => zapnutych: 1337763 vypnutych: 2374640 pevnych: 197061
zmena => zapnutych: 69254 vypnutych: 24586 Eout: 0.051769 Emin: 0.002000
hmotnost: 23.312100 maximalne napatie: 130.511000 cas riesenia: 5852 sekund
Iteracia: 46, zapnute elementy 38.12%
pocet => zapnutych: 1293095 vypnutych: 2419308 pevnych: 197061
zmena => zapnutych: 73636 vypnutych: 27554 Eout: 0.056946 Emin: 0.002000
hmotnost: 22.609000 maximalne napatie: 132.363000 cas riesenia: 6327 sekund
Iteracia: 47, zapnute elementy 36.94%
pocet => zapnutych: 1247013 vypnutych: 2465390 pevnych: 197061
zmena => zapnutych: 78113 vypnutych: 30887 Eout: 0.062640 Emin: 0.002000
hmotnost: 21.874800 maximalne napatie: 134.581000 cas riesenia: 6039 sekund
Iteracia: 48, zapnute elementy 35.73%
pocet => zapnutych: 1199787 vypnutych: 2512616 pevnych: 197061
zmena => zapnutych: 82670 vypnutych: 34626 Eout: 0.068904 Emin: 0.002000
hmotnost: 21.152500 maximalne napatie: 136.112000 cas riesenia: 6061 sekund
Iteracia: 49, zapnute elementy 34.50%
pocet => zapnutych: 1151743 vypnutych: 2560660 pevnych: 197061
zmena => zapnutych: 87296 vypnutych: 38817 Eout: 0.075795 Emin: 0.002000
hmotnost: 20.394500 maximalne napatie: 139.291000 cas riesenia: 5756 sekund
Iteracia: 50, zapnute elementy 33.26%
pocet => zapnutych: 1103264 vypnutych: 2609139 pevnych: 197061
zmena => zapnutych: 91984 vypnutych: 43507 Eout: 0.083374 Emin: 0.002000
hmotnost: 19.672900 maximalne napatie: 140.778000 cas riesenia: 5432 sekund
Iteracia: 51, zapnute elementy 32.02%
pocet => zapnutych: 1054787 vypnutych: 2657616 pevnych: 197061
zmena => zapnutych: 96736 vypnutych: 48747 Eout: 0.091712 Emin: 0.002000
hmotnost: 18.888500 maximalne napatie: 144.817000 cas riesenia: 5505 sekund
Iteracia: 52, zapnute elementy 30.79%
pocet => zapnutych: 1006798 vypnutych: 2705605 pevnych: 197061
zmena => zapnutych: 101569 vypnutych: 54590 Eout: 0.100883 Emin: 0.002000
hmotnost: 18.888500 maximalne napatie: 239.829000 cas riesenia: 5224 sekund
Iteracia: 52, zapnute elementy 30.82%
pocet => zapnutych: 1007808 vypnutych: 2704595 pevnych: 197061
zmena => zapnutych: 50835 vypnutych: 27285 Eout: 0.050441 Emin: 0.002000
hmotnost: 18.231700 maximalne napatie: 146.735000 cas riesenia: 5145 sekund
Iteracia: 53, zapnute elementy 30.22%
pocet => zapnutych: 984258 vypnutych: 2728145 pevnych: 197061
zmena => zapnutych: 54612 vypnutych: 30275 Eout: 0.055486 Emin: 0.002000
hmotnost: 17.750200 maximalne napatie: 148.136000 cas riesenia: 5506 sekund
Iteracia: 54, zapnute elementy 29.59%
pocet => zapnutych: 959921 vypnutych: 2752482 pevnych: 197061
zmena => zapnutych: 58588 vypnutych: 33599 Eout: 0.061034 Emin: 0.002000
hmotnost: 17.750200 maximalne napatie: 251.515000 cas riesenia: 5294 sekund
Iteracia: 54, zapnute elementy 29.58%
pocet => zapnutych: 959269 vypnutych: 2753134 pevnych: 197061
zmena => zapnutych: 29274 vypnutych: 16803 Eout: 0.030517 Emin: 0.002000
hmotnost: 17.750200 maximalne napatie: 150.146000 cas riesenia: 5165 sekund
Iteracia: 54, zapnute elementy 29.90%
pocet => zapnutych: 971787 vypnutych: 2740616 pevnych: 197061
zmena => zapnutych: 14828 vypnutych: 8364 Eout: 0.015259 Emin: 0.002000
hmotnost: 17.603900 maximalne napatie: 148.781000 cas riesenia: 4863 sekund
Iteracia: 55, zapnute elementy 29.73%

pocet => zapnutych: 965323 vypnutych: 2747080 pevnych: 197061
zmena => zapnutych: 16202 vypnutych: 9222 Eout: 0.016784 Emin: 0.002000
hmotnost: 17.484900 maximalne napatie: 148.485000 cas riesenia: 5225 sekund
Iteracia: 56, zapnute elementy 29.55%
pocet => zapnutych: 958343 vypnutych: 2754060 pevnych: 197061
zmena => zapnutych: 17694 vypnutych: 10170 Eout: 0.018463 Emin: 0.002000
hmotnost: 17.364900 maximalne napatie: 148.957000 cas riesenia: 5234 sekund
Iteracia: 57, zapnute elementy 29.36%
pocet => zapnutych: 950819 vypnutych: 2761584 pevnych: 197061
zmena => zapnutych: 19310 vypnutych: 11217 Eout: 0.020309 Emin: 0.002000
hmotnost: 17.256100 maximalne napatie: 149.519000 cas riesenia: 5467 sekund
Iteracia: 58, zapnute elementy 29.15%
pocet => zapnutych: 942726 vypnutych: 2769677 pevnych: 197061
zmena => zapnutych: 21060 vypnutych: 12375 Eout: 0.022340 Emin: 0.002000
hmotnost: 17.256100 maximalne napatie: 150.083000 cas riesenia: 5567 sekund
Iteracia: 58, zapnute elementy 29.14%
pocet => zapnutych: 942134 vypnutych: 2770269 pevnych: 197061
zmena => zapnutych: 10524 vypnutych: 6189 Eout: 0.011170 Emin: 0.002000
hmotnost: 17.256100 maximalne napatie: 150.084000 cas riesenia: 5235 sekund
Iteracia: 58, zapnute elementy 29.25%
pocet => zapnutych: 946484 vypnutych: 2765919 pevnych: 197061
zmena => zapnutych: 5286 vypnutych: 3090 Eout: 0.005585 Emin: 0.002000
hmotnost: 17.192500 maximalne napatie: 149.525000 cas riesenia: 5434 sekund
Iteracia: 59, zapnute elementy 29.19%
pocet => zapnutych: 944288 vypnutych: 2768115 pevnych: 197061
zmena => zapnutych: 5801 vypnutych: 3401 Eout: 0.006143 Emin: 0.002000
hmotnost: 17.135200 maximalne napatie: 149.513000 cas riesenia: 5402 sekund
Iteracia: 60, zapnute elementy 29.13%
pocet => zapnutych: 941888 vypnutych: 2770515 pevnych: 197061
zmena => zapnutych: 6365 vypnutych: 3745 Eout: 0.006758 Emin: 0.002000
hmotnost: 17.108300 maximalne napatie: 149.721000 cas riesenia: 5328 sekund
Iteracia: 61, zapnute elementy 29.07%
pocet => zapnutych: 939268 vypnutych: 2773135 pevnych: 197061
zmena => zapnutych: 6982 vypnutych: 4123 Eout: 0.007434 Emin: 0.002000
hmotnost: 17.048400 maximalne napatie: 149.993000 cas riesenia: 5482 sekund
Iteracia: 62, zapnute elementy 28.99%
pocet => zapnutych: 936409 vypnutych: 2775994 pevnych: 197061
zmena => zapnutych: 7657 vypnutych: 4540 Eout: 0.008177 Emin: 0.002000
hmotnost: 17.048400 maximalne napatie: 150.371000 cas riesenia: 5410 sekund
Iteracia: 62, zapnute elementy 28.99%
pocet => zapnutych: 936151 vypnutych: 2776252 pevnych: 197061
zmena => zapnutych: 3827 vypnutych: 2270 Eout: 0.004088 Emin: 0.002000
hmotnost: 17.048400 maximalne napatie: 150.339000 cas riesenia: 5249 sekund
Iteracia: 62, zapnute elementy 29.03%
pocet => zapnutych: 937711 vypnutych: 2774692 pevnych: 197061
zmena => zapnutych: 1917 vypnutych: 1134 Eout: 0.002044 Emin: 0.002000
hmotnost: 17.026300 maximalne napatie: 149.905000 cas riesenia: 5385 sekund
Iteracia: 63, zapnute elementy 29.01%
pocet => zapnutych: 936928 vypnutych: 2775475 pevnych: 197061
zmena => zapnutych: 2107 vypnutych: 1248 Eout: 0.002249 Emin: 0.002000
hmotnost: 17.007600 maximalne napatie: 149.872000 cas riesenia: 5376 sekund
Iteracia: 64, zapnute elementy 28.98%
pocet => zapnutych: 936069 vypnutych: 2776334 pevnych: 197061
zmena => zapnutych: 2315 vypnutych: 1373 Eout: 0.002474 Emin: 0.002000
hmotnost: 16.994600 maximalne napatie: 149.859000 cas riesenia: 5417 sekund
Iteracia: 65, zapnute elementy 28.96%
pocet => zapnutych: 935127 vypnutych: 2777276 pevnych: 197061
zmena => zapnutych: 2544 vypnutych: 1511 Eout: 0.002721 Emin: 0.002000
hmotnost: 16.994600 maximalne napatie: 150.053000 cas riesenia: 5129 sekund
Iteracia: 65, zapnute elementy 28.96%
pocet => zapnutych: 935036 vypnutych: 2777367 pevnych: 197061
zmena => zapnutych: 1272 vypnutych: 756 Eout: 0.001360 Emin: 0.002000

hmotnost: 16.994600 maximalne napatie: 150.109000 cas riesenia: 5248 sekund

Cas riesenia topologickej optimalizacie: 408244 sekund.
Vysledna hmotnost 16.977, zmena hmotnosti o 75%.

The geometry of the initial model and the distribution of the equivalent stress field according to HMH theory is shown in Figure 4. The stress field in the second loading mode is displayed.

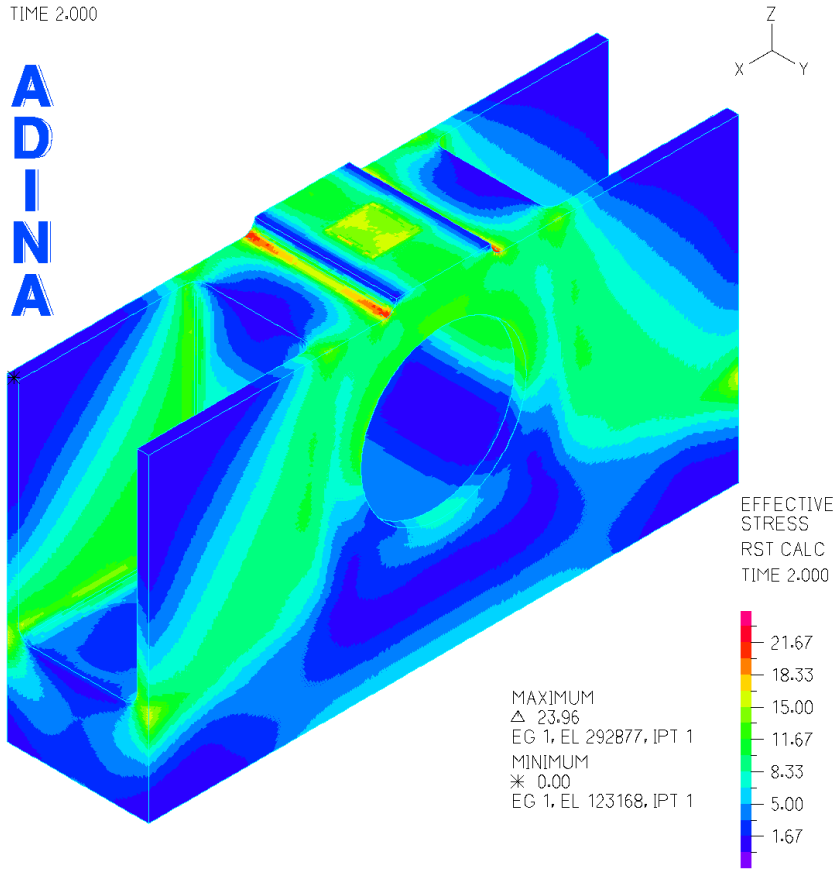

Fig. 4 Initial geometry and equivalent stress field distribution according to HMH theory, for the second loading mode

The topology optimization resulted in the structural geometry shown in Figure 5, where the equivalent stress field according to HMH theory is also displayed.

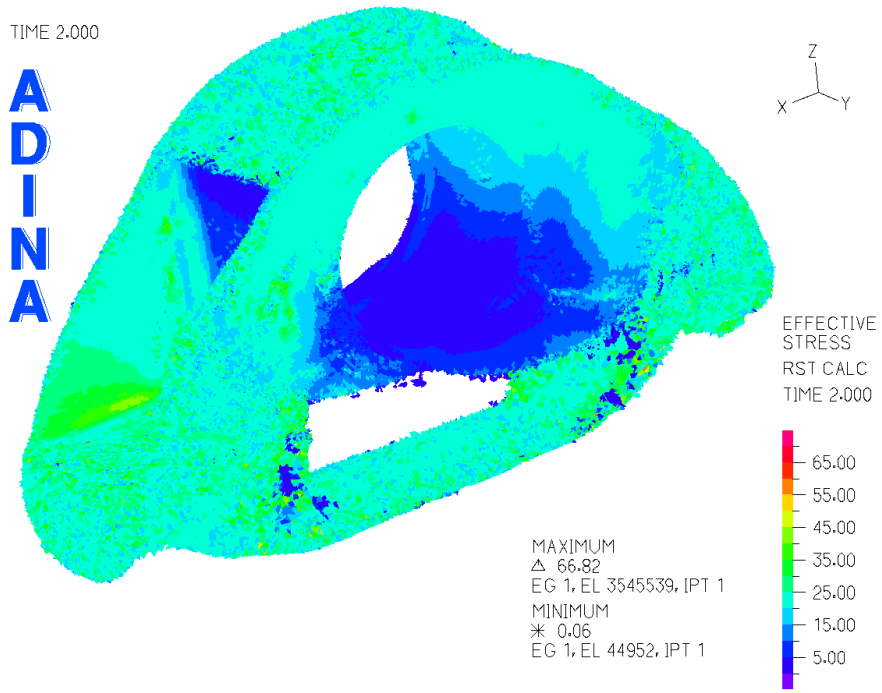

Fig. 5 Bearing housing geometry with equivalent stress distribution after topology optimization

In the topology optimization model, we use linear tetrahedral elements. There are several reasons for using this type of element:

- The algorithm for hexahedral meshes generates hexahedrons, triangular prisms, pyramids, and tetrahedrons. Each of these elements has a different number of integration points and a different format in the stress values file.
- The algorithm for tetrahedral elements creates exclusively tetrahedral elements, and the format of the stress values in the file is the same for all elements.
- To achieve sufficient solution accuracy with tetrahedral elements, we need a dense mesh of small elements. This requirement is identical to the requirement for topology optimization, where we also require a large number of small elements. In topology optimization, we want to turn off small parts of the model to create the most suitable structural shape.
- Quadratic elements with the same number of elements have a significantly larger number of nodes. In topology optimization, we want to minimize the number of nodes and maximize the number of elements.

In the developed topology optimization algorithm, a portion of the algorithm is designed to reactivate a small number of elements from the group of deactivated elements. This step serves to reactivate elements in case of a significant change in the stress distribution caused by the deactivation of elements in other parts of the model. In topology optimization, up to 60% or more of the elements can be deactivated, so the number of reactivated elements is chosen to be roughly 10 to 20% of the number of deactivated elements. This ratio is chosen to prevent the number of deactivated and reactivated elements from equalizing at a certain stage of the optimization process, which would stop the convergence of the proposed topology optimization algorithm.

CONCLUSION

The presented topology optimization algorithm demonstrates the connection and data exchange between the MATLAB and Adina software packages. The presented procedure can be applied to any other software package, or a different program or programming language such as MATLAB can be used to control the calculations. A necessary element of such a connection is the existence of input text files in the form of a sequence of commands for creating a calculation task in the Adina program.

ACKNOWLEDGEMENT

This work has been supported by the gran project KEGA 005ŽU-4/2024.

REFERENCES

[1] M. Handrik, M. Vaško, J. Handriková: Tvorba aplikačného softvéru v MATLAB-e. Edis – vydavateľstvo UNIZA, 2021.

[2] Matlab. On-line help. https://www.mathworks.com/help/matlab/

[3] Theory and Modeling Guide, Volume I: ADINA, ADINA 23.00, September 2023, Bentley Systems, Inc.

[4] ADINA User Interface Command Reference Manual, Volume I: Solids & Structures, ADINA 23.00, September 2023, Bentley Systems, Inc.

[5] ADINA User Interface Command Reference Manual, Volume V: Display Processing, ADINA 23.00, September 2023, Bentley Systems, Inc.

APPLIED MECHANICS 2024

April 17th – 19th, 2024
Hotel Toliar, Štrbské Pleso
Slovakia

MATERIAL FATIGUE DURING MULTIAXIAL LOADING

M. FUSEK[1]*, A. TOŠKOVÁ [2]

The contribution generally discusses the problem of material fatigue, further deals with fatigue multiaxial criteria and their distribution with a focus on the Jiang criterion, which combines the concepts of multiaxial criteria together with the introduction of material memory.

Keywords: Fatigue; Jiang criterion; multiaxial loading; experimental verification

INTRODUCTION

The operation of machines and devices leads to the degradation of component materials, which can result in a limit state - loss of functionality of the equipment. Among the most common limit states is material fatigue, which is responsible for a large part of machine failures. It is reported that up to 90 % of all failures are related to fatigue. The limit state of material fatigue can be defined as a state in which the functionality of a component (or device) is violated due to the action of a time-varying load. When a material is subjected to repeated loading, it gradually "weakens and weakens" until it fails. The stress that a material can withstand before failure is often lower in the case of material fatigue than under static loading. Material fatigue is manifested by the formation and propagation of microscopic cracks. These cracks usually form on the surface of the material and their growth affects the state of the surface layer (e.g. corrosion, wear). The cracks gradually enlarge and weaken the material until it suddenly breaks. Material degradation due to fatigue is a cumulative process, that is, material damage accumulates with each loading cycle. Unlike living organisms, which can recover from damage, this process is irreversible for materials. Although the name "material fatigue" is not entirely accurate, it is commonly used and historically established. Material fatigue research plays an important role in engineering and construction. By understanding the mechanisms of material fatigue, it is possible to design components and equipment with longer life and resistance to failure. This leads to greater machine safety and reliability and reduces the risk of breakdowns and accidents. Despite extensive research, there is no universal predictive solution to the issue of material fatigue. However, research in this area continues with the aim of minimizing the risks of breakdowns and extending the life of machines and devices. New materials and

[1]**doc. Ing. Martin Fusek, Ph.D.**, Department of Applied Mechanics, Faculty of Mechanical Engineering, VSB - Technical University of Ostrava, 17. listopadu 2172/15, Ostrava - Poruba, Czech Republic; martin.fusek@vsb.cz
[2] **Ing. Anna Tošková**, Department of Applied Mechanics, Faculty of Mechanical Engineering, VSB - Technical University of Ostrava, 17. listopadu 2172/15, Ostrava - Poruba, Czech Republic; anna.toskova@vsb.cz

technologies, such as 3D printing, open up further possibilities for the study and prevention of material fatigue.

MULTIAXIAL MATERIAL FATIGUE CRITERIA

In recent years, a large number of criteria (hypotheses) have been created for the calculation of service life under multiaxial fatigue stress. They can, under certain conditions, be used to evaluate the service life of components or a larger unit under fatigue stress. Despite significant progress in recent decades, the situation in the given area is not entirely satisfactory.

There are therefore a number of fatigue hypotheses which, without sufficient verification, cannot be generally applied for different types of materials and for different loading methods, considering their limited validity. Criteria creators generally do not specify the area of use of the criteria. Another problem is the choice of parameters and constants in calculation formulas.

Many ways of sorting criteria can be found in the literature. The most basic division is into criteria suitable for high-cycle fatigue (HCF) and low-cycle fatigue (LCF). Furthermore, division according to the control variable (stress, strain) is used. Several approaches have been established to determine life in low-cycle multiaxial fatigue. The most well-known approaches include:

a) effective strain approach,
b) critical plane approaches (strain approach, strain-stress approach),
c) energy approaches.

However, it should be noted that even this division is imprecise and some criteria can be classified into several groups. Based on the study of the mentioned issue, it is possible to conclude that the most frequently used (cited) criteria, whether in cases of proportional or non-proportional loading, in the field of multiaxial low-cycle fatigue, are the following:

- Critical plane strain approach – the control parameter is strain (e.g. Brown-Miller criterion, Wang-Brown criterion).
- Critical plane strain-stress approach - the primary control parameter is strain and the secondary parameter is stress (e.g. Fatemi-Socie criterion, Socie et al. criterion).
- Energy approach - fatigue damage of the material is related to the strain energy accumulated during the load cycle. The given group of criteria includes the S-W-T approach, Glinka criterion, Jiang-Sehitoglu criterion, etc.

JIANG CRITERION

The authors take a deeper look at Jiang criterion, which is significantly different in its concept from other criteria that are applied in the prediction of fatigue damage in the field of multiaxial loading. This criterion combines the concept of a critical plane, the effect of plastic strain energy, and the principle of material memory is also introduced here.

Jiang's criterion was published relatively recently, in 2000, see [1]. It is a pity that the author himself does not develop the proposed criterion further. The basic form of the criterion is as follows:

$$dD = \langle \sigma_{mr} - \sigma_0 \rangle^m \left(1 + \frac{\sigma}{\sigma_f}\right) dY, \tag{1}$$

where

$$dY = a\sigma d\varepsilon^p + \frac{1-a}{2}\tau d\gamma^p. \tag{2}$$

In the previous two expressions (1) and (2) σ represents the normal stress on the material plane, τ the shear stress on the material plane, ε^p represents the plastic normal strain on the material plane, γ^p represents the plastic shear strain on the material plane. Furthermore, there are two material constants in the equations. Constant a characterizing the fracture behavior of the material, m is the exponent. σ_0 represents the fatigue limit of the material in symmetric tension-compression. σ_f is the true fracture stress. The variable σ_{mr} represents the material memory parameter. The quantity Y is the modified plastic strain energy density on the material plane. The symbol D represents fatigue damage. The symbol $\langle \quad \rangle$ represents the so-called MacCauley brackets.

The critical plane is defined as the material plane at which the accumulated damage D reaches the critical value D_0. If the stress σ_{mr} is below σ_0 or the strain is elastic, the fatigue damage is minimal. The criterion defines plastic strain energy on a given material plane as the main cause of fatigue failure.

Looking at equation (1), we can see that the first part on the right-hand side captures the effect of loading sequences. As in cyclic plasticity, a memory area is introduced here that "works" depending on changes in the load history, i.e. shrinks or expands. Memory area expansion is faster than its contraction. This captures the effect of loading sequences. The second part on the right-hand side of the equation is designed to capture the effect of the mean stress, where the control variable is the normal stress on the given plane. As a new approach, in the calculation of fatigue damage, the memory parameter σ_{mr} is introduced in the criterion. The memory area is introduced as an analogy to the memory area known from cyclic plasticity.

MODIFIED JIANG CRITERION

During the conducted research activities, two basic modifications of the original criterion were created.

First Modification

Service life is determined according to the following equations:

$$\Delta D N_f = \sum_{i=1}^{N_f} \Delta D_i = D_0, \tag{3}$$

$$\sum_{i=1}^{N_f} \frac{\Delta D_i}{D_0} = 1. \tag{4}$$

If we take the expression (3) it is possible to rewrite it in the form

$$\Delta D = D_0 N_f^{-1}. \tag{5}$$

It can be seen that the increase in damage within one cycle is inversely proportional to the number of cycles to failure. Remark that the parameter D_0 represents the critical value of fatigue failure and is assumed to be constant throughout the service life. The initiation and propagation of a fatigue crack is significantly related to the type of material, its structure, the surrounding environment and also depends on the amplitude of cyclic plastic strain. It is evident that in the case of high load levels, the area affected by plastic strain is significantly larger than in the case of low loads, and this environment also significantly affects the initialization itself. Equation (3) can be generalized to the form

$$\Delta D = A_0 N_f^{b_0}, \tag{6}$$

where the parameter A_0 is the generalization parameter and the parameter b_0 is the exponent of the generalization. These are constants that are related to the material and must be determined in the phase of identifying other constants of Jiang model. It is evident that in the case of the choice

$A_0 = D_0$ and then $b_0 = -1$, equation (6) becomes the original equation (3). So the model remains consistent. With this approach, nonlinearity is introduced into the computational model. Although this generalization introduces additional unknowns into the damage model, additional experiments are not needed to identify them, just those needed to fitting the basic model.

Second Modification

Everything remains as with the initial criterion, however, a non-proportional parameter was added to the model, which considers the strengthening caused by the non-proportional load, in the form:

$$\mathrm{A} = 1 + \frac{d\boldsymbol{s} : \boldsymbol{s}}{\sqrt{\boldsymbol{s} : \boldsymbol{s}}\sqrt{d\boldsymbol{s} : d\boldsymbol{s}}}\,, \tag{7}$$

where $\boldsymbol{s}$ is the deviator part of the stress tensor and $d\boldsymbol{s}$ is its increment. This parameter is based on the works of Benallal and Marquis [2]. The linear rule (5) is used for cumulation.

Various metrics can be used for prediction quality. The simplest metric given by the formula was chosen here

$$k = \frac{N_{fp}}{N_{fe}}, \tag{8}$$

where k is the given metric, N_{fp} represents the number of cycles obtained using prediction and N_{fe} represents the number of cycles obtained from experiment. A ratio in the range can be considered a good result

$$\begin{gathered} 0{,}5 \le k \le 2, \\ k < 1 \ldots conservative\ and\ k > 1 \ldots non - conservative. \end{gathered} \tag{9}$$

The following results were obtained from tests performed on SS316L material:

Tab. 1 Results of used metric for two modifications

	Mean value of k	Range of k
Original criterion	1.53	0.63
Modification No. 1	1.16	0.53
Modification No. 2	1.06	0.42

For more information on individual modifications, see [3].

CONCLUSION

The paper discussed with the issue of estimating the behavior of test samples, and consequently bodies, during low-cycle fatigue. Various prediction methods are discussed, where estimation methods can be divided into several groups - effective strain approach, critical plane approaches (strain approach, strain-stress approach), and energy approaches. The issue of the so-called Jiang criterion is discussed in more detail. Two modifications are briefly introduced, and prediction results on SS316L steel are presented.

ACKNOWLEDGEMENT

This work has been supported by Specific Research „Experimental and Numerical Modeling for Solving Problems in Mechanics and Biomechanics“ (SP2024/037).

REFERENCES

[1] Y.-Y. Jiang. A fatigue criterion for general multiaxial loading. *Fatigue & fracture of engineering materials & structures* **2000**. 23 (1). 2000, 19–32.

[2] A. Benallal, D. Marquis. Constitutive equations for nonproportional cyclic elastoviscoplasticity. *ASME J. Eng. Mater. Technol*. 1987, 109, 326.

[3] M. Fusek, R. Halama, D. Lickova. Two modifications of Jiang criterion for constant amplitude multiaxial loading of AA2124-T851 and SS316L. *Continuum Mechanics and Thermodynamics* **2020**, 1–17.

MATLAB® & SIMULINK®

MathWorks®

Campus-Wide License

celouniverzitní licence

MATLAB Access for Everyone, Anywhere

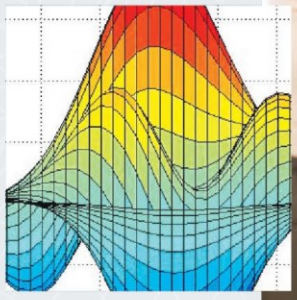

- » MATLAB & Simulink Full Suite
- » Online kurzy MATLAB Academy
- » MATLAB Online
- » MATLAB Mobile
- » MATLAB Drive
- » MATLAB Grader
- » Jednoduchá správa licence

"If you want to work at Google, make sure you can use MATLAB."
Jonathan Rosenberg, Senior Vice President of Products, Google

https://www.mathworks.com/academia/matlab-campus

https://www.humusoft.cz/matlab/academia/campus

"Díky zavedení celouniverzitní licence je možné, aby studenti plně využívali všech možností systému MATLAB nejen v laboratořích univerzity, ale i při zpracování samostatných prací na svých domácích počítačích. V rámci celouniverzitní licence je možné velmi elegantně a rychle řešit řadu úloh, které bylo dříve nutné složitě programovat."
Zdeněk Plíva, děkan FM TUL

"Možno si študenti položia otázku: prečo sa mám učiť pracovať s MATLABom? Pretože jeho znalosť zvyšuje šance na trhu práce a prispieva k lepšiemu uplatneniu. Znalosť MATLABu môže pomôcť pri rozbehu vlastného podnikania."
Karol Matiaško, prorektor UNIZA

HUMUSOFT®

Humusoft s.r.o.
Pobřežní 20, Praha 8

E-mail: info@humusoft.cz
Tel: +420 284 011 730

Láka ťa elektromobilita? Staň sa súčasťou nášho R&D tímu v Schaeffler Kysuce

V Schaeffler Kysuce staviame moderné výskumné a vývojové centrum, ktoré bude prinášať inovatívne riešenia v oblasti elektromobility pre automobilky z celého sveta.

Už dnes naši kolegovia vyvíjajú kompletné integrované elektrické pohonné systémy. A neskôr to budú aj mechatronické riešenia pre autonómne riadenie vozidiel.

Výnimočnosť nášho nového centra podčiarkuje aj fakt, že viaceré riešenia, ktoré naši kolegovia navrhnú, sa budú na Kysuciach aj vyrábať.

Pridať sa k nám možeš už teraz!

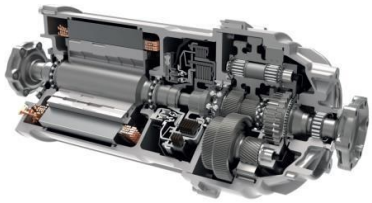

Veríme, že možnosť vyvíjať technologické riešenia pre udržateľnú mobilitu, ktoré dokážu zvýšiť dojazd a bezpečnosť vozidiel, bude motiváciou pre mnohé mladé talenty, ako si aj ty.

Túto príležitosť si nemôžeš nechať ujsť!

Benefity

Naši zamestnanci si môžu vybrať zo širokej škály atraktívnych benefitov.

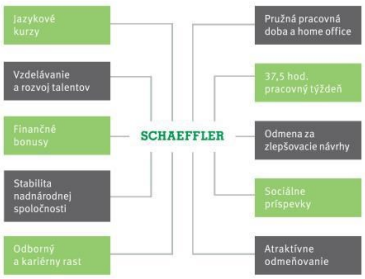

Kontakt

Ak sa chceš dozvedieť viac, navštív našu stránku
https://emobility-schaeffler.sk

Aktuálny zoznam voľných pozícií nájdeš na:
jobs.schaeffler.com
www.emobility-schaeffler.sk/kariera

Na tvoje otázky radi odpovieme aj telefonicky na
+421 910 867 840

Zaujali sme ťa? Neváhaj a prihlás sa!

We pioneer motion

Naštartuj svoju kariéru v Schaeffler

Schaeffler – spoločnosť s perspektívou!

Skupina Schaeffler ako popredný svetový dodávateľ pre automobilový a ostatný priemysel je už 75 rokov priekopníkom vynálezov a vývoja v oblastiach pohybu a mobility. Vďaka inovatívnym technológiám, produktom a službám pre elektromobilitu, pohonom efektívnym z hľadiska CO_2, Priemyslu 4.0, digitalizácii a obnoviteľnej energii je spoločnosť spoľahlivým partnerom pre efektívnejší, inteligentnejší a udržateľnejší pohyb a mobilitu.

už 30 rokov na Slovensku

Schaeffler so svojimi dvoma závodmi v Skalici a Kysuckom Novom Meste a 9000 zamestnancami, patrí k najväčším zamestnávateľom na Slovensku.

Schaeffler Kysuce vyvíja a vyrába riešenia pre oblasť elektromobility pre motory, prevodovky a podvozky. Ide napríklad o modulárnu, vysoko integrovanú technologickú platformu pre elektromotory, hybridné pohonné jednotky, plne elektrické nápravy, elektrické parkovacie brzdy alebo mechatronické stabilizátory náklonu vozidla. Jeho súčasťou bude aj nové výskumno-vývojové centrum, ktoré sa bude špecializovať na nové technologické riešenia v oblasti mobility pre svetové automobilové značky.

Výrobné portfólio **Schaeffler Skalica** tvoria ložiskové riešenia, klietky i krúžky, lineárne a priame pohony, servisné prvky, produkty na údržbu výrobných liniek a inteligentné monitorovacie systémy. Súčasťou závodu je aj špeciálne mechatronické laboratórium, výskum a vývoj nových riešení.

Prepoj svoje vedomosti s praxou

Vyber si z našej ponuky a začni kariéru s nami

Si absolvent VŠ v odboroch mechatronika, elektrotechnika, strojárstvo so zameraním na programovanie, fyzika, alebo iného podobného zamerania? Komunikuješ aktívne anglicky (slovom i písmom)? Zaujímaš sa o novinky v oblasti automotive a návrhu systémov pre elektrické a hybridné vozidlá?

Čo ponúkame?
Uplatnenie v nasledovných oblastiach:

- návrh systémov,
- tvorba dizajnu,
- vývoj softvéru,
- požiadavkové inžinierstvo,
- simulácie komponentov a systémov,
- skúšobníctvo a test manažment,
- projektové riadenie,
- analýzy nákladov a iné oblasti pre podporu projektov.

Čaká ťa:

- práca s najmodernejšími technológiami v medzinárodnom tíme,
- odborné zaškolenie seniornými kolegami,
- jazykové vzdelávanie,
- sebarealizácia na zodpovednej pozícii s možnosťou odborného a profesijného rastu.

Schaeffler Kysuce
Dr. G. Schaefflera 1
02401 Kysucké Nové Mesto
SchaefflerKysuce@schaeffler.com

Schaeffler Skalica
Dr. G. Schaefflera 1
90901 Skalica
SchaefflerSkalica@schaeffler.com

www.emobility-schaeffler.sk
www.schaeffler.sk

Title: APPLIED MECHANICS 2024
Book of Articles

Editors: Milan VAŠKO
Ondrej PIROH
Marián HANDRIK
Jaroslav MAJKO

Published by: Department of Applied Mechanics
Faculty of Mechanical Engineering
University of Žilina
Univerzitná 8215/1, 010 26 Žilina

252 pages

All contributions in the proceedings were anonymously reviewed.

All papers were printed without linguistic proofreading.

ISBN 978-80-554-2090-5